THE UNIVERSITY
of ADELAIDE

The palaeoenvironmental context of Neoproterozoic carbon-isotope excursions

Robert M. Klaebe

Earth Sciences
School of Physical Sciences
The University of Adelaide

December 2015

Table of Contents

Supplementary appendices

Abstract

The Neoproterozoic record of sedimentary carbonates preserves > 20‰ of variability in carbon-isotope ($\delta^{13}C$) values that dwarfs the ~4‰ variability recorded in Phanerozoic marine carbonates known to record changes in the Earth's carbon cycle through time. When interpreted as primary seawater values, large magnitude $\delta^{13}C$ swings in Neoproterozoic strata are commonly interpreted to reflect significant changes to the biosphere that are causally related to the oxygenation of the Earth's atmosphere, global-scale glaciations and the evolution of complex metazoan life. This thesis considers each of the key isotopic features used to define the $\delta^{13}C$ record of Neoproterozoic seawater to identify the potential for local sedimentary controls on $\delta^{13}C$ variation versus global secular change by focussing on the origin of the host carbonate phases from which the $\delta^{13}C$ values are recorded.

The expected bias toward shallow-water intracratonic basins preserved in the Precambrian record predicts that intervals of the record are particularly susceptible to hydrologic restriction and physical isolation from marine connections. The Bitter Springs Formation of the Amadeus Basin in central Australia records a positive-negative-positive stratigraphic $\delta^{13}C$ trend in its upper Gillen Member. This $\delta^{13}C$ excursion has been termed the Bitter Springs Anomaly and is routinely used as a global stratigraphic tie point at ~800 Ma. A detailed sedimentological study of the Wallara-1 and BRO5 drill cores and two field sections in the Amadeus Basin reveal that two distinctly different facies associations occur, a lower unit of cyclic-bedded microbial and grainstone marine limestones and an upper unit of red beds and dolostones interbedded with evaporites and characterised by evidence of subaerial exposure and desiccation. The abrupt decline in recorded $\delta^{13}C$ values from +6‰ to -4‰ and the following recovery back to +6‰ occurs across the stratigraphic transitions between the evaporative lacustrine and shallow-marine carbonate intervals. Positive $\delta^{13}C$ values occur exclusively in the evaporative lacustrine facies and were likely modified locally by evaporative processes in a highly restricted sabkha-type basin, indicated by interbedded and nodular anhydrites, halite pseudomorphs and karstic dissolution. Where local facies changes to subaqueous cyclic stromatolitic facies are preserved, $\delta^{13}C$ values abruptly fall to -4‰ producing the binary isotopic shift that defines the Bitter Springs Anomaly here. The recurrence of this stratigraphic and isotopic association across the basin suggests that changes to local depositional conditions resulting from periodic hydrological restriction and evaporation explain the Bitter Springs Anomaly here rather than global isotopic change in a seawater value that should be decoupled from changes in local sediment composition.

The Trezona Formation in the South Australian Flinders Ranges records a -18‰ decline in $\delta^{13}C$ values stratigraphically below Marinoan-aged (~635 Ma) glacial deposits that is used to argue for a link between carbon cycle perturbations reflected in seawater DIC and global glaciation. A high resolution sedimentary study of 9 field sections across the Flinders Ranges shows that the lower Trezona Formation records evidence of deposition at or near base level, indicated by a sequence boundary at its base described by palaeosols and trough cross bedded channelised sandstones, and mud cracks and channelised siliciclastic (fluvial) deposits throughout. The upper Trezona Formation records an uninterrupted sequence of microbial and grainstone carbonates with little evidence of emergence. The vertical recovery from $\delta^{13}C$ values of -9‰ towards modest values of -2‰ begins across the facies change between lower Trezona Formation interbedded mudstones and limestones and upper Trezona Formation microbial limestones in each section examined, regardless of variations in the stratigraphic thickness of each unit. Indicators of shallow water and exposure coupled with the limited aerial distribution of the Trezona Formation describes a water body that was physically isolated during sea level fall and may have periodically supported phases of non-marine deposition. Here, the dominance of meteoric fluids bearing negative $\delta^{13}C$ values over seawater exchange allowed for a -9‰ carbonate phase to be precipitated that is likely primary,

but is unrepresentative of coeval seawater chemistry. This value then systematically recovered to -2‰ with changing sediment composition as local basinal conditions developed along a deepening trend, inconsistent with the shoaling upward trend toward glacial lowstand proposed by previous studies and obscuring the interpreted causal link between isotope values and the onset of glaciation.

The stratigraphic reproducibility of Neoproterozoic $\delta^{13}C$ profiles of similar age within and between basins provides a principal line of evidence supporting their utility as global chronological tie points and monitors of whole-ocean change. The upper Andrée Land Group of NE Greenland records a shift in $\delta^{13}C$ values from +6‰ to variable negative values of -4‰ to -10‰, before recovering to +6‰ stratigraphically below Sturtian-aged (~720 Ma) deposits interpreted as glaciogenic in origin, and is termed the Islay Anomaly. The upper platform to slope transition that precedes the onset of diamictite deposition was studied on Ella Ø in NE Greenland and compared to a lateral section on Kap Weber that was calibrated along two regionally traceable sequence boundaries, providing time-significant surfaces along which spatially disparate $\delta^{13}C$ profiles can be compared. In both sections, platform carbonates comprising dolomitised stromatolites, pisolitic limestones, and laminated microsparites exclusively record positive $\delta^{13}C$ values of ~+6‰ while dolomite-bearing siltstones, mudstones and carbonate debrites associated with slope deposition record negative values of -4‰ to -10‰. On Kap Weber, a return to positive $\delta^{13}C$ values follows slope-mudstone deposition coincident with a return to platform carbonate deposition that is absent on Ella Ø, which instead records negative $\delta^{13}C$ values into the base of Sturtian-aged glacial diamictites with no unconformity, confirmed by interbedding and soft sediment deformation across the facies transition. This disparity in terminal $\delta^{13}C$ values at the base of the glaciogenic Ulvesø Formation suggests that the most negative $\delta^{13}C$ values recorded in the basin (-10‰) occur broadly synchronous with values of +6‰, but are related to local sediment composition and the dominant process by which carbonate was precipitated on the platform versus the slope. Further, the onset of diamictite deposition occurs asynchronously across the basin, with a correlative conformity at the base of the Ulvesø Formation on Ella Ø corresponding to erosion and subaerial exposure on Kap Weber. Elemental mapping of slope mudstones shows that the carbonate phase that records the negative $\delta^{13}C$ values that define the Islay Anomaly here is a rhombic dolomite phase that is unsorted with surrounding sediment and associated with clays, organic matter and euhedral pyrite, supporting an authigenic origin associated with bacterial sulphate reduction that is not expected to constrain marine water-column $\delta^{13}C$ variation.

The Neoproterozoic $\delta^{13}C$ record in general preserves a positive 'background' value of approximately +6‰ that is punctuated by negative excursions. When interpreted in the same way as Phanerozoic deep-ocean records, sustained $\delta^{13}C$ values of +6‰ implies significantly elevated rates of global carbon burial as photosynthetic biomass, inconsistent with the low oxygen conditions during the Neoproterozoic. While Cenozoic deep-marine pelagic sediments record $\delta^{13}C$ values as positive as +2.5‰, a compilation of coeval platform carbonates shows values as positive as +6‰ attributed to photosynthetic effects under hydrologically restricted conditions. Positive $\delta^{13}C$ values from eight different Neoproterozoic sections from Australia, NW Canada, East Svalbard and NE Greenland, including six intervals that preserve analogous carbonate platform sedimentation as thick packages of microbial and grainstone carbonates, karstic features, desiccation cracks and dolomitisation, are compared with these modern data and are shown to largely plot within the < +6‰ range of $\delta^{13}C$ variation. As the majority of Neoproterozoic carbonate successions are known to have accumulated above carbonate platforms and ramps, in inland seas, and in other cratonic and transitional-marginal environments, it is proposed that some portion of the positive background $\delta^{13}C$ value reflects the inherent bias in Neoproterozoic stratigraphy towards these types of depositional conditions.

Declaration

I certify that this work contains no material which has been accepted for the award of any other degree or diploma in my name in any university or other tertiary institution and, to the best of my knowledge and belief, contains no material previously published or written by another person, except where due reference has been made in the text. In addition, I certify that no part of this work will, in the future, be used in a submission in my name for any other degree or diploma in any university or other tertiary institution without the prior approval of the University of Adelaide and where applicable, any partner institution responsible for the joint award of this degree.

I give consent to this copy of my thesis, when deposited in the University Library, being made available for loan and photocopying, subject to the provisions of the Copyright Act 1968.

I also give permission for the digital version of my thesis to be made available on the web, via the University's digital research repository, the Library Search and also through web search engines, unless permission has been granted by the University to restrict access for a period of time.

Robert M. Klaebe

Acknowledgements

First and foremost I would like to thank my supervisor Prof. Martin Kennedy for his guidance over the last few years. Martin's encouragement, honesty, clarity of thought and both academic and financial support has been critical throughout the term of my candidature and this work and the great opportunities I've had would not have been possible without him. His commitment to pursuing the scientific method in its purest form has undoubtedly made me a better scientist and for that I am especially grateful.

Thanks also to my co-supervisor Prof. Ian Fairchild for his ongoing support, discussion and feedback of my work. In particular I am indebted to Ian for providing the opportunity to participate in a 5 week field season on Ella Ø in remote East Greenland in 2012; this was indeed a life-changing experience. Very special thanks go to Prof. Paul Smith who generously volunteered to act as my informal supervisor and field assistant for the duration of this field trip, I could not have asked for a better mentor to have stepped in and I am extremely grateful. Thanks to GAINS and the rest of the Ella Ø field team: Carl Stevenson, Edward Fleming, Michael Hambrey and Mike Petronis, John, Jon and Sarah the fossil hunters, Frederick in particular for keeping us alive on the fjords, as well as the Sirius guys, all of whom enriched such a wonderful experience.

Thanks to the Sprigg Geobiology centre for their comradery and discussion of all things geological, in particular Lisa Baruch and Stefan Löhr for their support, advice and ongoing help with analyses. Special thanks go to Alex Corrick for his many weeks helping out in the field, often at a single day's notice, Mark Rollog for his time spent helping collect my isotope data, and Tony Hall for solving just about every problem I presented him with. I thank all the other Adelaide University academic and professional staff and fellow postgraduate students for making my time here memorable. I acknowledge and thank my examiners Prof. Paul Knauth and Prof. Peter Swart who provided valuable advice and comments that improved this thesis greatly.

Many thanks to the DENR, Flinders Ranges pastoralists, the Yellow Footed Rock Wallaby Preservation Association and of course the traditional owners of the Flinders Ranges region, the Adnyamathanha people, for land access during field work in South Australia. Jane and Bill from Gum Creek Station, Kaz Herbst, Jim Kennelly, Kym Groves and the Coulthard family are thanked in particular. Thanks to the NTGS and the staff at the Alice Springs core library, and to Ross River Station for access to samples and their hospitality respectively during my work in central Australia.

I'd like to acknowledge and dearly thank my family and friends who showed limitless patience and support for me over the years. In particular Mum, Dad, James and Jess with whom I've grown with my entire life, I dedicate all of my accomplishments to you. Finally, words cannot express my gratitude to Katie who supported me through all the ups and downs, late nights, weekends in the lab and months away in the field over the last few years, I cannot imagine having done this without you.

Chapter 1

Introduction and theoretical framework

1. Introduction

The Ediacaran period marks the abrupt appearance of complex multicellular life on Earth following 3 billion years of simple single-celled organisms as the Earth's only inhabitants (Knoll, 2004). The evolution and rapid diversification of complex life is thought to be triggered by changes to the Earth's biosphere. The nature of this environmental change represents a fundamental question in geobiology and is a topic of vigorous debate in the scientific community (Knoll and Carroll, 1999; Hoffman and Schrag, 2002; Grey et al., 2003; Narbonne and Gehling, 2003; Kennedy et al., 2006). Coupled with the first physical evidence of complex animals in the geologic record is the increase in atmospheric oxygen required to support their radiation (Runnegar, 1982; Knoll et al., 2006; Payne et al., 2009; Kump et al., 2011), and a series of climatic events of interpreted global influence (Kirschvink, 1992; Hoffman et al., 1998; Sohl et al., 1999; Abbot et al., 2011), that at face-value describe a highly dynamic and systematically different Earth-system that changed into the Ediacaran (Figure 1). As the oxygenation of the Earth's atmosphere and oceans, proliferation of complex metazoan life, and the movement of carbon between Earth's surface reservoirs are processes thought to be intrinsically linked, understanding past changes in the Earth's carbon cycle is fundamental in interpreting the environmental conditions that lead to the most significant evolutionary step in Earth history.

Changes in the carbon isotopic ($\delta^{13}C$) composition of marine carbonate-bearing sediments directly inform our understanding of the state of Earth's carbon cycle through time. Following the observation of isotopic fractionation of carbon during photosynthesis (Urey, 1948), the balance of ^{13}C to ^{12}C (expressed as $\delta^{13}C$ in per mil [‰] compared to VPDB [Vienna Pee Dee Belemnite]) in the ocean-atmosphere system has been used to monitor the movement of carbon between Earth's surface reservoirs through time. As the synthesis of primary organic matter through photosynthetic pathways preferentially selects the light isotope of carbon (^{12}C), generated organic biomass is significantly depleted in ^{13}C relative to dissolved inorganic carbon (DIC) in seawater. The burial and storage of organic carbon in sedimentary rocks effectively removes from the Earth's surface environment. The carbon isotope mass-balance of the Earth's surface reservoir can thus be expressed as:

$$\delta^{13}C_{in} = \delta^{13}C_{org} f_{org} + \delta^{13}C_{carb}(1 - f_{org})$$

$\delta^{13}C_{in}$ = surface reservoir inputs

$\delta^{13}C_{org}$ = organic carbon burial flux

$\delta^{13}C_{carb}$ = inorganic carbon burial flux

f_{org} = fractional burial of organic versus inorganic carbon

Where ($\delta^{13}C_{in}$) is the isotopic value of the input flux of carbon to the Earth's surface reservoirs and $\delta^{13}C_{carb}$ / $\delta^{13}C_{org}$ are the values for the burial fluxes of organic carbon as biomass and inorganic carbon as calcium carbonate respectively into sedimentary archives. In the modern Earth system, the carbon input flux ($\delta^{13}C_{in}$) includes the outgassing of mantle carbon, return of carbon as CO_2 from the subduction and metamorphism of oceanic carbon reservoirs, and the weathering of carbonate and organic matter on the continents, carrying an average $\delta^{13}C$ value of ~-5‰ (Kump, 1991; Kump and Arthur, 1999). Organic carbon carries $\delta^{13}C$ values of around -25‰, the burial of which balances the Earth's surface carbon inputs to approximately 0‰ for much of the Phanerozoic (Hayes et al., 1999; Zachos et al., 2001). Where marine carbonate has precipitated in equilibrium with seawater DIC, variations in the fractional burial of organic carbon relative to carbonate carbon (f_{org}) should be expressed in the marine carbonate record through geologic time.

This framework guides the interpretation of $\delta^{13}C$ variations recorded by marine carbonates as a monitor for

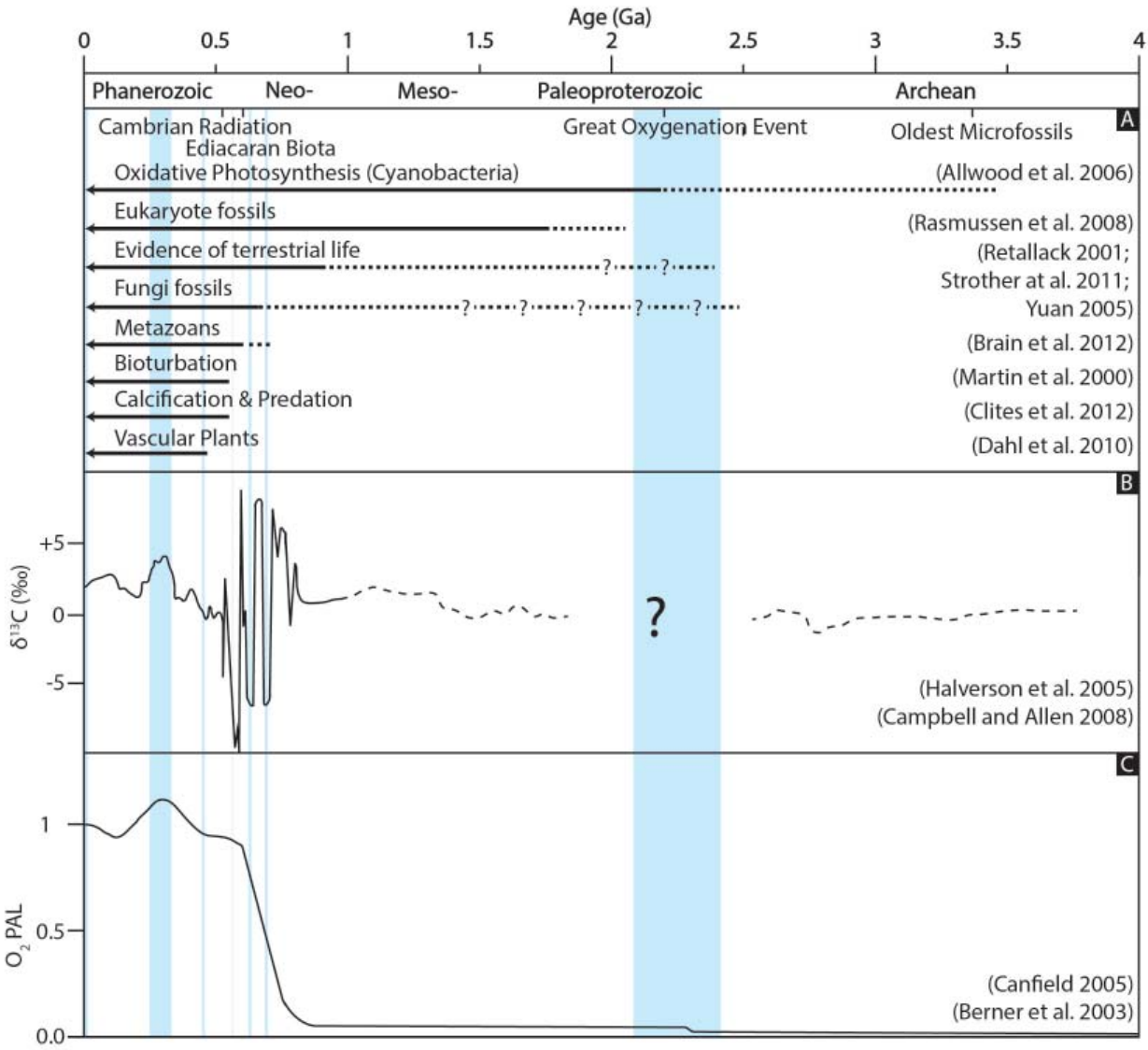

Figure 1. Summary of the major evolutionary and biospheric events in the Earth System after Kennedy (2013). A) Putative fossil evidence (solid lines) and possible examples and/or predicted ranges of major evolutionary events (dashed lines). The first evidence of complex metazoan life occurs during the late Neoproterozoic and is quickly followed by occurrences of more advanced biological developments such as calcification. These changes are superimposed over interpreted evidence for pan-glaciation (blue panels), extreme $\delta^{13}C$ variability (B) and the calculated increase in atmospheric pO_2 (C). B) The synthesised $\delta^{13}C$ record of the past 4 billion years. Phanerozoic values from marine carbonate show significantly less variability compared to the Neoproterozoic record that preserves $\delta^{13}C$ ranges > 20‰. Data prior to the Neoproterozoic is scarce and often altered through metamorphism. C) Estimates of atmospheric oxygen concentration through Earth history. Two major increases in O_2 concentration are identified at 2.2 Ga and during the Neoproterozoic.

changes in the ocean-atmosphere system throughout Earth's history. Cenozoic $\delta^{13}C$ records preserve $\delta^{13}C$ variability of ~2‰ as multi-million year trends recorded in deep-ocean carbonate archives that reflect steady-state changes in the global rates of organic carbon burial versus rates of carbon liberation through oxidative continental weathering (Zachos et al., 2001). The magnitude of $\delta^{13}C$ variability increases to 0 ± 4‰ in marine

sedimentary records older than the Mesozoic (Veizer et al., 1999), that in part reflects major evolutionary events such as the proliferation of terrestrial plants that periodically increased the volume of terrestrial biomass and thus net burial of organic carbon and is expressed as elevated $\delta^{13}C$ values in late Palaeozoic sedimentary records (Broecker, 1970). $\delta^{13}C$ variability increases dramatically in the Precambrian sedimentary record where $\delta^{13}C$ values as high as +10‰ and as low as -12‰ are documented and shifts of > 10‰ between anomalous values are common (Shields and Veizer, 2002). As global trends in ocean-atmosphere $\delta^{13}C$ are intrinsically linked to the burial of organic carbon, satisfying anomalous values of the observed magnitude in atmospheric equilibrium requires a fundamental reorganisation of the Earth's carbon cycle that is at odds with present understanding of the Earth's carbon and oxidant budgets (Bristow and Kennedy, 2008). As the $\delta^{13}C$ value of the Earth's surface reservoir carbon inputs is approximately -5‰, values on the order of -12‰ that persist for millions of years at steady-state (Le Guerroue et al., 2006) are challenging to explain (Melezhik et al., 2005; Bristow and Kennedy, 2008). While non-steady state processes such as methane destabilisation and release are shown to produce excursions in seawater to negative $\delta^{13}C$ values during the Phanerozoic, these are transient excursions of -2‰ to -3‰ and are orders of magnitude shorter in duration than those interpreted in the Neoproterozoic (eg. Dickens et al., 1995). Models offered by previous authors such as the collapse of all photosynthetic productivity (Hoffman et al., 1998) the oxidation of a large reservoir of suspended organic carbon in the oceans (Fike et al., 2006), and the slow oxidation of a large methanogenic pool in deep-ocean sediments (Bjerrum and Canfield, 2011) rely on catastrophic perturbations to the biosphere and/or hypothetically expanded carbon reservoirs that are difficult to confirm using primary geological evidence. In contrast, under the basic framework discussed above sustained $\delta^{13}C$-carb values > +5‰ imply a staggering increase in the global rates of organic carbon burial and/or a significant decrease in rates of continental oxidative weathering (Knoll et al., 1986; Kump et al., 2011). Either of these changes should lead to a significant net increase in atmospheric oxygen which is at odds with current calculations and geologic evidence of Precambrian oxygen availability which was limited in the Neoproterozoic compare to the modern atmospheric levels (Catling and Claire, 2005; Lyons et al., 2014). The difficulty in resolving large magnitude binary swings in Precambrian $\delta^{13}C$ records under our current understanding of global carbon-cycle dynamics indicates that a level of complexity may exist in these records that is routinely overlooked.

2. Carbon-isotope chemostratigraphy in the Neoproterozoic

Despite the origin of anomalous Precambrian $\delta^{13}C$ values being unresolved and it being uncertain whether they record comparable oceanographic processes to those active in the Phanerozoic, the $\delta^{13}C$ record of Neoproterozoic carbonates is increasingly utilised as a stratigraphic tool to support the correlation of sedimentary successions between basins (Kaufman and Knoll, 1995; Halverson et al., 2005). This is particularly true for Precambrian sedimentary archives where radiometric ages and other independent time constraints such as high resolution biostratigraphic records used to confirm stratigraphic correlations in the Phanerozoic are absent. The correlation of $\delta^{13}C$ stratigraphic records between Precambrian successions often relies on fragments of carbonate-bearing stratigraphy that are pieced together based on similarities in the shape, magnitude and inferred duration of vertical $\delta^{13}C$ patterns. These patterns are broadly calibrated by associations with other interpreted time significant features such as deposits associated with glacial environments thought to represent discrete global ice ages, post-glacial cap carbonate sequences, and radiometric ages where ash-beds or other suitable igneous deposits are present. The construction of these records provide a continuous history of $\delta^{13}C$ variation through time that is interpreted to be representative of secular changes in the seawater $\delta^{13}C$ composition (Halverson et al., 2005;

Shields-Zhou et al., 2012) that increasingly constrains the chronology of the Neoproterozoic Era, even providing criteria for the ratification of geological time at a period-level (Knoll et al., 2004).

This method of stratigraphic correlation of Neoproterozoic sedimentary successions is supported by a recurring tripartite motif of isotopic and sedimentological features that is interpreted to have been emplaced globally in response to the Earth's most severe climatic events (Hoffman et al., 1998; Sohl et al., 1999; Fairchild and Kennedy, 2007). Abrupt excursions in $\delta^{13}C$ values to ~-10‰ recorded in carbonate sedimentary rocks are commonly overlain by diamictite and interpreted glaciomarine facies that are further overlain by distinctive 'cap carbonate' deposits. This recurring sequence is documented at similarly-aged stratigraphic intervals on nearly all continents (eg. James et al., 2001; McKirdy et al., 2001; Halverson et al., 2002; Halverson et al., 2004; Caxito et al., 2012), leading to the interpretation of a series of climatic events of global extent termed 'Snowball Earth' climate states (Kirschvink, 1992; Hoffman et al., 1998; Hoffman and Schrag, 2002; Schrag et al., 2002). Because they directly precede glaciogenic deposits, stratigraphic negative $\delta^{13}C$ excursions to values of -10‰ are thought to be intimately linked to the onset of pan-glaciation. While two episodes of glaciation are established as the Sturtian and Marinoan glacial epochs (Kennedy et al., 1998) at ~720Ma and ~635Ma respectively, the scale and duration of these events remains speculative (Hoffman et al., 1998; Eyles and Januszczak, 2004; Abbot et al., 2011). Regardless, the recurring appearance of pre-glacial negative excursions and post-glacial cap-carbonates provides a general framework by which $\delta^{13}C$ records can be broadly calibrated and supports their interpretation as a global-scale phenomenon. This interpretation however approaches circularity where the motif of negative $\delta^{13}C$ values that precede glaciogenic deposits is considered globally coeval as it is thought to equally record the same biospheric event that these very features fundamentally establish.

3. The case for diagenesis

The $\delta^{13}C$ value of any given carbonate mineral phase fundamentally records the isotopic balance of the precipitating fluid. As such, $\delta^{13}C$ variations are also used as a monitor for a range of other processes that are not necessarily of global influence. A growing body of literature now exists that challenges whether large-magnitude $\delta^{13}C$ excursions recorded in the Neoproterozoic stratigraphic record are representative of past ocean-water chemistry, preferring an alternative interpretation of post-depositional alteration of an originally marine carbonate phase (Knauth and Kennedy, 2009; Derry, 2010; Frimmel, 2010; Swart and Kennedy, 2011; Schrag et al., 2013). All marine carbonate is initially precipitated as metastable carbonate minerals, most commonly calcite and aragonite. In the Phanerozoic the bulk of this carbonate is secreted as shells by marine organisms while the majority of Precambrian carbonate is likely to be microbially mediated. During lithification, primary carbonate precipitates are dissolved and recrystallise into more stable mozaics of calcite and/or dolomite spar through early diagenetic reactions, where mixing and re-equilibration is achieved between the mineral phases and ambient pore fluids (Land, 1986). These types of early diagenetic reactions are well understood in the Phanerozoic to be capable of altering and overprinting primary isotopic values and producing negative $\delta^{13}C$ excursions of similar magnitude and stratigraphic thickness to those observed in Neoproterozoic records (Melim et al., 2002; Swart and Eberli, 2005), and have been directly compared (Swart and Kennedy, 2011). In these examples, meteoric fluids are incorporated into shallowly-buried marine sediments across the continental shelf as surficial outflows and through groundwater discharge that mix with marine fluids in the pore space of unlithified or semi-lithified carbonate sediment. Meteoric fluids are characteristically depleted in their oxygen-isotopic composition ($\delta^{18}O$) and are capable of acquiring $\delta^{13}C$ values of DIC on the order of -25‰ that are derived from the oxidative degradation of organic carbon (Irwin et al., 1977; Fogel and Cifuentes, 1993). The mixing

of meteoric waters with marine pore fluids can drive the precipitation of carbonate phases that carry negative $\delta^{13}C$ and $\delta^{18}O$ values over hundreds ofmetres of stratigraphy, producing a vertical stratigraphic trend of similar magnitude and shape to many Neoproterozoic negative $\delta^{13}C$ excursions that is seemingly unrelated to original seawater chemistry (Swart and Kennedy, 2011). This process is best demonstrated in Pleistocene-aged sediment cores taken on the Great Bahama Bank where a well-documented stratigraphic excursion in $\delta^{13}C$ from anomalously enriched values as high as +6‰ is shown to gradually decline to a minimum of -10‰ in carbonate precipitates that were bathed in meteoric waters during sealevel drawdown and subaerial exposure (Swart and Eberli, 2005; Swart and Kennedy, 2011). Subsequent fluid-rock interactions between lithified carbonates and high pCO_2 burial fluids that carry negative $\delta^{13}C$ values of DIC have also been shown capable of producing or enhancing large magnitude negative $\delta^{13}C$ excursions (Derry, 2010). While tests for a dominantly diagenetic influence on preserved $\delta^{13}C$ values is standard practice in chemostratigraphic studies of Neoproterozoic carbonate successions, actual diagnostic parameters for or against a diagenetic origin for these values are vague and often rely on the subjective interpretation of cryptic petrographic textures and trace-element ratios as proxies for recrystallisation. More often, the reproducibility of a discrete $\delta^{13}C$ signal within and between basins globally is cited as unequivocal evidence for a primary whole-ocean origin (Husson et al., 2015).

4. Comparisons with the Cenozoic record

The construction and use of synthetic $\delta^{13}C$ records as monitors for global changes in the Earth's biosphere fundamentally relies on the assumption that the carbonate precipitates recording anomalous $\delta^{13}C$ values mineralised in equilibrium with atmospheric CO_2 and therefore reflect changes in this reservoir. In Cenozoic marine records, $\delta^{13}C$ values are predominantly derived from deep-water accumulations of carbonate shells that were secreted by planktonic organisms in the well-mixed surface waters of the open ocean (Zachos et al., 2001). These types of deposits are ideal recorders of seawater $\delta^{13}C$ variations as they accumulate beyond the influence of subtle variations in sea level as well as terrestrial clastic and fluid inputs, can be precisely calibrated along a number of other independent proxies and chronostratigraphic frameworks, and provide a relatively uninterrupted record of sedimentation. Further, mechanisms such as 'vital effects' that can influence the recorded $\delta^{13}C$ values in secreted calcareous shells can be accounted for (Grossman, 1987; Weiner and Dove, 2003; Ziveri et al., 2003) to ensure that the controlling function on $\delta^{13}C$ variation that is recorded is atmospheric exchange. The dominant mechanisms that control $\delta^{13}C$ variability in Precambrian carbonate-bearing successions are more ambiguous as the prevailing mode of carbonate accumulation is necessarily different. First, the pelagic flux of biogenic carbonate secreted by marine planktonic organisms does not exist prior to the Cambrian where the appearance and radiation of marine calcifiers is first apparent. The vast majority of Precambrian carbonate was therefore directly precipitated by microbial, evaporative and diagenetic processes under often cryptic palaeoenvironmental conditions. Second, all Precambrian carbonate accumulated in marginal marine basins, intracratonic seaways and in non-marine basins above continental crust. There are no deep-ocean records older than the Mesozoic as they have since been subducted. In the absence of the marine skeletal flux that dominates carbonate deposition in modern offshore environments, the deepest-water (generally outer slope) marine carbonate sediment that is preserved in the Neoproterozoic record exists either as detrital grains eroded and swept from landward shallow-water environments of enigmatic palaeoenvironmental origin during storms, as authigenic and/or diagenetic phases in organic-rich, fine-grained sediment, or as cryptic inorganic carbonate muds and whitings.

5. Palaeoenvironmental constraints on Neoproterozoic $\delta^{13}C$ excursions

Given these considerations, an alternative explanation exists for many Neoproterozoic $\delta^{13}C$ excursions and is the subject of this thesis. As the Neoproterozoic stratigraphic record is expected to be biased toward marginal and intracratonic environments, it is expected to be inherently sensitive to minor variations in sea level. Where deep-ocean environments are largely insensitive to sea-level rise or fall of a fewmetres, in coeval shallow-water marginal environments shorelines are capable of migrating hundreds of kilometres leading to abrupt changes in local palaeoenvironmental conditions. The records of $\delta^{13}C$ change preserved within this archive should first be considered under these constraints before global correlations and biospheric models can be confidently established. Modern analogues of marine, restricted marine, and terrestrial environments that accumulate carbonate routinely show significant spatial gradients in $\delta^{13}C$ that are unrelated to global values (Figure 2). The degree of $\delta^{13}C$ decoupling between cratonic and open-ocean settings in the Cenozoic appears to rely largely on their connectivity, terrestrial hydrologic regime, and rates of primary production. The influence of these effects is diluted in the open ocean, but have increasing influence as a basin becomes increasingly hydrologically restricted. For example, a comparison of deep-ocean sediment cores with surface sediment and drill core from the shallow Great Bahama Bank shows a systematic increase in $\delta^{13}C$ in aragonitic bank-top sediments of up to +6‰ (Melim, 2001; Swart and Eberli, 2005) compared to precisely correlated pelagic equivalents (Miller and Katz, 1987; Shackleton, 1987; Zachos et al., 2001). Further, as sea level fell across the platform, meteoric fluids carrying depleted $\delta^{13}C_{DIC}$ repeatedly bathed the unlithified sediment and altered these values to as low as -10‰, producing a binary $\delta^{13}C$ signal resulting from modest sea-level variation and entirely unrelated to changes in whole-ocean chemistry (Swart and Eberli, 2005). Maximum $\delta^{13}C$ values of +5.5‰ and +4.5‰ are preserved in other marginal basins in both skeletal and non-skeletal allochems, on the modern Belize-Yucatan platform and Kuwait ramp in the Persian Gulf respectively (Gischler and Lomando, 2005; Gischler et al., 2007). In both cases, these shallow-marine carbonate sediments that accumulate primarily under subaqueous conditions are up to 6‰ more enriched compared to coeval deep-water pelagic sediments and thus do not record open-ocean and atmospheric $\delta^{13}C$ values. In the Persian Gulf, $\delta^{13}C$ can vary by ~5‰ over just 15 km laterally (Gischler and Lomando, 2005). In more restricted environments, or basins that are physically isolated from marine connections during sea-level fall, the capacity of $\delta^{13}C$ values to decouple from seawater increases significantly.

The nature of $\delta^{13}C$ data allows two directions of change compared to seawater values of ~0‰. Positive $\delta^{13}C$ values in poorly-connected marine basins and in isolated terrestrial environments are largely the product of evaporation rates and local photosynthetic fractionation versus marine mixing and/or freshwater influx. Evaporating brines are shown to be enriched in $\delta^{13}C$ compared to marine and meteoric waters due to the fractionation of ^{12}C during evasion of CO_2 (Stiller et al., 1985). Other isolated (lacustrine) environments return comparable values in DIC ranging from +5‰ to as high as +26.4‰ resulting from a combination of enhanced evaporation, photosynthetic effects, and pore-fluid methanogenesis (Talbot and Kelts, 1986; Valero-Garces et al., 1999; Lamb et al., 2000; Gu et al., 2004; Rosqvist et al., 2007; Zhu et al., 2013). The decline of $\delta^{13}C$ values in unaltered carbonates under hydrologically restricted conditions is largely controlled by meteoric mixing where organic matter degradation is a major source of DIC or by in-situ organic matter degradation. As photosynthetically-fractionated carbon is depleted with respect to ^{13}C, locally depleted waters are often associated with the input of detrital organic carbon or dissolved organic acids (Talbot, 1990; Knauth and Kennedy, 2009). Under these conditions, $\delta^{13}C$ values of -30‰ have been reported while values ~-10‰ are common (Talbot, 1990; Bade et al., 2004). While comparable non-marine deposits are largely under-represented in the Neoproterozoic literature, they comprise a signifi-

cant proportion of depositional environments that accumulate carbonate in the modern Earth (Figure 2).

The assessment of $\delta^{13}C$ records as a chronostratigraphic tool and monitor of carbon cycle perturbations unique to the Neoproterozoic relies on an intimate understanding of each $\delta^{13}C$ feature in isolation and in the context of the local palaeoenvironmental conditions that may have influenced it. Where the reproducibility of Neoproterozoic $\delta^{13}C$ patterns is commonly taken as primary evidence for their coeval and global extent, the internal systematic variation between different isotopic systems and palaeoenvironmental parameters should be diagnostic of a local control on $\delta^{13}C$ (Kaufman and Knoll, 1995). As all Neoproterozoic carbonate is expected to accumulate within the influence of sea-level variation that can be tectonically or climatically driven, with the possible exception of carbonate phases precipitated during later burial, abrupt variations in water depth and the migration of shorelines is expected to be tracked by local variations in various geochemical parameters as local basin hydrology opens to marine connections or is restricted behind connecting sills and undergoes transient restricted to non-marine conditions. Analogous studies of Silurian-Ordovician aged intracontinental seaways show systematic time-significant lateral gradients in $\delta^{13}C$ related to the relative influence of various local-scale carbon cycling processes, variations in which may be forced by variations in relative base-level (Melchin and Holmden, 2006; Panchuk et al., 2006; Fanton and Holmden, 2007). A negative covariation between $\delta^{13}C$ and $\delta^{44/40}Ca$ values and a co-occurrence of isotopic inflection points and major lithological reorganisations during the Hirnantian Glaciation event indicate that these parameters can be forced by base-level in a hydrologically-restricted intracratonic basin (Holmden et al., 2012). Other indicators of seawater decoupling include covariant trends between $\delta^{13}C$ and $\delta^{18}O$ that are linked to residence time effects under hydrologically closed basinal conditions and common in modern palaeolimnological studies (Talbot, 1990). In these examples, stratigraphic variations in $\delta^{13}C$ are considered in the context of the host palaeoenvironment where anomalous isotopic values can be linked to processes of basinal rather than global influence, and are confirmed with biostratigraphic data. It is possible that these types of processes also impart a first-order control on many Neoproterozoic $\delta^{13}C$ excursions.

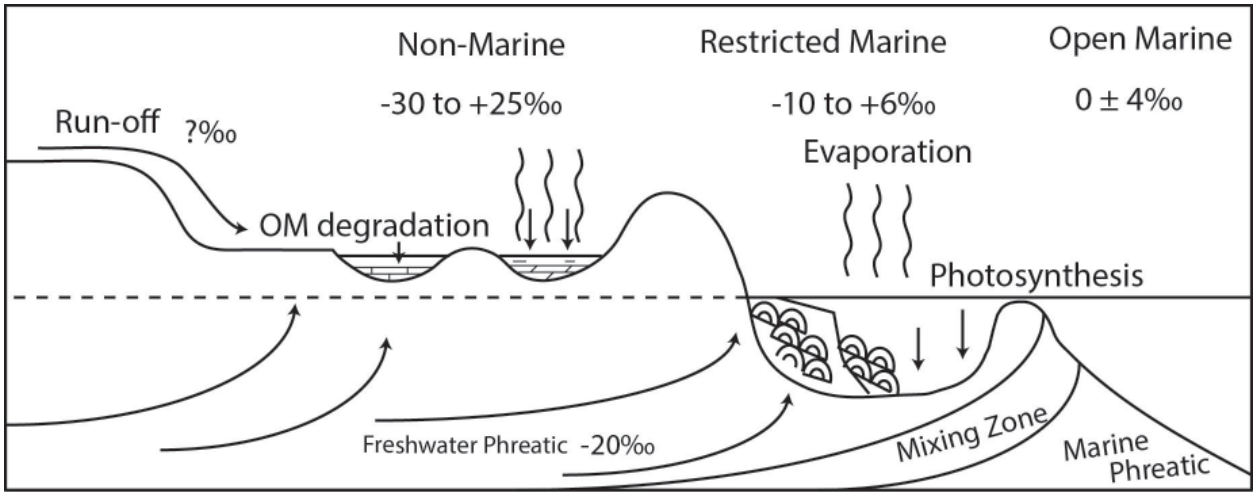

Figure 2. Summary of processes that contribute to lateral $\delta^{13}C$ gradients in shallow-water carbonate depositional environments. While these processes are diluted in the open ocean, they impart a significant effect on the $\delta^{13}C$ values recorded by precipitating carbonate mineral phases where complete mixing with marine waters is not achieved.

6. Project aims

The aims of this project are:

1. To investigate the influence of palaeoenvironmental conditions that are isotopically decoupled from contemporaneous seawater on the construction of synthetic Neoproterozoic-aged carbon-isotope records.

2. To provide geological context to a number of the major carbon-isotopic features that characterise the Neoproterozoic stratigraphic record.

3. To test chemostratigraphic timelines using independent physical frameworks in order to investigate whether carbon-isotopic patterns between individual sections in Neoproterozoic strata can be shown to be coeval.

7. Thesis outline

Chapter 2 examines the Bitter Springs Anomaly $\delta^{13}C$ excursion as it is preserved in its type section in central Australia. While previous interpretations of the Bitter Springs Formation is that much of its deposition occurred under non-marine, hyper evaporative conditions, the Bitter Springs Anomaly is widely considered a robust stratigraphic marker and indicator of carbon cycle perturbations that is notably unrelated to Neoproterozoic glaciation. Paired sedimentological and stable-isotopic ($\delta^{13}C$ and $\delta^{18}O$) data show that the isotopic variability that defines the Bitter Springs Anomaly is facies-dependent. The inflection points from positive (+5‰) to negative (-4‰) $\delta^{13}C$ values that define the excursion occur systematically with major lithofacies changes from evaporative lacustrine environments to restricted marine carbonates respectively. This study highlights the ease by which a simple binary $\delta^{13}C$ signal can be produced in an isolated basin as a direct response to variations in base-level that act to sever marine connections and decouple ambient DIC from that of seawater.

Chapter 3 re-interprets the depositional environment of the Trezona Formation in the South Australian Flinders Ranges and considers the observed stratigraphic $\delta^{13}C$ variation (the Trezona Anomaly) in terms of changes in local basinal conditions. An unconformity documented at the base of the Trezona Formation, coupled with it's restricted spatial distribution and physical evidence of shallow-water to exposure as mud cracks and fluvial deposits indicates that $\delta^{13}C$ values of -9‰ recorded as the Trezona Anomaly accumulated under highly restricted and periodically lacustrine conditions. As the basin opened, a reproducible facies change from calcareous muds and intraclastic carbonate to microbial mats and oolitic shoals is tracked by a recovery in $\delta^{13}C$ values from -9‰ to as high as -2‰. As internally systematic $\delta^{13}C$ variability tracks changes in lithofacies, the Trezona Anomaly in its type section in South Australia is more consistent with a record of local carbon cycling processes than whole ocean change, where sea-level fall behind a connecting sill periodically isolated the basin from marine connections.

Chapter 4 provides a stratigraphic test for the timing and reproducibility of the pre-Sturtian Islay Anomaly $\delta^{13}C$ excursion in ramp and slope carbonates in the North-East Greenland Caledonides, as well as investigates the sequence of basinal sea level events that lead in to the Sturtian Glaciation at this locality. Here, sustained enriched $\delta^{13}C$ values of +6‰ are recorded in shallow-water marginal limestones and dolostones that precede a negative excursion to $\delta^{13}C$ values as low as -10‰ (the Islay Anomaly) and interpreted glaciogenic sediments correlated as Sturtian in age. The onset of the Islay Anomaly in NE Greenland corresponds to a major flooding event that drowned the carbonate ramp and superimposed slope-facies calcareous mudstones carrying highly-depleted $\delta^{13}C$ values above enriched platform sediments. The mineralogy that hosts depleted $\delta^{13}C$ values is preserved as an authigenic dolomitic phase that is best interpreted as catalysed by bacterial sulphate reduction of organic carbon under anoxic conditions in the sediment column and is thus unrelated to seawater chemistry. Further, a conformable contact between terminal carbonate-bearing sediment and the base of the Sturtian-aged Ulvesø Formation presents a

situation where either the recorded $\delta^{13}C$ signal, onset of (interpreted global) diamictite deposition, or both, are strongly diachronous across the basin, a geologic and geochemical condition that is inconsistent with a global origin of $\delta^{13}C$ values.

Chapter 5 compiles several thousand published and newly generated $\delta^{13}C$ and $\delta^{18}O$ data in order to assess the influence of typical shallow-water carbonate platform variability on the construction of Neoproterozoic $\delta^{13}C$ curves. These data demonstrate that the enriched background $\delta^{13}C$ values recorded through much of the Neoproterozoic carbonate record plots largely within the range of $\delta^{13}C$ values common to modern carbonate platforms and ramps. In the closest Cenozoic analogues to Neoproterozoic marginal carbonate deposits, $\delta^{13}C$ values are decoupled with coeval deep-ocean carbonate accumulations that sample the surface waters of the open ocean, indicating that bank top enrichment of non-skeletal carbonates occurs artificially under poorly circulated marine waters influenced by enhanced autotrophic fractionation and evaporation. While many of the Neoproterozoic data considered fall within this domain, values > +6‰ may have been further influenced by the effects on $\delta^{13}C$ during the transformation of primary aragonite and calcite to diagenetic dolomite or in extreme cases, may have been periodically isolated entirely from marine connections.

Chapter 6 offers concluding statements and some implications for the major findings of this project.

References Cited

Abbot, D. S., Voigt, A., and Koll, D., 2011, The Jormungand global climate state and implications for Neoproterozoic glaciations: Journal of Geophysical Research-Atmospheres, v. 116.

Bade, D. L., Carpenter, S. R., Cole, J. J., Hanson, P. C., and Hesslein, R. H., 2004, Controls of $\delta^{13}C$-DIC in lakes: Geochemistry, lake metabolism, and morphometry: Limnology and Oceanography, v. 49, no. 4, p. 1160-1172.

Bjerrum, C. J., and Canfield, D. E., 2011, Towards a quantitative understanding of the late Neoproterozoic carbon cycle: Proceedings of the National Academy of Sciences of the United States of America, v. 108, no. 14, p. 5542-5547.

Bristow, T. F., and Kennedy, M. J., 2008, Carbon isotope excursions and the oxidant budget of the Ediacaran atmosphere and ocean: Geology, v. 36, no. 11, p. 863-866.

Broecker, W. S., 1970, A boundary condition on the evolution of atmospheric oxygen: Journal of Geophysical Research, v. 75, no. 18, p. 3553-3557.

Catling, D. C., and Claire, M. W., 2005, How Earth's atmosphere evolved to an oxic state: a status report: Earth and Planetary Science Letters, v. 237, no. 1, p. 1-20.

Caxito, F. A., Halverson, G. P., Uhlein, A., Stevenson, R., Gonçalves Dias, T., and Uhlein, G. J., 2012, Marinoan glaciation in east central Brazil: Precambrian Research, v. 200, p. 38-58.

Derry, L. A., 2010, A burial diagenesis origin for the Ediacaran Shuram-Wonoka carbon isotope anomaly: Earth and Planetary Science Letters, v. 294, no. 1-2, p. 152-162.

Dickens, G. R., Oneil, J. R., Rea, D. K., and Owen, R. M., 1995, Dissociation of oceanic methane hydrate as a cause of the carbon-isotope excursion at the end of the Paleocene: Paleoceanography, v. 10, no. 6, p. 965-971.

Eyles, N., and Januszczak, N., 2004, 'Zipper-rift': a tectonic model for Neoproterozoic glaciations during the breakup of Rodinia after 750 Ma: Earth-Science Reviews, v. 65, no. 1, p. 1-73.

Fairchild, I. J., and Kennedy, M. J., 2007, Neoproterozoic glaciation in the earth system: Journal of the Geological Society, v. 164, p. 895-921.

Fanton, K. C., and Holmden, C., 2007, Sea-level forcing of carbon isotope excursions in epeiric seas: implications for chemostratigraphy: Canadian Journal of Earth Sciences, v. 44, no. 6, p. 807-818.

Fike, D. A., Grotzinger, J. P., Pratt, L. M., and Summons, R. E., 2006, Oxidation of the Ediacaran Ocean: Nature, v. 444, no. 7120, p. 744-747.

Fogel, M. L., and Cifuentes, L. A., 1993, Isotope fractionation during primary production, Organic geochemistry, Springer, p. 73-98.

Frimmel, H. E., 2010, On the reliability of stable carbon isotopes for Neoproterozoic chemostratigraphic correlation: Precambrian Research, v. 182, no. 4, p. 239-253.

Gischler, E., and Lomando, A. J., 2005, Offshore sedimentary facies of a modern carbonate ramp, Kuwait, northwestern Arabian-Persian Gulf: Facies, v. 50, no. 3-4, p. 443-462.

Gischler, E., Swart, P. K., and Lomando, A. J., 2007, Stable isotopes of carbon and oxygen in modern sediments of carbonate platforms, barrier reefs, atolls, and ramps: patterns and implications: Perspectives in carbonate geology: a tribute to the career of Robert Nathan Ginsburg, p. 61-74.

Grey, K., Walter, M. R., and Calver, C. R., 2003, Neoproterozoic biotic diversification: Snowball Earth or aftermath of the Acraman impact?: Geology, v. 31, no. 5, p. 459-462.

Grossman, E. L., 1987, Stable isotopes in modern benthic foraminifera; a study of vital effect: The Journal of Foraminiferal Research, v. 17, no. 1, p. 48-61.

Gu, B. H., Schelske, C. L., and Hodell, D. A., 2004, Extreme C-13 enrichments in a shallow hypereutrophic lake: Implications for carbon cycling: Limnology and Oceanography, v. 49, no. 4, p. 1152-1159.

Halverson, G. P., Hoffman, P. F., Schrag, D. P., and Kaufman, A. J., 2002, A major perturbation of the carbon cycle before the Ghaub glaciation (Neoproterozoic) in Namibia: Prelude to snowball Earth?: Geochemistry Geophysics Geosystems, v. 3, no. 6, p. 1-24.

Halverson, G. P., Hoffman, P. F., Schrag, D. P., Maloof, A. C., and Rice, A. H. N., 2005, Toward a Neoproterozoic composite carbon-isotope record: Geological Society of America Bulletin, v. 117, no. 9-10, p. 1181-1207.

Halverson, G. P., Maloof, A. C., and Hoffman, P. F., 2004, The Marinoan glaciation (Neoproterozoic) in northeast Svalbard: Basin Research, v. 16, no. 3, p. 297-324.

Hayes, J. M., Strauss, H., and Kaufman, A. J., 1999, The abundance of ^{13}C in marine organic matter and isotopic fractionation in the global biogeochemical cycle of carbon during the past 800 Ma: Chemical Geology, v. 161, no. 1, p. 103-125.

Hoffman, P. F., Kaufman, A. J., Halverson, G. P., and Schrag, D. P., 1998, A Neoproterozoic snowball earth: Science, v. 281, no. 5381, p. 1342-1346.

Hoffman, P. F., and Schrag, D. P., 2002, The snowball Earth hypothesis: testing the limits of global change: Terra nova, v. 14, no. 3, p. 129-155.

Holmden, C., Panchuk, K., and Finney, S., 2012, Tightly coupled records of Ca and C isotope changes during the Hirnantian glaciation event in an epeiric sea setting: Geochimica et Cosmochimica Acta, v. 98, p. 94-106.

Husson, J. M., Maloof, A. C., Schoene, B., Chen, C. Y., and Higgins, J. A., 2015, Stratigraphic expression of Earth's deepest $\delta^{13}C$ excursion in the Wonoka Formation of South Australia: American Journal of Science, v. 315, no. 1, p. 1-45.

Irwin, H., Curtis, C., and Coleman, M., 1977, Isotopic evidence for source of diagenetic carbonates formed during burial of organic-rich sediments: Nature, v. 269, no. 5625, p. 206-213.

James, N. P., Narbonne, G. M., and Kyser, T. K., 2001, Late Neoproterozoic cap carbonates: Mackenzie Mountains, northwestern Canada: precipitation and global glacial meltdown: Canadian Journal of Earth Sciences, v. 38, no. 8, p. 1229-1262.

Kaufman, A. J., and Knoll, A. H., 1995, Neoproterozoic variations in the C-isotopic composition of seawater: stratigraphic and biogeochemical implications: Precambrian Research, v. 73, no. 1–4, p. 27-49.

Kennedy, M., 2013, The Nonlinear Effects of Evolutionary Innovation Biospheric Feedbacks on Qualitative Environmental Change: From the Microbial to Metazoan World: American Naturalist, v. 181, p. S100-S111.

Kennedy, M., Droser, M., Mayer, L. M., Pevear, D., and Mrofka, D., 2006, Late Precambrian oxygenation; In-

ception of the clay mineral factory: Science, v. 311, no. 5766, p. 1446-1449.

Kennedy, M. J., Runnegar, B., Prave, A. R., Hoffmann, K.-H., and Arthur, M. A., 1998, Two or four Neoproterozoic glaciations?: Geology, v. 26, no. 12, p. 1059-1063.

Kirschvink, J. L., 1992, Late Proterozoic low-latitude global glaciation: the snowball Earth.

Knauth, L. P., and Kennedy, M. J., 2009, The late Precambrian greening of the Earth: Nature, v. 460, no. 7256, p. 728-732.

Knoll, A., Hayes, J., Kaufman, A., Swett, K., and Lambert, I., 1986, Secular variation in carbon isotope ratios from Upper Proterozoic successions of Svalbard and East Greenland: Nature, v. 321, p 832-838.

Knoll, A. H., 2004, Life on a young planet: the first three billion years of evolution on earth, Princeton University Press.

Knoll, A. H., and Carroll, S. B., 1999, Early animal evolution: emerging views from comparative biology and geology: Science, v. 284, no. 5423, p. 2129.

Knoll, A. H., Javaux, E. J., Hewitt, D., and Cohen, P., 2006, Eukaryotic organisms in Proterozoic oceans: Philosophical Transactions of the Royal Society B-Biological Sciences, v. 361, no. 1470, p. 1023-1038.

Knoll, A. H., Walter, M. R., Narbonne, G. M., and Christie-Blick, N., 2004, A new period for the geologic time scale: Science, v. 305, no. 5684, p. 621-622.

Kump, L. R., 1991, Interpreting carbon-isotope excursions: Strangelove oceans: Geology, v. 19, no. 4, p. 299-302.

Kump, L. R., and Arthur, M. A., 1999, Interpreting carbon-isotope excursions: carbonates and organic matter: Chemical Geology, v. 161, no. 1-3, p. 181-198.

Kump, L. R., Junium, C., Arthur, M. A., Brasier, A., Fallick, A., Melezhik, V., Lepland, A., CČrne, A. E., and Luo, G., 2011, Isotopic evidence for massive oxidation of organic matter following the Great Oxidation Event: Science, v. 334, no. 6063, p. 1694-1696.

Lamb, A. L., Leng, M. J., Lamb, H. F., and Mohammed, M. U., 2000, A 9000-year oxygen and carbon isotope record of hydrological change in a small Ethiopian crater lake: Holocene, v. 10, no. 2, p. 167-177.

Land, L. S., 1986, Limestone diagenesis—some geochemical considerations: US Geol. Surv. Bull, v. 1578, p. 129-137.

Le Guerroue, E., Allen, P. A., Cozzi, A., Etienne, J. L., and Fanning, M., 2006, 50 Myr recovery from the largest negative delta C-13 excursion in the Ediacaran ocean: Terra Nova, v. 18, no. 2, p. 147-153.

Lyons, T. W., Reinhard, C. T., and Planavsky, N. J., 2014, The rise of oxygen in Earth/'s early ocean and atmosphere: Nature, v. 506, no. 7488, p. 307-315.

McKirdy, D. M., Burgess, J. M., Lemon, N. M., Yu, X. K., Cooper, A. M., Gostin, V. A., Jenkins, R. J. F., and Both, R. A., 2001, A chemostratigraphic overview of the late Cryogenian interglacial sequence in the Adelaide Fold-Thrust Belt, South Australia: Precambrian Research, v. 106, no. 1-2, p. 149-186.

Melchin, M. J., and Holmden, C., 2006, Carbon isotope chemostratigraphy of the Llandovery in Arctic Canada: Implications for global correlation and sea-level change: Gff, v. 128, p. 173-180.

Melezhik, V. A., Fallick, A. E., and Pokrovsky, B. G., 2005, Enigmatic nature of thick sedimentary carbonates depleted in ^{13}C beyond the canonical mantle value: The challenges to our understanding of the terrestrial carbon cycle: Precambrian Research, v. 137, no. 3-4, p. 131-165.

Melim, L. A., 2001, Meteoric and marine-burial diagenesis in the subsurface of Great Bahama Bank. In: R.N. Ginsburg (Editor), The Bahamas Drilling Project. SEPM Concepts in Sedimentology.

Melim, L. A., Westphal, H., Swart, P. K., Eberli, G. P., and Munnecke, A., 2002, Questioning carbonate diagenetic paradigms: evidence from the Neogene of the Bahamas: Marine Geology, v. 185, no. 1-2, p. 27-53.

Miller, K. G., and Katz, M. E., 1987, Oligocene to Miocene

benthic foraminiferal and abyssal circulation changes in the North-Atlantic: Micropaleontology, v. 33, no. 2, p. 97-149.

Narbonne, G. M., and Gehling, J. G., 2003, Life after snowball: the oldest complex Ediacaran fossils: Geology, v. 31, no. 1, p. 27-30.

Panchuk, K. M., Holmden, C. E., and Leslie, S. A., 2006, Local controls on carbon cycling in the Ordovician mid-continent region of North America, with implications for carbon isotope secular curves: Journal of Sedimentary Research, v. 76, no. 1-2, p. 200-211.

Payne, J. L., Boyer, A. G., Brown, J. H., Finnegan, S., Kowalewski, M., Krause, R. A., Jr., Lyons, S. K., McClain, C. R., McShea, D. W., Novack-Gottshall, P. M., Smith, F. A., Stempien, J. A., and Wang, S. C., 2009, Two-phase increase in the maximum size of life over 3.5 billion years reflects biological innovation and environmental opportunity: Proceedings of the National Academy of Sciences of the United States of America, v. 106, no. 1, p. 24-27.

Rosqvist, G. C., Leng, M. J., and Jonsson, C., 2007, North Atlantic region atmospheric circulation dynamics inferred from a late-Holocene lacustrine carbonate isotope record, northern Swedish Lapland: Holocene, v. 17, no. 7, p. 867-873.

Runnegar, B., 1982, Oxygen requirements, biology and phylogenetic significance of the late Precambrian worm dickinsonia, and the evolution of the burrowing habit: Alcheringa, v. 6, no. 3-4, p. 223-239.

Schrag, D. P., Berner, R. A., Hoffman, P. F., and Halverson, G. P., 2002, On the initiation of a snowball Earth: Geochemistry Geophysics Geosystems, v. 3.

Schrag, D. P., Higgins, J. A., Macdonald, F. A., and Johnston, D. T., 2013, Authigenic carbonate and the history of the global carbon cycle: Science (New York, N.Y.), v. 339, no. 6119, p. 540-543.

Shackleton, N., 1987, The carbon isotope record of the Cenozoic: History of organic carbon burial and of oxygen in the ocean and atmosphere: Geological Society, London, Special Publications, v. 26, no. 1, p. 423-434.

Shields-Zhou, G., Hill, A., and Macgabhann, B., 2012, The Cryogenian Period, The Geologic Time Scale, Elsevier.

Shields, G., and Veizer, J., 2002, Precambrian marine carbonate carbonate isotope database: Version 1.1: Geochem. Geophys. Geosyst, v. 3, no. 6, p. 1031.

Sohl, L. E., Christie-Blick, N., and Kent, D. V., 1999, Paleomagnetic polarity reversals in Marinoan (ca. 600 Ma) glacial deposits of Australia: implications for the duration of low-latitude glaciation in Neoproterozoic time: Geological Society of America Bulletin, v. 111, no. 8, p. 1120-1139.

Stiller, M., Rounick, J. S., and Shasha, S., 1985, Extreme carbon-isotope enrichments in evaporating brines: Nature, v. 316, no. 6027, p. 434-435.

Swart, P. K., and Eberli, G., 2005, The nature of the $\delta^{13}C$ of periplatform sediments: Implications for stratigraphy and the global carbon cycle: Sedimentary Geology, v. 175, no. 1-4, p. 115-129.

Swart, P. K., and Kennedy, M. J., 2011, Does the Global Stratigraphic Reproducibility of $\delta^{13}C$ in Neoproterozoic Carbonates Require a Marine Origin? A Plio-Pleistocene Comparison: Geology, v. 40, no. 1, p. 87-90..

Talbot, M. R., 1990, A review of the paleohydrological interpretation of carbon and oxygen isotopic-ratios in primary lacustrine carbonates: Chemical Geology, v. 80, no. 4, p. 261-279.

Talbot, M. R., and Kelts, K., 1986, primary and diagenetic carbonates in the anoxic sediments of lake Bosumtwi, Ghana: Geology, v. 14, no. 11, p. 912-916.

Urey, H. C., 1948, Oxygen isotopes in nature and in the laboratory: Science, v. 108, no. 2810, p. 489-496.

Valero-Garces, B. L., Delgado-Huertas, A., Ratto, N., and Navas, A., 1999, Large ^{3}C enrichment in primary carbonates from Andean Altiplano lakes, northwest Argentina: Earth and Planetary Science Letters, v. 171, no. 2, p. 253-266.

Veizer, J., Ala, D., Azmy, K., Bruckschen, P., Buhl, D., Bruhn, F., Carden, G. A. F., Diener, A., Ebneth, S., Godderis, Y., Jasper, T., Korte, C., Pawellek, F., Podlaha, O. G.,

and Strauss, H., 1999, $^{87}Sr/^{86}Sr$, $\delta^{13}C$ and$\delta^{18}O$ evolution of Phanerozoic seawater: Chemical Geology, v. 161, no. 1-3, p. 59-88.

Weiner, S., and Dove, P. M., 2003, An overview of biomineralization processes and the problem of the vital effect: Reviews in Mineralogy and Geochemistry, v. 54, no. 1, p. 1-29.

Yuan, X. L., Xiao, S. H., and Taylor, T. N., 2005, Lichen-like symbiosis 600 million years ago: Science, v. 308, no. 5724, p. 1017-1020.

Zachos, J., Pagani, M., Sloan, L., Thomas, E., and Billups, K., 2001, Trends, rhythms, and aberrations in global climate 65 Ma to present: Science, v. 292, no. 5517, p. 686-693.

Zhu, Z. J., Chen, J. A., and Zeng, Y., 2013, Abnormal positive delta C-13 values of carbonate in Lake Caohai, southwest China, and their possible relation to lower temperature: Quaternary International, v. 286, p. 85-93.

Ziveri, P., Stoll, H., Probert, I., Klaas, C., Geisen, M., Ganssen, G., and Young, J., 2003, Stable isotope 'vital effects' in coccolith calcite: Earth and Planetary Science Letters, v. 210, no. 1, p. 137-149.

Chapter 2

Statement of Authorship

Title of Paper	Paleoenvironmental controls on the Bitter Springs Anomaly carbon isotope excursion
Publication Status	☐ Published ☐ Accepted for Publication ☐ Submitted for Publication ☑ Unpublished and Unsubmitted w ork w ritten in manuscript style
Publication Details	N/A

Principal Author

Name of Principal Author (Candidate)	Robert Klaebe		
Contribution to the Paper	Project design, fieldwork and sampling, sample preparation, data collection and processing, data interpretation, manuscript design and composition, generation of figures.		
Overall percentage (%)	80		
Certification:	This paper reports on original research I conducted during the period of my Higher Degree by Research candidature and is not subject to any obligations or contractual agreements with a third party that would constrain its inclusion in this thesis. I am the primary author of this paper.		
Signature		Date	14/10/2015

Co-Author Contributions

By signing the Statement of Authorship, each author certifies that:

i. the candidate's stated contribution to the publication is accurate (as detailed above);
ii. permission is granted for the candidate in include the publication in the thesis; and
iii. the sum of all co-author contributions is equal to 100% less the candidate's stated contribution.

Name of Co-Author	Martin Kennedy		
Contribution to the Paper	Project design, fieldwork, guidance with data interpretation, manuscript review.		
Signature		Date	14/10/2015

Name of Co-Author	Amber Jarret		
Contribution to the Paper	Fieldwork, data collection, helped edit manuscript.		
Signature		Date	12/10/2015

Name of Co-Author	Jochen Brocks		
Contribution to the Paper	Fieldwork, helped edit manuscript.		
Signature		Date	7/10/2015

Palaeoenvironmental controls on the Bitter Springs Anomaly carbon-isotope excursion

Abstract

Large magnitude (>10‰) carbon isotope ($\delta^{13}C$) excursions in carbonate-bearing sediments are increasingly used to constrain the chronology of the Neoproterozoic stratigraphic record and as a monitor of changes in the Precambrian biosphere. The Tonian aged Bitter Springs Anomaly shows a 9‰ $\delta^{13}C$ excursion in carbonate rocks in the Amadeus Basin of central Australia that is used as a test case of a marine origin for large-magnitude $\delta^{13}C$ excursions because it meets the most stringent tests of secular change offered ; it is regionally reproducible, and $\delta^{13}C$ values in organic carbon covary with $\delta^{13}C$ of inorganic carbon arguing against a secondary diagenetic origin. We show that $\delta^{13}C$ values defining the excursion coincide with palaeoenvironmental shifts from restricted marine conditions to alkaline lacustrine settings and terrestrial environments indicated by binary changes in lithofacies. The stratigraphic $\delta^{13}C$ pattern in both organic and carbonate carbon is reproducible across the basin, but in each case is controlled by sea level fall restricting or isolating silled sub-basins in a broad, shallow intracratonic setting rather than whole-ocean secular change. As the shallow intracratonic setting of the Bitter Springs Formation is typical of other Neoproterozoic successions used to establish the present $\delta^{13}C$ seawater record and thus changes in the exogenic cycle, it highlights the need to not only identify diagenetic influence, but also local palaeoenvironmental controls on stratigraphic $\delta^{13}C$ variation.

1. Introduction

The carbon-isotope ($\delta^{13}C$) record of carbonate-bearing sediments has assumed an important role in interpreting environmental evolution through time (Derry, 2010b; Hoffman et al., 1998; Knauth and Kennedy, 2009; Knoll et al., 1986), and as a stratigraphic tool to support the correlation of sedimentary successions between basins (Halverson et al., 2005; Kaufman and Knoll, 1995). This is particularly true in the Precambrian where there are few radiometric ages and other independent time constraints such as biostratigraphic records of sufficient resolution. Composite $\delta^{13}C$ stratigraphic records are assembled from Precambrian successions by piecing together fragments of sections based on similarities in isotopic patterns in association with other potentially time significant features such as lithologically distinct units (eg. cap carbonates), deposits associated with glacial environments thought to represent discrete global ice ages, and radiometric ages where present, in order to provide a continuous history of global $\delta^{13}C$ change through time (Halverson et al., 2005; Shields-Zhou et al., 2012). The basis for the correlation of $\delta^{13}C$ values relies on the assumption that marine carbonates precipitate in equilibrium with an isotopically homogenous oceanic carbon pool that changes through time in response to the Earth's exogenic cycle. Carbonate successions thus record this changing value between isolated basins as a signal that is widely considered to be time significant (Knoll et al., 1986). Precambrian stratigraphic sections contain particularly large-magnitude $\delta^{13}C$ excursions of up to 18‰ that are readily recognisable and are commonly used as tie-points to support correlations.

The persistence of $\delta^{13}C$ values as depleted as -12‰ or enriched as +10‰ through tens to hundreds of metres of stratigraphy implies that the Precambrian carbon cycle was capable of supporting a range of marine $\delta^{13}C$ > 20‰ over extended periods of time (Le Guerroue et al., 2006), likely to reflect steady-state conditions rather than singular rapid perturbations or adjustments in the ocean-atmosphere system. This contrasts with the observed < 4‰ range of variability in the comparatively

well constrained Cenozoic pelagic record and has yet to be reconciled with a carbon isotope mass balance that has a theoretical lower limit of the Earth's < -5‰ mantle value (Bristow and Kennedy, 2008; Kump and Arthur, 1999; Melezhik et al., 2005). In interpreting anomalous negative $\delta^{13}C$ values from Precambrian strata, present debate surrounds the question of whether $\delta^{13}C$ excursions do represent secular change in seawater (Johnston et al., 2012), or a secondary signal derived from mixtures of marine and meteroric values (Knauth and Kennedy, 2009) or burial fluids (Derry, 2010a) in the diagenetic environment.

Alternatively, anomalous Neoproterozoic values could simply record the natural spatial $\delta^{13}C$ variability common in Phanerozoic-aged shallow, restricted, and non-marine environments where systematic, large scale (>15‰) $\delta^{13}C$ stratigraphic patterns (Swart and Kennedy, 2011) are demonstrably at odds with coeval open marine (pelagic) records available from deep sea cores (Swart and Eberli, 2005). This spatial variability in $\delta^{13}C$ values is controlled by local processes occurring in shallow depositional environments such as platforms (Gischler et al., 2007; Patterson and Walter, 1994; Swart and Eberli, 2005), lakes (Bade et al., 2004) and intracratonic basins (Holmden et al., 1998; Panchuk et al., 2006). In these settings, drivers such as input/output water composition, local productivity, and evaporation control the $\delta^{13}C$ balance of ambient waters and can lead to abrupt shifts in $\delta^{13}C$ with a change in these local palaeoenvironmental conditions.

The Bitter Springs Anomaly is considered a robust example of secular change in $\delta^{13}C$ recorded as a global excursion because a) the excursion has a similar magnitude over comparable stratigraphic thickness to excursions recorded in other Tonian-aged strata from NW Canada (Halverson, 2006; Macdonald et al., 2010), Svalbard (Halverson et al., 2007), Ethiopia (Alene et al., 2006) and Scotland (Prave et al., 2009) and b) $\delta^{13}C$ values derived from organic matter ($\delta^{13}C_{org}$) have been shown to covary with carbonate $\delta^{13}C$ (Swanson-Hysell et al., 2010) arguing against diagenetic exchange. Here we address the influence of local carbon-cycling processes that result from restriction and isolation, versus a continuous open marine record reflecting secular change of a global seawater signal, on the $\delta^{13}C$ values defining the Bitter Springs Anomaly in cores and outcrop from the Bitter Springs Formation. We show that major facies changes coincide with the $\delta^{13}C$ inflection points that define the Bitter Springs Anomaly, and that these lithology changes are a function of local palaeoenvironments, as changes in base level periodically isolated sub-basins from marine connections.

2. Geological Setting

The Bitter Springs Formation comprises > 1500 metres of evaporites, dolomitic marls, siltstones, and microbial carbonates deposited in the Amadeus Basin, one

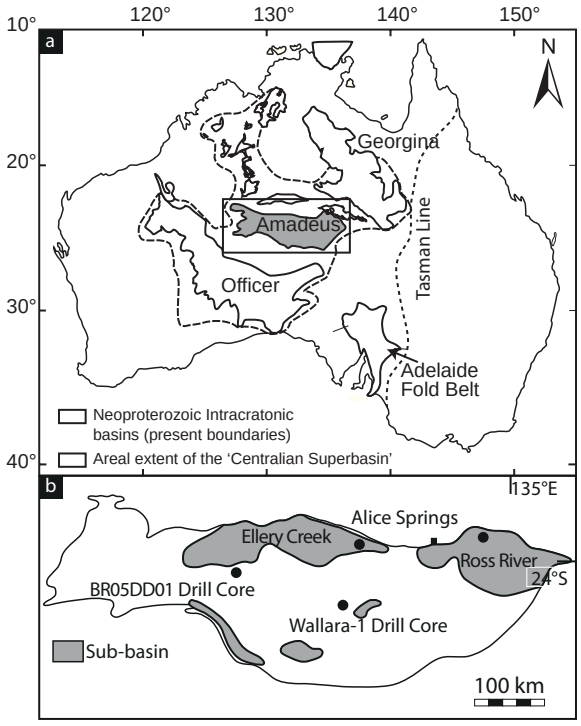

Figure 1. a) Map of the Centralian superbasin after (Munson et al., 2013). Tasman line indicates the eastern extent of Proterozoic cratonic Australia. b) Map of the Amadeus Basin after Lindsay and Korsch (1989). Field and drill core localities are indicated by black points. Regional sub-basins are shaded to highlight the limited distribution of sedimentation in the basin.

of a series of broad (~800 km) interconnected basins located on cratonic central Australia (Figure 1a). The absolute age of the Bitter Springs Formation is poorly constrained to a window of 400 million years (Figure 2); it is variably truncated by an angular unconformity beneath glacial sediments of the Areyonga Formation inferred as Sturtian in age (Hill and Walter, 2000), constrained by Re-Os > 657 ± 5 Ma (Kendall et al., 2006), and unconformably overlies intrusive rocks of ca. 1070 Ma (Schmidt et al., 2006). The Bitter Springs Anomaly, which comprises a ~200 m interval of the Bitter Springs Formation is inferred as ~811 Ma that relies on $\delta^{13}C$ correlation with better-constrained strata (Macdonald et al., 2010) and comparison of $^{87}Sr/^{86}Sr$ values of 0.7057 to 0.7063 taken to reflect the seawater composition of that age (Shields-Zhou et al., 2012). Thus, the $\delta^{13}C$ inflection points that bracket the excursion provide the primary stratigraphic tie-point that global correlatives are calibrated to.

A thick succession (up to 1350m) of salt deposited in the basal Bitter Springs Formation Gillen Member subsequently modified depositional conditions of overlying units through diapirism and salt withdrawal (Kennedy, 1993) resulting in complex basin floor topography (Figure 1b) in combination with regional sub-basins interconnected across localised sills. Laterally variable shallow water depositional conditions, evaporative facies, terrestrial deposits and exposure/karst surfaces interpreted to be marine, restricted marine and lacustrine intervals (Hill et al., 2000; Southgate, 1986, 1991) characterise the upper Bitter Springs Formation that hosts the Bitter Springs Anomaly. The Bitter Springs Anomaly $\delta^{13}C$ excursion is defined by abrupt $\delta^{13}C$ changes from +5‰ to -4‰ and back to ~ +5‰ in the Loves Creek Member and informal Johnnys Creek beds of the Formation (Figure 3).

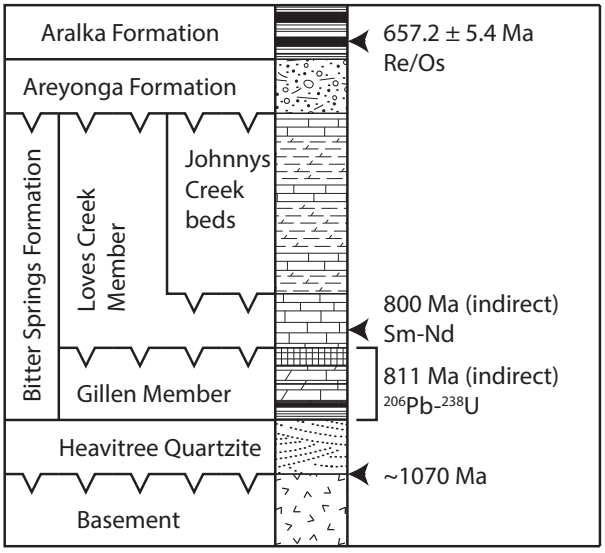

Figure 2. General stratigraphy and radiogenic age constraints of the lower Neoproterozoic in the Amadeus Basin, central Australia. Adapted from Marshall et al. (2007) and Haines et al. (2010). 1070 Ma age from Schmidt et al. (2006) and 657.2 Ma age from Kendall et al. (2006). 811 Ma date is derived from NW Canada, based on δ13C correlation (Macdonald et al., 2010) and the 800 Ma date is derived from dolerites in the Musgrave Province, central Australia, that are geochemically similar to spillites interbedding the Bitter Springs Formation (Zhao et al., 1994).

3. Analytical methods

All samples analyzed in this study were collected during logging of the Wallara-1 and BR05-DD01 drill cores of the Northern Territory Geological Survey at the Alice Springs Core Library, and logging of the Ellery Creek field section in the Northern Territory, Australia. Samples were slabbed, and then powdered subsamples were collected using a dentist drill. New stable isotope ($\delta^{13}C$ and $\delta18O$) measurements were performed on ~0.8mg powders using continuous-flow isotope-ratio mass spectrometry. Measurements were made on an Analytical Precision AP2003 (mean analytical precision for $\delta^{13}C$ and $\delta18O$ is ± 0.03‰ and ± 0.07‰ respectively) and on a Nu Horizon CF-IRMS (mean analytical precision for $\delta^{13}C$ is ± 0.1‰). Samples were digested in 105% phosphoric acid at 70°C and mass spectrometric measurements were made on evolved CO_2 gas following the method of Spötl and Vennemann (2003). Results were normalised to the Vienna Pee Dee Belemnite scale using internal working standards.

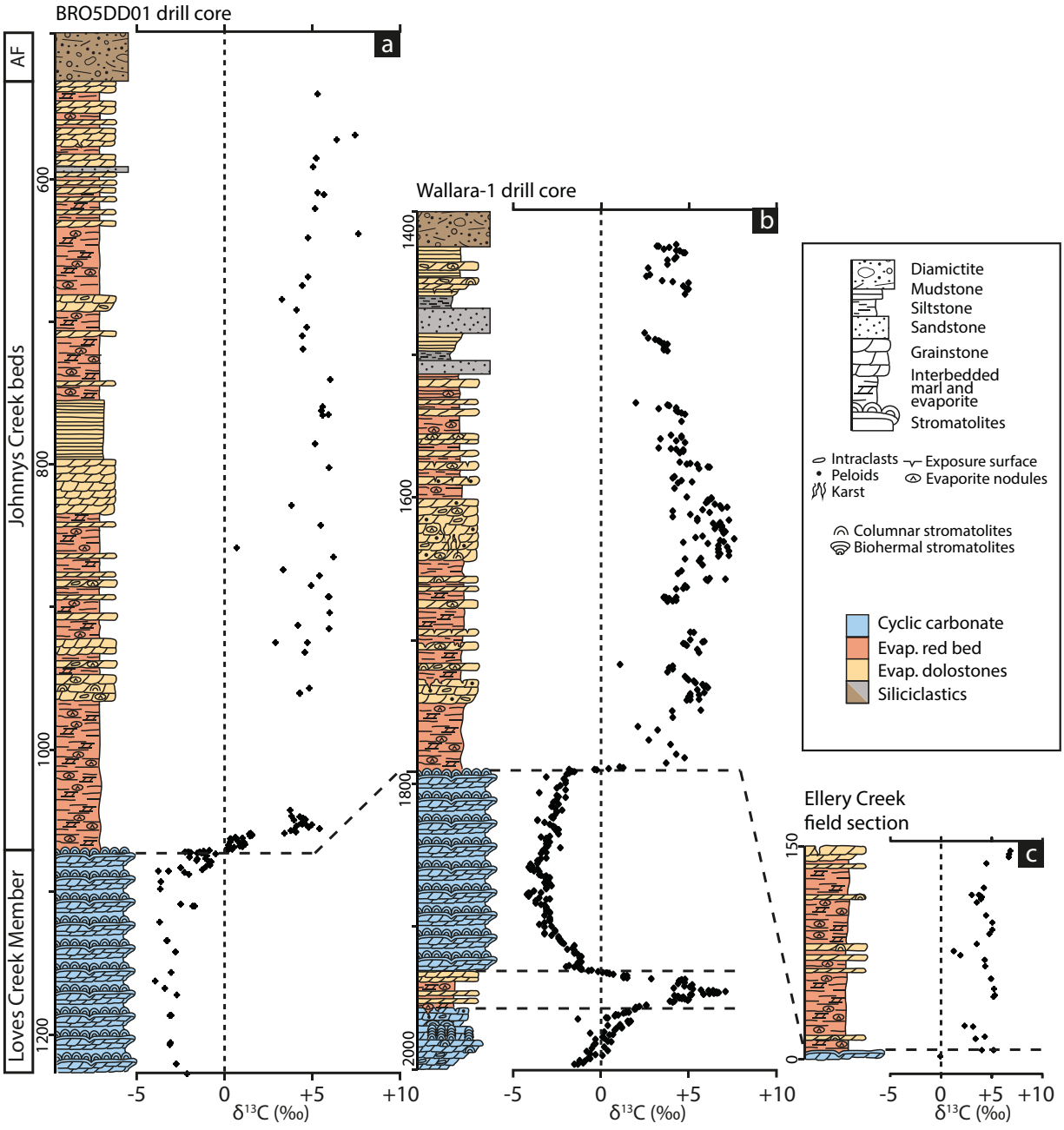

Figure 3. Stratigraphy and carbon isotope profiles of the Loves Creek Member and informal Johnnys Creek beds of the Bitter Springs Formation, central Australia, that show the relationship between lithology and $\delta^{13}C$ variation. Stratigraphic sections and coupled $\delta^{13}C$ values (black diamonds) show that isotopic shifts correspond to lithological changes in the host facies. Long dashed line indicates major facies transitions. a) NTGS BR05DDO1 stratigraphic core. b) NTGS Wallara-1 stratigraphic drill core, $\delta^{13}C$ values collated from Swanson-Hysell et al. (2010) and this study. c) Field transect at Ellery Creek. AF=Areyonga Formation diamictites. Y-axes are in metres.

4. Results

4.1 Sedimentology of the Bitter Springs Formation

The base of the Loves Creek Member comprises a single shallowing cycle of peloid and intraclast-grainstone to microbial carbonate capped by an erosion surface.

In the Wallara-1 core (Figure 3b), the erosion surface is sharply overlain by ~ 20 m of mottled red-coloured siltstone (Figure 4a) and interbedded grainstones and laminated dolostone (Figure 4b), the same facies that dominates the overlying Johnnys Creek beds (Figure 5a). Mottled red bed siltstones are variably comprised of rhombic dolomite crystals, siliciclastics (rare quartz) and up to 40% lathe and detrital anhydrite grains (Figure 4c, d) with ripple-cross lamination, scour surfaces, mudflake conglomerates and desiccation cracks. These red beds are punctuated by metre-thick resistant ridges of peloidal, stromatolitic and laminated dolostone with cm-scale gypsum rosettes (now replaced by chert) and common desiccation features including mud chip breccias and mud cracks. Carbonate beds are laterally discontinuous over hundreds of metres and isolated within the red beds (Southgate, 1991) indicating a local facies mosaic dominated by red bed deposition. Halite pseudomorphs (now chert) are preserved in the carbonate facies (Figure 4e) while nodular anhydrite occurs frequently in both facies (Figure 4f). Carbonate beds also show well developed karstic dissolution features in outcrop that are also evident in core. Karstic dissolution penetrates up to 3 metres into underlying strata and is filled by angular intraformational collapse breccias (Figure 4b).

The red bed facies with strong evidence of exposure and evaporative processes is in sharp contact with a cyclic carbonate facies in all studied sections (Figure 3). This facies is comprised of repetitive upward-shallowing carbonate cycles beginning with ooid, peloidal and intraclastic grainstones and passing upward through domal to columnar stromatolites (Figure 4g), and bedded dolostones with desiccation cracks (Southgate, 1989) and karstic features at cycle tops (Figure 5b). The upper beds of each cycle often preserve nodular gypsum pseudomorphs and bedded anhydrite indicating that local conditions were increasingly restricted leading to exposure at the tops of shallowing cycles (Figure 4h, i). The regularity of 2-12 m thick parasequences indicates the likely influence of fluctuating relative sea level, which periodically falls below the sediment interface allowing for desiccation, subaerial dissolution and erosion.

Based on these observations, the red bed facies is interpreted as a system of isolated evaporative alkaline lakes and ponds that periodically hosted microbial, grainstone and laminated carbonates. Multiple karsts/erosive surfaces and salts indicate periodic drying-out of lakes under hyper-arid conditions, subaerial erosion of anyhdrite, and redeposition by pluvial processes. These pass laterally into clay pans, salt flats and low relief playa systems preserved as evaporative and desiccated red marls and bedded salts, where detrital anhydrite occasionally dominates the composition of red beds. Dolomite likely grew as rhombs in unlithified sediment, while the minor siliciclastic fraction may be largely wind-blown. These interpretations are consistent with previous sedimentological and geochemical studies of this formation (Corkeron et al., 2012; Hill et al., 2000; Hill and Walter, 2000; Southgate, 1986, 1991). In contrast, the cyclic microbial carbonates and dolo-grainstones are consistent with a series of shoaling cycles in a shallow marine to restricted marine environment, indicated by exposure and evaporite precipitation at cycle tops.

4.2 Carbon-isotope systematics

Detailed sampling across facies transitions allows the more generalised $\delta^{13}C$ curve previously published (Swanson-Hysell et al., 2012; Swanson-Hysell et al., 2010) to be placed into context with the palaeoenvironmental record identified by these facies (Figure 3). Changes in $\delta^{13}C$ values occur abruptly along the major facies boundaries, with a shift to values of +7‰ preceding the excursion that coincides with an interval of evaporative red beds and carbonates. Following is an abrupt negative step of -3‰ over 1 m that then leads into the negative excursion (Figure 3). A +5‰ change over ~5 m occurs when the cyclical carbonate facies abruptly changes back to the red bed facies. While these transitions in $\delta^{13}C$ define the Bitter Springs Anomaly (Swanson-Hysell et al., 2012) they also coin-

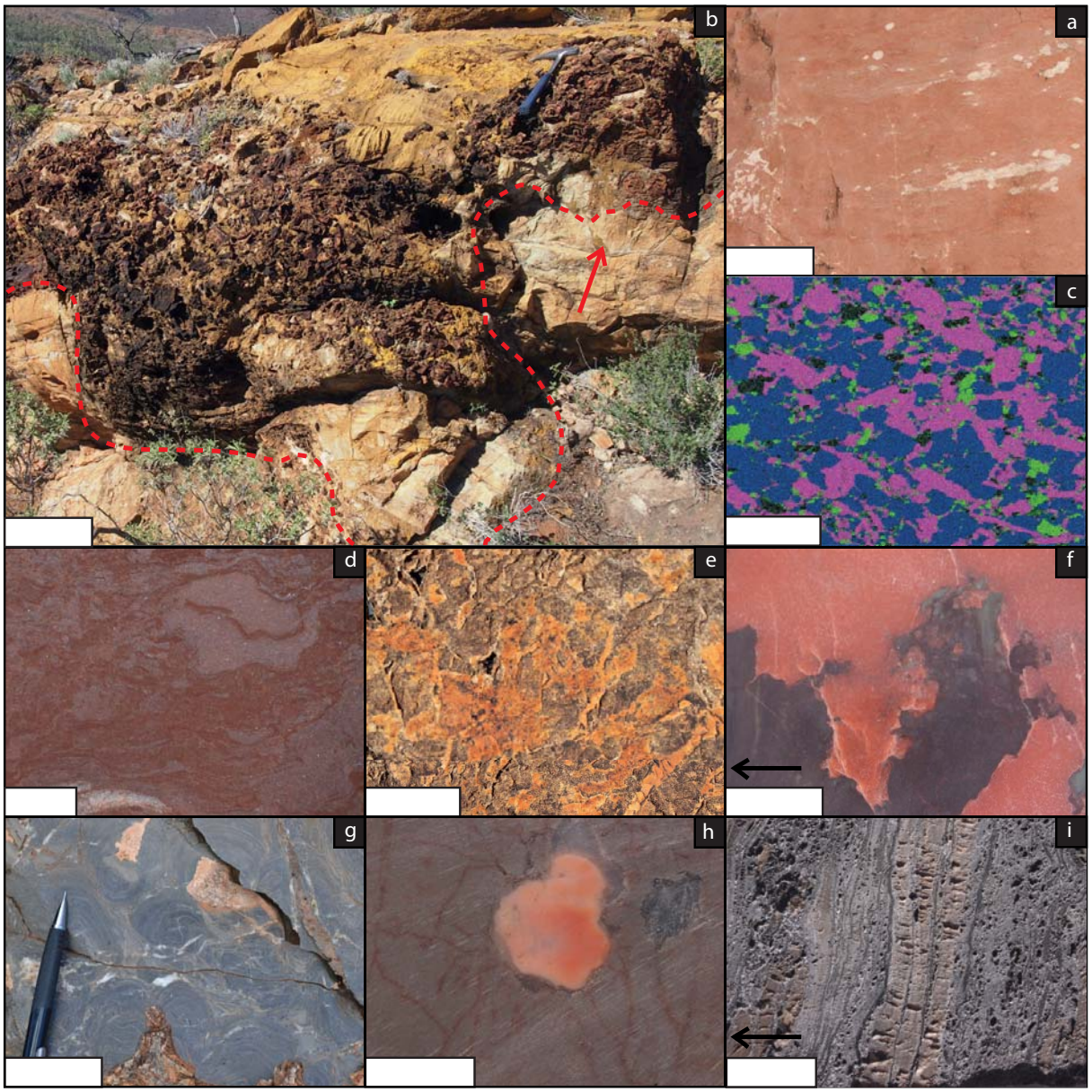

Figure 4. Sedimentary and textural features of the Bitter Springs Formation a) Typical evaporative redbed mudstone, Johnnys Creek beds, Ross River. Scale bar 2 cm. b) Karstic dissolution and collapse from the lower Johnnys Creek beds, Ross River. Karst penetrates up to 3 metres into dolostone interbeds and is filled by an intraformational, angular collapse breccia. Collapse breccia comprises angular chert and dolostone and is overlain by a finely laminated carbonate interpreted as a cave-filling flowstone. Collapse breccia is laterally persistent for ~20 m and passes into typical carbonate deposition. Red dashed line indicates dissolution boundary which truncates bedding. Arrow indicates younging direction of original bedding. Scale bar 0.25 m. c) Elemental map of red bed from Wallara-1 core at 1945.25 m depth. Blue=dolomite, green=aluminosilicates, purple=anhydrite. Rhombic dolomite suggests early evaporative precipitation in unlithified sediment. Anhydrite grains comprise ~40% of the sample volume. Scale bar 50 µm. d) Polished slab of typical evaporative mudstone showing wrinkled marl structure and disseminated anhydrite aggregates. Scale bar 0.5 cm. e) Putative silicified halite pseudomorphs in interbedded carbonate facies, Johnnys Creek beds, Ross River. Scale bar 2 cm. f) Displacive nodular anhydrite textures in laminated carbonates from the upper Johnnys Creek beds, NTGS

BRO5 drill core. Arrow indicates younging direction of core. Scale bar 2 cm. g) Typical columnar stromatolites in cyclic microbial carbonate facies, Loves Creek Member. Scale bar 4 cm. h) Nodular sulphate pseudomorph (now chert) in cyclic carbonates. Scale bar 2 cm. i) Bedded anhydrites from the Loves Creek Member. Sulphate occurs in upper beds of shallowing-upward cycles indicating isolation and evaporation. Vugs indicate partial dissolution of salt laminae. Scale bar 2 cm.

cide with the abrupt facies changes. This pattern of coincident change in $\delta^{13}C$ and facies occurs across the inflection point in the Wallara-1 and BRO5-DD01 stratigraphic cores (Figure 3a, b), and the Ellery Creek field section (Figure 3c) producing a seemingly reproducible excursion. When considered in stratigraphic context, abrupt variations in recorded $\delta^{13}C$ values are defined by shifts between two distinctive and isolated depositional environments that, given the local influence on relative sea level of salt movement and tectonics, are unlikely to be synchronous across the basin. These environments have characteristic and consistent $\delta^{13}C$ values associated with them, enriched values of +3‰ to +7‰ associated with evaporative lacustrine intervals and depleted values of -4‰ unique to the cyclic carbonates of the Loves Creek Member (Figure 3). A covariation between $\delta^{13}C$ of organic carbon and $\delta^{13}C$ of carbonate carbon occurs because both facies have undergone little diagenetic exchange between organic and inorganic carbon during diagenesis, also supported by the typical rhombic form of dolomite and examples of intercalation with lathe anhydrites (Figure 4c) that suggests it precipitated pre-compaction.

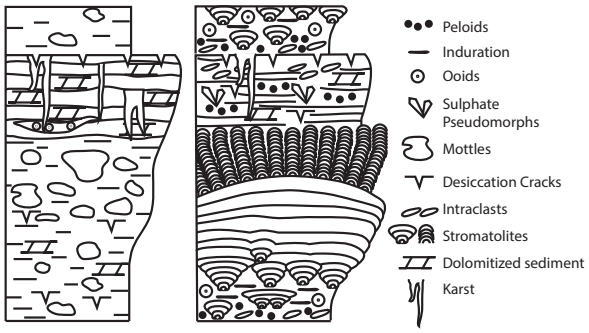

Figure 5. Generalised facies models for the red bed (left) and cyclic microbial facies (right, after Southgate (1991)). Variations of each facies motif comprise the entire thickness of the Johnnys Creek beds and Loves Creek Member of the Bitter Springs Formation respectively.

5. Discussion

The Bitter Springs Anomaly as recorded in central Australia has been used as an example where the observed $\delta^{13}C$ variation cannot be explained by a simple diagenetic overprint as suggested for some other Precambrian excursions. It's lateral reproducibility across the Amadeus Basin, similarity with sections of comparable stratigraphic position in other basins, and covariation between $\delta^{13}C$carb and $\delta^{13}C_{org}$, argues against isotopic exchange in sediments and, taken at face-value, supports proposed models of steady-state whole ocean change. However, all three of these criteria are satisfied by locally developed palaeoenvironments that are neither diagenetically altered nor reflective of secular seawater variation (Figure 6). Recorded $\delta^{13}C$ values are associated with particular lithofacies which are genetically related to the local depositional environment as are the $\delta^{13}C$ values that record alkaline lake or restricted marine palaeoenvironments. In the case of the Bitter Springs Anomaly in central Australia, a shift from cyclic stromatolitic carbonates to evaporative red beds is accompanied by an abrupt shift in $\delta^{13}C$ values from -4‰ to +5‰. Interbedding of these facies occurs as restricted and non-marine environments develop within sub-basins in response to rising and falling sea level relative to local connecting sills. As with the binary nature of the sediments (red beds or marine carbonates), the $\delta^{13}C$ reflecting these environments (-4 ‰ or +5‰) creates a binary stratigraphic isotope pattern. In the same way that similar lithology does not form a basis for global correlation because lithofacies are understood to be diachronous, $\delta^{13}C$ values that are geneticall-ly linked to a particular palaeoenvironment and record the spatial limitation of that environment at any given time are also unsuitable for global correlation.

The expression of the Bitter Springs Anomaly in non-marine intervals of the Bitter Springs Formation may have

implications for correlative sections that record the excursion, as well as other examples of Precambrian $\delta^{13}C$ anomalies. This is particularly true for intervals where $\delta^{13}C$ values change systematically with lithofacies and/or abruptly along sequence boundaries, flooding surfaces, and unconformities, such as the commonly correlated Bitter Springs Anomaly equivalent recorded in Svalbard (Halverson et al., 2007) that shows abrupt variation across unconformable stratigraphic boundaries. Specific $\delta^{13}C$ ranges need not be associated with lithofacies identical to those described in the Bitter Springs Formation, the Phanerozoic record illustrates that both highly enriched and depleted values are common across a range of environments. These include shelves and inland seaways (+6‰ to -10‰ (Fanton and Holmden, 2007; Panchuk et al., 2006; Swart and Eberli, 2005)), and lakes (-30‰ to +13‰ (Bade et al., 2004; Stiller et al., 1985), all of which are typically shallow (<200m) and thus particularly amenable to isolation and the influence of sea level fall and the dominance of local carbon-cycling processes. This model also potentially addresses the up to 7‰ variation in magnitude of the interpreted excursion between some correlatives (eg. Macdonald et al., 2010; Prave et al., 2009), the inconsistency in shape of the excursion from basin to basin, and the different chemostratigraphic expression of the onset and recovery of depleted $\delta^{13}C$ values as both abrupt and gradual within and between basins (Halverson et al., 2007; Macdonald et al., 2010; Swanson-Hysell et al., 2012). While the sustained $\delta^{13}C$ values of -2 to -4‰ recorded in microbial-grainstone intervals in the Bitter Springs Formation could faithfully record depleted open-ocean $\delta^{13}C_{DIC}$ pool, precluding isotopically enriched terrestrial phases from the $\delta^{13}C$ curve means that the scale of $\delta^{13}C$ variability observed becomes relatively unremarkable and the critical inflection points that anchor the global Bitter Springs Anomaly here become ambiguous.

The Precambrian stratigraphic record may be particularly prone to the influence of shallow water conditions that are commonly dominated by local C-cycling effects, hydrologic restriction, and physical truncation of isotopic signals. The subduction of almost all deep marine deposits that accumulated on oceanic crust have left the Precambrian record biased toward shallow-water basins formed on continental crust that are commonly within the range of eustatic variation. The challenge of separating lacustrine from marine sediments in the absence of diagnostic fossils, coupled with the obscuring effects of diagenetic recrystallisation on primary carbonate textures, means that the depositional origin and timing of carbonate phases in many Neoproterozoic sections is more difficult to assign to an open marine origin than the pelagic faunal records from the

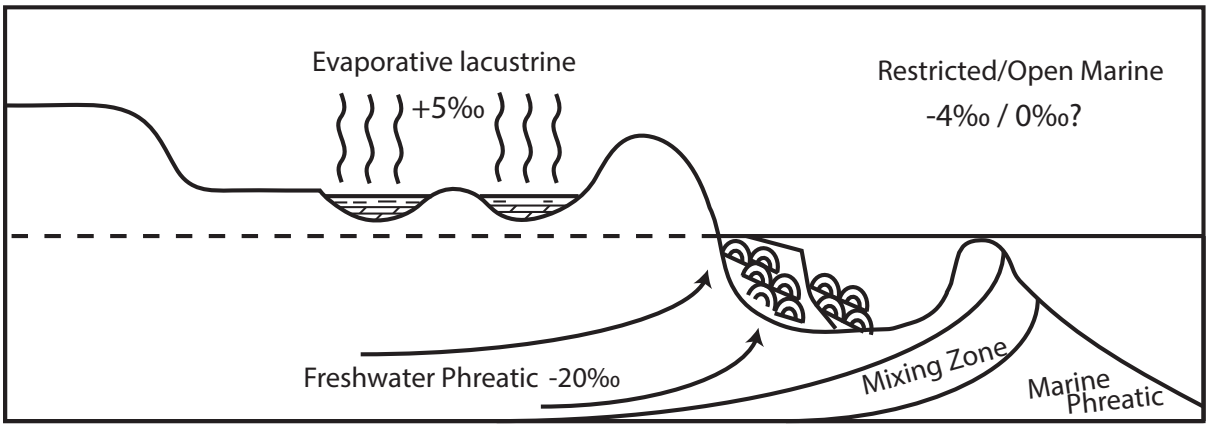

Figure 6. Simplified distribution of sedimentation across the Amadeus basin. Precipitation of isotopically-enriched dolomite is restricted to landward terrestrial environments dominated by evaporative conditions. Restricted-open marine microbial carbonates accumulate in deeper-water marginal environments that migrate landward as the basin floods.

Phanerozoic. Thus, the systematic variation of $\delta^{13}C$ values with changing lithology may provide a standard test for determining the origin of the $\delta^{13}C$ signal in a given section.

6. Conclusions

This study shows that large magnitude $\delta^{13}C$ excursions in Neoproterozoic strata can reflect local palaeoenvironmental controls rather than whole-ocean secular change. While this may not be true for all Neoproterozoic $\delta^{13}C$ values, the Bitter Springs Formation highlights the ease by which a simple binary signal can be produced in an isolated basin as local conditions change, a signal that is similar enough to other patterns globally to be used as part of the seawater composite curve. This interpretation does not downplay the role of the $\delta^{13}C$ record in palaeoenvironmental interpretation; rather it stresses the need to assess the influence of restricted or lacustrine intervals that do not provide a record of the global carbon mass-balance and are not time significant. This is particularly true in the broad, shallow, intracratonic and marginal basins that are typical of the Neoproterozoic record, where local topographic controls and changes in relative sea level can lead to regional isolation and restriction.

Acknowledgements

We thank the Sprigg Geobiology Centre (S. L□hr, T. Hall, J. Tyler, P.Ward) for comments and discussion of this manuscript. A. Corrick, P. Abballe, R. Drysdale and M. Rollog are thanked for fieldwork and analytical contributions. This work was supported by Australian Research Council grants DP120100104, DP110104367, LP120200086 and Australian Synchrotron beam-time (ref. AS133/XFM/7150) awarded to Kennedy. Drill core material and imagery provided by the Northern Territory Geological Survey.

References

Alene, M., Jenkin, G. R. T., Leng, M. J., and Darbyshire, D. P. F., 2006, The Tambien Group, Ethiopia: An early Cryogenian (ca. 800-735 Ma) Neoproterozoic sequence in the Arabian-Nubian Shield: Precambrian Research, v. 147, no. 1-2, p. 79-99.

Bade, D. L., Carpenter, S. R., Cole, J. J., Hanson, P. C., and Hesslein, R. H., 2004, Controls of delta C-13-DIC in lakes: Geochemistry, lake metabolism, and morphometry: Limnology and Oceanography, v. 49, no. 4, p. 1160-1172.

Bristow, T. F., and Kennedy, M. J., 2008, Carbon isotope excursions and the oxidant budget of the Ediacaran atmosphere and ocean: Geology, v. 36, no. 11, p. 863-866.

Corkeron, M., Webb, G. E., Moulds, J., and Grey, K., 2012, Discriminating stromatolite formation modes using rare earth element geochemistry: Trapping and binding versus in situ precipitation of stromatolites from the Neoproterozoic Bitter Springs Formation, Northern Territory, Australia: Precambrian Research, v. 212, p. 194-206.

Derry, L. A., 2010a, A burial diagenesis origin for the Ediacaran Shuram-Wonoka carbon isotope anomaly: Earth and Planetary Science Letters, v. 294, no. 1-2, p. 152-162.

Derry, L. A., 2010b, On the significance of delta(13)C correlations in ancient sediments: Earth and Planetary Science Letters, v. 296, no. 3-4, p. 497-501.

Fanton, K. C., and Holmden, C., 2007, Sea-level forcing of carbon isotope excursions in epeiric seas: implications for chemostratigraphy: Canadian Journal of Earth Sciences, v. 44, no. 6, p. 807-818.

Gischler, E., Swart, P. K., and Lomando, A. J., 2007, Stable isotopes of carbon and oxygen in modern sediments of carbonate platforms, barrier reefs, atolls, and ramps: patterns and implications: Perspectives in carbonate geology: a tribute to the career of Robert Nathan Ginsburg, p. 61-74.

Haines, P., Allen, H., and Grey, K., 2010, Reassessment of

the geology and exploration potential of the Western Australian Amadeus Basin: GSWA 2010 Extended Abstracts, p. 27-29.

Halverson, G., 2006, A Neoproterozoic chronology: Neoproterozoic Geobiology and Paleobiology, p. 231-271.

Halverson, G. P., Hoffman, P. F., Schrag, D. P., Maloof, A. C., and Rice, A. H. N., 2005, Toward a Neoproterozoic composite carbon-isotope record: Geological Society of America Bulletin, v. 117, no. 9-10, p. 1181-1207.

Halverson, G. P., Maloof, A. C., Schrag, D. P., Dudas, F. O., and Hurtgen, M., 2007, Stratigraphy and geochemistry of a ca 800 Ma negative carbon isotope interval in northeastern Svalbard: Chemical Geology, v. 237, no. 1-2, p. 5-27.

Hill, A. C., Arouri, K., Gorjan, P., and Walter, M. R., 2000, Geochemistry of marine and nonmarine environments of a Neoproterozoic cratonic carbonate/evaporite: The Bitter Springs Formation, central Australia, in Grotzinger, J. P., and James, N. P., eds., Carbonate sedimentation and diagenesis in the evolving Precambrian world, p. 327-344.

Hill, A. C., and Walter, M. R., 2000, Mid-Neoproterozoic (similar to 830-750 Ma) isotope stratigraphy of Australia and global correlation: Precambrian Research, v. 100, no. 1-3, p. 181-211.

Hoffman, P. F., Kaufman, A. J., Halverson, G. P., and Schrag, D. P., 1998, A Neoproterozoic snowball earth: Science, v. 281, no. 5381, p. 1342-1346.

Holmden, C., Creaser, R. A., Muehlenbachs, K., Leslie, S. A., and Bergstrom, S. M., 1998, Isotopic evidence for geochemical decoupling between ancient epeiric seas and bordering oceans: Implications for secular curves: Geology, v. 26, no. 6, p. 567-570.

Johnston, D. T., Macdonald, F. A., Gill, B. C., Hoffman, P. F., and Schrag, D. P., 2012, Uncovering the Neoproterozoic carbon cycle: Nature, v. 483, no. 7389, p. 320-323.

Kaufman, A. J., and Knoll, A. H., 1995, Neoproterozoic variations in the C-isotopic composition of seawater: stratigraphic and biogeochemical implications: Precambrian Research, v. 73, no. 1–4, p. 27-49.

Kendall, B., Creaser, R. A., and Selby, D., 2006, Re-Os geochronology of postglacial black shales in Australia: Constraints on the timing of "Sturtian" glaciation: Geology, v. 34, no. 9, p. 729-732.

Kennedy, M., 1993, The Undoolya sequence: Late Proterozoic salt influenced deposition, Amadeus basin, central Australia: Australian Journal of Earth Sciences, v. 40, no. 3, p. 217-228.

Knauth, L. P., and Kennedy, M. J., 2009, The late Precambrian greening of the Earth: Nature, v. 460, no. 7256, p. 728-732.

Knoll, A., Hayes, J., Kaufman, A., Swett, K., and Lambert, I., 1986, Secular variation in carbon isotope ratios from Upper Proterozoic successions of Svalbard and East Greenland.

Kump, L. R., and Arthur, M. A., 1999, Interpreting carbon-isotope excursions: carbonates and organic matter: Chemical Geology, v. 161, no. 1-3, p. 181-198.

Le Guerroue, E., Allen, P. A., Cozzi, A., Etienne, J. L., and Fanning, M., 2006, 50 Myr recovery from the largest negative delta C-13 excursion in the Ediacaran ocean: Terra Nova, v. 18, no. 2, p. 147-153.

Lindsay, J. F., and Korsch, R., 1989, Interplay of tectonics and sea-level changes in basin evolution: an example from the intracratonic Amadeus Basin, central Australia: Basin Research, v. 2, no. 1, p. 3-25.

Macdonald, F. A., Schmitz, M. D., Crowley, J. L., Roots, C. F., Jones, D. S., Maloof, A. C., Strauss, J. V., Cohen, P. A., Johnston, D. T., and Schrag, D. P., 2010, Calibrating the Cryogenian: Science, v. 327, no. 5970, p. 1241-1243.

Marshall, T., Dyson, I., and Liu, K., Petroleum systems in the Amadeus Basin, central Australia: Were they all oil prone, in Proceedings Proceedings of the Central Australian Basins Symposium, Alice Springs2007, p. 136-146.

Melezhik, V. A., Fallick, A. E., and Pokrovsky, B. G., 2005, Enigmatic nature of thick sedimentary carbonates depleted in^{13}C beyond the canonical mantle value: The

challenges to our understanding of the terrestrial carbon cycle: Precambrian Research, v. 137, no. 3-4, p. 131-165.

Munson, T., Kruse, P., and Ahmad, M., 2013, Chapter 22: Centralian Superbasin, in M, A., and TJ, M., eds., Geology and mineral resources of the Northern Territory, Volume 5.

Panchuk, K. M., Holmden, C. E., and Leslie, S. A., 2006, Local controls on carbon cycling in the Ordovician midcontinent region of North America, with implications for carbon isotope secular curves: Journal of Sedimentary Research, v. 76, no. 1-2, p. 200-211.

Patterson, W. P., and Walter, L. M., 1994, Depletion of C-13 in seawater sigma-CO_2 on modern carbonate platforms - significance for the carbon isotopic record of carbonates: Geology, v. 22, no. 10, p. 885-888.

Prave, A., Fallick, A., Thomas, C., and Graham, C., 2009, A composite C-isotope profile for the Neoproterozoic Dalradian Supergroup of Scotland and Ireland: Journal of the Geological Society, v. 166, no. 5, p. 845-857.

Schmidt, P. W., Williams, G. E., Camacho, A., and Lee, J. K., 2006, Assembly of Proterozoic Australia: implications of a revised pole for the~ 1070 Ma Alcurra Dyke Swarm, central Australia: Geophysical Journal International, v. 167, no. 2, p. 626-634.

Shields-Zhou, G., Hill, A., and Macgabhann, B., 2012, The Cryogenian Period, The Geologic Time Scale, Elsevier.

Southgate, P. N., 1986, Depositional environment and mechanism of preservation of microfossils, upper Proterozoic Bitter Springs Formation, Australia: Geology, v. 14, no. 8, p. 683-686.

Southgate, P. N., 1989, Relationships between cyclicity and stromatolite form in the Late Proterozoic Bitter Springs Formation, Australia: Sedimentology, v. 36, no. 2, p. 323-339.

Southgate, P. N., 1991, A sedimentological model for the Loves Creek Member of the Bitter Springs Formation, northern Amadeus Basin, in Korsch, R. J., and Kennard, J. M., eds., Geological and Geophysical Studies in the Amadeus Basin, Central Australia: Australian Bureau of Mineral Resources, Geology and Geophysics Bulletin 236, p. 113-126.

Spötl, C., and Vennemann, T. W., 2003, Continuous-flow isotope ratio mass spectrometric analysis of carbonate minerals: Rapid communications in mass spectrometry, v. 17, no. 9, p. 1004-1006.

Stiller, M., Rounick, J. S., and Shasha, S., 1985, Extreme carbon-isotope enrichments in evaporating brines: Nature, v. 316, no. 6027, p. 434-435.

Swanson-Hysell, N. L., Maloof, A. C., Kirschvink, J. L., Evans, D. A. D., Halverson, G. P., and Hurtgen, M. T., 2012, Constraints on Neoproterozoic paleogeography and Paleozoic orogenesis from paleomagnetic records of the Bitter Springs Formation, Amadeus Basin: American Journal of Science, v. 312, no. 8, p. 817-884.

Swanson-Hysell, N. L., Rose, C. V., Calmet, C. C., Halverson, G. P., Hurtgen, M. T., and Maloof, A. C., 2010, Cryogenian Glaciation and the Onset of Carbon-Isotope Decoupling: Science, v. 328, no. 5978, p. 608-611.

Swart, P. K., and Eberli, G., 2005, The nature of the delta ^{13}C of periplatform sediments: Implications for stratigraphy and the global carbon cycle: Sedimentary Geology, v. 175, no. 1-4, p. 115-129.

Swart, P. K., and Kennedy, M. J., 2011, Does the Global Stratigraphic Reproducibility of $\delta^{13}C$ in Neoproterozoic Carbonates Require a Marine Origin? A Plio-Pleistocene Comparison: Geology, v. 40, no. 1, p. 87-90.

Zhao, J.-x., McCulloch, M. T., and Korsch, R. J., 1994, Characterisation of a plume-related ~800 Ma magmatic event and its implications for basin formation in central-southern Australia: Earth and Planetary Science Letters, v. 121, no. 3, p. 349-367.

Chapter 3

Statement of Authorship

Title of Paper	The geologic context of the Trezona Anomaly carbon-isotope excursion
Publication Status	☐ Published ☐ Accepted for Publication ☐ Submitted for Publication ☑ Unpublished and Unsubmitted w ork w ritten in manuscript style
Publication Details	N/A

Principal Author

Name of Principal Author (Candidate)	Robert Klaebe		
Contribution to the Paper	Project design, fieldwork and sampling, sample preparation, data collection and processing, data interpretation, manuscript design and composition, generation of figures.		
Overall percentage (%)	80		
Certification:	This paper reports on original research I conducted during the period of my Higher Degree by Research candidature and is not subject to any obligations or contractual agreements with a third party that would constrain its inclusion in this thesis. I am the primary author of this paper.		
Signature		Date	14/10/2015

Co-Author Contributions

By signing the Statement of Authorship, each author certifies that:

i. the candidate's stated contribution to the publication is accurate (as detailed above);
ii. permission is granted for the candidate in include the publication in the thesis; and
iii. the sum of all co-author contributions is equal to 100% less the candidate's stated contribution.

Name of Co-Author	Martin Kennedy		
Contribution to the Paper	Project design, fieldwork, guidance with data interpretation, manuscript review.		
Signature		Date	14/10/2015

The geologic context of the Trezona Anomaly carbon-isotope excursion

Abstract

The carbon isotope ($\delta^{13}C$) record of Neoproterozoic marine sediments is central to interpretations of past environmental change. The pre-Marinoan (~635 Ma) Trezona Formation records $\delta^{13}C$ values on the order of -9‰ that constrain pre-glacial biospheric change commonly related to the theoretical Snowball Earth climate state, are correlated as a time-significant oceanographic event, and has more recently been linked to metazoan evolution that precedes the Ediacaran Period. A sedimentological study of 9 field sections across the Flinders Ranges in South Australia reveals a basal sequence boundary indicated by palaeosols and fluvial deposits that separates the Trezona Formation from underlying deep-water shelf siliciclastics. Field observations including fluvial sediments and mudcracks indicate persistently shallow-water conditions dominated deposition of the lower Trezona Formation which records sustained $\delta^{13}C$ values of -9‰. A gradual vertical increase in $\delta^{13}C$ values from -9‰ toward -2‰ occurs in each studied section synchronously with an abrupt change in lithofacies from interbedded mudstones and limestones to stacked microbial and grainstone carbonates in the upper Formation, as do changes in Fe concentrations and ranges of Mn/Sr values. A positive linear covariation of $\delta^{13}C$ and $\delta^{18}O$ values in the lower Trezona Formation ($r = 0.39$ and 0.69) ceases across the same stratigraphic boundary. The recorded vertical trend in $\delta^{13}C$ values is similar in shape and magnitude to Pliocene-aged carbonate platform sediments altered by meteoric fluids during diagenesis, and with modern alkaline lakes, but is difficult to explain as a primary oceanographic signal. The systematic variation of isotopic and trace metal data, indicators of shallow water to subaerial exposure, and the limited spatial distribution of the Trezona Formation (< 200 km2) describes a restricted marine to non-marine depositional environment that likely supported periodic lacustrine conditions. Thus, the Trezona Formation likely records common $\delta^{13}C$ patterns of alteration of coastal or lacustrine carbonates responding to exposure and sea level fall rather than a shift in global biogeochemical dynamics.

1. Introduction

A critical difference between the carbon-isotope ($\delta^{13}C$) records of Cenozoic pelagic sediments and the synthesised Precambrian $\delta^{13}C$ record is the water depths under which each record accumulates. Robust Cenozoic $\delta^{13}C$ records able to constrain variations in global carbon-cycle dynamics rely on pelagic metazoan shells that accumulate in deep-water basins continually through time (eg. Berger and Vincent, 1986; Maslin and Swann, 2005; Ravizza and Zachos, 2003). These special conditions allow a relatively uninterrupted sampling and characterisation of the $\delta^{13}C$ chemistry of the well-mixed surface waters of the open ocean as mineralising carbonates record the ambient $\delta^{13}C$ balance of the ocean-atmosphere in equilibrium. Significantly, this condition is absent from more ancient sedimentary records, in particular those older than the Phanerozoic, as the oceanic crust bearing deep-water pelagic accumulations has since been subducted and pelagic calcifiers had yet to evolve (Martin, 1995; Ridgwell, 2005). Thus, preservation of Precambrian stratigraphy is predicted to be heavily biased toward marginal and intracratonic sedimentary environments that deposit sediment on continental crust where water depths are typically < 200 m. Shallower still are the platforms and ramps that likely accounted for the majority of marine carbonate precipitation in the Precambrian, most of which would have accumulated under tens of metres of water. Where the influence of a few metres of sea-level change on deeper-water environments is relatively minor with respect to the continuous accumulation of

pelagic material, the shallow marginal settings typical of Precambrian carbonate records are expected to be highly sensitive to this type of variation that can lead to the migration of shorelines, emergence of sediment, depositional hiatuses, and abrupt hydrologic restriction of local topographic lows. Where topography allows, sea-level fall of a few metres across the shelf can even lead to the severing of marine connections entirely behind sills, where isolated water bodies may then undergo significant periods of deposition under restricted marine to non-marine conditions such as in the Mediterranean and the Black Sea. These considerations pose the question: to what extent do shallow, restricted and non-marine environments influence the construction of synthetic Precambrian $\delta^{13}C$ records?

Given the sensitivity of shallow marginal basins to restriction and exposure, it is critical to recognise examples where sedimentary processes and variations in $\delta^{13}C$ values occur in a systematic way. This implies a common origin that is inconsistent with a globally-representative signal (Kaufman and Knoll, 1995), where sediment supply and ambient $\delta^{13}C$ values shift together in response to sea level. Here we conduct a palaeoenvironmental study on a succession housing one of the most well established $\delta^{13}C$ excursions recognised in the Neoproterozoic stratigraphic record in order to determine the influence of sea-level variation on recorded $\delta^{13}C$ values. The Trezona Formation contains a $\delta^{13}C$ excursion to values of -9‰ termed the Trezona Anomaly that lies stratigraphically below Marinoan-aged (~635 Ma) glaciogenic deposits related to models of Snowball glaciation (Hoffman and Schrag, 2002) and serves as a standard feature used to correlate between Neoproterozoic successions in basins around the world (Halverson et al., 2005; McKirdy et al., 2001). Evidence of shallow water depths to periodic exposure throughout the deposition of the Trezona Formation, abrupt shifts in depositional mode, and a limited distribution focused on localised diapir salt withdrawal basins, suggest that the Trezona Formation is comprised of multiphase deposits that record restricted marine and carbonate lake environments that are spatially confined to a discrete sub-basin as a result of sea-level fall behind a connecting sill. The systematic nature of $\delta^{13}C$ variations with changes in lithofacies and the association with shallow-water sediments likely to be sensitive to hydrological restriction indicates that local water-depth and isotope values are linked, inconsistent with an interpretation of global secular carbon-cycle change where these parameters are predicted to vary independently.

2. Geological Setting

The Trezona Formation is preserved in the South Australia Flinders Ranges (Figure 1) as a mixed siliciclastic and carbonate deposit. It is well known for its distinctive hieroglyphic limestone facies, interpreted by Douglas Mawson as mud clasts but recently reinterpreted by Maloof et al. (2010) as early metazoan body-fossils that potentially represent a period of deposition coeval with pre-Ediacaran metazoan fauna. The Trezona Formation typically comprises a lower shale interval with limestone mudclast storm beds and intraclastic shoals that passes upwards into oolite shoals and microbial facies that are further capped by a siliciclastic red bed sequence in sections that crop out in the central Flinders Ranges (Figure 2). These distinct phases of deposition are distributed across a bulls-eye pattern with a maximum thickness of ~450 m focussed on the central Flinders Ranges (Figure 1), with a sharp reverse-thickness gradient away from this central zone that wedges out laterally beneath overlying units. A complex history of syn-depositional salt movement prevailed here prior to and during the deposition of Trezona Formation sediments (Lemon, 1988). Diapiric uplift is illustrated by locally developed karst surfaces and sediment thickness variations around the diapirs attributed to syn-sedimentary salt-withdrawal (Figure 1c), as well as extruded diapiric breccias (Lemon, 1988; McKirdy et al., 2001).

The Trezona Formation depositional environment has been variably interpreted. Initially suggested as a lacustrine basin based on its highly limited distribution, shallow water depths, and evidence of local exposure (Preiss, 1987), the Trezona Formation has previously

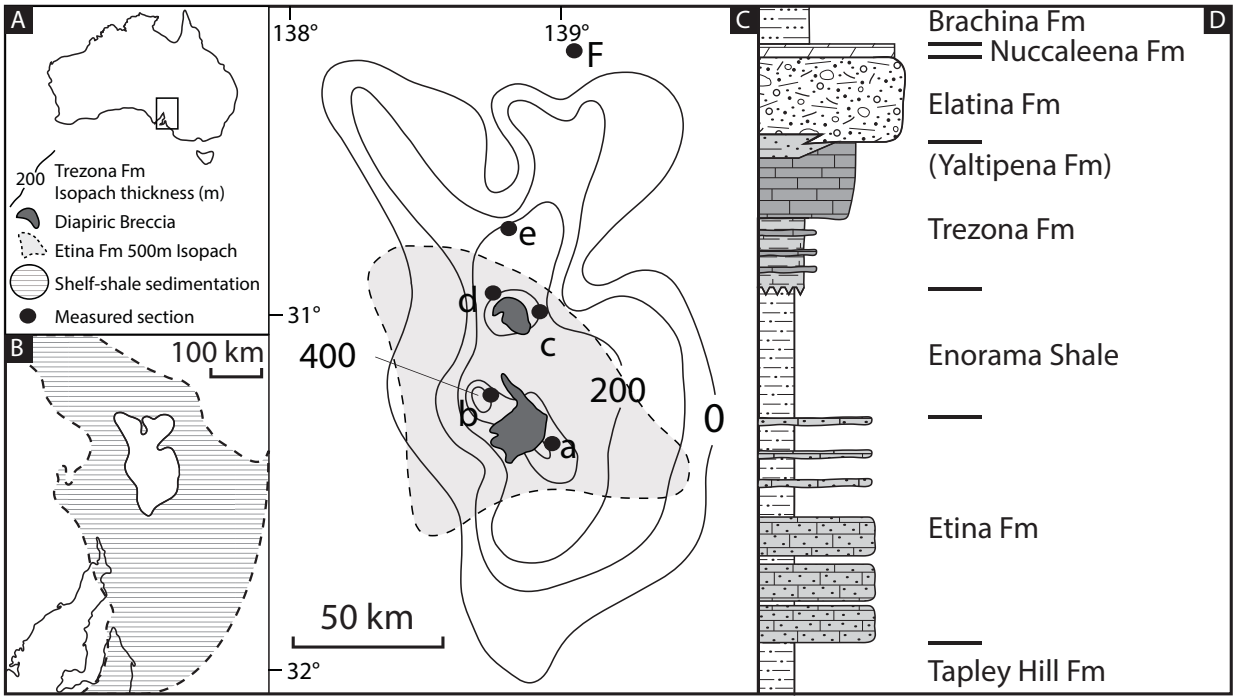

Figure 1. a) Regional map b) Distribution of Trezona Formation carbonates (white) compared with Enorama Shale and equivalents across the shelf and c) Isopachs of the Trezona Formation with adjacent diapirs indicated (dark grey) adapted from Preiss (1987). a-f correspond to measured sections in Fig 2 and Fig 6. d) Generalised stratigraphy of the central Flinders Ranges capped by the base-Ediacaran Nuccaleena Formation (not to scale).

been reinterpreted as a shoaling sequence from the underlying shelfal Enorama Shale to shallow carbonate ramp facies (McKirdy et al., 2001) to, in part, outer shelf-slope deposits (Rose et al., 2012). Further, its top contact has been variably interpreted as erosive (McKirdy et al., 2001) and conformable (Rose et al., 2012) with overlying glacial deposits of the Elatina Formation. In the central Flinders Ranges, 100 m of red bed silts and sands overly carbonate sediments following interbedding with carbonate facies in the upper Trezona Formation, are termed the Yaltipena Formation (Lemon and Reid, 1998), and are further overlain by Marinoan-aged glacial deposits.

3. Methods

All samples analysed in this study were collected during stratigraphic logging of 9 stratigraphic sections of the Trezona Formation in the central and equivalent units in the northern Flinders Ranges, South Australia. Samples of limestone and carbonate-cemented siltstones were collected across all lithofacies, with limestones > 95% calcite in composition used to construct $\delta^{13}C$ profiles in Figure 2. Samples were slabbed, and then powdered ~15mg subsamples were collected from individual textures and laminations using a dentist drill. 50 thin sections were cut and analysed to assess sample quality. New stable isotope ($\delta^{13}C$ and $\delta^{18}O$) measurements were performed on ~0.8mg powders using continuous-flow isotope-ratio mass spectrometry. Measurements were made on an Analytical Precision AP2003 at the University of Melbourne (mean analytical precision for $\delta^{13}C$ and $\delta^{18}O$ is ± 0.03‰ and ± 0.07‰ respectively) and on a Nu Horizon CF-IRMS at the University of Adelaide (mean analytical precision for $\delta^{13}C$ and $\delta^{18}O$ is ± 0.1‰). Samples were digested in 105% phosphoric acid at 70°C and mass spectrometric measurements were made on evolved CO_2 gas following the method of Spötl and Vennemann (2003). Results were normalised to the Vi-

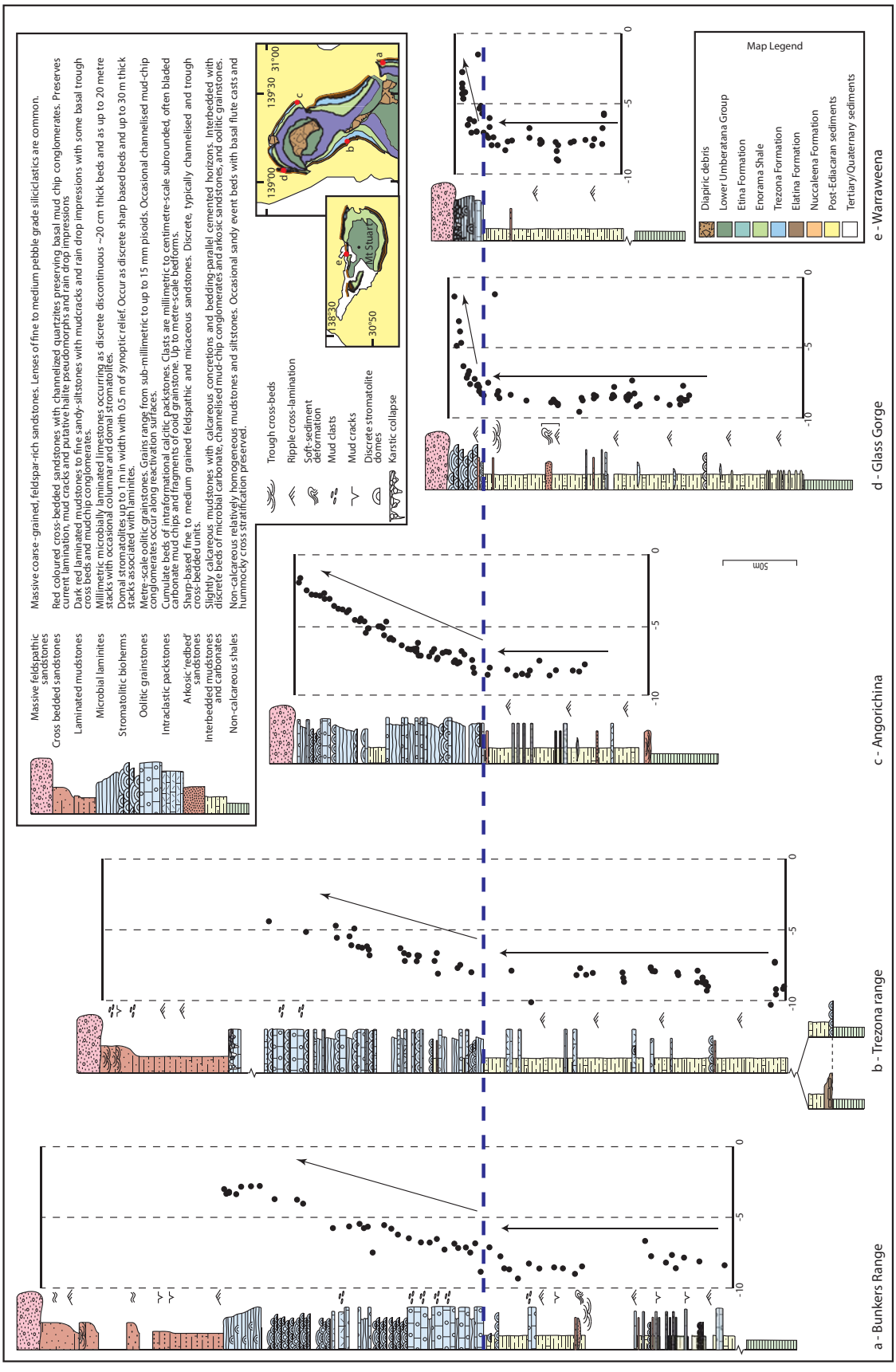

Figure 2. Stratigraphic logs with coupled $\delta^{13}C$ profiles. Dashed line indicates major facies shift from interbedded mudstones to carbonate allochems. Arrows indicate direction of isotopic change. All $\delta^{13}C$ values are derived from pure (>95%) limestones and dolostones.

enna Pee Dee Belemnite scale using internal working standards.

4. Results

4.1 – Sedimentology of the Trezona Formation

New field observations at the contact between the Trezona Formation and underlying Enorama Shale identifies a regionally traceable unconformity that separates up to 450 m of continuous deeper-shelfal shale deposition from the first shallow-water carbonates of the Trezona Formation. At Angorichina Station Station, >75 m of continuous non-calcareous shales are sharply overlain by a 10 m thick interval of laminated to cross-stratified micaceous sandstones that are immediately followed by the first concretionary carbonate cements of the lower Trezona Formation (Figure 3a-b). Similarly, at Enorama Creek an abrupt step to stromatolitic carbonate and interbedded mudstones follows continuous non-calcareous shale deposition (Figure 3c). A third locality at Bulls Gap is characterised by a distinctive 30 cm thick interval of massive, poorly-structured feldspathic and quartz coarse sand (Figure 3d). Fragments of shale are incorporated into the matrix at the base of the unit as tabular to elongate clasts up to 6 cm, and are aligned parallel to the original bedding plane (Figure 3e). In some examples, tabular fragments pass laterally into preserved lamination, indicating that fragmentation took place in-situ, consistent with the development of a soil horizon. These observations indicate subaerial exposure of deeper-shelfal shales and a depositional hiatus prior to Trezona Formation shallow-water deposition.

The Trezona Formation can be subdivided into two distinctive stratigraphic intervals that vary in relative thickness away from the central Flinders Ranges diapirs (Figure 1c, 2) and record conditions of shallow water, exposure and local erosion. The lower Trezona Formation comprises 150 to 200 m of laminated fissile mudstones with ~5 to 15 cm bedding-parallel sparry calcite concretions and discrete resistant beds of cemented siltstone often preserving 1 to 2 cm thick ripple cross-beds (Figure 4a). Interbedded at a metre scale are 5 to 15 cm thick intraformational mudflake conglomerates, stromatolite mounds, red arkosic silts and sands, and rare oolitic packstones (Figure 4b-d). Mudflake conglomerates are often confined to broad channels that thin laterally over tens of metres, are sharp based, preserve clast-rosettes indicating sporadic high current velocity, and are capped by 0.5 to 2 cm thick structureless micritic caps, consistent with reworking of carbonate mud-chips during storms (Figure 4b). The micritic caps themselves preserve mud cracks in the Bunkers Range section (Figure 4e) that penetrate down into mudclast conglomerates, indicating that mudflake debris accumulated at or near base-level and was subsequently subaerially exposed and desiccated. Locally, stromatolite mounds overlie intraclastic and siliciclastic substrates and are typically ~30 cm thick domes or thin (~15 cm) laminites (Figure 4c). Desiccation of this material likely provided intraclasts that were reworked locally into mudflake conglomerates, which occasionally fill the space between discrete domes. Red-coloured, poorly sorted, angular, micaceous, arkosic silts to fine sands are commonly cross-laminated and occur as sharp-based channels up to 45 cm thick with local evidence of trough cross bedding and syn-sedimentary slumping (Figure 4d). These discrete arkose sands interbed throughout the shallow and mudstone-dominated lower Trezona Formation across the Flinders Ranges (Figure 2), and represent the only coarse-grained siliciclastic component present in the Trezona Formation until the base of the locally preserved Yaltipena Formation that overlies it. Resistant strike ridges of carbonate punctuate interbedded mudstones and limestones facies, typically comprising cumulate polymict intraformational conglomerates with decimetre-scale bedforms that are often draped by mud along depositional reactivation surfaces. Clasts comprise bladed mud flakes, subangular to subrounded mud fragments and ooids that are mineralogically and texturally similar to local in-situ equivalents. Individual beds thin laterally over hundreds of metres but are not apparently confined to channels and occasionally act as a substrate for stromatolite domes. The lower Trezona Formation interbedded facies is distinctly shallow from the base of the unit compared with the under-

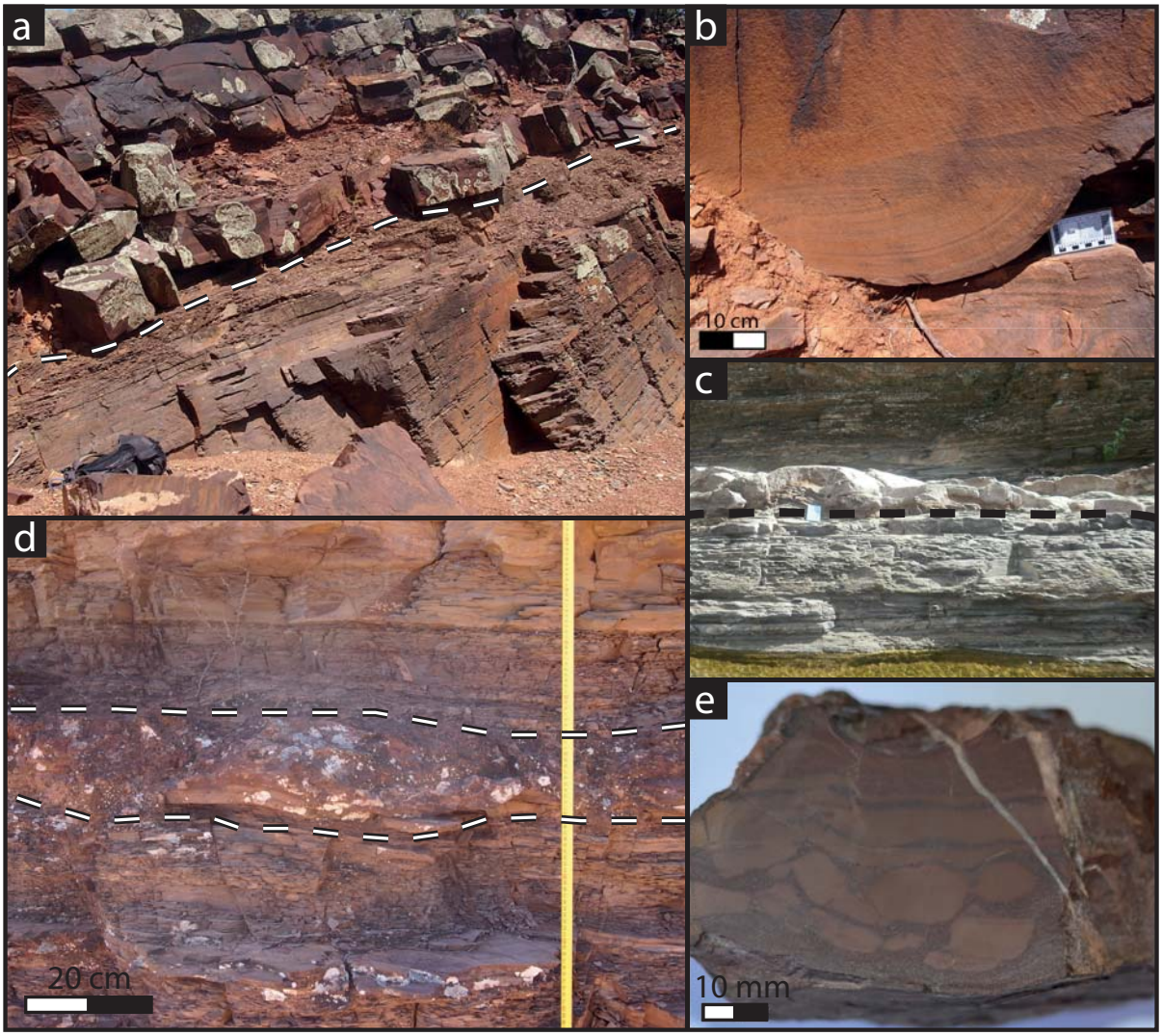

Figure 3. a-b) Outcrop of basal Trezona Formation unconformity at Angorichina Station. Arkosic trough-cross bedded sand lie sharply above continuous non-calcareous shales of the Enorama Formation. The first Trezona Formation carbonates occur within 10 m of this boundary. c) Outcrop of basal unconformity at Enorama Creek preserved as an abrupt step from continuous shales to stromatolitic carbonates. d-e) Putative palaeosoil horizon defining the base of the Trezona Formation at Bulls Gap. Following >75 m of continuous non-calcareous shale deposition, the basal Trezona Formation unconformity here is characterised by bedding-parallel fragments of shale in an arkosic matrix, consistent with in-situ weathering of Enorama Shale siliciclastics rather than sedimentary brecciation and transport. Immediately above this horizon is a typical lower-Trezona Formation limestone mudclast conglomerate (e).

lying Enorama Shale and it's lateral shelfal equivalents that is characterised by finely laminated siltstones and occasional cm-scale fine sands with local evidence for hummocky cross-stratification (McKirdy et al., 2001).

In all sections, an abrupt shift in facies toward microbial and subordinate grainstone carbonate deposition is recorded following 150 to 200 m of shallow mudstone and carbonate deposition (Figure 2). Microbial limestones occur as laminated mats in up to 15 m thick stacks, up to 1 m wide domes that show ~50 cm of synoptic relief (Figure 4f), and as sheets of ~3 to 5 cm wide columnar forms. Oolitic (locally pisolitic) and

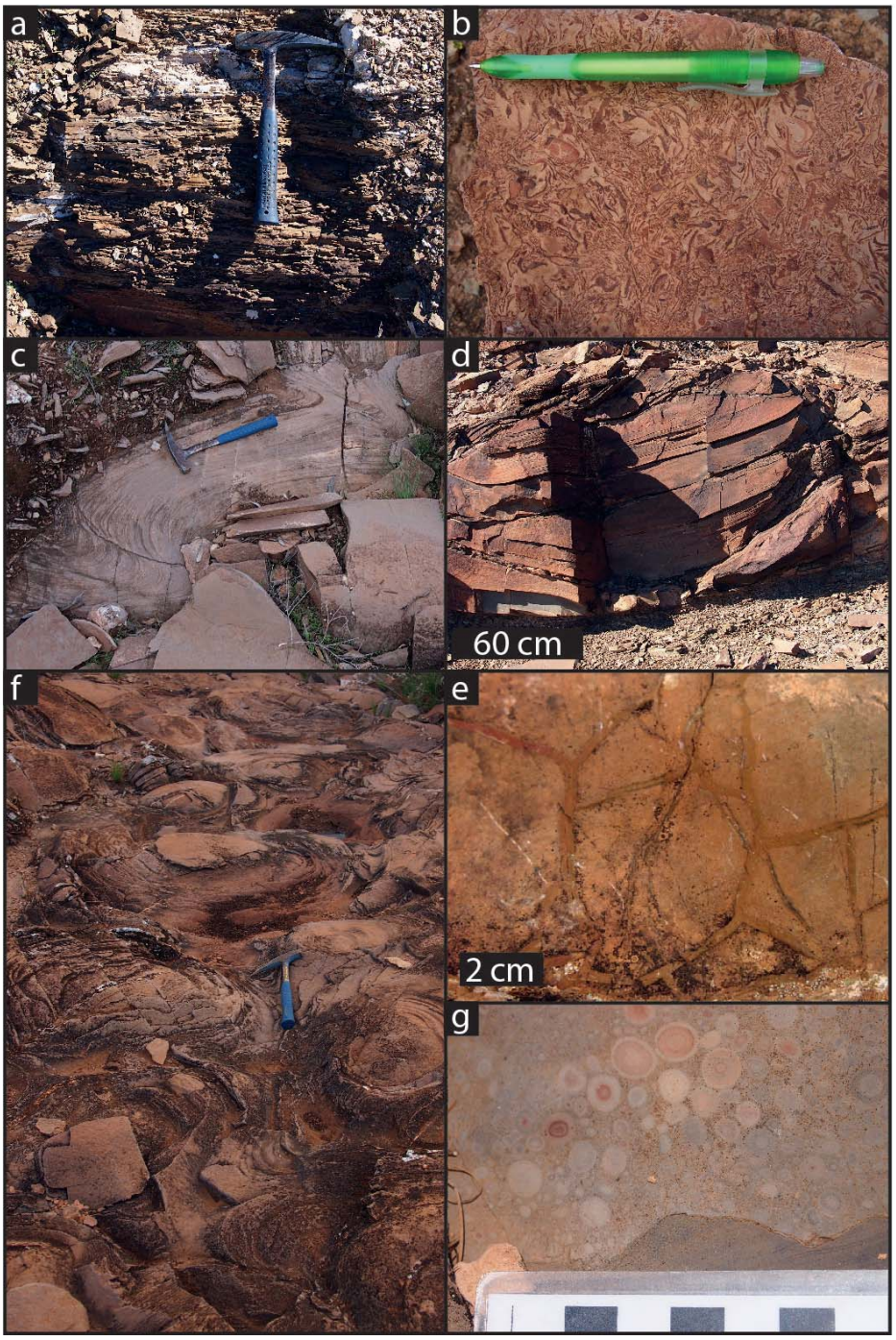

Figure 4. Facies of the Trezona Formation: a) Concretionary mudstones and siltstones, lower Trezona Formation, Trezona Range. b) Typical mud-chip conglomerate with evidence for shallow-water reworking of mud chips in storms, lower Trezona Formation, Trezona Range. c) Stromatolite draping siltstones in the lower Trezona Formation, Bulls Gap. d) Channelised cross-bedded sandstone, lower Trezona Formation, Bunkers Range. e) Mud-cracked marl cap overlying mud-chip conglomerate storm bed, lower Trezona Formation, Bunkers Range. f) Stromatolitic bioherms in plan-view from the upper Trezona Formation, bulls Gap g) Pisolitic limestone from the upper Trezona Formation, Angorichina Station. Scale bar is in 1 cm increments.

intraclastic shoals form metre-scale (up to 12 m) sharp based strike ridges that often act as the substrate for microbial mats and are well developed across the major facies change in the Bunkers Range region (Figure 4g). The abrupt shift from interbedded shale to microbial carbonate-dominated facies is reproducible across all sections examined, however stratigraphic thickness of the upper microbial carbonate-dominated unit varies significantly depending on proximity to the central Flinders Ranges diapirs. Sections measured in the Trezona and Bunkers Range and at Angorichina Station, all adjacent to likely active diapirs, preserve 150 – 200 m of microbial and grainstone carbonates while more distal sections to the north at Waraweena and Glass Gorge preserve just 20 m and 30 m respectively and lack grainstone shoal deposits (Figure 2).

The contact between the Trezona Formation and overlying Elatina Formation glaciogenic sediments is largely variable across the Flinders Ranges. At Waraweena, microbial carbonates are capped by heavily dolomitised karstic collapse-fill breccias of stromatolitic material that sharply contact massive feldspathic beds with quartz grit-lenses and pebble-clasts. Similarly, a sharp interface between carbonate and structureless, feldspathic, pebble-bearing sands occurs at Glass Gorge and Angorichina Station, and is assigned in all three locations to the glaciogenic Elatina Formation based on the presence of lonestones at Glass Gorge, lithological similarity between sections, and the unit's stratigraphic position directly below the Nuccaleena Formation cap-carbonate (Williams et al., 2008).

In diapir-proximal sections to the south, a sequence of red bed siltstones and sandstones lies between the upper Trezona Formation and lower Elatina Formation. The lower contact of this sequence, the Yaltipena Formation (Lemon and Reid, 1998), is bounded by a karst collapse breccia in the Trezona Range. This siliciclastic interval is only preserved stratigraphically above the exposures of the Trezona Formation peripheral to the Enorama and Oraparinna diapirs. The lower interval is characterised by laminated muds to angular arkosic fine sands that pass upwards into coarsening-up fine-medium red sandstones. These sandstones show evidence of current reworking as millimetric-scale ripples and cross-lamination, and evidence of periodic exposure as casts of rain drop impressions (Figure 5a) common mudcracks (Figure 5b), and halite pseudomorphs. Coarse sandstones occur as distinct channels that often preserve basal mud-clast conglomerates and are planar to trough cross-bedded (Lemon and Reid, 1998).

4.2 Palaeoenvironmental interpretation of the Trezona Formation

Following sea-level drawdown across the extensive shallow-shelf that dominated sedimentation in Neo-

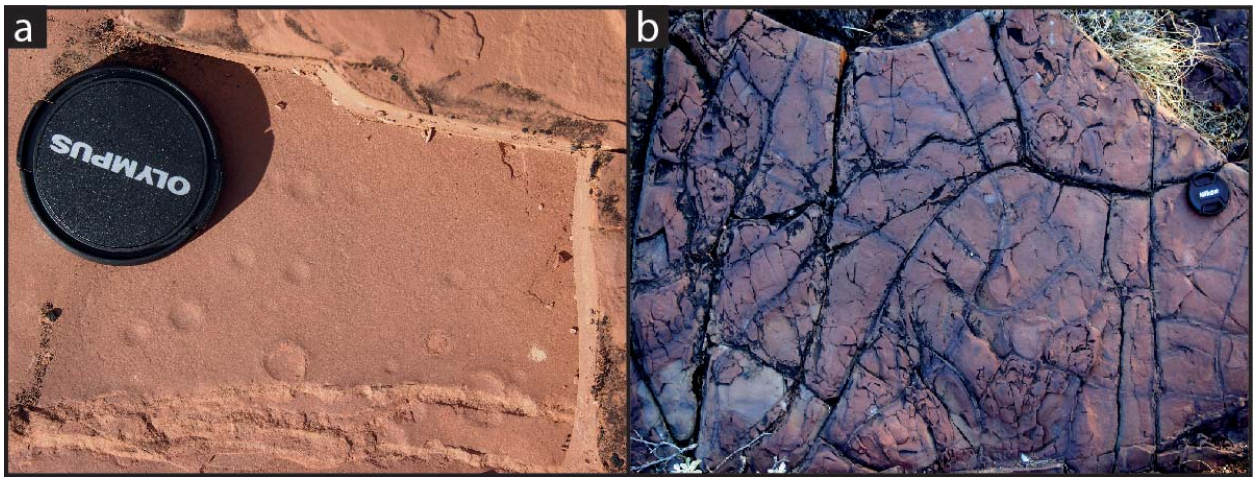

Figure 5. a) Rain-drop impression casts in non-calcareous mudstones of the Yaltipena Formation, Bulls gap and b) Mudcracks in the Yaltipena Formation, Bunkers Range. Lens cap is 37 mm in diameter.

proterozoic cratonic Australia, a period of exposure was followed by the accumulation of calcareous muds in a shallow depression peripheral to the Oraparinna and Enorama diapirs. Microbial carbonates accumulated as bioherms or thin mats on the shallow margins of the basin and above local topographic highs where periodic emergence allowed for desiccation of sediment, resulting in mudflake conglomerate deposition during storms in shallow channels and between stromatolite synoptic relief. Intraclastic and oolitic shoals formed in the relatively deeper parts of the basin while red arkosic sands brought in by a prograding fluvial system were deposited in channels incised from the basin margin. Following a relative rise in base-level, deposition in the deeper diapir-proximal areas of the basin shifted abruptly to dominantly microbial laminites, where thick oolitic shoals accumulated and migrated providing a substrate for new microbial sequences. Occasional salt-driven activity periodically exposed sediments to water-table fluid interactions that allowed local dissolution and karst-collapse (McKirdy et al., 2001). To the south, the fluvial system feeding the basin prograded, incising calcareous sediment further north and preserving as the Yaltipena Formation red beds in the Trezona Range as it filled into the basin. While previously presented as a simple shoaling cycle from continuous siliciclastic shelf-shale deposition, the Trezona Formation is more consistent with a spatially restricted basin such as an alkaline lake that records a history of deposition at or near base-level throughout, with an associated fluvial system represented by the overlying Yaltipena Formation siliciclastics and interbedding of mineralogically similar arkosic sandy channels in its lower interval.

4.3 Controls on spatial distribution

The limited lateral extent and distinctive bulls-eye pattern of deposition of the Trezona Formation has been variably interpreted by previous workers as consistent with a lacustrine basin focussed on the central Flinders Ranges (Preiss, 1987) and with a model of sub-glacial erosion in regions away from the central Flinders Ranges diapirs (McKirdy et al., 2001; Rose et al., 2013), truncating the upper Trezona Formation and the entire Yaltipena Formation across the continental shelf. The thickness distribution observed in the Trezona Formation is not unique to this subglacial stratigraphic interval however, with a similar pattern of distribution occurring in an underlying unit, the Etina Formation, that is not stratigraphically related to glacial deposits. The Etina Formation directly underlies the Enorama Shale in the central Flinders Ranges and comprises up to 1200 m of mixed shallow-water carbonate and deeper-water shale deposits, with the internal cyclicity between these facies associated with sea-level rise and fall across the shelf (McKirdy et al., 2001). In analogy to the Trezona Formation, maximum thicknesses in the Etina Formation occur peripheral to the Enorama and Oraparinna diapirs, and a similar reverse-thickness gradient occurs away from these regional depocenters. Diapiric debris is abundant in the Etina Formation (Lemon, 1988) indicating that salt tectonic processes were particularly active syn-depositionally, relating the distribution of sediment to local accommodation space resulting from local salt-withdrawal.

Local differences in the upper contact between the Trezona Formation and Elatina Formation glaciogenic deposits are also more consistent with the Trezona Formation recording much of its original depositional thickness. The karst surface documented at Waraweena for example, indicates that conditions of subaerial exposure and dissolution dominated prior to the deposition of glaciogenic material in place of a deep and sharp erosional contact offered to account for the ~350 m less stratigraphy here when compared to diapir-proximal sections (McKirdy et al., 2001; Rose et al., 2013). The pre-Elatina Formation interval was also documented at two localities ~50 km north of the typically mapped extent of the Trezona Formation with sections at Punches Rest and Umberatana Station recording a different relationship to water-depth and overlying glaciogenic deposits, and recently re-interpreted as deeper-water basinal sections of Trezona Formation equivalence (Rose et al., 2013). At Umberatana Station, shales of

the Amberoona Formation (Enorama Shale equivalent) pass gradually upward into increasingly carbonate-rich siltstones before transitioning into a rhythmically-laminated arkosic fine sandstone and heavily recrystallised sandy limestone that is punctuated by massive to parallel-laminated non-calcareous arkosic medium sandstones. At Punches Rest, carbonates also occur locally as anastomosing concretionary pods orientated parallel to laminae in arkose sandstone beds that occasionally coalesce into discontinuous, laterally-thinning interbeds. This facies is consistent for up to 400 m at Umberatana (Figure 6), after which compositionally identical sandstones are cut by channelised conglomerate mass-flows and incorporate discrete outsized clasts (Figure 6b). This 55 m thick interval is overlain by a 2 m thick dolomitic cap-carbonate consistent with the base-Ediacaran Nucaleena Formation, consistent with and interpretation that it is equivalent to the Elatina Formation. At Punches Rest, the rhythmic calcareous sandstone facies persists for ~80 m, is comparatively carbonate poor, and culminates in a single 1.8 m thick horizon of microbial carbonate. Rose et al. (2012) document granitoid boulders that are overgrown by microbial carbonates here, which they interpret as ice-rafted debris deposited synchronously with the uppermost carbonates of the Trezona Formation. Boulder

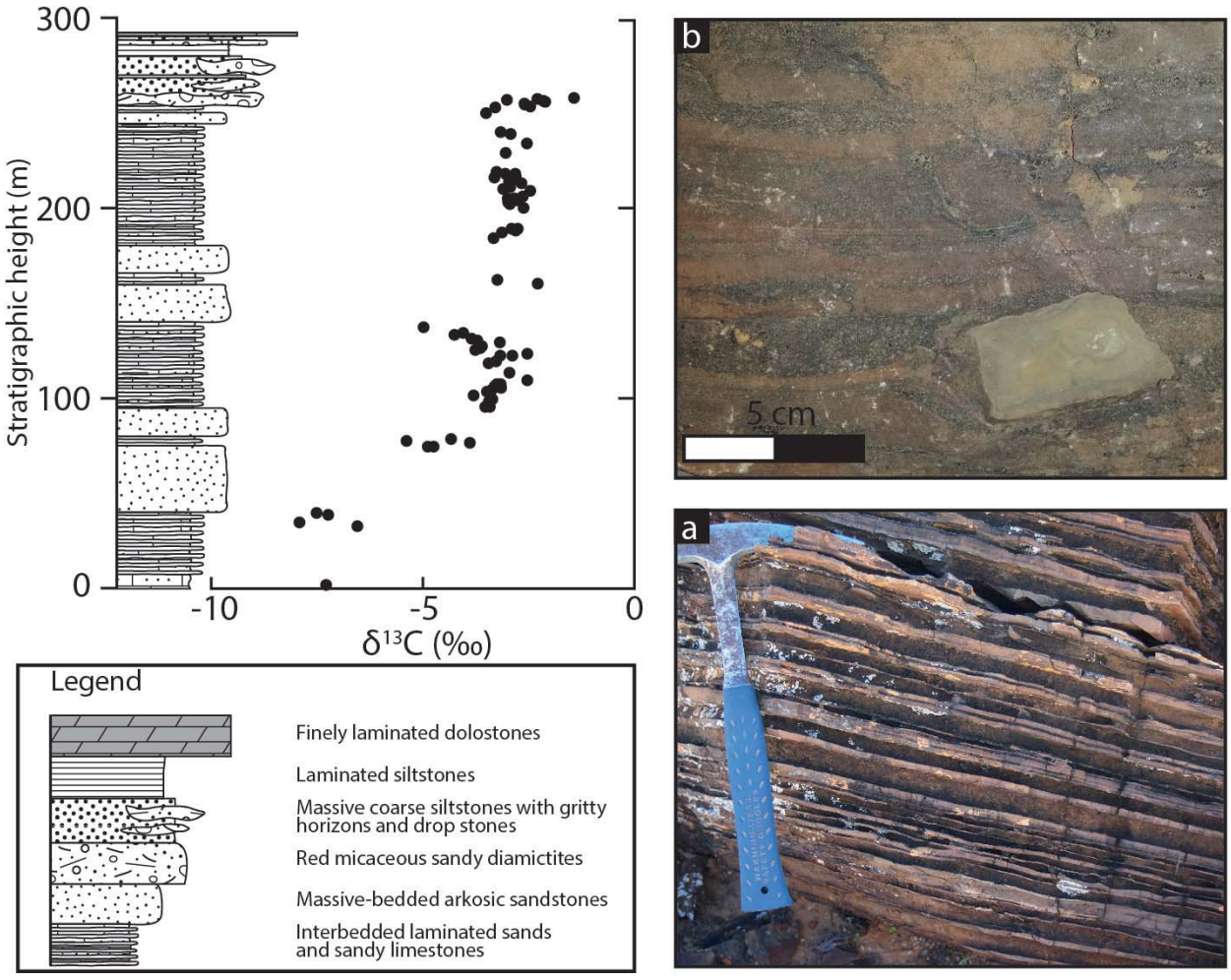

Figure 6. Isotope stratigraphy of the pre-Marinon interval in the northern Flinders Ranges (Umberatana section). a) Centimetre-interbedded sandstones and carbonate cemented sandstones. b) Elatina Formation glaciomarine facies with outsized clasts and grit-lenses.

diamictites containing both local and basement clasts follow this interval and are further overlain by the Nuccaleena Formation cap dolostone. In either section, no evidence of a significant hiatus is documented at any level for ~500 m prior to the onset of glaciogenic deposition, nor does a deep subglacial erosion surface exist capable of removing the Trezona Formation, nor have any of the distinctive facies of the Trezona Formation been documented interfingering with these northern sections. Further, these sections (Figure 6) seemingly record an entirely different sequence of $\delta^{13}C$ variations that bear little resemblance to the typical isotopic transitions recorded in the Trezona Formation proper. These observations are at odds with the interpretation that significant thicknesses of the Trezona Formation were removed by subglacial erosion progressively across the shelf (McKirdy et al., 2001; Rose et al., 2013; Rose et al., 2012) as deeper-water laminated silts-sands and calcareous sands pass apparently conformably into glacial deposits and no northern transition from shallow-water Trezona Formation carbonates to rhythmically-bedded carbonates and siliciclastics has been documented thus far.

4.4 Geochemical trends

As predicted for a shallow-water terrestrial basin, variations in a number of geochemical parameters occur in parallel to the changing basinal conditions recorded by the Trezona Formation stratigraphy. When the generalised Trezona Formation $\delta^{13}C$ profile previously published (McKirdy et al., 2001; Rose et al., 2013; Rose et al., 2012) is considered at sufficient resolution in individual sections, a correlation is evident between the major isotopic inflection point as sustained values of -9‰ begin to increase toward more modest values of -3‰ to -1‰, and the major facies shift between interbedded cemented mudstones and carbonates of the lower Trezona Formation and thick packages of microbial and grainstone carbonate that characterise the upper Trezona Formation (Figure 2). This trend is reproducible across the basin, where the most depleted values of -9‰ are exclusively recorded within sparry carbonate cements and concretions in mudstones, and interbedded carbonate beds within the lower Trezona Formation. $\delta^{13}C$ values that gradually increase do so immediately following the recurring facies shift toward microbial laminites and metre-bedded carbonate allochems, where the only detrital carbonate occurs as thin (< 5 mm) drapes of micrite.

Other geochemical parameters show step changes across the facies transition from lower interbedded mudstones and limestones and upper microbial and grainstone carbonates in the Trezona Formation. Bulk Fe data from the Bunkers Range section (Figure 7a) shows generally elevated concentrations across all samples ranging from ~1000 to 6000 ppm. These data record a stratigraphic shift in concentration across the $\delta^{13}C$ inflection point (and facies transition), with samples from the lower interbedded mudstone interval consistently ~1000 to 2000 ppm more enriched in Fe than the overlying microbial and grainstone carbonates. Mn/Sr ratios show a systematic shift along the $\delta^{13}C$ inflection point and facies change. Limestones in the upper microbial and allochem dominated interval of the Trezona Formation record a range of Sr values as high as 3000 ppm and somewhat elevated Mn concentrations of 100 to 200 ppm. In contrast, the lower interbedded mudstone and carbonate interval records an inverse relationship where Sr values are generally < 1000 ppm while Mn concentrations approach 2500 ppm (Figure 7b).

The return from -9‰ to values on the order of -1‰ to -3‰ occurs over significantly different stratigraphic thicknesses depending on the proximity of a given section to the Enorama and Oraparinna diapirs in the central Flinders Ranges (Figure 1), and is confined to the microbial and grainstone carbonates in the upper Trezona Formation. At Glass Gorge, $\delta^{13}C$ values shift abruptly across the facies change from lower Trezona Formation interbedded mudstones and limestones to upper microbial limestones, where recorded $\delta^{13}C$ values increase from -9‰ to -1‰ over 20 m of uninterrupted microbial carbonate facies (Figure 2c). In contrast, a gradual increase from $\delta^{13}C$ values of -9‰ to values of -2‰ and

-3.5‰ in the Angorichina Station and Bunkers Range sections respectively occurs over ~150 m of stratigraphic thickness and along a comparatively shallow gradient (Figure 2a, c). The section at Waraweena records an abrupt $\delta^{13}C$ increase over just 10 m to values of -1.5‰ that is associated with a dolomitised and karstic interval of microbial carbonates immediately overlain by Elatina Formation massive feldspathic deposits (Figure 2e). The differences in stratigraphic thickness that $\delta^{13}C$ values increase across is consistent with laterally variable sedimentation rates across the basin or with an interpretation that lateral $\delta^{13}C$ profiles are diachronous, but is inconsistent with the upper Trezona Formation being removed by subglacial erosion where the $\delta^{13}C$ signal is expected to be truncated before reaching the most enriched values expected. The most positive values presented here actually occur at Glass Gorge (-1.4‰) after only 20 m of microbial sedimentation while the ~350 m thick section in the Bunkers Range reaches a nadir of just -3‰ $\delta^{13}C$ and becomes ~1‰ more negative before passing upward into siliciclastic deposits.

Paired $\delta^{13}C$ and $\delta^{18}O$ data derived from limestones in diapir-proximal sections identifies three distinct populations associated with discrete stratigraphic intervals of the Trezona Formation that can also be related to changes in local conditions as the basin developed. Values derived from limestones in the lower shale-dominated interval record a linear covariant relationship at Angorichina Station ($r = 0.69$) that is stratigraphically confined to the interbedded shallow-water mudstone facies (Figure 8a). $\delta^{13}C$ and $\delta^{18}O$ values decouple following the facies change to the microbial carbonate interval, before a sharply divergent relationship characterises the uppermost 45 m ($r = 0.79$, Figure 8a). High-resolution published data (Maloof et al., 2010) from the Bunkers Range also shows these three distinct phases of isotopic variation that can also be broadly associated with stratigraphic interval and sediment type (Figure 8b), with a similar shift from a covariant relationship in the lower interbedded mudstone facies, and invariant to divergent trends in the lower and upper microbial and grainstone carbonate facies.

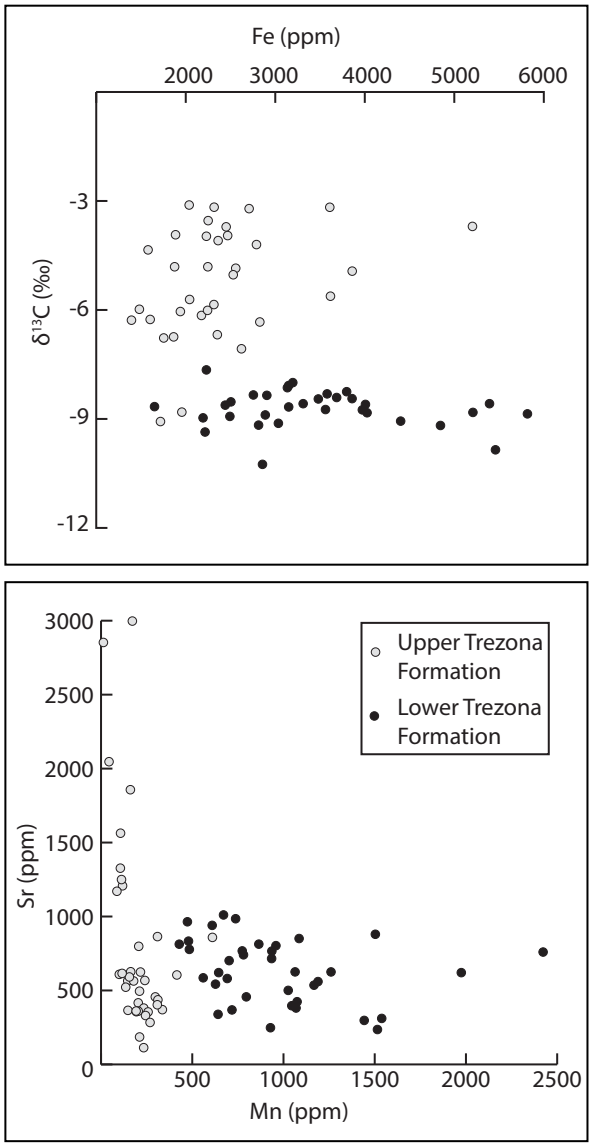

Figure 7. a) Crossplot of $\delta^{13}C$ composition versus Fe concentration in limestones, Bunkers Range. Closed circles are derived from the lower interbedded facies of the Trezona Formation, open circles are from the upper microbial/allochem interval. b) Crossplot of Sr concentration versus Mn concentration in limestones, Bunkers Range.

$\delta^{13}C$ values recorded by carbonate allochems carbonates such as grainstone and microbial lithologies compare favourably to those recorded in sparry calcite concretions that are abundant in lower Trezona Formation shales, and in intergranular carbonate cements in arkosic sandstones. In contrast, calcareous shales

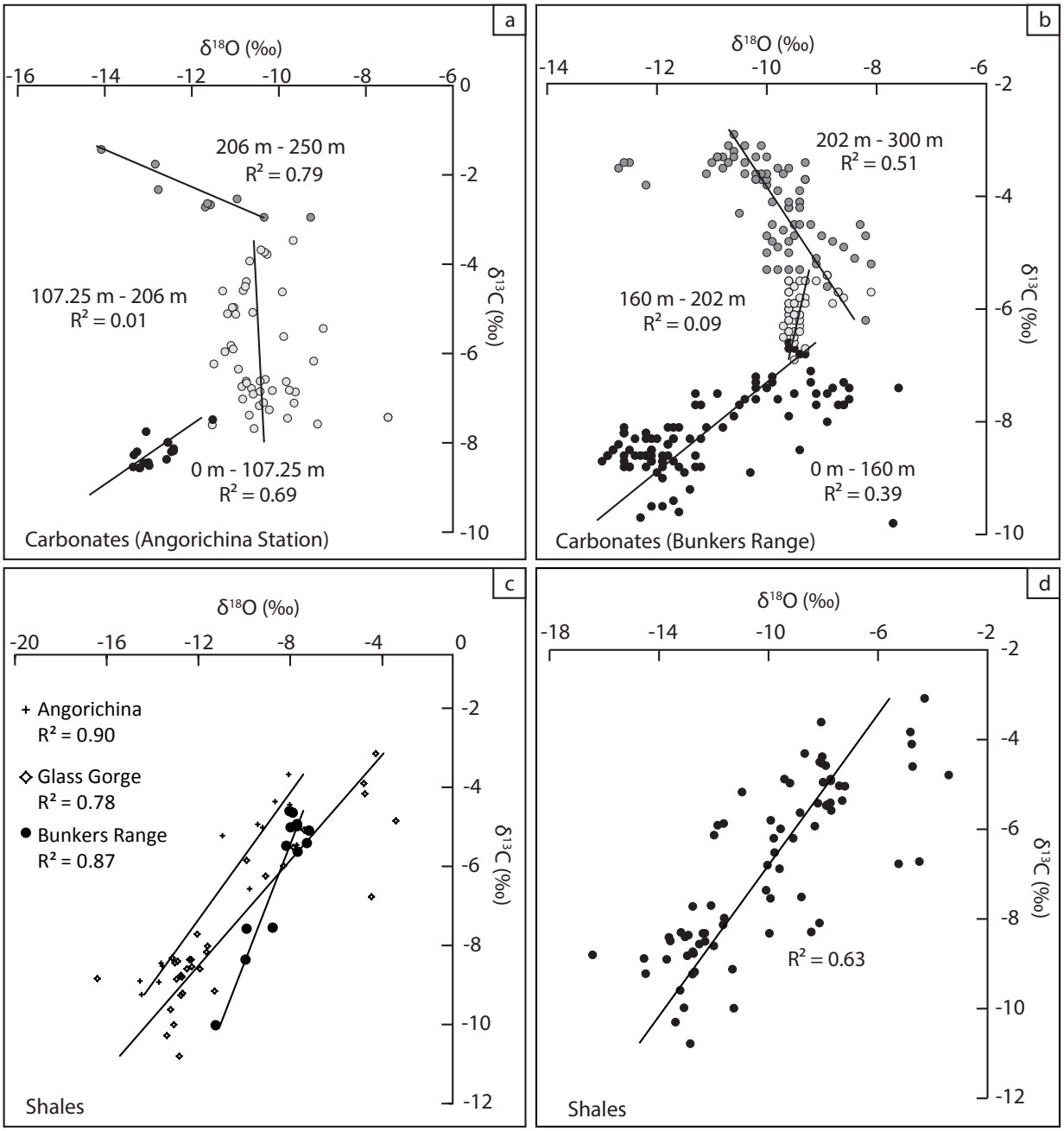

Figure 8. Scatterplots a) $\delta^{13}C$ vs $\delta^{18}O$ values from the Angorichina section (limestones, cemented sands and concretionary carbonates only). b) $\delta^{13}C$ vs $\delta^{18}O$ values from Emu Gap (Maloof 2010, carbonates only). c) Calcareous mudstones from the lower Trezona Formation at Glass Gorge, Angorichina and the Bunkers Range sections and d) Combined calc-mudstones from Glass Gorge, Angorichina and the Bunkers Range.

record a wide range of values from -3‰ to -11‰ and -3‰ to -16‰ for $\delta^{13}C$ and $\delta^{18}O$ respectively (Figure 8c). Variations in $\delta^{13}C$ and $\delta^{18}O$ are tightly coupled, illustrated by an r values up to 0.90 and a combined r=0.63 returned by calcareous mudstones from 3 sections across the basin (Figure 8d). The most negative values recorded in shales are isotopically similar to those recorded in adjacent limestones both in terms of $\delta^{13}C$ and $\delta^{18}O$, potentially indicating end-member mixing between an isotopically depleted (-9‰) and isotopically enriched

(~0‰) source that is not recorded by sparry limestones.

5. Discussion

Where $\delta^{13}C$ variability in Cenozoic pelagic records known to record changes in the ocean-atmosphere system is well constrained to < 3‰ (Shackleton, 1987; Zachos et al., 2001), the Neoproterozoic stratigraphic record preserves swings in $\delta^{13}C$ values of > 15‰ (Grotzinger et al., 2011; Shields and Veizer, 2002), occurring over hundreds of metres of sediment that can represent millions of years of Earth history (Le Guerroue et al., 2006). While variations of this magnitude are absent in Cenozoic pelagic records and are prohibitively large to satisfy with conventional carbon-cycle models (Bristow and Kennedy, 2008; Melezhik et al., 2005), they are directly comparable in magnitude, range, stratigraphic thickness and interpreted duration to examples recorded in shallow-water carbonate successions of Phanerozoic age and Cenozoic environments (Swart and Kennedy, 2011). In contrast to the Precambrian however, these stratigraphic excursions in $\delta^{13}C$ are not thought to constrain variability in the ocean-atmosphere system through time because these types of isotopic features are shown to be asynchronous within a given basin and in conflict with coeval and demonstrably open-marine $\delta^{13}C$ values (Swart and Eberli, 2005). Large magnitude variability in Phanerozoic carbonate $\delta^{13}C$ records occur in shallow marginal (Gischler and Lomando, 2005; Gischler et al., 2007; Swart and Eberli, 2005), intracratonic (Ludvigson et al., 2004; Panchuk et al., 2005; Saltzman, 2002), and non-marine (Bade et al., 2004; Talbot, 1990) environments where carbon-isotopic gradients exist both laterally across basins and vertically as ambient water chemistry shifts systematically in response to changing local hydrological and environmental conditions through time. These include rates of evaporation and organic matter degradation, the composition of input waters as riverine and groundwater discharge, and the fractionating effects of locally prolific phototrophic communities, the effects of which are diluted by the volume of the open ocean in deep-water environments but have an increasing influence on the $\delta^{13}C$ values recorded by precipitating carbonate as depositional environments become more shallow, are hydrologically restricted from marine connections, and shift landward where meteoric influx dominates over seawater exchange. The common constraint that fundamentally controls $\delta^{13}C$ variation in these types of environments is relative sea level and hydrologic connectivity. Sediment composition, diagenetic textures, evidence of shallowing and exposure, and $\delta^{13}C$ values, can be linked to changes in sea level across platforms and ramps, capable of producing depth-dependent gradients in $\delta^{13}C$ (Gischler and Lomando, 2005; Swart and Eberli, 2005). Similarly, sea-level drawdown that shifts shorelines basinward is capable of completely restricting water-bodies into transient phases of non-marine deposition that are then entirely reliant on local carbon-cycling processes and isotopically unrelated to sea-water. Critically, these are the types of environments that the Precambrian stratigraphic record is predicted to be dominated by.

While the inherent sensitivity of shallow-water basins to restriction and exposure is often not considered in Precambrian chemostratigraphic studies, the closest modern analogues indicate that they may impart a significant influence on our interpretations of Precambrian $\delta^{13}C$ records. Comparable modern equivalents to many Precambrian carbonate successions include sabkha environments on the Persian Gulf that flood during sea level-highstand (Evans et al., 1969), the Great Bahama Bank that records excursions to -10‰ coincident with meteoric-diagenetic intervals resulting from sea-level drawdown and exposure (Melim, 2001; Melim et al., 2002; Swart and Eberli, 2005), and the range of lacustrine environments that rely on fluvial inputs over seawater influx and record systematically evolving $\delta^{13}C$ profiles that reflect this local effect (Bade et al., 2004; Talbot, 1990). Where diagnostic fossil evidence of marine versus restricted/non-marine conditions is absent in the Precambrian record, sedimentary evidence and the stratigraphic context of individual sections can assist in constraining the origin and significance of re-

corded $\delta^{13}C$ variations. As predicted, features that indicate periods of restriction, evaporation and subaerial exposure such as salt deposits, desiccation features and palaeokarst are common to many Precambrian carbonate-bearing successions that also host anomalous $\delta^{13}C$ values (Calver, 2000; Day et al., 2004; Halverson et al., 2002; Halverson et al., 2004; Hill et al., 2000; Kenny and Knauth, 2001). Despite this, thick carbonate-bearing successions that are characteristic of the Neoproterozoic era are often presented as simple shoaling packages that record uninterrupted subaqueous conditions that persisted for millions of years and are thus linked to steady-state global exogenic processes.

The stratigraphic context of the Trezona Formation following siliciclastic-shelf deposition in the Enorama Shale has commonly led to the conclusion that the Trezona Formation represents a simple shallowing-upward trend toward the glacial lowstand of the Elatina Formation (McKirdy et al., 2001; Rose et al., 2013; Rose et al., 2012). This implies a conformable transition towards shallow-water carbonate deposition as a continuation of the overall regression expressed from the upper Enorama Shale, providing a constant accumulation of carbonate-bearing sediments through time. The sequence boundary identified in this study at the base of the Trezona Formation indicates that it represents its own distinct depositional cycle unrelated to progressive shoaling associated with the onset of glaciation. The thickness and complexity of the Trezona Formation in general argues against a single period of ice build-up and sea level fall, but is consistent with a regionally significant fall in base-level leading to erosion and hiatus prior to its deposition. The Trezona Formation is characterised by a sustained position of shallow-water deposition recorded from desiccated carbonate muds, conglomerates and fluvial deposits at the base, to microbial carbonates, karst, and fluvial facies at the top, and illustrates the establishment of an isolated alkaline water body that accumulated sediment in a shallow depression forming in the broad exposed shelf in response to local salt withdrawal, such as a restricted shallow sea or lake. A reproducible shift in facies that occurs across the basin to dominantly microbial facies that vary in thickness systematically away from diapiric sinks indicates a further shift in local base-level, abruptly altering local depositional conditions.

The palaeoenvironmental framework presented here coupled with shifts in stable isotopic and trace-element data across the major facies transition is difficult to reconcile with a previously interpreted marine origin. Negative and and covariant $\delta^{13}C$ and $\delta^{18}O$ values are a hallmark of hydrologically closed non-marine systems (Talbot, 1990) and marine systems that have been influenced by meteoric diagenesis (Quinn, 1991; Swart and Eberli, 2005) but are not consistent with ocean scale mechanisms as presently understood. In the context of the lower Trezona Formation where $\delta^{13}C$ values are consistently -8‰ to -9‰, either of these interpretations can be applied to a non-marine basin fed dominantly by terrestrial ground-water systems as would be predicted by a model of sea-level fall across the shelf where marine connections are severed. The occurence of $\delta^{18}O$ values <-8‰ throughout the Trezona Formation in general provides strong evidence for the involvement of meteoric waters over seawater exchange. Persistent brackish conditions would have supported ambient waters hosting heavily depleted $\delta^{13}C$ and $\delta^{18}O$ values as meteoric fluids charged with terrestrially-sourced organic acids carried the bulk of the dissolved carbon into the basin that subsequently precipitated as cements in mudstones and fluvial sands, and as primary limestones, with limited influence of seawater. As base-level rose, indicated by an abrupt shift in facies to carbonate allochems in diapir-proximal sections from mud crack-bearing interbedded mudstones, the Trezona basin became more hydrologically open, marked by the gradual increase in $\delta^{13}C$ values. This increase in isotopic values could indicate increased basinal productivity, or the mixing with an isotopically heavier source of dissolved carbon such as seawater. In contrast, a largely diagenetic origin for the most depleted values in the lower Trezona Formation that define the Trezona Anomaly may also be consistent with the strong observed facies association and positive linear

covariance. The Trezona Formation records no covariation with coupled $\delta^{13}C$ values derived from organic matter (Swanson-Hysell et al 2010), indicating that the preserved carbonate and organic phases fractionated from different and distinct carbon pools, although this test has recently proved controversial by studies of Cenozoic analogues that show a coupling of $\delta^{13}C$carb and $\delta^{13}C_{org}$ in sections demonstrably influenced by meteoric diagenesis (Oehlert et al., 2012; Oehlert and Swart, 2014). Comparatively high Mn/Sr ratios recorded in the lower Trezona Formation argue for multiple periods of in-situ remineralisation, consistent with poorly preserved and sparry carbonate textures. Further, calcareous siltstones from the lower Trezona Formation often carry relatively modest $\delta^{13}C$ and $\delta^{18}O$ values of -4‰ and -5‰ respectively that vary systematically along a mixing line (Figure 8c) and approach values on the order of -9‰ and -14‰ for $\delta^{13}C$ and $\delta^{18}O$, typical values recorded by lower Trezona Formation limestones. Where primary carbonate precipitates may have been readily recrystallised during diagenesis, fine-grained slightly calcareous muds and silts may have been only partially influenced by these processes and thus record a range of more positive values that may lie closer to the $\delta^{13}C$ balance of a primary depositional carbonate phase.

Fundamental to previous interpretations of the Trezona Anomaly representing a global signal is it's reproducibility between isolated basins across continents in carbonate successions directly below glacial deposits of inferred Marinoan age, where correlations rely on isotopic inflection points and terminal $\delta^{13}C$ values to provide a common datum to calibrate to (Halverson et al., 2005; Shields-Zhou et al., 2012). The Trezona Formation demonstrates the inherent ambiguity in this type of record where isotopes and sediment composition vary sympathetically as a basinal response to eustatic change and depositional hiatuses mean that a continuous and globally-representative record is not necessarily recorded. Similarly, correlative sections rarely provide demonstrably continuous records, and commonly contain depositional hiatuses and evidence of shallow-water deposition suggesting that they too are amenable to periods of restriction and the dominance of terrestrial processes. For example, the pre-Marinoan interval in Svalbard and NE Greenland records no depleted values in carbonate below Marinoan-aged glacial deposits, which is necessarily attributed to a cryptic depositional hiatus or erosion that seemingly removed the excursion in $\delta^{13}C$ here (Hoffman et al. 2012). The Trezona Anomaly as it is expressed in northen Namibia is associated with a series of shallow-water carbonate cycles that are subaerially exposed at cycle tops and are commonly truncated (Halverson et al., 2002).

The Trezona Formation, while ambiguous as a tracer for global-scale perturbations to the Earth's carbon cycle, may demonstrate that an extensive photosynthetic terrestrial biomass existed coeval with its deposition. Its isolated intracratonic position demands a terrestrial source of organic acids to allow the precipitation of a -9‰ carbonate phase. A Neoproterozoic expansion of terrestrial photosynthesising communities has been considered based on molecular (Heckman et al., 2001), mineralogical (Kennedy et al., 2006) and isotopic (Knauth and Kennedy, 2009) lines of evidence, but may in the case of the Trezona Formation be expanded to an association of more complex metazoans and non-marine environments (Maloof et al., 2010). Understanding the nature of $\delta^{13}C$ variations in restricted basins like the Trezona Formation may thus contribute significantly to answering the question of the conditions necessary for the profound evolutionary steps that characterise the Neoproterozoic record.

6. Conclusions

The Trezona Formation indicates that the sedimentological context of some Neoproterozoic $\delta^{13}C$ excursions can lead to a very different interpretation that need not invoke unprecedented steady-state perturbations to the Earth's carbon cycle to satisfy. The systematic nature of isotopic variation and sediment compositional change indicates that the characteristic $\delta^{13}C$ profile recorded in the Trezona Formation can be related to shifting basinal conditions as sea-level fell across the shelf,

likely including non-marine phases of deposition.

References

Bade, D. L., Carpenter, S. R., Cole, J. J., Hanson, P. C., and Hesslein, R. H., 2004, ontrols of δ^{13}C-DIC in lakes: Geochemistry, lake metabolism, and morphometry: Limnology and Oceanography, v. 49, no. 4, p. 1160-1172.

Berger, W., and Vincent, E., 1986, Deep-sea carbonates: reading the carbon-isotope signal: Geologische Rundschau, v. 75, no. 1, p. 249-269.

Bristow, T. F., and Kennedy, M. J., 2008, Carbon isotope excursions and the oxidant budget of the Ediacaran atmosphere and ocean: Geology, v. 36, no. 11, p. 863-866.

Calver, C. R., 2000, Isotope stratigraphy of the Ediacarian (Neoproterozoic III) of the Adelaide Rift Complex, Australia, and the overprint of water column stratification: Precambrian Research, v. 100, no. 1-3, p. 121-150.

Day, E. S., James, N. P., Narbonne, G. M., and Dalrymple, R. W., 2004, A sedimentary prelude to Marinoan glaciation, Cryogenian (Middle Neoproterozoic) Keele Formation, Mackenzie Mountains, northwestern Canada: Precambrian Research, v. 133, no. 3–4, p. 223-247.

Evans, G., Schmidt, V., Bush, P., and Nelson, H., 1969, Stratigraphy and geologic history of the sabkha, Abu Dhabi, Persian Gulf: Sedimentology, v. 12, no. 1-2, p. 145-159.

Gischler, E., and Lomando, A. J., 2005, Offshore sedimentary facies of a modern carbonate ramp, Kuwait, northwestern Arabian-Persian Gulf: Facies, v. 50, no. 3-4, p. 443-462.

Gischler, E., Swart, P. K., and Lomando, A. J., 2007, Stable isotopes of carbon and oxygen in modern sediments of carbonate platforms, barrier reefs, atolls, and ramps: patterns and implications: Perspectives in carbonate geology: a tribute to the career of Robert Nathan Ginsburg, p. 61-74.

Grotzinger, J. P., Fike, D. A., and Fischer, W. W., 2011, Enigmatic origin of the largest-known carbon isotope excursion in Earth's history: Nature Geoscience, v. 4, no. 5, p. 285-292.

Halverson, G. P., Hoffman, P. F., Schrag, D. P., and Kaufman, A. J., 2002, A major perturbation of the carbon cycle before the Ghaub glaciation (Neoproterozoic) in Namibia: Prelude to snowball Earth?: Geochemistry Geophysics Geosystems, v. 3, no. 6, p. 1-24.

Halverson, G. P., Hoffman, P. F., Schrag, D. P., Maloof, A. C., and Rice, A. H. N., 2005, Toward a Neoproterozoic composite carbon-isotope record: Geological Society of America Bulletin, v. 117, no. 9-10, p. 1181-1207.

Halverson, G. P., Maloof, A. C., and Hoffman, P. F., 2004, The Marinoan glaciation (Neoproterozoic) in northeast Svalbard: Basin Research, v. 16, no. 3, p. 297-324.

Heckman, D. S., Geiser, D. M., Eidell, B. R., Stauffer, R. L., Kardos, N. L., and Hedges, S. B., 2001, Molecular evidence for the early colonization of land by fungi and plants: Science, v. 293, no. 5532, p. 1129-1133.

Hill, A. C., Arouri, K., Gorjan, P., and Walter, M. R., 2000, Geochemistry of marine and nonmarine environments of a Neoproterozoic cratonic carbonate/evaporite: The Bitter Springs Formation, central Australia, in Grotzinger, J. P., and James, N. P., eds., Carbonate sedimentation and diagenesis in the evolving Precambrian world, p. 327-344.

Hoffman, P. F., and Schrag, D. P., 2002, The snowball Earth hypothesis: testing the limits of global change: Terra nova, v. 14, no. 3, p. 129-155.

Kaufman, A. J., and Knoll, A. H., 1995, Neoproterozoic variations in the C-isotopic composition of seawater: stratigraphic and biogeochemical implications: Precambrian Research, v. 73, no. 1–4, p. 27-49.

Kennedy, M., Droser, M., Mayer, L. M., Pevear, D., and Mrofka, D., 2006, Late Precambrian oxygenation; Inception of the clay mineral factory: Science, v. 311, no. 5766, p. 1446-1449.

Kenny, R., and Knauth, L. P., 2001, Stable isotope variations in the Neoproterozoic Beck Spring Dolomite and Mesoproterozoic Mescal Limestone paleokarst: Impli-

cations for life on land in the Precambrian: Geological Society of America Bulletin, v. 113, no. 5, p. 650-658.

Knauth, L. P., and Kennedy, M. J., 2009, The late Precambrian greening of the Earth: Nature, v. 460, no. 7256, p. 728-732.

Le Guerroue, E., Allen, P. A., Cozzi, A., Etienne, J. L., and Fanning, M., 2006, 50 Myr recovery from the largest negative $\delta^{13}C$ excursion in the Ediacaran ocean: Terra Nova, v. 18, no. 2, p. 147-153.

Lemon, N., and Reid, P., 1998, The Yaltipena Formation of the central Flinders Ranges: MESA Journal, v. 8, p. 37-39.

Lemon, N. M., 1988, Diapir recognition and modelling with examples from the late Proterozoic Adelaide Geosyncline, central Flinders Ranges, South Australia [Ph.D]: The University of Adelaide.

Ludvigson, G. A., Witzke, B. J., Gonzalez, L. A., Carpenter, S. J., Schneider, C. L., and Hasiuk, F., 2004, Late Ordovician (Turinian-Chatfieldian) carbon isotope excursions and their stratigraphic and paleoceanographic significance: Palaeogeography Palaeoclimatology Palaeoecology, v. 210, no. 2-4, p. 187-214.

Maloof, A. C., Rose, C. V., Beach, R., Samuels, B. M., Calmet, C. C., Erwin, D. H., Poirier, G. R., Yao, N., and Simons, F. J., 2010, Possible animal-body fossils in pre-Marinoan limestones from South Australia: Nature Geoscience, v. 3, no. 9, p. 653-659.

Martin, R. E., 1995, Cyclic and secular variation in microfossil biomineralization: clues to the biogeochemical evolution of Phanerozoic oceans: Global and Planetary Change, v. 11, no. 1–2, p. 1-23.

Maslin, M. A., and Swann, G. E., 2005, Isotopes in marine sediments: Isotopes in Palaeoenvironmental Research. Developments in Paleoenvironmental Research, Springer, Dordrecht, The Netherlands (2005), p. 227-290.

McKirdy, D. M., Burgess, J. M., Lemon, N. M., Yu, X. K., Cooper, A. M., Gostin, V. A., Jenkins, R. J. F., and Both, R. A., 2001, A chemostratigraphic overview of the late Cryogenian interglacial sequence in the Adelaide Fold-Thrust Belt, South Australia: Precambrian Research, v. 106, no. 1-2, p. 149-186.

Melezhik, V. A., Fallick, A. E., and Pokrovsky, B. G., 2005, Enigmatic nature of thick sedimentary carbonates depleted in ^{13}C beyond the canonical mantle value: The challenges to our understanding of the terrestrial carbon cycle: Precambrian Research, v. 137, no. 3-4, p. 131-165.

Melim, L. A., 2001, Meteoric and marine-burial diagenesis in the subsurface of Great Bahama Bank. In: R.N. Ginsburg (Editor), The Bahamas Drilling Project. SEPM Concepts in Sedimentology.

Melim, L. A., Westphal, H., Swart, P. K., Eberli, G. P., and Munnecke, A., 2002, Questioning carbonate diagenetic paradigms: evidence from the Neogene of the Bahamas: Marine Geology, v. 185, no. 1-2, p. 27-53.

Oehlert, A. M., Lamb-Wozniak, K. A., Devlin, Q. B., Mackenzie, G. J., Reijmer, J. J. G., and Swart, P. K., 2012, The stable carbon isotopic composition of organic material in platform derived sediments: implications for reconstructing the global carbon cycle: Sedimentology, v. 59, no. 1, p. 319-335.

Oehlert, A. M., and Swart, P. K., 2014, Interpreting carbonate and organic carbon isotope covariance in the sedimentary record: Nat Commun, v. 5.

Panchuk, K. M., Holmden, C., and Kump, L. R., 2005, Sensitivity of the epeiric sea carbon isotope record to local-scale carbon cycle processes: Tales from the Mohawkian Sea: Palaeogeography Palaeoclimatology Palaeoecology, v. 228, no. 3-4, p. 320-337.

Preiss, W. V. C., 1987, The Adelaide Geosyncline-late Proterozoic stratigraphy, sedimentation, palaeontology and tectonics., Bull. geol. Surv. S. Aust.

Quinn, T. M., 1991, Meteoric diagenesis of Plio-Pleistocene limestones at Enewetak Atoll: Journal of Sedimentary Petrology, v. 61, no. 5, p. 681-703.

Ravizza, G., and Zachos, J., 2003, Records of Cenozoic ocean chemistry: Treatise on geochemistry, v. 6, p. 551-

581.

Ridgwell, A., 2005, A Mid Mesozoic Revolution in the regulation of ocean chemistry: Marine Geology, v. 217, no. 3–4, p. 339-357.

Rose, C. V., Maloof, A. C., Schoene, B., Ewing, R. C., Linnemann, U., Hofmann, M., and Cottle, J. M., 2013, The End-Cryogenian Glaciation of South Australia: Geoscience Canada, v. 40, no. 4, p. 256–293.

Rose, C. V., Swanson-Hysell, N. L., Husson, J. M., Poppick, L. N., Cottle, J. M., Schoene, B., and Maloof, A. C., 2012, Constraints on the origin and relative timing of the Trezona $\delta^{13}C$ anomaly below the end-Cryogenian glaciation: Earth and Planetary Science Letters, v. 319–320, no. 0, p. 241-250.

Saltzman, M. R., 2002, Carbon isotope ($\delta^{13}C$) stratigraphy across the Silurian-Devonian transition in North America: evidence for a perturbation of the global carbon cycle: Palaeogeography Palaeoclimatology Palaeoecology, v. 187, no. 1-2, p. 83-100.

Shackleton, N., 1987, The carbon isotope record of the Cenozoic: History of organic carbon burial and of oxygen in the ocean and atmosphere: Geological Society, London, Special Publications, v. 26, no. 1, p. 423-434.

Shields-Zhou, G., Hill, A., and Macgabhann, B., 2012, The Cryogenian Period, The Geologic Time Scale, Elsevier.

Shields, G., and Veizer, J., 2002, Precambrian marine carbonate carbonate isotope database: Version 1.1: Geochem. Geophys. Geosyst, v. 3, no. 6, p. 1031.

Spötl, C., and Vennemann, T. W., 2003, Continuous-flow isotope ratio mass spectrometric analysis of carbonate minerals: Rapid communications in mass spectrometry, v. 17, no. 9, p. 1004-1006.

Swart, P. K., and Eberli, G., 2005, The nature of the $\delta^{13}C$ of periplatform sediments: Implications for stratigraphy and the global carbon cycle: Sedimentary Geology, v. 175, no. 1-4, p. 115-129.

Swart, P. K., and Kennedy, M. J., 2011, Does the Global Stratigraphic Reproducibility of $\delta^{13}C$ in Neoproterozoic Carbonates Require a Marine Origin? A Plio-Pleistocene Comparison: Geology, v. 40, no. 1, p. 87-90.

Talbot, M. R., 1990, A review of the paleohydrological interpretation of carbon and oxygen isotopic-ratios in primary lacustrine carbonates: Chemical Geology, v. 80, no. 4, p. 261-279.

Williams, G. E., Gostin, V. A., McKirdy, D. M., and Preiss, W. V., 2008, The Elatina glaciation, late Cryogenian (Marinoan Epoch), South Australia: Sedimentary facies and palaeoenvironments: Precambrian Research, v. 163, no. 3, p. 307-331.

Zachos, J., Pagani, M., Sloan, L., Thomas, E., and Billups, K., 2001, Trends, rhythms, and aberrations in global climate 65 Ma to present: Science, v. 292, no. 5517, p. 686-693.

Chapter 4

Statement of Authorship

Title of Paper	Constructing a Neoproterozoic carbon-isotope record
Publication Status	☐ Published ☐ Accepted for Publication ☐ Submitted for Publication ☑ Unpublished and Unsubmitted w ork w ritten in manuscript style
Publication Details	N/A

Principal Author

Name of Principal Author (Candidate)	Robert Klaebe		
Contribution to the Paper	Project design, fieldwork and sampling, sample preparation, data collection and processing, data interpretation, manuscript design and composition, generation of figures.		
Overall percentage (%)	85		
Certification:	This paper reports on original research I conducted during the period of my Higher Degree by Research candidature and is not subject to any obligations or contractual agreements with a third party that would constrain its inclusion in this thesis. I am the primary author of this paper.		
Signature		Date	14/10/2015

Co-Author Contributions

By signing the Statement of Authorship, each author certifies that:

i. the candidate's stated contribution to the publication is accurate (as detailed above);
ii. permission is granted for the candidate in include the publication in the thesis; and
iii. the sum of all co-author contributions is equal to 100% less the candidate's stated contribution.

Name of Co-Author	Martin Kennedy		
Contribution to the Paper	Project design, fieldwork, guidance with data interpretation, manuscript review.		
Signature		Date	14/10/2015

Constructing a Neoproterozoic carbon-isotope record

Abstract

The carbon-isotope ($\delta^{13}C$) record of Neoproterozoic carbonate-bearing sediments provides a critical monitor for changes in Earths biosphere through time, as well as providing time-significant tie-points used for global correlation of sedimentary strata. This study presents a stratigraphic test of the intrabasinal reproducibility of the commonly correlated pre-Sturtian glacial (~720 Ma) negative $\delta^{13}C$ excursion from +6‰ to -10‰ in the Andrée Land Group of the NE Greenland Caledonides, termed the Islay Anomaly. The upper platform to slope transition that precedes the onset of diamictite deposition was studied on Ella Ø in NE Greenland and compared to a lateral section in the north of the basin on Kap Weber. These sections are calibrated along two regionally traceable sequence boundaries identified by palaeokarst, subaerial erosion and major reorganisations of lithofacies in response to the drowning and emergence of ramp carbonates, and provide physical time-significant surfaces along which spatially separate $\delta^{13}C$ profiles can be tested for their reproducibility along strike. Platform carbonates comprising dolomitised stromatolites, pisolitic limestones, and laminated microsparites exclusively record positive $\delta^{13}C$ values of ~+6‰ while fine grained dolomite-bearing siliciclastics and interbedded carbonate debrites deposited on the slope record negative values of -4‰ to -10‰. On Kap Weber, a return to positive $\delta^{13}C$ values (+6‰) follows slope-mudstone deposition coincident with a return to platform carbonate deposition that is absent on Ella Ø, where negative $\delta^{13}C$ values are recorded into the base of Sturtian-aged glacial diamictites of the Ulvesø Formation. Critically, interbedding and soft sediment deformation across this facies transition indicates that no unconformity is present here. This disparity in $\delta^{13}C$ values at the base of the Ulvesø Formation suggests that the most negative $\delta^{13}C$ values recorded in the basin (-10‰) occur synchronously with values of +6‰, but are related to local sediment composition and the dominant process driving carbonate precipitation. Elemental mapping of slope mudstones shows that the carbonate component preserved is a rhombic dolomite phase that is unsorted with surrounding sediment and associated with clays, organic matter and euhedral pyrite, supporting an authigenic origin related to bacterial sulphate reduction that is not expected to constrain marine water-column $\delta^{13}C$ variation. $\delta^{13}C$ variability recorded in the upper Andrée Land Group is therefore interpreted as the result of systematically different palaeoenvironmental and diagenetic conditions that were abruptly superimposed by eustatic change, inconsistent with a continuous record of a global seawater value.

1. Introduction

Variations in carbon-isotope ($\delta^{13}C$) values recorded in sedimentary carbonate records are an important monitor of the Earth's carbon cycle through geologic time. Sharp declines in recorded $\delta^{13}C$ values to as low as -10‰ are recorded in Neoproterozoic-aged sedimentary archives and occur stratigraphically below diamictite and cap carbonate sequences interpreted to record globally synchronous ice ages (Fairchild and Kennedy, 2007; Hoffman et al., 1998; Sohl et al., 1999). The recurrence of this isotopic and stratigraphic motif across spatially isolated basins establishes a climatostratigraphic concept of globally synchronous panglaciation (Hoffman et al., 1998; Schrag et al., 2002) that is heralded by large-magnitude seawater $\delta^{13}C$ perturbations. Such a relationship inherently implies that the onset of global glaciation may have been triggered by catastrophic steady-state shifts in the mode of atmospheric carbon cycling that are expressed as a secular $\delta^{13}C$ shift that is recorded by accumulating marine carbonate. However, the precise timing of interpreted environmental and climatic change and how these forcings might inter-

nally relate remains limited by available physical stratigraphic data. In particular, the nature of glaciogenic deposition often provides an incomplete archive that does not necessarily reflect a time-continuous series of depositional phases. Thus, understanding the timing relations of isotopic and stratigraphic events leading in to the most severe climatic shifts in Earth history is critical in determining whether $\delta^{13}C$ values and the onset of global glaciation during the Neoproterozoic can be genetically linked through the carbon cycle.

The Neoproterozoic sequences exposed across the Caledonian fold belt in NE Greenland provide a natural laboratory where the sedimentary and stratigraphic transition between a routinely correlated $\delta^{13}C$ signal and overlying glaciogenic deposits can be closely examined. Here, the critical glacial transition can be observed in lateral basinal sections that also record preceding carbonate sediment bearing depleted $\delta^{13}C$ values. The continuity of sediment in individual sections with overlying evidence of glaciation directly informs whether depleted $\delta^{13}C$ values and the onset of glaciation can be linked in time and is consistent with a causal relationship. In contrast, a preserved sub glacial unconformity confounds this relationship and has the potential to decouple climatic events with the mode of the Neoproterozoic carbon cycle. This study examines a series of stratigraphic and isotopic events that are commonly correlated to global $\delta^{13}C$ curves in lateral basinal sections across the NE Greenland Caledonides to investigate the precise timing relationship between isotopic variation and the onset of glaciation.

2. The Islay Anomaly

A recurring $\delta^{13}C$ profile and stratigraphic motif is recognised in Neoproterozoic sequences of NE Greenland, Svalbard and Scotland where $\delta^{13}C$ values of +6‰ in carbonate-bearing sediments abruptly decline to $\delta^{13}C$-depleted values of -6‰ (as low as -10‰), that then locally recover to enriched values of +6 to +8‰ (Brasier and Shields, 2000; Halverson et al., 2005; Halverson et al., 2004; Knoll et al., 1986; Prave et al., 2009). This isotopic feature has been termed the 'Islay Anomaly' (Prave et al., 2009), serves as one of the key criteria used to support both a Marinoan (Halverson et al., 2004) and Sturtian (Hoffman et al., 2012) age for overlying glaciogenic deposits, and is a standard chronostratigraphic feature that Neoproterozoic $\delta^{13}C$ records derived from distal basins are calibrated to (Halverson et al., 2005; Shields-Zhou et al., 2012). Correlation of this isotopic feature in both basinal sections and with global $\delta^{13}C$ curves relies on a common datum chosen as 0‰ that follows the $\delta^{13}C$ decline from stable enriched values of ~+6‰, a return to enriched $\delta^{13}C$ values of +8‰ in some sections, and an interpreted sub-glacial surface that is assumed to be contemporaneous between distal sections (Figure 1). Where the upper $\delta^{13}C$ recovery is absent and/or large variations in sedimentary thickness of carbonate beds occur below interpreted Sturtian-aged glacial deposits, a model of simple sub-glacial erosional truncation is invoked to account for the isotopic discrepancy. The binary nature of isotopic and stratigraphic change that establishes these timelines fundamentally supports their correlation within Caledonian basins and between basins globally (Hoffman et al., 2012).

3. The Andrée Land Group

The Cryogenian Andrée Land Group is the upper portion of the Eleonore Bay Supergroup that crops out in a confined belt within the NE Greenland Fjord region over ~500km N-S (Figure 2). Correlative sections in Scotland and Ireland (Brasier and Shields, 2000; Prave et al., 2009), and the closely similar Hecla Hoek succession in NE Svalbard (Higgins et al., 2001), support the interpretation of a series of broad, shallow-water, connected ensialic basins that are associated with the onset of pre-Iapetus extension and subsidence (Sønderholm et al., 2008 and references therein). Capping 12 km of dominantly siliciclastic shelf sedimentation and ~2 km of stable carbonate platform deposition, the upper Andrée Land Group is in turn overlain by the diamictite-dominated Tillite Group, interpreted to record sustained conditions of pan-glaciation (Hoffman

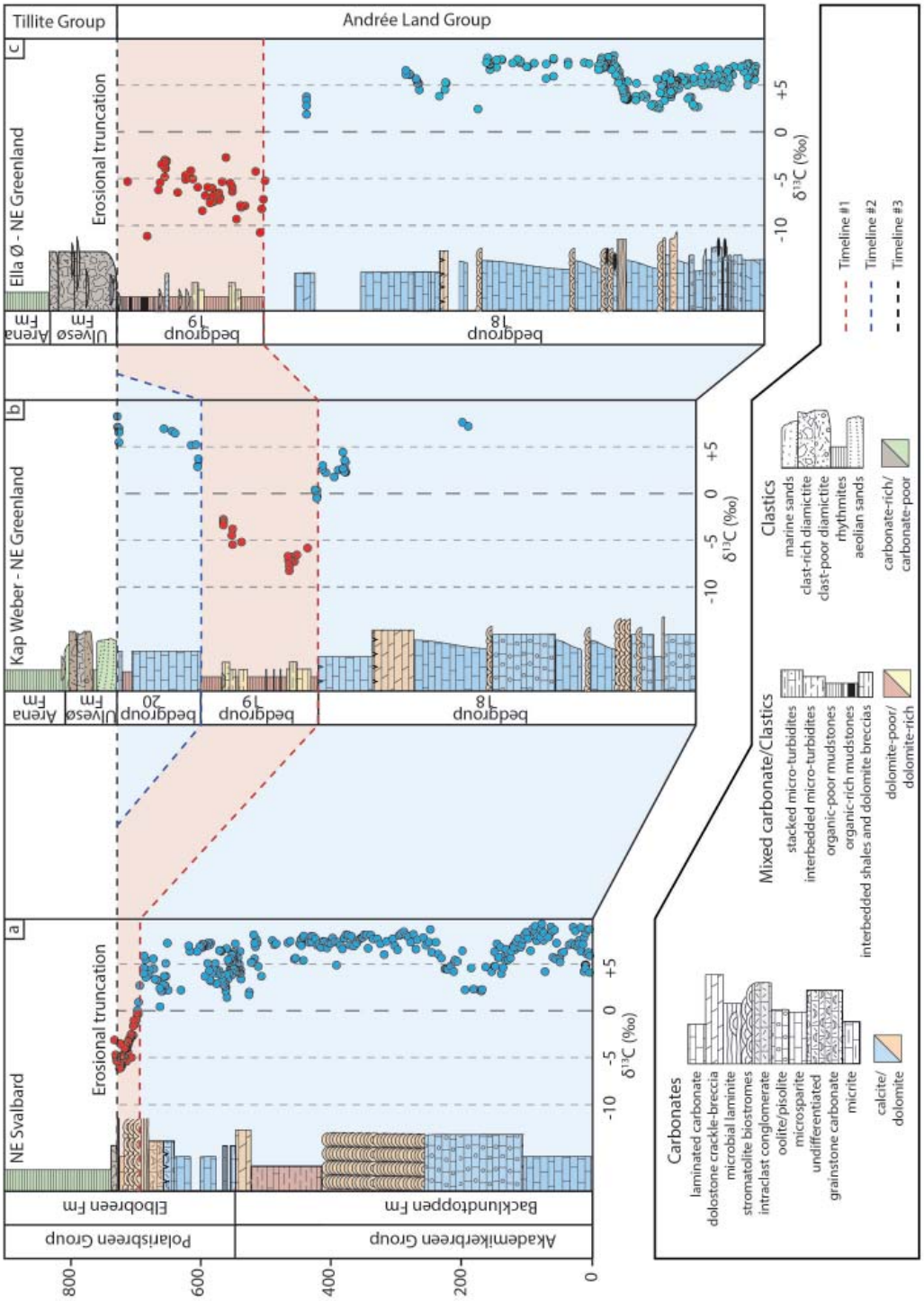

Figure 1. Traditional litho- and chemostratigraphic correlation of the Upper Andrée Land group Kap Weber (Fairchild et al., 2000) and Ella Ø (this study) sections from NE Greenland and a composite section constructed from the Backlundtoppen and Elbobreen Formations (Russøya Member) in NE Svalbard after Halverson et al. (2004), Halverson et al. (2005) and Knoll et al. (1989). Interbasinal correlation of the Islay Anomaly relies on 2 chemostratigraphic tie points (red and blue dashed lines) and a subglacial surface (black dashed line) indicating the base of the Sturtian glaciation (Halverson et al., 2005; Hoffman et al., 2012). Subglacial erosion and truncation is invoked to account for the lack of positive pre-glacial $\delta^{13}C$ values in sections in Svalbard and in southern regions of the NE Greenland Caledonides.

et al., 2012).

The carbonates and fine-grained siliciclastics of the Andrée Land Group and the overlying deposits of the Tillite group are well described in terms of the major lithostratigraphic and palaeoenvironmental transitions preserved (Fairchild and Hambrey, 1995; Fairchild et al., 2000; Frederiksen, 2000; Hambrey and Spencer, 1987; Herrington and Fairchild, 1989; Moncrieff and Hambrey, 1990; Sønderholm et al., 2008). The Andrée Land Group is informally subdivided into 'bed group' formations 1-20 (Sønderholm and Tirsgaard, 1993) of which the present study deals with the uppermost three. Bed group 18 records carbonate ramp sedimentation with lagoonal intervals and is characterised by neomorphosed microsparites with tepee and molar-tooth structures, channelised oolitic to pisolitic grainstones, and dolomitised intraclast packstones and stromatolitic biostromes (Fairchild et al., 2000; Frederiksen, 2000, Figure 1). Following a regionally-traceable interval of exposure, dissolution and collapse, upper bed group 18 comprises a sequence of neomorphosed laminated microsparites interpreted as outer-ramp deposits. An abrupt step from ramp carbonates to base of slope dolomitic silts and muds of bed group 19 illustrates the drowning and shoreward migration of stable shallow-water ramp conditions, interpreted as tectonically forced (Frederiksen, 2000; Sønderholm et al., 2008). A return to shallow water ramp carbonates is recorded as bed group 20, but is restricted to exposures in the North of the basin (Hambrey and Spencer, 1987, Figure 2). An abrupt facies transition from ramp carbonates to cross-bedded quartz sandstones interpreted as ae-

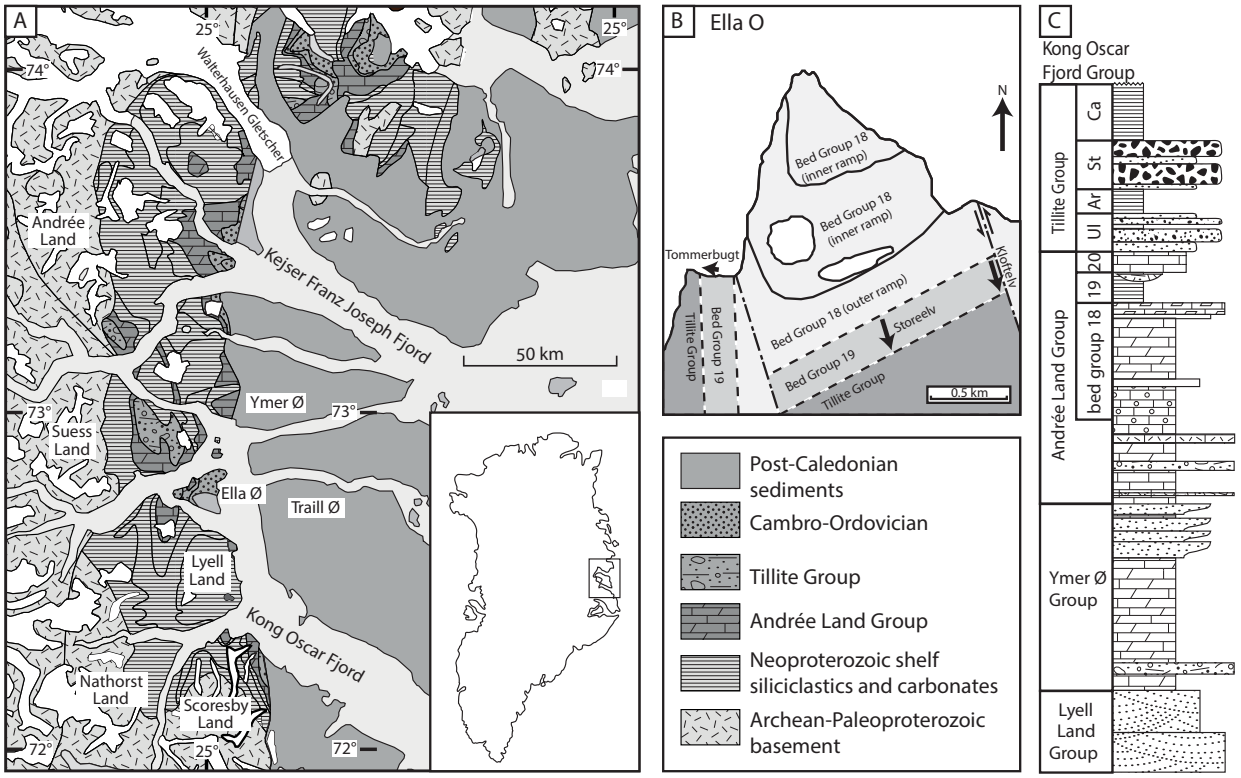

Figure 2. Study Area. A) Simplified geological map of Eastern Greenland (central fjord zone) showing the sediments of the Neoproterozoic Eleonore Bay Basin. Sections marked corresponds to Figure 6 field sections at Kap Weber (North) and Ella Ø (South). B) Enlarged image of Neoproterozoic deposits on Ella Ø after Fairchild et al. (2000). Measured section locations indicated by arrows. C) Generalised stratigraphy of the upper Eleonore Bay Supergroup and overlying Tillite Group.

olian in origin marks the base of the Ulvesø Formation (Tillite Group) that, following a subsequent marine transgression, is further overlain by relatively thin (10 to 20 m), massive to stratified clast-poor diamictites (Hambrey and Spencer, 1987; Moncrieff and Hambrey, 1990). Further South bed group 20 is absent in its entirety; a sharp contact with massive diamictites mineralogically similar to northern equivalents marks the base of the Ulvesø Formation here, with no preceding return to ramp-carbonate deposition or development of aeolianites. Further, the thickness of Ulvesø Formation diamictites approaches 200 m in the most distal sections (Hambrey and Spencer, 1987, Figure 1). The contrast in pre-glacial carbonate sequences across the basin has led to its variable interpretation as both removed due to significant subglacial erosion (Hoffman et al., 2012) and as locally conformable (Hambrey and Spencer, 1987). Ramp carbonates are inferred to have accumulated on a shallowly-dipping bank top with laterally extensive facies belts. As such, the N-S exposures across the NE Greenland Caledonides are considered to provide an approximate cross-section parallel to the palaeoshelf margin (Tirsgaard and Sønderholm, 1997).

The observed positive-negative-positive $\delta^{13}C$ sequence occurs along major lithofacies changes in bed groups 18-20 (Figure 1). $\delta^{13}C$-enriched values of +6‰ occur in relatively shallow-water ramp carbonates of bed group 18, which are overlain by variably depleted (-4‰ to -10‰) $\delta^{13}C$ values in base-of-slope calcareous mudstones and siltstones of bed group 19, and further overlain by enriched $\delta^{13}C$ values of +6‰ recorded by the uppermost platformal carbonates of bed group 20. In southern exposures where the return to ramp carbonates in bed group 20 is absent, the associated $\delta^{13}C$ recovery to ~+6‰ recorded in bed group 20 carbonates does not occur, with $\delta^{13}C$ values of -4‰ to -10‰ recorded into the base of the Ulvesø Formation (Figure 1c).

4. Analytical Methods

New stable isotope ($\delta^{13}C$ and $\delta^{18}O$) measurements were performed on ~0.8mg carbonate powders sub-sampled from rock slabs using continuous-flow isotope-ratio mass spectrometry. Measurements were made on an Analytical Precision AP2003 (mean analytical precision for $\delta^{13}C$ and $\delta^{18}O$ is ± 0.03‰ and ± 0.07‰ respectively) and on a Nu Horizon CF-IRMS (mean analytical precision for $\delta^{13}C$ and $\delta^{18}O$ is ± 0.1‰). Samples were digested in 105% phosphoric acid at 70°C and mass spectrometric measurements were made on evolved CO_2 gas following the method of Spötl and Vennemann (2003). Results were normalised to the Vienna Pee Dee Belemnite scale using internal working standards.

5. The Andrée Land Group – Tillite Group transition

5.1 Bed Group 19 on Ella Ø

The transition from ramp carbonates of upper bed group 18 through slope deposits of bed group 19 to the base of the Ulvesø Formation was examined on Ella Ø. Here, bed group 18 records ~600 m of repeatedly cyclic shallow-water limestones and dolostones (Figure 1c). Following ~20 m of laminated, scoured, neomorphosed dolomicrosparites with tepee and molar-tooth structures, lower bed group 18 records 100 m of decimetre cross-bedded, channelised oolitic and pisolitic grainstones (Figure 3a), undifferentiated microsparites (Figure 3b), and minor intraformational carbonate conglomerates, that shallow through 10 m of dolomitised intraclastic packstones capped by a distinctive ~3 m thick unit of dolomitised stromatolitic biostromes (Figure 3c). Up to 7 more abbreviated cycles (5 to 10 m in thickness) and a further 150 m thick cycle caps this sequence. Following an interval of exposure (Figure 3d), dissolution and collapse is a sequence of neomorphosed laminated microsparites that terminate with brecciated dolostones on Kap Weber (Fairchild et al., 2000). The first mudstones of bed group 19 occur directly above this surface.

In general, mudstones, siltstones and clastic debrites recorded in bed group 19 are arranged as a series of shallowing cycles (Figures 3e and 4). Cycle bases are dominantly non-calcareous to slightly calcareous mud-

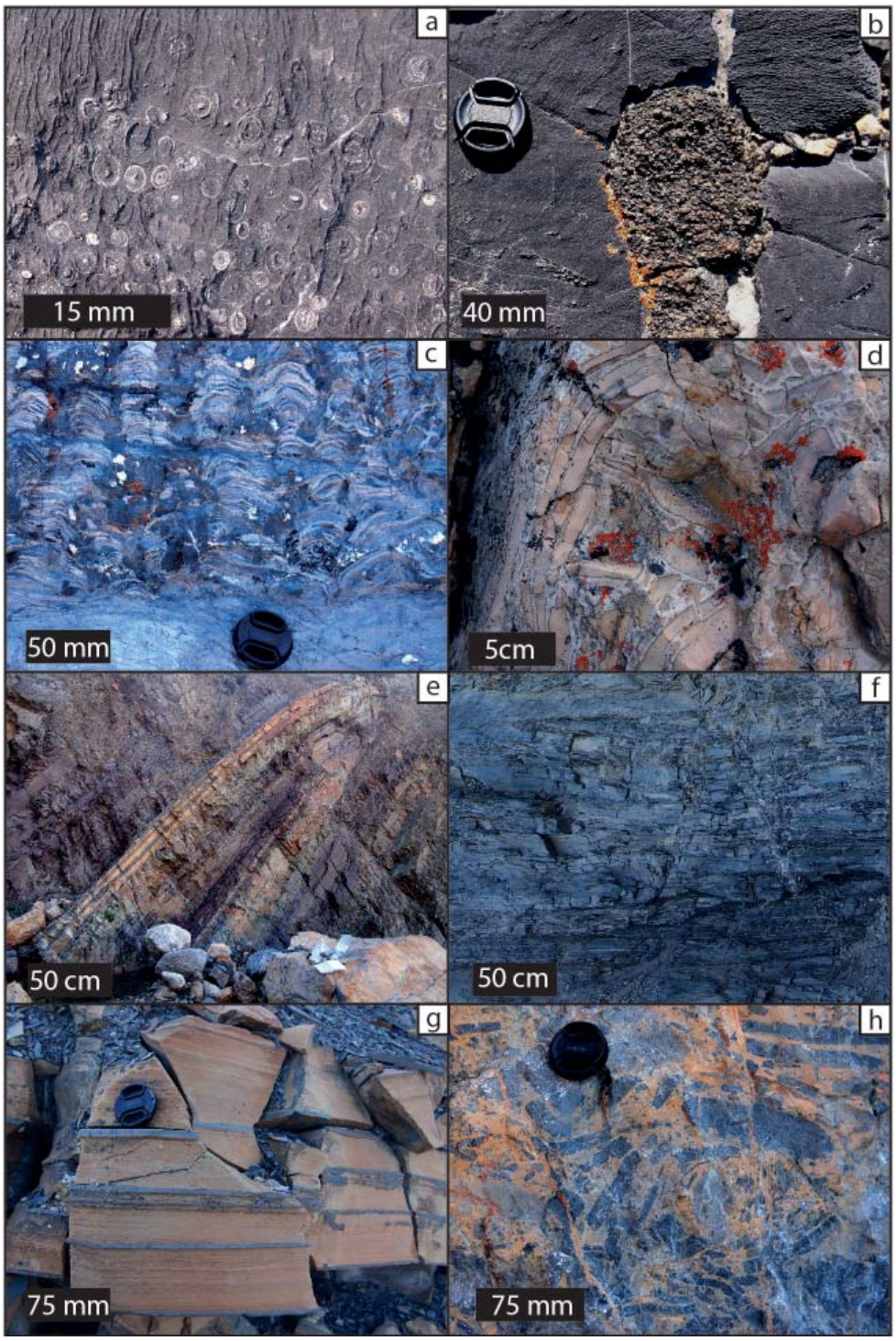

Figure 3. Representative facies of bed group 18 and 19 from Ella Ø. a) Channelised pisolitic and microsparry carbonate from lower bed group 18. Diffuse boundaries between pisoid allochems and overlying microsparite indicates that much of the preserved sparry limestones here are destructively-recrystallised allochems. b) Chert nodules in bed group 18 microsparite. Chert preserves original pisolitic textures of the sediment that is now homogeneous structureless microspar. c) Bed group 18 dolomitised columnar stromatolites that build into ~2m wide stromatolite domes. d) Upper bed group 18 dolomitic karst-collapse breccia with cm-thick fibrous dolospar interstitial cements. e) 4th order shallowing cycles

in lower bed group 19. Basal mudstones (red) transition up-section into interbedded then stacked fine-grained, dolomite-rich turbidite sequences. f) Typical carbonate-poor mudstone from bed group 19. g) Packages of mm-scale microturbidite sequences (current lamination and massive hemipelagic cap couplets), middle bed group 19. h) Channelised tabular-clast slope debrite showing clast rosette, middle bed group 19. Lens cap in all images is 37 mm in diameter.

stones occurring as both massive and locally laminated units with occasional organic-rich horizons (Figure 3f). Up-section, mudstones are increasingly interbedded with sharp-based dolomitic silt-mudstone horizons up to 5 cm thick, preserving irregular couplets of parallel laminated silt and massive dolomicrite, and occasionally basal current ripples and sub-mm mudflake conglomerates, consistent with DE and CDE bouma divisions respectively. Turbidite abundance increases towards the top of each cycle, where cycle tops comprise stacked turbidite facies exclusively for up to 5 m which are abruptly overlain by basal mudstones of the following cycle. Further up-section, matrix-supported debrites that preserve coarse-sand to cobble-sized material interbed with mustone and turbidite facies (Figure 3h). Diamictites either carry rounded or tabular-bladed limestone fragments occasionally arranged in clast-rosettes that are suspended in dominantly dolomite sand-grade matrix sediment, and mark the first evidence of pure carbonate following basal flooding of the ramp. Mineralised molar-tooth cements also occur at this interval. Debrites are capped by laminated silts and massive dolo-mudstones, consistent with suspension settling following mass flows. The upper interval of bed group 19 records an abrupt return to slightly-calcareous massive-laminated mudstone deposition, with a variable abundance of organic laminae and pyritic concretions and a distinct lack of turbidite event-beds. This facies passes vertically into diamictites of the Ulvesø Formation.

5.2 Nature of the basal Sturtian contact

The interval spanning the upper Andrée Land Group and lower Ulvesø Formation was studied at three localities on Ella Ø (Figure 2b) to address whether a time-continuous transition exists between bed group 19 mudstones and overlying glaciogenic deposits. In two of these examples (the Tømmerbugt and Kløftelv sections) the contact itself was continuously vertically exposed. A transitional relationship between the uppermost mudstones of bed group 19 into the glacial deposits (Figure 5) of the Ulvesø Formation is supported by the following observations:

1) Within 2 m below the contact at Tømmerbugt, mudstones of bed group 19 and diamictites compositionally identical to the basal Ulvesø Formation are seen to be interbedded (Figure 5a). Concave-up lenses of diamictite are 0.3 to 1 m in width with ~80% tan-weathering matrix material of sand-sized carbonate. Clasts comprise subrounded sand-pebble microsparites, oolitic and pisolitic carbonates, often replaced by chert, subangular often tabular sandstone up to 3 cm, subrounded sand-pebble dolostones, 0.1-0.5 cm angular (vein) quartz and angular and often tabular mudstones that are compositionally similar to the mudstone substrate (Figure 5b). Clast composition is consistent with that of the overlying Ulvesø Formation diamictites (Figure 5c).

2) At both Tømmerbugt and Kløftelv, dolomitic muds are incorporated into the lower ~5 m of Ulvesø Formation diamictite (Figure 5d). Muds typically occur as 5 to 15 cm stringers that are comparable to those of the uppermost beds of bed group 19 mudstone. Their irregular morphologies and diffuse margins indicate entrainment of semi-lithified mud into basal diamictite mass flows (Figure 5d).

3) At Kløftelv, the bed group 19 - Ulvesø Formation interface is abrupt, but shows well-preserved flame structures indicating that unlithified muds were loaded by overlying mass flows.

4) At Kløftelv, rafts of calcite-rich packstone occur within the lowest 15 m of the glacial deposits. Lenticu-

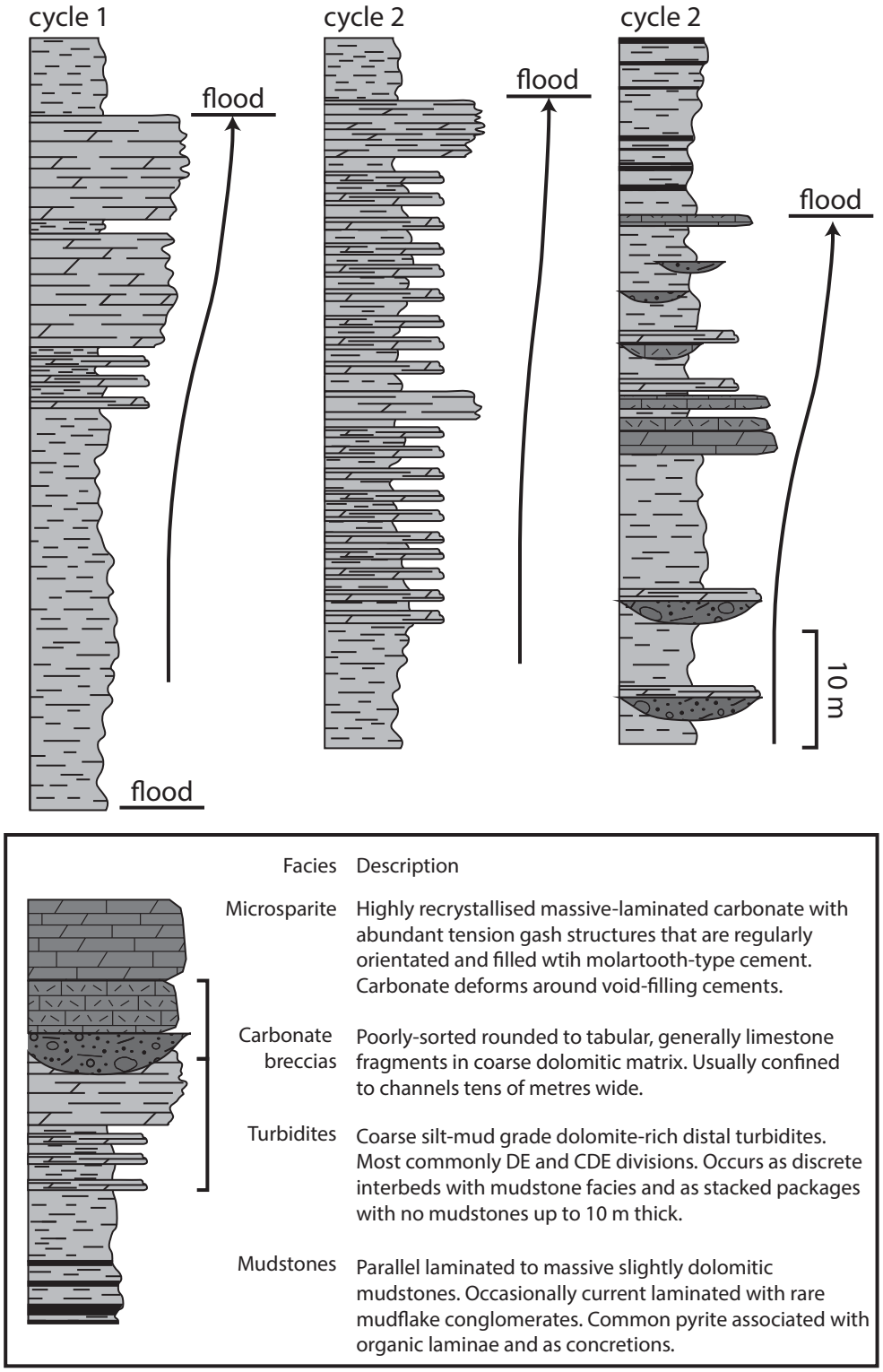

Figure 4. Summary of cyclic sedimentation in bed group 19 from Storeelv and Kløftelv sections on Ella Ø. Cycles 1-3 correspond to lower 3 cycles generalised in Fig. 6. Flooding surfaces are indicated by sharp vartical transitions from stacked distal turbidite facies and/or clastic debrites to deeper-water mudstones.

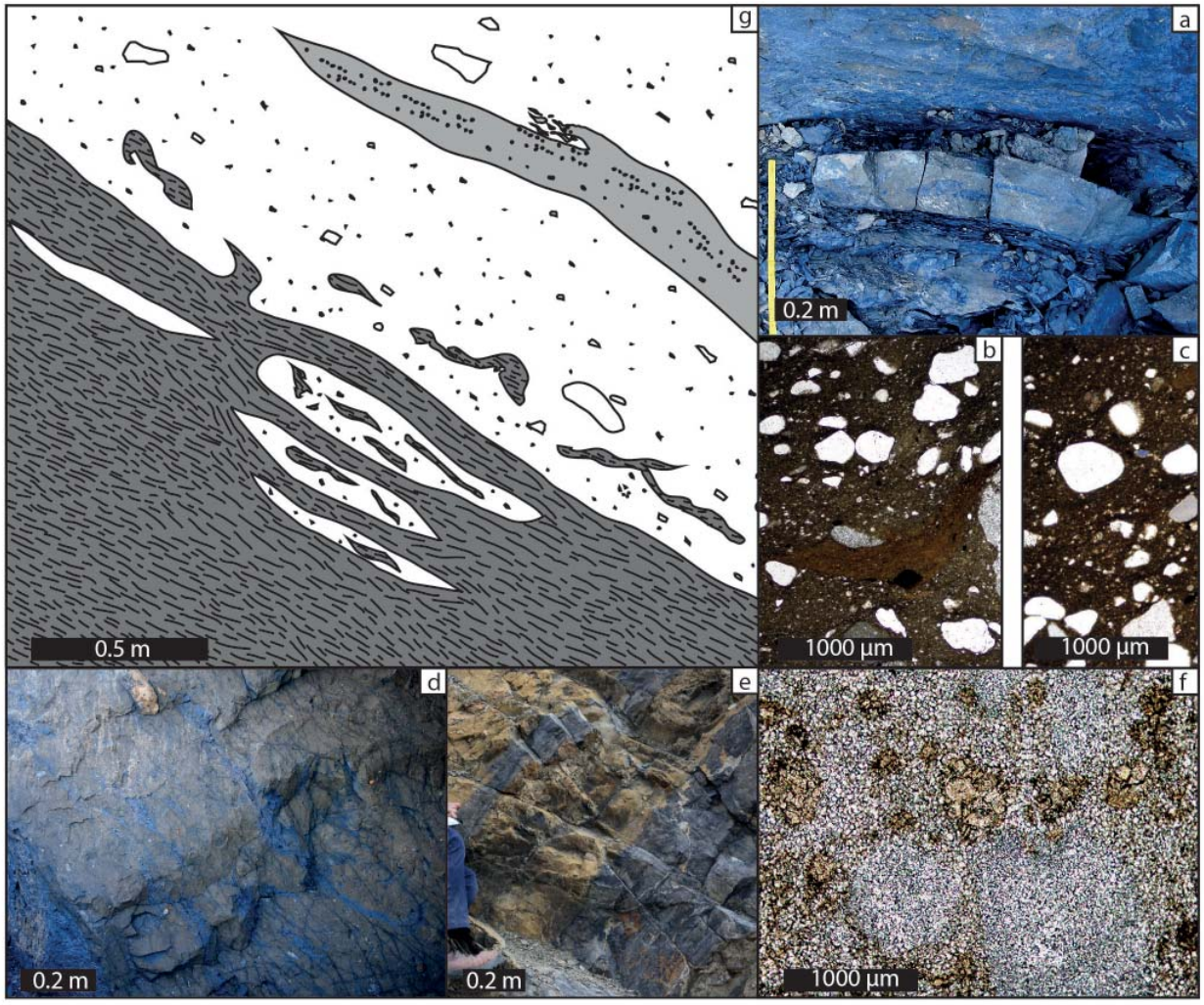

Figure 5. Basal contact between upper bed group 19 and the Ulvesø Formation on Ella Ø. a) Sharply channelised diamictite embedded into the uppermost mudstone beds of bed group 19, Tømmerbugt Ella Ø. b) Plane-polarised thin section image of channelised diamictite in upper bedgroup 19 c) Thin section image of lower Ulvesø Formation diamictite from Tømmerbugt on Ella Ø. Clast composition is dominated by subrounded quartz and calcite microspar. Mud stringer is visible in channelised diamictite sample. d) Mudstone stringers incorporated into the lower ~5 m of the Ulvesø Formation at Tømmerbugt on Ella Ø. Muds occur as elongate stringers that are discontinuous and approximately bedding-parallel with underlying mudstones. e) Concave-up limestone structures within the lower ~10 m of Ulvesø Formation diamictites at Kløftelv. These lens-shaped bodies are ~100% carbonate and are dominantly calcitic compared to the dolomitic carbonate cements dominating surrounding diamictite. f) Thin section image of relict allochems (likely ooids) in basal Ulvesø Formation limestone rafts. Some grains are partially dolomitised at their margins. f) Composite schematic sketch of the basal Ulvesø Formation on Ella Ø, illustrating the conformable nature of the contact.

lar bodies range from 10 cm to 10 m in width with sharp convex bases and flat to low angle concave tops (Figure 5e). Lenses comprise matrix-supported intraclasts of calcite microspar and reworked sub-mm allochems (peloids) that have been heavily recrystallised to calcite spar with occasional dolomicrospar overgrowths. Matrix material comprises a relatively clean mosaic of calcite microspar. Stringers of more typical diamictite

incorporated at the base of limestone rafts indicate syn-depositional emplacement.

5.3 Relation to sea level

By comparison with a coupled section at Kap Weber ~60 km north of Ella Ø, the interval of brecciated dolostones at the base of bed group 19 marks the first major landward translation of facies following ~2 km of relatively stable carbonate ramp deposition. This interface records a flooding event of regional extent that drowned subaerially exposed ramp carbonates of bed group 18 and marks a basal sequence boundary. Above this level, cyclic deposition of mudstones and siltstones (Figure 4) occurs in slope environments on both Ella Ø and Kap Weber, with two major 60 to 90 m cycles identified at each locality. A third cycle is identified on Ella Ø that includes interbedded mudstones and channelised carbonate breccias which abruptly flood to a fourth cycle of organic-rich mudstones that lack interbedded debrites and turbidites and pass abruptly, but conformably (Figure 3), into Ulvesø Formation diamictite. In contrast, the third cycle identified on Kap Weber comprises a lower interval of carbonate-poor mudstones that are overlain by a ~100 m thick interval of laminated to wave-rippled microsparry limestones. A fourth cycle begins at a flooding surface marked by the return of carbonate-poor mudstones that again shoal into laminated and finally conglomeratic microsparry carbonates. At this level on Kap Weber, limestones are abruptly overlain by interpreted aeolian quartz sandstones that indicate a period of subaerial exposure and erosion associated with a significant basinward migration of the shoreline. A major translation of facies on Ella Ø occurs at the base of Ulvesø Formation diamictites where organic carbonate-poor mudstones are abruptly, but conformably, succeeded by > 100 m of carbonate diamictite. A correlative conformity along this interface is therefore inferred that corresponds to erosion along terminal ramp carbonates in the relatively shallow North of the basin at Kap Weber and defines an upper sequence boundary.

The nature of cyclic deposition in bed group 19 mudstone and siltstone intervals is challenging to associate with any single process confidently. As the number of major coarsening upward cycles between the Ella Ø and Kap Weber sections is consistent with an allocyclic forcing in general, a tentative correlation of bed group 19 cycles along inferred major flooding surfaces is included in Figure 6. However, the lateral continuity of facies belts is difficult to resolve over distances > 1 km and as such, the migration of local geomorphological features such as submarine levees and channels that would have received relatively coarse-grained material shed from platformal positions cannot be easily be discounted, representing a local condition that is not expected to be time significant in a basinal context. Regardless, the sequence boundaries identified at the base on bed group 19 and the Ulvesø Formation provide two timelines by which the Ella Ø and Kap Weber sections may be calibrated, likely recording a significant fall in relative base-level of basinal extent.

6. Basin Evolution

The distribution of basinal sedimentation suggested by the calibrated Ella Ø and Kap Weber sections is summarised in Figure 7. This stratigraphic framework illustrates that the major facies transitions that characterise the upper Andrée Land Group can be broadly related to the rise and fall of relative base-level across the platform. The transition from inner to outer ramp carbonates in bed group 18 follows a period of exposure and dissolution collapse of dolostones that is regionally traceable but variable in thickness, with a ~60 m thick unit occurring on Kap Weber compared to just 15 m on Ella Ø. Modest base-level rise superimposed outer ramp carbonates above this surface (Figure 7b) before the ramp was again exposed. Following a period of non-deposition, a major marine transgression caused the shoreline to migrate landward drowning ramp carbonates (Figure 7c), with the accompanying facies change to pelagic mudstones and interbedded detrital carbonate shed from landward platforms and

deposited by density currents on the slope. The margin then shoaled into prograding outer ramp carbonates at Kap Weber while the relatively deeper conditions at Ella Ø received clastic material from shoreward platforms in channel-scoured debris flows which were drowned by a subsequent sea-level rise (Figure 7d). The uppermost platform carbonates at Kap Weber were exposed and eroded while the deeper regions of the basin received volumes of glacially reworked platformal carbonates as massive to stratified diamictites (Figure 7e). Aeolian sands developed above the exposed platform in landward positions before flooding allowing subaqueous deposition of reworked carbonate diamictites to proceed (Figure 7e, f).

7. Sources of bed group 19 carbonate

7.1 Carbon-isotopic trends

While low-resolution $\delta^{13}C$ data exist for some intervals of the upper Andrée Land Group (Fairchild et al., 2000; Knoll et al., 1986), 350 new coupled $\delta^{13}C$ and $\delta^{18}O$ analyses are presented in order to constrain the Islay Anomaly as recorded in the upper Andrée Land group on Ella Ø and Kap Weber in the context of host sediment composition and palaeoenvironmental observations. A scatter plot of coupled $\delta^{13}C$ and $\delta^{18}O$ analyses illustrates a number of distinctive lithologically and stratigraphically constrained populations (Figure 8). In general, all $\delta^{18}O$ values are in the range of -2 to -8‰ with no obvious systematic relationship observed, although values as high as -2‰ indicates that a component of these samples mineralised at relatively low temperatures arguing against pervasive resetting of $\delta^{18}O$ by hydrothermal or metamorphic fluids. End-member phases are defined by ranges of $\delta^{13}C$ values from +8 to -10‰ that are systematic with stratigraphic interval and host mineralogy. Ramp carbonates of bed group 18 and bed group 20 exclusively record $\delta^{13}C$ values on the order of +6 to +8‰, reaching minimum values of +2‰ approaching the major facies transition from outer ramp carbonate to slope mudstone. These elevated values are recorded in calcitic and dolomitic microspary grainstones, packstones and microbial facies (Figure 3a-c), and are typically > 98% carbonate. In bed group 18, a distinctive vertical stratigraphic shift and recovery of $\delta^{13}C$ values (150 to 210 m, Figure 1c) from +5‰ to +2‰, recovering to +8‰, occurs along a flooding and subsequent shoaling sequence, with the 6‰ increase in $\delta^{13}C$ occurring within dominantly microbial dolostones and minimum values of +2‰ associated with pisolitic limestones. At the base of bed group 20 on Kap Weber, similar $\delta^{13}C$ values in outer-ramp, generally calcitic limestones, record a steep increase over ~10m from +2 to +7‰, with enriched values maintained until the overlying sequence boundary and aeolian transition at the base of the Ulvesø Formation (Figure 1b). The stratigraphically lowest beds of bed group 19 mudstone exposed on Ella Ø return a range of $\delta^{13}C$ values from -4 to -10‰ (Figure 8). This range is maintained throughout bed group 19 within both mudstone facies (~10 - 15% dolomite) and microturbidite facies (up to 98% dolomite in hemipelagic cycle caps) to the base of the Ulvesø Formation on Ella Ø and the onset of carbonate ramp deposition in bed group 20 on Kap Weber. Debris flow material that is interbedded with mudstone and microturbidite facies typically returns comparatively modest values of -2.5 to -5‰ in clast and matrix spot-samples (Figure 8).

Clast and matrix material from Ulvesø Formation diamictites on Ella Ø were subsampled in an attempt to constrain the possible source of carbonate clasts and to test the timing of detrital reworking compared to the emplacement of the recorded $\delta^{13}C$ signal. These data show good overlaps with typical slope mudstone and ramp carbonates both isotopically and mineralogically (Figure 8), indicating that pervasive late-stage diagenesis is unlikely to account entirely for the $\delta^{13}C$ transitions recorded. In contrast, carbonate lens material (Figure 5e) within the lower Ulvesø Formation typically return $\delta^{13}C$ values in clasts and matrix on the order of 0 ± 2‰ and contain varying compositions of microspar matrix material and coarse sparry calcite/rhombic dolomite in recrystallised grainstone clasts (Figure 5f).

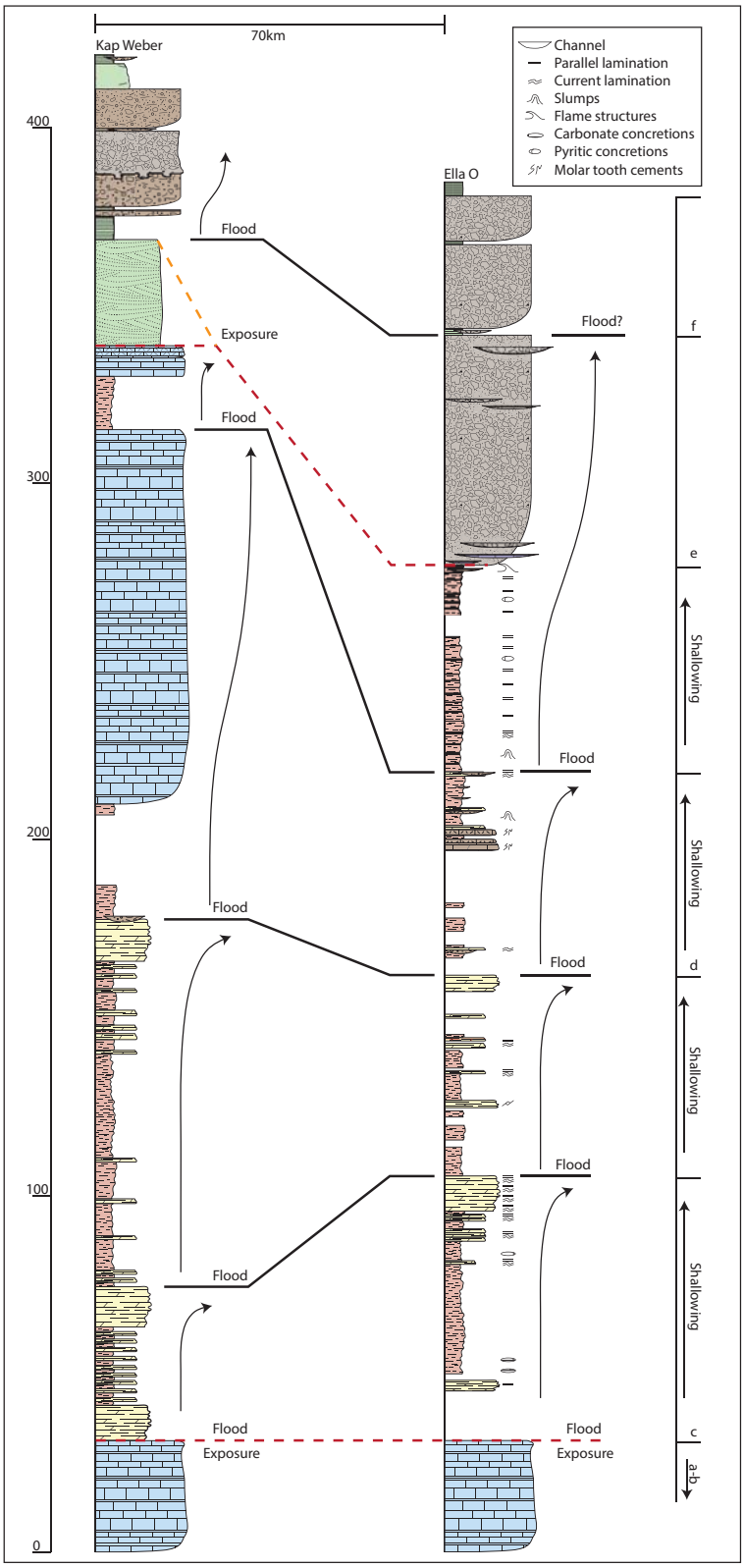

Figure 6. Stratigraphic correlation of the Ella Ø and Kap Weber (Fairchild et al. 2000) field sections based. Sequence boundaries are marked with dashed red lines. a-f correspond to basin model in Fig. 7.

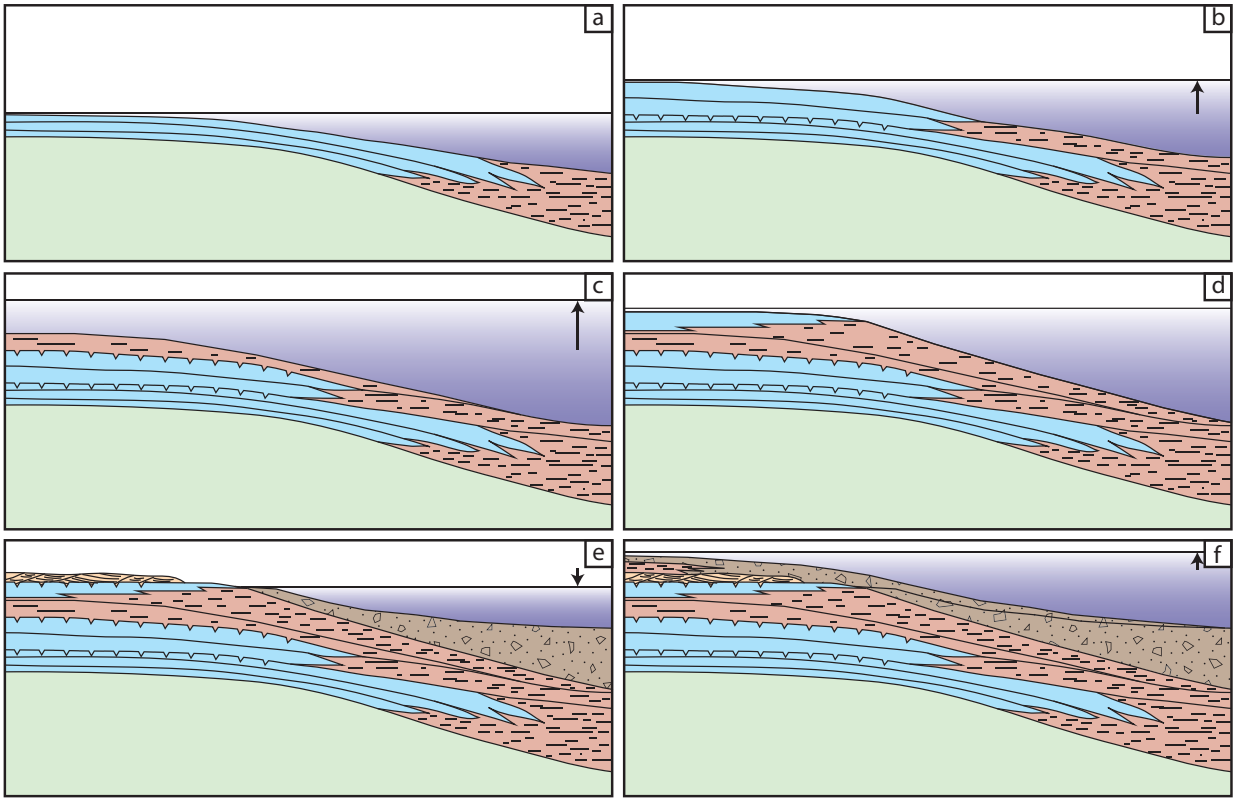

Figure 7. Basin evolution model of the upper Andrée Land Group. Blue = ramp carbonates, red=outer slope mudstones and debrites, green=lower Andrée Land Group ramp carbonates, brown=Ulvesø Formation diamictites, yellow=aeolian deposits. Purple line corresponds to relative sea level and arrow indicates direction of change compared to previous panel.

7.2 Mineral distribution

Whereas platform-derived (bed group 18 and 20) carbonate deposits are well mineralogically characterised as near-pure calcitic and dolomitic microspar, the nature of the carbonate preserved in bed group 19 slope-facies that contributes $\delta^{13}C$ values as low as -10‰ is more cryptic. Previous workers have reported that significant concentrations of siderite and Fe-bearing dolomite are present as the dominant carbonate phase preserved (Fairchild et al., 2000). Elemental mapping of representative mixed carbonate/siliciclastic samples from bed group 19 demonstrates that a distinctive rhombic dolomite phase provides the majority of carbonate preserved in bed group 19 (Figure 9). Across all examples of carbonate-poor mudstones, > 90% of the carbonate volume in any given sample (~15% bulk carbonate) occurs as dolomite. Euhedral rhombic dolomite crystals range from 2 µm to 15 µm in size and are uniformly disseminated throughout the sample matrix, which is dominantly comprised of clay-sized quartz, micas, and clay aggregates (Figure 9a) reported as berthierine in composition (Fairchild et al., 2000). The largest fraction of dolomite grains is systematically coarser than the surrounding siliciclastic material, is unsorted, and shows no preferred grain orientation. Well-rounded calcite grains ~5 µm in diameter are present in some samples but are rare (< 1%). Figure 9b illustrates that local lamination in mudstones is defined by interlayers of clays and silt-sized quartz and shows an interstitial calcite-spar cement that is commonly associated with coarse dolomitic rhombs, likely as a later overgrowth. The bed group 19 microturbidite facies hosts a similar subhedral rhombic dolomite phase that

occurs in concentrations > 90% of the rock volume in buff-weathering hemipelagic caps compared to 20-60% in coarser cycle bases. In carbonate-poor horizons, dolomite occurs concentrated in 1 to 2mm wide bedding-parallel lenses that are also relatively enriched in clay minerals (Figure 9c). While dolomite volume varies between compositional and textural layering within microturbidite sequences, grains remain unsorted and well disseminated in terms of crystal size across textural boundaries while adjacent siliciclastic material may vary by an order of magnitude (Figure 9d).

8. Origin of the isotopically depleted carbonate

The carbonate that records the most negative values that define the Islay Anomaly on Ella Ø is characteristically a euhedral rhombic dolomite phase in representative examples analysed from bed group 19. Dolomite grains are typically unsorted with respect to adjacent siliciclastic components that have undergone physical sorting through transport by density currents, indicating their in-situ growth within unlithified sediment. The only significant quantities of calcite in any samples examined occurs as interstitial cements seen to overgrow earlier dolomite rhombs (Figure 9b) and as void-filling molar tooth cements at a single stratigraphic level within upper bed group 19 debris flows (Fairchild et al., 2000). Rare well-rounded calcite grains ~5µm in size are disseminated throughout all samples examined and may represent a relict primary detrital carbonate phase. This material was likely reworked from shoreward platformal environments in mass flows, transported and deposited as distal turbidites, and replaced by dolomite in-situ, now accounting for < 1% of the carbonate

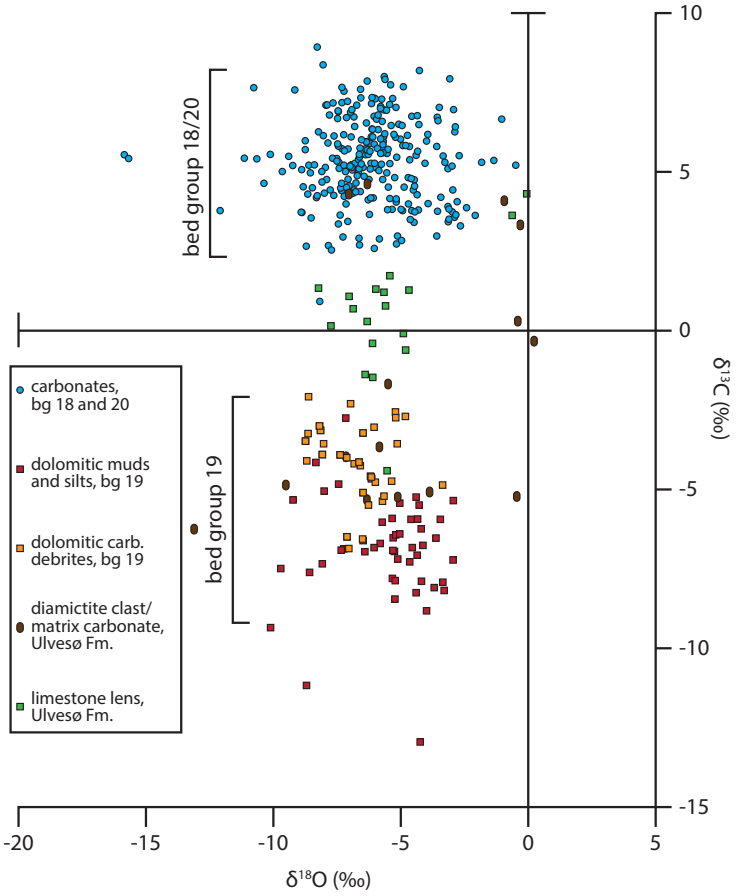

Figure 8. Scatter plot of $\delta^{13}C$ (x) versus $\delta^{18}O$ (y) values from bed group 18, bed group 19 and the basal Ulvesø Formation (Ella Ø) and bed group 20 (Kap Weber).

volume preserved. The carbonate phase recording the $\delta^{13}C$ values that fundamentally define the Islay Anomaly in the Andrée Land Group is therefore assigned to an early authigenic origin either as a primary precipitate that nucleated within pore spaces, or as a secondary diagenetic phase.

In the context of the host sediment, bacterial sulphate reduction likely played a dominant role in dolomite precipitation. Bacterial sulphate reduction resumes in organic-rich sediment at depths below the maximum level of dissolved oxygen diffusion, typically on the order of 0.1 m at modern atmospheric pO_2. Liberated light CO_2 (~-25‰ $\delta^{13}C$) readily dissolves in porewaters of assumed marine DIC concentration and, combined with the incorporation of relatively isotopically heavy detrital calcite and/or aragonite would be expected to produce a mixed authigenic phase (Irwin et al., 1977). Euhedral dolomite and pyrite occurs in association with berthierine clay minerals, providing a local source of Mg^{2+} and Fe^{2+} cations that also drove the precipitation

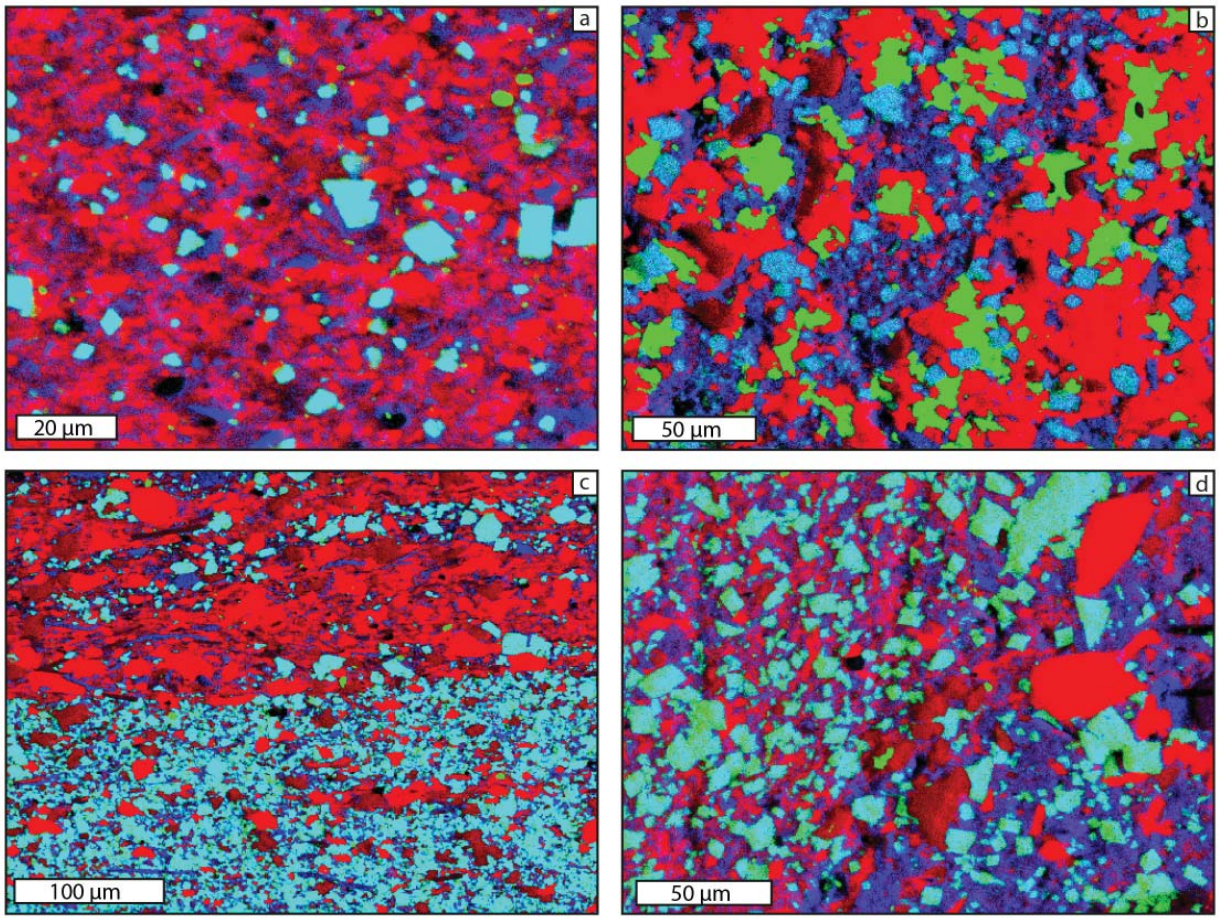

Figure 9. EDAX elemental maps of representative bed group 19 lithologies, Ella Ø . Colours in each image correspond to the following: Cyan=Dolomite, green=calcite, red=quartz, purple=clay minerals (dominantly berthierine) and micas. a) typical carbonate-poor mudstone from lower bed group 10 at Storeelv. b) Laminated carbonate-poor mudstone, middle bed group 19 at Storeelv. Lamination is defined by alternating coarse quartz-rich and fine clay-rich horizons. c) Coarse siliciclastic turbidite base cutting the dolomite-rich hemipelagic cap of the previous cycle. d) contact between top of previous microturbidite cycle and base of the subsequent cycle, showing that while siliciclastic grains are well-sorted depending on position in the cycle, dolomite rhombs are evenly disseminated throughout the cycle and show no sorting.

of siderite and magnesite phases. The precipitation of dolomite was likely limited by available Ca^{2+} from detrital calcite and low volumes of aragonitic cements (Fairchild et al., 2000), the neomorphism of which would have contributed to the precipitation of calcitic phases that occur as void-filling and interstitial mosaics. The relative $\delta^{13}C$ offset of ~+3‰ recorded in debris-flow material compared to interbedded dolomitic mudstones may reflect a larger preserved detrital component, where organic carbon concentrations were low and therefore liberated light CO_2 was relatively dilute. Significantly, calc- packstone lenses embedded in lower Ulvesø Formation diamictites return values near 0‰ (Figure 8) and contain relatively low dolomite concentrations, reflecting the greatly subdued influence of bacterial mediation of pore fluid DIC. On the basis of calcitic molar tooth cements in bedgroup 19 that record isotopically similar $\delta^{13}C$ values to adjacent dolomite-bearing siliciclastics, Fairchild et al. (2000) invoke a model of basin stratification where strong bathymetric $\delta^{13}C$ gradients explain the association of deep-water lithofacies and negative $\delta^{13}C$ values. In this model, either anoxic bottom waters or near-surface pore fluids bearing high concentrations of Fe^{2+} are responsible for the precipitation of isotopically-depleted Fe-bearing carbonate phases. The textural data presented here favours a pore-fluid origin for the bulk of the preserved carbonate in bed group 19, where dolomite precipitation is controlled primarily by the local availability of clay minerals, and calcitic phases might indicate a local deficit in Mg^{2+} cations in voids. Regardless, this type of authigenic phase is an unlikely monitor of whole-ocean secular change (Schrag et al., 2013) where depletion of recorded $\delta^{13}C$ values depends on fractionation at or below the sediment-water interface.

9. Construction of the Islay Anomaly

The sequence boundaries that bracket the bed group 19/20 sequence in the upper Andrée Land Group provide two regionally traceable surfaces that are time-significant. Critically, these surfaces allow the comparison and calibration of lateral basinal sections along timelines that are independent, providing a stratigraphic test of the synchroneity and continuity of recorded $\delta^{13}C$ signals. The sequence boundary at the base of bed group 19 corresponds to a shift in $\delta^{13}C$ values from ~+6‰ to negative values of -4‰ to -10‰. This occurs both at Kap Weber and on Ella Ø and is illustrated as a regionally traceable shift in lithofacies from relatively shallow-water ramp carbonates to deep-water slope mudstones and debrites. The upper sequence boundary is defined differently between Kap Weber and Ella Ø, where the abrupt juxtaposition of aeolian sandstones above outer-ramp carbonates on Kap Weber records a sea-level fall that is synchronously expressed at Ella Ø by a rapid transition from homogeneous mudstone deposition to boulder-bearing diamictites. Where a recovery from negative $\delta^{13}C$ values to values on the order of +6‰ occurs on Kap Weber along the lithofacies change back to ramp carbonates in bed group 20, such a recovery is absent on Ella Ø. This presents a situation where the recorded $\delta^{13}C$ profile differs by up to 18‰ between Kap Weber and Ella Ø along a time-calibrated surface. In this case, erosional truncation that has been suggested by previous workers to have occurred along the top of bed group 19 on Ella Ø that removed the recovery of $\delta^{13}C$ values from -10‰ to +6‰ is unsupported by primary sedimentological evidence. Rather, the transition from slope mudstones to glacially-reworked diamictite occurs gradually over several metres and is coeval with mudstone deposition, illustrated by interbedding relationships and soft-sediment deformation and incorporation into diamictic mass flows at the base of the Ulvesø Formation. As such, the upper beds of the Andrée Land Group on Ella Ø likely retain the majority of their original depositional thickness and the sustained $\delta^{13}C$ values of -4‰ to -10‰ that are recorded by these sediments into the base of the Ulvesø Formation represent a record that is continuous.

The bulk of preserved Precambrian carbonate in general occurs as heavily recrystallised shallow-water allochems, microbially-mediated precipitates, and often reworked carbonate mud of ambiguous palaeoenvi-

ronmental origin. As such, the utility of $\delta^{13}C$ values derived from this record is verified primarily by the reproducibility of similar signals between basins, arguing for a primary seawater signal of global scale that is equally recorded by all carbonates. The model of basin evolution described here illustrates that the highly depleted $\delta^{13}C$ values that represent the Islay Anomaly in the upper Andrée Land Group do not follow enriched values of +6‰ in time, but occur contemporaneously in outer-slope environments within the deeper parts of the basin. The flooding of ramp environments at the base of bed group 19 superimposed deep-water mudstones and turbidites above shallow water carbonates as the carbonate factory abruptly migrated landward. There, new carbonate platforms developed that shed detrital carbonate and organic particles onto the slope where in-situ modification mediated by anoxic bacterial processes mineralised ^{12}C-depleted dolomite as the dominant carbonate phase now preserved. With sea-level fall or simply local differences in geomorphology related bathymetry, relatively shallower conditions at Kap Weber allowed outer ramp limestones to prograde across bed group 19 mudstones, carrying modest $\delta^{13}C$ values of +2‰ that quickly increased to +7‰ as the platform became increasingly established and abruptly juxtaposing isotopically enriched carbonate above isotopically depleted slope deposits (Figure 10). Deep-water slope deposition at Ella Ø remained dominant at this time while coarse clastic material was shed from local carbonate producing environments in debris and density flows related to typical platform collapse and shedding. $\delta^{13}C$ values remain negative into the base of the Ulvesø Formation here that is marked by channelised deposition of diamictite carrying clasts mineralogically and texturally similar to stratigraphically lower ramp carbonates. This abrupt but conformable transition on Ella Ø corresponds to the development of an erosional unconformity on Kap Weber, which was locally shallow enough for terminal ramp carbonates to be subaerially exposed with sea level fall. The construction of the Islay Anomaly in the upper Andrée Land Group relies on end-member depositional and pore-fluid conditions that are superimposed upon one another in a fragmented series of lithofacies transitions. This results in a binary vertical $\delta^{13}C$ trend that also shows a first-order coupling with eustatic change. An isotopic excursion constructed in this way is predicted to produce a strong coupling of isotope values and lithofacies, where end-member carbonate phases record the locally dominant palaeoenvironmental or diagenetic controls rather than a single changing seawater value that is pervasive across the basin at any given time. In the case of the upper Andrée Land Group, positive values are exclusively recorded by carbonate sediment that accumulated as allochems and microbial mats on shallow water bank tops while negative values are closely associated with deep-water pore fluid processes that occurred under anoxic reducing conditions.

Under the basinal and diagenetic constraints discussed here, the linkage of glaciogenic sediment and negative $\delta^{13}C$ values in the upper Andrée Land Group becomes convoluted. While these likely represent discrete local signals rather than a progression of isotopic change in seawater DIC, a conformable transition between negative $\delta^{13}C$ values and the first glaciogenic sediment of the Ulvesø Formation on Ella Ø does indicate that these processes are directly related in time and that this relationship could potentially be causal in nature. This linkage however is unlikely to be through the carbon cycle, but simply in response to eustatic change that may be climatically forced. The fall in sea level responsible for the formation of the upper sequence boundary at the base of the Ulvesø Formation occurs coincidentally with the first evidence of coarse locally-derived limestone material. These clasts show striations and facets consistent with glacial reworking, and are often deposited as mass flows or interpreted to have been rafted from a landward ice shelf (Moncrieff and Hambrey, 1990). The first diagnostic evidence of glacially reworked sediment does not occur on Kap Weber until after a subsequent flooding event and marine phase, reflecting the strong influence that local geomorphology had on the distribution of glacial sediment across the basin laterally and through time. This is further demonstrated by the emplacement of semi-lithified, shallow-water limestones

as lenticular olistostrome-type units at multiple levels within the Ulvesø Formation suggesting that carbonate production continued on local platforms that shed material whilst diamictites accumulated on the slope.

The utility of binary stratigraphic shifts in Neoproterozoic $\delta^{13}C$ records is implicitly considered comparable to that of modern pelagic records in many chemostratigraphic studies. These types of deposits are ideal recorders of seawater $\delta^{13}C$ variation as they accumulate in deep-water environments and thus provide a relatively uninterrupted sampling of the surface waters of the open ocean where ambient $\delta^{13}C_{DIC}$ is determined by atmospheric exchange (eg. Berger and Vincent, 1986; Maslin and Swann, 2005; Ravizza and Zachos, 2003). The controlling function on $\delta^{13}C_{DIC}$ variation in the Neoproterozoic record is more difficult to constrain since diagnostic evidence for a time-continuous open-marine pelagic record is absent. Instead, preserved Neoproterozoic records are known to have accumulated exclusively above continental crust in relatively shallow water marginal and inland basins such as the Eleonore Bay Basin considered here that are inherently sensitive to modest eustatic change. The majority of preserved marine carbonate of Neoproterozoic age was depos-

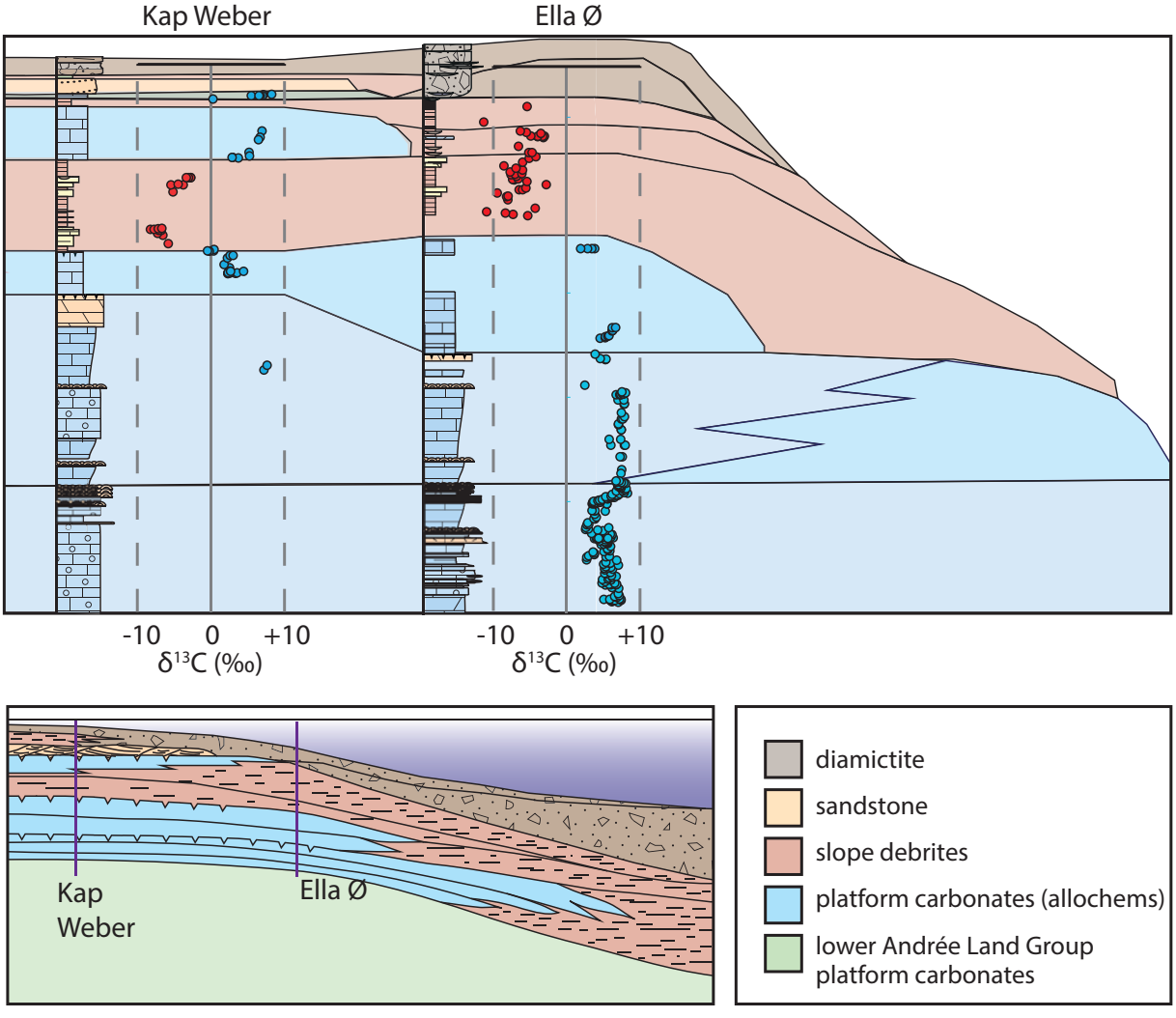

Figure 10. The Kap Weber (left) and Ella Ø (right) stratigraphic and chemostratigraphic profiles superimposed onto the basin evolution model presented in Figure 7 (height-corrected for local stratigraphic thickness).

ited on shallow-water platforms and ramps that are periodically restricted, evaporative, and flushed with meteoric fluids during subaerial exposure, all processes known to decouple local $\delta^{13}C$(DIC) from that of ambient seawater (Allan and Matthews, 1982; Patterson and Walter, 1994). These types of processes are fundamentally forced by variations in sea level in marginal basins that can lead to binary but systematic trends in both sediment composition and recorded isotopic signal (Swart and Eberli, 2005). In lieu of the marine skeletal flux in modern offshore environments, much of the deeper-water sediment that is preserved in the Neoproterozoic record exists either as detrital grains eroded from unrepresented environments and deposited in density currents on the slope, or as authigenic phases in organic-rich, fine-grained sediment. This is well demonstrated by deposits of bed group 19 both in terms of texture, mineralogy and method of carbonate accumulation.

Conformable sections hundreds to thousands of metres in thickness that accumulated under continuously subaqueous open-marine conditions should be relatively rare in the Neproterozoic record, but are assumed in many chemostratigraphic studies. Rather, these sections are predicted to comprise a number of transient depositional phases that build through time as the host basin responds to fluctuations in accommodation space, variations in climate, and changes in detrital inputs. The lack of independent high-resolution chronostratigraphic markers in Neoproterozoic strata means that the continuity of $\delta^{13}C$ records through time and whether they are truly synchronous within and between basins is difficult to verify . Even if evidence of low-latitude glaciation is considered coeval between basins, the synchroneity of preceding chemostratigraphic features remains difficult to resolve, particularly when interpreted truncation of sediment provides an incomplete record (eg. Halverson et al., 2002; Halverson et al., 2004; Hill and Walter, 2000). The resulting paradigm approaches circularity where extreme $\delta^{13}C$ values are taken as genetically related to overlying glaciogenic deposits and thus record the same biospheric event that these very features fundamentally establish. The identification of major time surfaces in basinal sections allows an independent means to calibrate isotopic records and thus provide a stratigraphic test of their reproducibility across a given basin.

The sedimentological and basinal constraints on the Islay Anomaly as it is recorded in the Andrée Land Group in NE Greenland has implications for its interbasinal correlatives. The best constrained sections that are routinely correlated lithologically and isotopically to the Andrée Land Group occur in the Svalbard Heckla Hoek succession comprising a similarly thick sequence of shallow-water carbonates. The Russøya Member of the Elbobreen Formation in general comprises a lower interval recording a ~135 m thick shoaling cycle of laminated carbonates, microbial laminites and capping carbonate grainstones and sandstones that record $\delta^{13}C$ values of +3‰ to +5‰. The upper Russøya interval comprises a series of < 10 m cycles of organic-rich shales and limestones that shoal to dolomitic grainstones and shales associated with pyrite nodules and evaporite minerals. The uppermost beds of the Russøya Formation are laterally variable, typically dolomitic, and are cut at multiple locations by a terminal karstic unconformity (Halverson et al., 2004). It is this upper organic-rich and dolomitised interval that frames a gradual decline in $\delta^{13}C$ values from +5‰ to -6‰ (-10‰ in some samples) that occurs over just ~30 m of shallow-water stratigraphy in the most complete reference section (Halverson et al., 2004) compared to ~200 m of slope mudstone in the NE Greenland central fjord region. Significantly, where the onset of $\delta^{13}C$-depleted values occurs in NE Greenland is associated with flooding across the basin, the comparable interval in Svalbard occurs broadly along shoaling and subaerial exposure of now heavily dolomitised sediment. While a primary seawater origin for the negative $\delta^{13}C$ excursion on Svalbard has recently been supported on the grounds of loosely covarying $\delta^{13}C$(org) values (Hoffman et al., 2012), recent workers have shown that this parameter is ambiguous on modern non-skeletal carbonate platforms where internally covariant trends and

terminal depleted values can occur associated with the bathing of carbonate sediment by meteoric fluids (Oehlert et al., 2012; Oehlert and Swart, 2014). The association between karst, organic carbon and depleted $\delta^{13}C$ values here suggests that a more cryptic origin to the negative $\delta^{13}C$ excursion may be recorded. Regardless, the contrast in sea-level change between Svalbard and NE Greenland successions indicates that the onset and recovery of $\delta^{13}C$ values (which is absent on Svalbard) are unlikely to be time-significant.

10. Conclusions

Not all Neoproterozoic $\delta^{13}C$ excursions can be easily explained as variations in the $\delta^{13}C$ balance of ambient seawater DIC. Rather, these types of records can be constructed through time as basinal conditions vary with relative sea level, stacking a series of transient depositional phases that record the $\delta^{13}C$ constraints of each given palaeoenvironment. The synchroneity of the most enriched and depleted $\delta^{13}C$ values along a spatial and bathymetric gradient in the upper Andrée Land Group is inconsistent with the assumption that a single changing seawater values is recorded in carbonate sediment across the basin. As the latter interpretation demands that variations in the preserved $\delta^{13}C$ record between basinal sections are necessarily related to incomplete section, the gradual transition into the Ulvesø Formation on Ella Ø demonstrates well that the lack of a comparable $\delta^{13}C$ recovery in this section is a primary time-continuous feature. Where relative base-level and sediment inputs are comparable between sections as in the lower interval of bed group 19, recorded isotopic and sedimentological archives are predicted to be relatively similar. However where local geomorphology means that strike-sections periodically accumulated under significantly different palaeoenvironmental conditions that also respond differently to changes in base-level, an entirely unique sequence of lithological transitions (and associated $\delta^{13}C$ values) is expected. While lithofacies are understood not to be coeval across an entire basin, sea-level forcing is in basins that are open to marine connections and thus provides a powerful tool in confirming or challenging purely chemostratigraphic correlations.

References

Allan, J. R., and Matthews, R. K., 1982, Isotope signatures associated with early meteoric diagenesis: Sedimentology, v. 29, no. 6, p. 797-817.

Berger, W., and Vincent, E., 1986, Deep-sea carbonates: reading the carbon-isotope signal: Geologische Rundschau, v. 75, no. 1, p. 249-269.

Brasier, M. D., and Shields, G., 2000, Neoproterozoic chemostratigraphy and correlation of the Port Askaig glaciation, Dalradian Supergroup of Scotland: Journal of the Geological Society, v. 157, p. 909-914.

Fairchild, I. J., and Hambrey, M. J., 1995, Vendian basin evolution in East Greenland and NE Svalbard: Precambrian Research, v. 73, no. 1, p. 217-233.

Fairchild, I. J., and Kennedy, M. J., 2007, Neoproterozoic glaciation in the earth system: Journal of the Geological Society, v. 164, p. 895-921.

Fairchild, I. J., Spiro, B., and Herrington, P. M., 2000, Controls on Sr and C isotope compositions of Neoproterozoic Sr-rich limestones of East Greenland and North China, in Grotzinger, J. P., and James, N. P., eds., Carbonate Sedimentation and Diagenesis in the Evolving Precambrian World, Volume 67, p. 297-313.

Frederiksen, K. S., 2000, Evolution of a Late Proterozoic Carbonate Ramp (Ymer O and Andrée Land Groups, Eleonore Bay Supergroup, East Greenland): Response to Relative Sea-Level Rise: Polarforschung, v. 68, p. 125-130.

Halverson, G. P., Hoffman, P. F., Schrag, D. P., and Kaufman, A. J., 2002, A major perturbation of the carbon cycle before the Ghaub glaciation (Neoproterozoic) in Namibia: Prelude to snowball Earth?: Geochemistry Geophysics Geosystems, v. 3, no. 6, p. 1-24.

Halverson, G. P., Hoffman, P. F., Schrag, D. P., Maloof, A.

C., and Rice, A. H. N., 2005, Toward a Neoproterozoic composite carbon-isotope record: Geological Society of America Bulletin, v. 117, no. 9-10, p. 1181-1207.

Halverson, G. P., Maloof, A. C., and Hoffman, P. F., 2004, The Marinoan glaciation (Neoproterozoic) in northeast Svalbard: Basin Research, v. 16, no. 3, p. 297-324.

Hambrey, M. J., and Spencer, A. M., 1987, Late Precambrian glaciation of central east Greenland, Nyt Nordisk Forlag.

Herrington, P. M., and Fairchild, I. J., 1989, Carbonate shelf and slope facies evolution prior to Vendian glaciation, central East Greenland, in Gayer, R. A., ed., The Caledonide geology of Scandinavia: London, Graham Trotman, p. 285-297.

Higgins, A., Smith, M., Soper, N., Leslie, A., Rasmussen, J. A., and Sønderholm, M., 2001, The Neoproterozoic Hekla Sund Basin, eastern North Greenland: a pre-lapetan extensional sequence thrust across its rift shoulders during the Caledonian orogeny: Journal of the Geological Society, v. 158, no. 3, p. 487-500.

Hill, A. C., and Walter, M. R., 2000, Mid-Neoproterozoic (similar to 830-750 Ma) isotope stratigraphy of Australia and global correlation: Precambrian Research, v. 100, no. 1-3, p. 181-211.

Hoffman, P. F., Halverson, G. P., Domack, E. W., Maloof, A. C., Swanson-Hysell, N. L., and Cox, G. M., 2012, Cryogenian glaciations on the southern tropical paleomargin of Laurentia (NE Svalbard and East Greenland), and a primary origin for the upper Russøya (Islay) carbon isotope excursion: Precambrian Research, v. 206-207, p. 137-158.

Hoffman, P. F., Kaufman, A. J., Halverson, G. P., and Schrag, D. P., 1998, A Neoproterozoic snowball earth: Science, v. 281, no. 5381, p. 1342-1346.

Irwin, H., Curtis, C., and Coleman, M., 1977, Isotopic evidence for source of diagenetic carbonates formed during burial of organic-rich sediments: ature, v. 269, no. 5625, p. 206-213.

Knoll, A., Hayes, J., Kaufman, A., Swett, K., and Lambert, I., 1986, Secular variation in carbon isotope ratios from Upper Proterozoic successions of Svalbard and East Greenland: Nature, v. 321, p 832-838.

Maslin, M. A., and Swann, G. E., 2005, Isotopes in marine sediments: Isotopes in Palaeoenvironmental Research. Developments in Paleoenvironmental Research, Springer, Dordrecht, The Netherlands (2005), p. 227-290.

Moncrieff, A., and Hambrey, M., 1990, Marginal-marine glacial sedimentation in the late Precambrian succession of East Greenland: Geological Society, London, Special Publications, v. 53, no. 1, p. 387-410.

Oehlert, A. M., Lamb-Wozniak, K. A., Devlin, Q. B., Mackenzie, G. J., Reijmer, J. J. G., and Swart, P. K., 2012, The stable carbon isotopic composition of organic material in platform derived sediments: implications for reconstructing the global carbon cycle: Sedimentology, v. 59, no. 1, p. 319-335.

Oehlert, A. M., and Swart, P. K., 2014, Interpreting carbonate and organic carbon isotope covariance in the sedimentary record: Nat Commun, v. 5.

Patterson, W. P., and Walter, L. M., 1994, Depletion of ^{13}C in seawater sigma-CO_2 on modern carbonate platforms - significance for the carbon isotopic record of carbonates: Geology, v. 22, no. 10, p. 885-888.

Prave, A., Fallick, A., Thomas, C., and Graham, C., 2009, A composite C-isotope profile for the Neoproterozoic Dalradian Supergroup of Scotland and Ireland: Journal of the Geological Society, v. 166, no. 5, p. 845-857.

Ravizza, G., and Zachos, J., 2003, Records of Cenozoic ocean chemistry: Treatise on geochemistry, v. 6, p. 551-581.

Schrag, D. P., Berner, R. A., Hoffman, P. F., and Halverson, G. P., 2002, On the initiation of a snowball Earth: Geochemistry Geophysics Geosystems, v. 3.

Schrag, D. P., Higgins, J. A., Macdonald, F. A., and Johnston, D. T., 2013, Authigenic carbonate and the history of the global carbon cycle: Science (New York, N.Y.), v. 339, no. 6119, p. 540-543.

Shields-Zhou, G., Hill, A., and Macgabhann, B., 2012, The Cryogenian Period, The Geologic Time Scale, Elsevier.

Sohl, L. E., Christie-Blick, N., and Kent, D. V., 1999, Paleomagnetic polarity reversals in Marinoan (ca. 600 Ma) glacial deposits of Australia: implications for the duration of low-latitude glaciation in Neoproterozoic time: Geological Society of America Bulletin, v. 111, no. 8, p. 1120-1139.

Sønderholm, M., Frederiksen, K. S., Smith, M. P., and Tirsgaard, H., 2008, Neoproterozoic sedimentary basins with glacigenic deposits of the East Greenland Caledonides: Geological Society of America Memoirs, v. 202, p. 99-136.

Sønderholm, M., and Tirsgaard, H., 1993, Lithostratigraphic framework of the Upper Proterozoic Eleonore Bay Supergroup of East and North-East Greenland (No.167): Grønlands geologiske undersøgelse.

Spötl, C., and Vennemann, T. W., 2003, Continuous-flow isotope ratio mass spectrometric analysis of carbonate minerals: Rapid communications in mass spectrometry, v. 17, no. 9, p. 1004-1006.

Swart, P. K., and Eberli, G., 2005, The nature of the $\delta^{13}C$ of periplatform sediments: Implications for stratigraphy and the global carbon cycle: Sedimentary Geology, v. 175, no. 1-4, p. 115-129.

Tirsgaard, H., and Sønderholm, M., 1997, Lithostratigraphy, sedimentary evolution and sequence stratigraphy of the Upper Proterozoic Lyell Land Group (Eleonore Bay Supergroup) of East and North-East Greenland: Geology of Greenland Survey Bulletin, v. 178, p. 60.

Chapter 5

Statement of Authorship

Title of Paper	Environmental controls on ^{13}C enrichment in the Neoproterozoic carbon-isotope record
Publication Status	☐ Published ☐ Accepted for Publication ☐ Submitted for Publication ☑ Unpublished and Unsubmitted w ork w ritten in manuscript style
Publication Details	N/A

Principal Author

Name of Principal Author (Candidate)	Robert Klaebe		
Contribution to the Paper	Project design, fieldwork and sampling, sample preparation, data collection and processing, published data compilation, data interpretation, manuscript design and composition, generation of figures		
Overall percentage (%)	85		
Certification:	This paper reports on original research I conducted during the period of my Higher Degree by Research candidature and is not subject to any obligations or contractual agreements with a third party that would constrain its inclusion in this thesis. I am the primary author of this paper.		
Signature		Date	14/10/2015

Co-Author Contributions

By signing the Statement of Authorship, each author certifies that:

i. the candidate's stated contribution to the publication is accurate (as detailed above);
ii. permission is granted for the candidate in include the publication in the thesis; and
iii. the sum of all co-author contributions is equal to 100% less the candidate's stated contribution.

Name of Co-Author	Martin Kennedy		
Contribution to the Paper	Project design, fieldwork, guidance with data interpretation, manuscript review.		
Signature		Date	14/10/2015

Environmental controls on ^{13}C enrichment in the Neoproterozoic carbon-isotope record

Abstract

The Neoproterozoic $\delta^{13}C$ record preserves $\delta^{13}C$ values > +3‰ and up to +10‰ that are sustained over thousands of metres of shallow-water carbonate sediment representing millions of years of deposition, suggesting at face value a very different distribution of carbon across the Earth's surface reservoirs that was unique to the Neoproterozoic. While Cenozoic deep-marine pelagic sediments known to record variations in seawater DIC and linked to net global variations in organic carbon burial record $\delta^{13}C$ values as positive as +2.5‰, a compilation of $\delta^{13}C$ values recorded by coeval platform carbonates shows values as positive as +6‰ that are attributed to photosynthetic effects and evaporation under hydrologically restricted conditions and are unrelated to global carbon cycle variation. Positive $\delta^{13}C$ values from eight different Neoproterozoic sections in Australia, NW Canada, East Svalbard and NE Greenland, including six intervals that preserve shallow-water carbonate platform sedimentation as thick packages of microbial and grainstone carbonates, karstic features, desiccation cracks and dolomitisation are shown to largely plot within the < +6‰ range of $\delta^{13}C$ variation expected by comparison with Cenozoic data. As the majority of Neoproterozoic carbonate successions are known to have accumulated above carbonate platforms and ramps, in inland seas, and in other cratonic and transitional-marginal environments, it is proposed that the positive 'background' $\delta^{13}C$ value common to Neoproterozoic-aged carbonate successions reflects the inherent preservational bias in the Neoproterozoic stratigraphic record towards these types of shallow-water depositional conditions that are expected to be periodically dominated by local scale processes that are reflected in the recorded $\delta^{13}C$ value.

1. Introduction

Changes in the carbon isotopic ($\delta^{13}C$) composition of marine carbonate sediments directly inform our understanding of variations in the Earth's carbon cycle through time. In general, mantle inputs to the Earth's surface carbon reservoirs carry $\delta^{13}C$ values of approximately -5‰ and are balanced by the preferential fractionation of ^{12}C over ^{13}C into organic matter during photosynthesis and the subsequent storage of biomass in the sedimentary record, effectively buffering the ocean-atmosphere system to sustained $\delta^{13}C$ values of ~0‰. Approximately 2‰ of variability in this value exists as multi-million year trends in Cenozoic deep-marine carbonate records (Shackleton, 1987; Zachos et al., 2001) that reflect steady-state fluctuations in global rates of organic carbon burial, or rates of carbon liberation through oxidative continental weathering. Tens of thousands of published $\delta^{13}C$ values from Neoproterozoic carbonate-bearing strata now illustrate that the range of variability recorded in sedimentary records of this age approaches 20‰. Where intervals of ^{13}C-depleted carbonate as low as -10‰ are largely preserved as discrete phenomena that are often stratigraphically associated with evidence for glaciation, a significant proportion of Neoproterozoic-aged carbonates record $\delta^{13}C$ values that fluctuate between +3‰ and +10‰ (Halverson et al., 2005).

Maintaining seawater $\delta^{13}C_{DIC}$ values > +5‰ at steady-state for tens of millions of years during the Neoproterozoic is challenging under our current understanding of Earth's carbon and oxidant budgets. When interpreted in the same way as Cenozoic deep-ocean pelagic records, these sustained positive $\delta^{13}C$ values are consistent with a ~200% increase in fractional organic carbon burial and/or reduction of organic carbon weathering that was relatively constant throughout the Neoproterozoic (Hayes et al., 1999; Knoll et al., 1986; Kump et al., 2011). However, this

type of model becomes problematic at steady state under the relatively low pO_2 conditions interpreted during the Neoproterozoic (Lyons et al., 2014), where the expansion of net photosynthetic biomass required predicts a coupled increase in atmospheric oxygen. More recent models invoke enhanced carbon reservoirs such as authigenic carbonates that mineralise as ^{13}C-depleted phases (< -10‰) in sediment pore fluids during diagenesis, providing a sink for ^{12}C that becomes negligible by volume following the oxygenation of the atmosphere but was potentially significant during the Neoproterozoic (Schrag et al., 2013). As these types of models invoke unrivalled reorganisations of the Earth's surface carbon reservoirs and are directly linked to the oxygenation state of the atmosphere, understanding the pervasiveness of ^{13}C-enriched carbonate throughout the Neoproterozoic record and the palaeoenvironmental conditions responsible for this enrichment has significant implications for understanding the evolution of the Earth's biosphere into the Ediacaran.

An alternative interpretation links ^{13}C enrichment in Neoproterozoic-aged carbonate archives to natural carbon-cycling processes that influence Cenozoic equivalents. The closest available modern analogues to the shallow-water, non-skeletal carbonate platforms interpreted for the often kilometre-thick packages of carbonate sediment common to Neoproterozoic-aged sedimentary archives show a surprisingly large range of $\delta^{13}C$ values as high as +6‰. These deposits are known not to have been precipitated in isotopic equilibrium with open-ocean DIC as they contrast with coeval deep-ocean (pelagic) records that show $\delta^{13}C$ values on the order of 0‰ (Gischler et al., 2013; Gischler et al., 2007; Swart and Eberli, 2005). Instead, shallow-water marginal and intracratonic carbonate sediments frequently record the $\delta^{13}C$ values of ambient waters that have been modified by hydrologic, biological and geochemical processes of local influence that drive recorded $\delta^{13}C$ values in mineralising carbonate phases higher. These types of processes are diluted by the volume of the open ocean that is dominated isotopically by atmospheric exchange, but increasingly influence marginal marine basins as they are periodically restricted from seawater connections during sea level fall, or simply poorly-mixed under sustained shallow water conditions. As the shallow-water coastal and intracratonic basins that comprise the Neoproterozoic carbonate record are expected to be sensitive to changes in relative sea level on the order of metres, a coupling of lithofacies, mineralogy and $\delta^{13}C$ is predicted if local-scale carbon cycling processes have influenced the composition of ambient DIC. This study tests the hypothesis that the controlling processes driving ^{13}C-enrichment of Neoproterozoic-aged carbonate sediments mirror those acting in the Cenozoic on modern coastal and intracratonic settings. A significant portion of the ^{13}C-enriched carbonate preserved in Neoproterozoic-aged sedimentary records that contribute to composite $\delta^{13}C$ curves used for global correlation is shown to fall within the range of $\delta^{13}C$ variability documented on Cenozoic shallow-water platforms. Sustained $\delta^{13}C$ values > +3‰ recorded through much of the Neoproterozoic stratigraphic record are therefore interpreted to reflect, in part, the inherent preservational bias in this archive toward shallow-water bank-top carbonate sediments where ambient waters are locally ^{13}C-enriched by local hydrological and photosynthetic processes.

2. ^{13}C enrichment in coastal settings

Excluding species-specific vital effects, enrichment of ^{13}C in carbonates that precipitate from hydrologically restricted coastal marine waters depends on the balance of seawater mixing, freshwater influx, evaporation and local photosynthetic productivity in the ambient surface and pore fluids. Where seawater recharge provides the dominant source of precipitating fluids, primary carbonate phases are expected to largely reflect this seawater $\delta^{13}C_{DIC}$ value demonstrated by studies of Phanerozoic strata where carbonate platform and shelly pelagic sediment that are chronologically related using biostratigraphy show little variation (eg.

Amodio et al., 2008). Increasing isolation of a water body often leads to increased evaporation of surface waters where the evasion of isotopically light CO_2 leaves ambient fluids enriched in ^{13}C, recording $\delta^{13}C_{DIC}$ values as high as +16.5‰ under highly evaporative, completely isolated natural conditions (Stiller et al., 1985). In addition to evaporative effects, locally prolific photosynthetic communities may further enhance the bulk fractionation of ^{12}C from ambient poorly-mixed waters, even in examples that remain physically connected to seawater (eg. Jahnert and Collins, 2012; Swart and Eberli, 2005). In the context of Neoproterozoic carbonates this photosynthetic effect is predicted to be particularly significant, where mineralised laminated algal mats and stromatolites often comprise the dominant lithology and can be preserved as uninterrupted stacks of microbial carbonate > 100 m in stratigraphic thickness. The transformation of primary calcite phases to dolomite during diagenesis imparts a further positive fractionation of ~2‰ (Sheppard and Schwarcz, 1970), with dolomite comprising the dominant mineralogy in a significant fraction of Neoproterozoic carbonates.

The lack of a skeletal pelagic flux that samples the well-mixed surface waters of the open ocean means that the majority of preserved carbonate that accumulated during the Neoproterozoic was originally precipitated directly by microbial processes or as inorganic cements and coatings. Most commonly, this occurred on shallow carbonate platforms and ramps, and in inland seaways and alkaline lakes. In analogy, non-skeletal aragonitic precipitates that record $\delta^{13}C$ values as high as +6‰ accumulate on the Cenozoic Great Bahama bank-top that are locally modified by photosynthetic effects under poorly circulated waters (Melim, 2001; Swart and Eberli, 2005). Maximum $\delta^{13}C$ values of +5.5‰ and +4.5‰ are preserved in both skeletal and non-skeletal allochems on the modern Belize-Yucatan platform and Kuwait carbonate ramp respectively in surface sediment and in core (Gischler and Lomando, 2005; Gischler et al., 2007), where in the latter case the most positive values occur in oolitic sediment proximal to the shoreline. Aragonite precipitated by subtidal stromatolites and algal mats in Shark Bay on the coast of Western Australia similarly returns ^{13}C-enriched values of +4.5‰ to +6‰ that are attributed to locally enhanced microbial photosynthesis under evaporative and poorly circulated waters (Jahnert and Collins, 2012). In each example, shallow-marine sediments that accumulated under subaqueous conditions and precipitated from ambient fluids that are physically connected to seawater (but poorly circulated) are up to 6‰ more ^{13}C-enriched compared to coeval deep-ocean pelagic sediments and therefore do not record ocean-atmosphere $\delta^{13}C$ values (Swart and Eberli, 2005). These modern examples provide a useful reference point by which the anomalously enriched $\delta^{13}C$ values recorded through much of the Neoproterozoic stratigraphic record can be compared (Figure 1).

3. Neoproterozoic comparisons with Cenozoic platforms

As radiometric ages in Neoproterozoic stratigraphic records are generally poor in resolution, the construction of composite $\delta^{13}C$ records relies primarily on the correlation of similar vertical changes in recorded $\delta^{13}C$ values between basins globally. Previous compilations are broadly calibrated by the Sturtian and Marinoan glacial intervals and reveal that during the early Cryogenian (pre-Sturtian) carbonate-bearing intervals are consistently ^{13}C-enriched for > 100 m.y, recording variable $\delta^{13}C$ values of +3‰ to +10‰ (excluding the isotopically negative Bitter Springs Anomaly and Islay Anomaly in each reference section respectively) and is the focus of this study. Coupled sedimentological and $\delta^{13}C$ data are considered from the intracratonic Amadeus Basin in central Australia, the platformal Fifteenmile Group in the Coal Creek Inlier in NW Canada, and the platformal Eleonore Bay and Hecla Hoek Basins in NE Greenland and NE Svalbard respectively, that contain key reference sections supporting global correlation (Halverson et al., 2005; Shields-Zhou et al., 2012, Figure 2). Further, the Etina

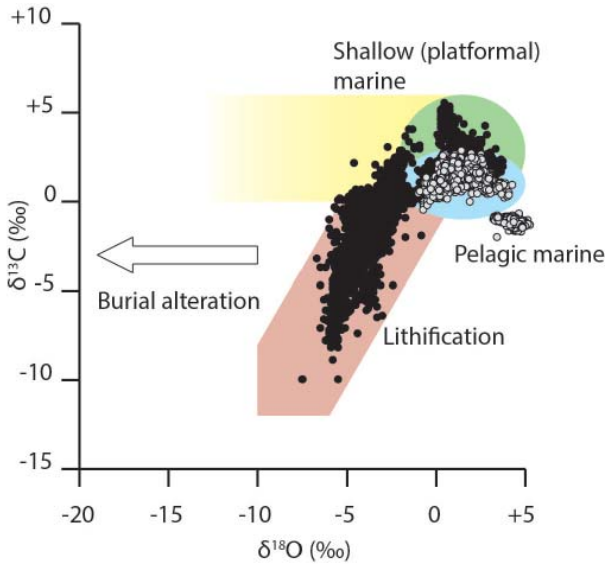

Figure 1. Stable isotopic variability in Phanerozoic carbonates. Filled circles are Phanerozoic carbonates that define the 'lithification zone' of Knauth and Kennedy (2009) (red field) including Cenozoic platform carbonates (green field) that show the isotopic range of ^{13}C enrichment in coastal fluids. Cenozoic values are extended toward increasingly negative $\delta^{18}O$ values (yellow field) where ancient carbonates are predicted to plot following isotopic re-equilibration and alteration of $\delta^{18}O$ values during burial and diagenesis assuming near-primary $\delta^{13}C$ values are retained (Banner and Hanson, 1990). Open circles (blue field) are unfiltered deep-ocean pelagic and benthic carbonate values from Cenozoic deep-ocean records used to construct Cenozoic variation in ocean-atmosphere $\delta^{13}C$ (Flower and Kennett, 1995; Shackleton and Hall, 1984; Shackleton et al., 1983; Wright et al., 1992; Zachos et al., 1994).

Formation in the South Australian Flinders Ranges is examined that records an interval of the most positive sustained $\delta^{13}C$ values (+10‰) recorded during the Neoproterozoic that are interpreted as marine in origin.

3.1 Bitter Springs Formation, central Australia

The upper Loves Creek Member (Johnnys Creek beds) of the ~800 Ma Bitter Springs Formation in central Australia preserves sustained $\delta^{13}C$ values of +2‰ to +6‰ following negative values of -2‰ to -4‰ that define the Bitter Springs Anomaly $\delta^{13}C$ excursion interpreted as a global oceanographic event and provides a standard $\delta^{13}C$ feature used for global correlation (Halverson et al., 2005; Swanson-Hysell et al., 2012). Positive $\delta^{13}C$ values throughout are recorded by dolomitised grainstone and microbial carbonates, and in dolomite-bearing mudstones (Figure 2). These carbonates and mixed carbonate-siliciclastics accumulated under hyper-arid conditions indicated by tens of metres of anhydrite deposition and are known to be periodically non-marine (Chapter 2, Hill et al., 2000; Southgate, 1991). Both the range of $\delta^{13}C$ values and sediment composition are consistent with periodic playa-type environments where local waters are isotopically enriched in response to evaporative processes. In contrast, marine to restricted marine intervals that lack extensive evidence of evaporation record all $\delta^{13}C$ values ranging from -2‰ to -4‰ in the lower Loves Creek Member, and are likely influenced by pore fluid interactions with meteoric waters based on their position relative to the lithification domain of Knauth and Kennedy (2009, Figure 3). The ^{13}C-enriched data recorded in the Bitter Springs Formation fit well within the $\delta^{13}C$ range (< +6‰) predicted for a periodically isolated marine basin that becomes dominated by evaporative processes as sea-level falls behind a connecting sill.

3.2 Upper Fifteenmile Group, NW Canada

The ~811 Ma upper Fifteenmile group of NW Canada records $\delta^{13}C$ values that vary between 0‰ and +6‰, with a single interval recording $\delta^{13}C$ values as high as +10‰ (Figure 2). The gradual decline to values of 0‰ from the most positive values preserved (+10‰) is commonly correlated to the interpreted global Bitter Springs $\delta^{13}C$ Anomaly. Further, the only direct radiometric ages used to constrain the Bitter Springs Anomaly are derived from an interbedded tuff deposit in the upper Fifteenmile Group that therefore represents an important chronostratigraphic marker for global

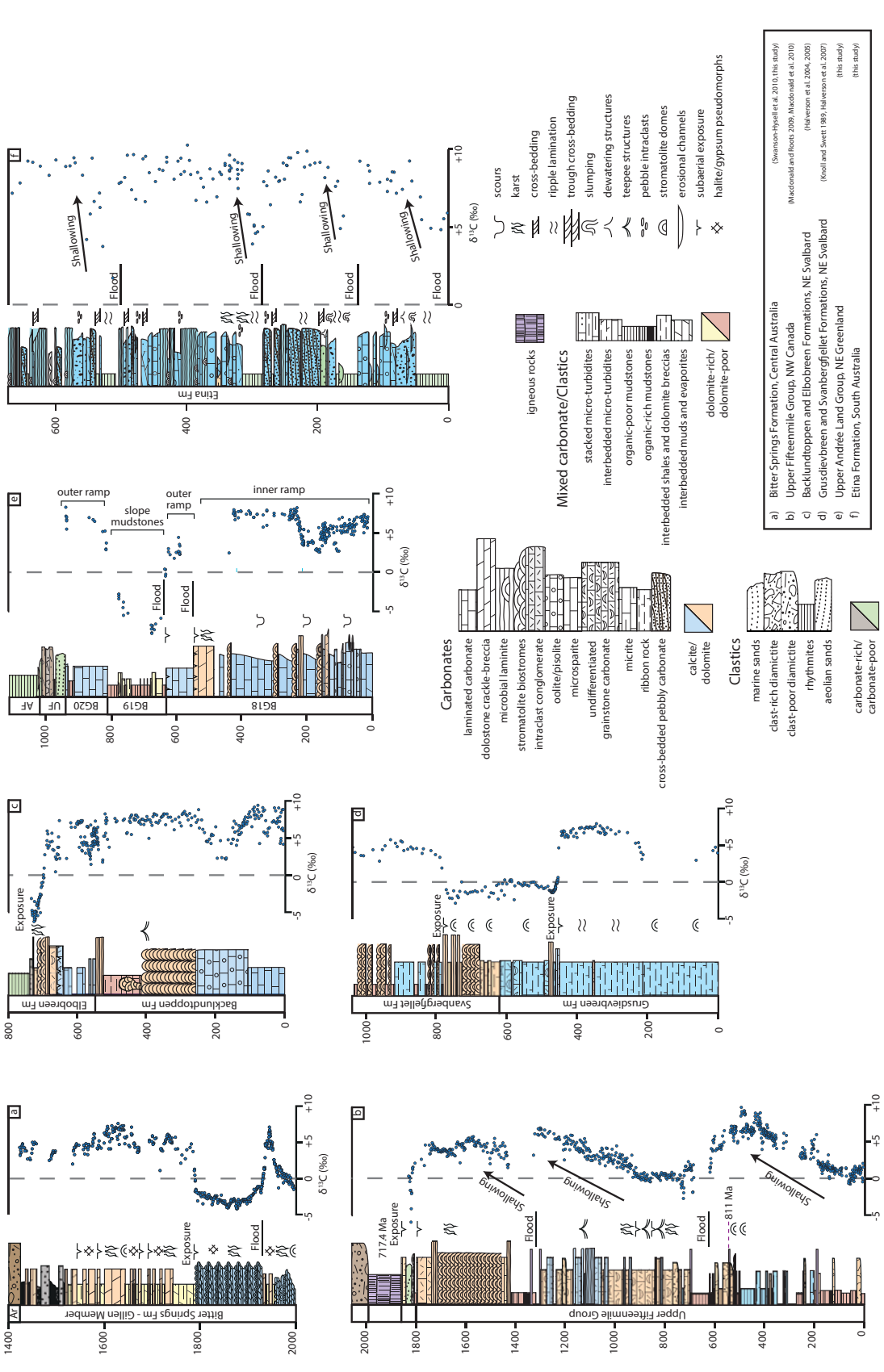

Figure 2. Reference Neoproterozoic stratigraphic sections and coupled $\delta^{13}C$ data from Australia, NW Canada, NE Svalbard and NE Greenland. a) Wallara-1 core of the Bitter Springs Formation, Amadeus basin, central Australia. AR is the Areyonga Formation diamictite, interpreted as Sturtian in age. $\delta^{13}C$ data is from Swanson-Hysell et al. (2012) and an unpublished data set (appendix 3.1). b) Reference section from the pre-Sturtian glacial upper Fifteenmile Group in NW Canada.

Stratigraphic section is redrafted from Macdonald and Roots (2009) and Macdonald et al. (2010). $\delta^{13}C$ data is from Macdonald et al. 2010. c) Composite stratigraphic section from the pre-Sturtian Backlundtoppen and lower Elbobreen Formations of NE Svalbard. Composite section and $\delta^{13}C$ data combines the MS1 and MS7 sections of Halverson et al. (2004) and the lower Backlundtoppen Formation from Halverson et al. (2005). d) Composite stratigraphic section and $\delta^{13}C$ data from the Grusdievbreen and Svanbergfjellet Formations of NE Svalbard after Halverson et al. (2007). e) Composite stratigraphic section of the upper Andrée Land Group, NE Greenland. BG 18/19/20 are informal bedgroup formations 18 – 20 respectively. UF and AF are the Sturtian Ulvesø Formation and post-Sturtian Arena Formation. Lower bedgroup 18 stratigraphy and $\delta^{13}C$ data is from the Ella Ø field section (appendix 5.1). Upper bedgroup 18 and remaining stratigraphy and $\delta^{13}C$ data is from the Kap Weber field section (appendix 5.3). f) Stratigraphic section from the lower Etina Formation, the informal 'Winna Limestone of Mckirdy et al. (2001). Stratigraphic information and $\delta^{13}C$ data were collected from a single reference section in the Bunkers Range region of the central Flinders Ranges (Appendix 6).

correlation (Macdonald et al., 2010). The progression of sedimentation and associated isotopic values in the upper Fifteenmile Group can be generally related within three 400 to 600 m thick shallowing cycles separated by sharp transgressive surfaces (Macdonald and Roots, 2009, Figure 2). The lower two cycles record minimum $\delta^{13}C$ values in basal carbonates between 0‰ and +2‰ that gradually increase to values of +10‰ and +6‰ for the first and second cycles respectively (Macdonald et al., 2010). The first cycle records relatively deep-water deposition as organic dolomitic siltstones with interbedded limestone debris flows that shallow upward into laminated limestone-dominated facies with minor stromatolites and grainstones and is capped by a ~100 m thick interval dominated by massive dolomitic debris flows interpreted as material shed from up-slope carbonate platforms (Macdonald and Roots, 2009). These allodapic limestones and dolostones are expected to record the $\delta^{13}C$ values of up-slope platform-top carbonate where they mineralised, with the upper intervals of the basal cycle preserving the greatest proportion of this platform-derived material and also recording the most positive $\delta^{13}C$ values in the Formation. The middle cycle, following ~100 m of laminated, variably organic and dolomitic shales, records a 300 m interval dominated by dolomitic grainstone deposition with common tepee structures and exposure surfaces. As the proportion of microbial laminites increases up-section, $\delta^{13}C$ values increase from 0‰ to +2‰ in the lower grainstone-dominated unit to +4‰, and preserving maximum values of +6‰ below the successive flooding surface at the base of the upper cycle (Macdonald et al., 2010). Overlying

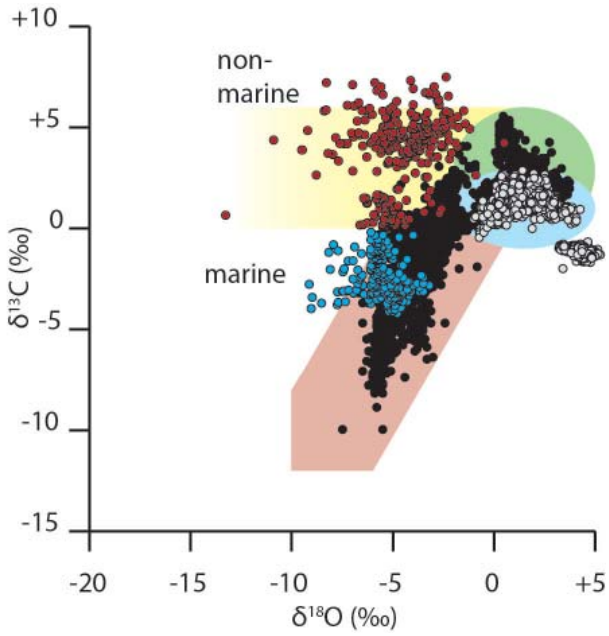

Figure 3. Carbon and oxygen isotope data for the Loves Creek Member of the Bitter Springs Formation in central Australia. The upper evaporitic mudstone and dolostone unit (informal Johnnys Creek beds) record $\delta^{13}C$ values that plot entirely within the range expected in modern coastal carbonates (red). $\delta^{13}C$ values from marine limestones of the lower Loves Creek Member plot on and to the left of the lithification domain of Knauth and Kennedy (2009). $\delta^{13}C$ and $\delta^{18}O$ data collected from Swanson-Hysell et al. (2012) and unpublished data sets from the NTGS Wallara-1 and BR05 stratigraphic cores.

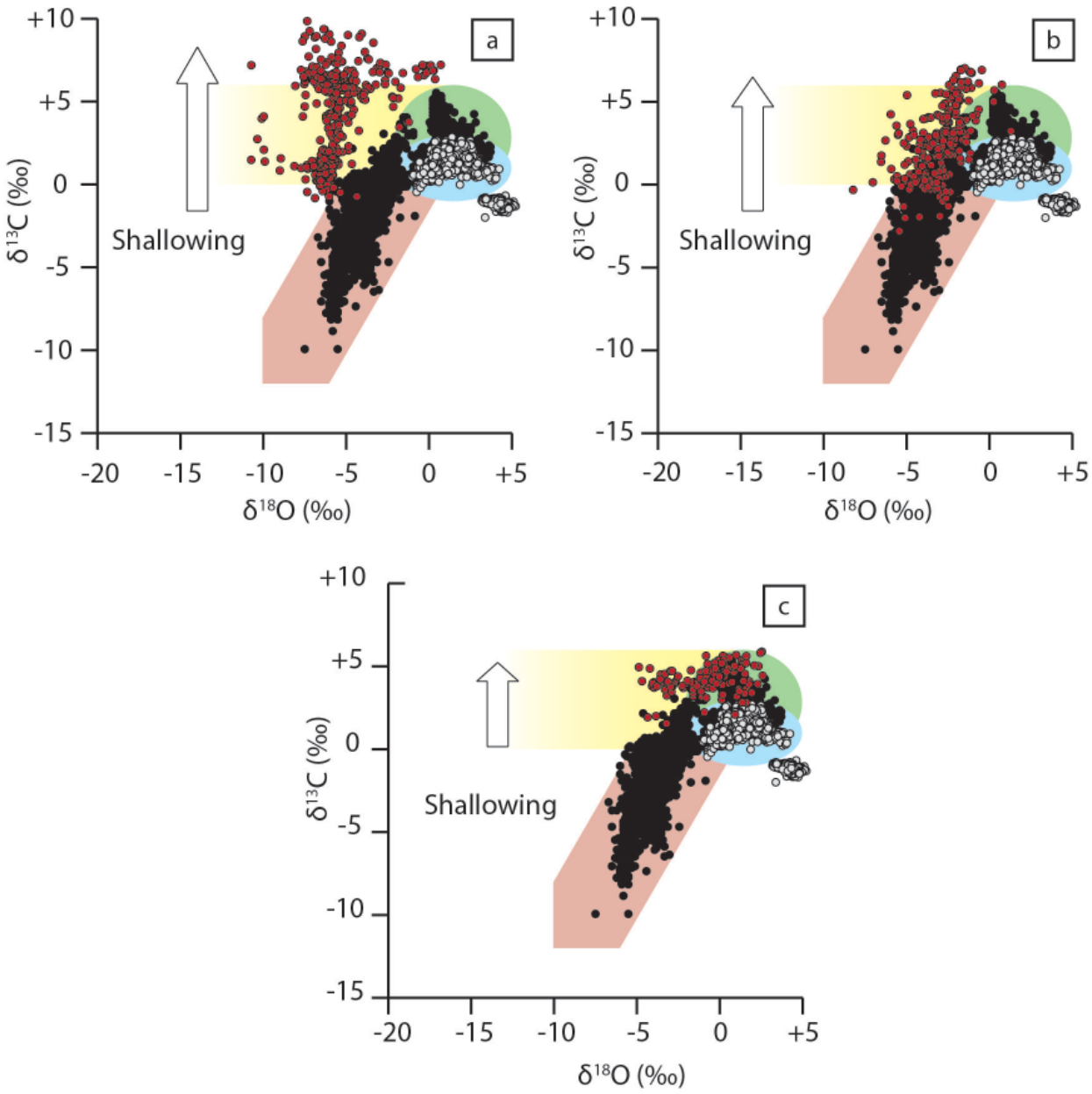

Figure 4. Carbon and oxygen isotope data from the upper Fifteenmile Group in NW Canada. Data is binned based on the stratigraphic designation of each sample after Macdonald and Roots (2009) to their units PF1a, PF1 and PF3 (corresponding to the lower, middle and upper shoaling cycle); a) Lower siliciclastic and debris flow-dominated shallowing cycle, b) Middle grainstone and microbial laminite-dominated shallowing cycle and c) stromatolite-dominated shallowing cycle. The vertical shallowing trend of each cycle is indicated by an arrow. $\delta^{13}C$ and $\delta^{18}O$ data from Macdonald et al. (2010).

~100 m of mudstone deposition, the upper cycle preserves ~300 m of stromatolitic dolostones with minor grainstones and conglomeratic carbonates. This facies records values between +2‰ and +6‰ before sharply declining to negative values directly below a palaeokarst surface (Macdonald and Roots, 2009; Macdonald et al., 2010). In each cycle, the most positive $\delta^{13}C$ values recorded occur in dolomitised sediment

that precipitated on shallow-water platforms at or near base-level indicated by common evidence of exposure. Excluding a single interval that approaches $\delta^{13}C$ values of +10‰ and is associated with re-deposited sediment, all values recorded in the upper Fifteenmile Group plot entirely within the range of Cenozoic $\delta^{13}C$ variability documented on shallow-water platforms (Figure 4).

3.3 East Greenland – East Svalbard Platform sequences

Deposition above a laterally-extensive, stable, shallow-water carbonate ramp characterises the late Tonian to early Cryogenian stratigraphic record of North East Greenland and East Svalbard (Fairchild and Hambrey, 1995; Higgins et al., 2001; Sønderholm et al., 2008). Carbonate-dominated sections preserved here provide much of the basis for correlation of pre-Sturtian stratigraphy based on a series of $\delta^{13}C$ variations between +3‰ to +8‰ recorded in shallow water carbonates (Knoll et al., 1986), as well as the Bitter Springs Anomaly and pre-Sturtian glacial Islay Anomaly negative $\delta^{13}C$ excursions (Halverson et al., 2005). The Grusdievbreen and Svanbergfjellet Formations (Akademikerbreen Group, NE Svalbard) record variable $\delta^{13}C$ values of +3‰ to +8‰, with a decline to negative values of 0‰ to -4‰ correlated as the Bitter Springs Anomaly and bracketed by a pair of unconformities in the upper Grusdievbreen and lower Svanbergfjellet Formations respectively (Halverson et al., 2007). Excluding the negative $\delta^{13}C$ excursion interval, a gradual increase from near 0‰ occurs over ~50 m of stratigraphy in the lower Grusdievbreen Formation and is followed by sustained $\delta^{13}C$ values of +5‰ to +8‰ recorded by ~200 m of 'ribbon' limestones intercalated with mudflake conglomerates that shoal upward (Knoll and Swett, 1989). This unit is capped by a sequence boundary at the base of the upper Grusdievbreen

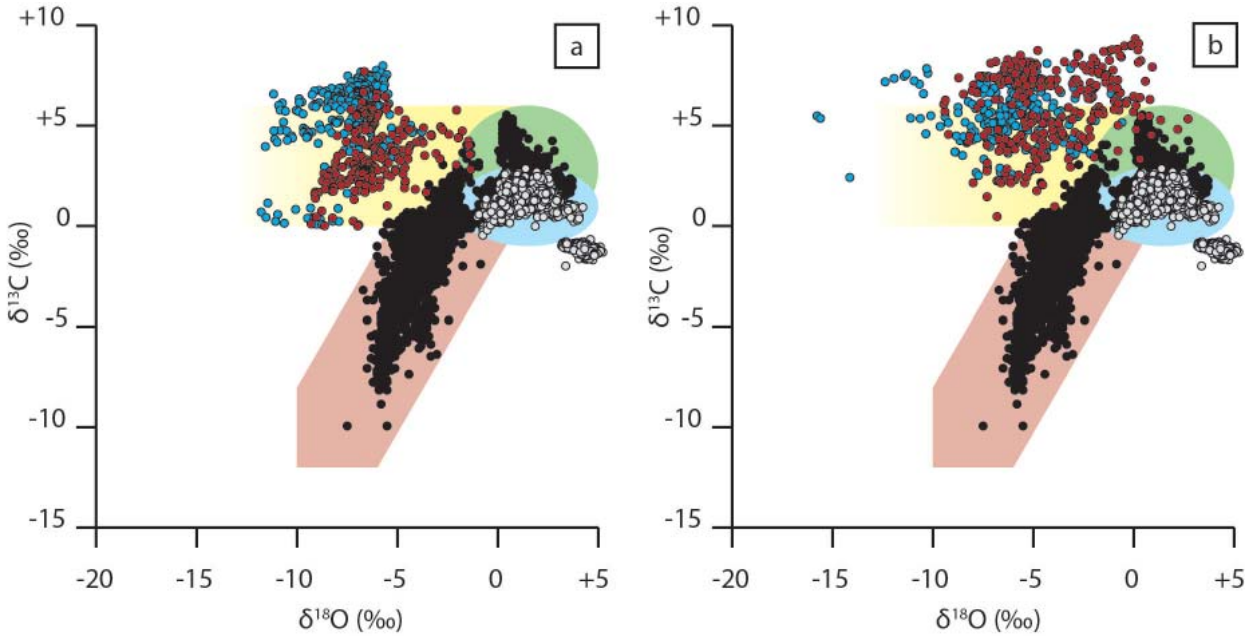

Figure 5. Carbon and oxygen isotope data from NE Greenland and E Svalbard carbonate platform sections. a) Isotopic data from the Svanbergfjellet (red circles) and Grusdievbreen (blue circles) Formations, E Svalbard b) Isotopic data from the Backlundtoppen and Elbobreen Formations in E Svalbard (red circles) and the upper Andrée Land group in NE Greenland (blue circles). Negative $\delta^{13}C$ excursions are not shown. Svalbard $\delta^{13}C$ and $\delta^{18}O$ data from (Halverson et al., 2005; Halverson et al., 2007; Hoffman et al., 2012)

Formation with evidence for subaerial exposure, erosion and palaeokarst (Halverson et al., 2007). Following an interval of negative $\delta^{13}C$ values up to 300 m in thickness and comprising microbial and grainstone carbonates with evidence for subaerial exposure in the upper Grusdievbreen and lower Svanbergfjellet Formations, the upper Svanbergfjellet Formation records ~350 m of ribbon limestones and stromatolitic carbonate that record $\delta^{13}C$ values of +3‰ to +6‰. These data plot well within the range of Cenozoic $\delta^{13}C$ variability common to carbonate platform environments, with only a single ~75 m interval of the Grusdievbreen Formation recording $\delta^{13}C$ values as high as +8‰ that plot beyond this range (Figure 5).

The Backlundtoppen and Elbobreen Formations (NE Svalbard) and the laterally equivalent upper Andrée Land Group (NE Greenland) record the vertical transition from platform carbonates to diamictite-dominated facies correlated globally as deposits associated with the Sturtian glaciation, including a decline in recorded $\delta^{13}C$ values to minimum values of -10‰ directly below the first glacial deposits. $\delta^{13}C$ values throughout each platform section plot largely within the domain of Cenozoic platform carbonate variability but are up to 3‰ more positive in some intervals (Figure 5). The upper Backlundtoppen Formation preserves ~200 m of uninterrupted stromatolitic dolostones (Knoll et al., 1989), followed by mixed microbial and fine-grained siliciclastic facies, that record sustained $\delta^{13}C$ values as high as +8‰ (Figure 2). Stratigraphically above this level, the lower Elbobreen Formation comprises a lower ~135 m thick interval of upward-shoaling laminated carbonates, microbial laminites, and capping carbonate grainstones that record $\delta^{13}C$ values of +3‰ to +5‰ before the decline into the pre-Sturtian Islay Anomaly (Halverson et al., 2004; Hoffman et al., 2012). In the upper Andrée Land Group, limestones and dolostones preserve $\delta^{13}C$ values that typically range from +5‰ to +8‰ in shallow water pisolitic and microbial facies that accumulated in an inner-ramp setting (Frederikson, 2001, Chapter 4). Following subaerial exposure and dissolution collapse, $\delta^{13}C$ values decline to +2‰ to +5‰ in outer-ramp limestones before sharply falling to -10‰ across a flooding surface and abrupt facies change to outer-slope mudstones. Maximum values of +8‰ between each section contrast with maximum Cenozoic deep-marine $\delta^{13}C$ values by ~6‰ but remain within 2‰ to 3‰ of the most ^{13}C-enriched Cenozoic platform carbonate sediments (Figure 5). In many cases where recorded $\delta^{13}C$ values exceed +6‰, dolomite is preserved as the dominant carbonate mineralogy (eg. Halverson et al., 2004), either as a primary authigenic phase or early diagenetic cement. In either case, a ~+2‰ $\delta^{13}C$ fractionation is predicted during the transformation of primary calcite to dolomite (Sheppard and Schwarcz, 1970) that would be capable of driving already ^{13}C-enriched shallow-water accumulations beyond the upper limits defined by modern shallow-marine environments where carbonate is preserved almost exclusively as calcite or aragonite. Further, the placement of the NE Greenland - E Svalbard platform within a narrow, tectonically active continental basin (Sønderholm et al., 2008) attests to the potential of further hydrologic restriction and even, periodically, complete isolation from seawater.

3.4 Etina Formation, South Australia

The late Cryogenian Etina Formation in the South Australian Flinders Ranges records $\delta^{13}C$ values that range from +3‰ to as high as +10‰ (Figure 6). The Etina Formation records a relatively bimodal distribution of sedimentation; ripple-laminated calcareous siltstones coarsen-upward through interbedded and channelised cross-laminated fine sands and are abruptly but conformably overlain by 200 m thick packages of microbial, ooid grainstone, and polymict pebbly packstone limestones with evidence for shallow water to exposure in rip-up clasts, erosive surfaces, and minor karstic features (Figure 2). These limestone complexes are sharply overlain by subsequent shale units along interpreted flooding surfaces (McKirdy et al., 2001), however channelised arkosic sandstones, rare limestone conglomerates, and minor carbonate beds

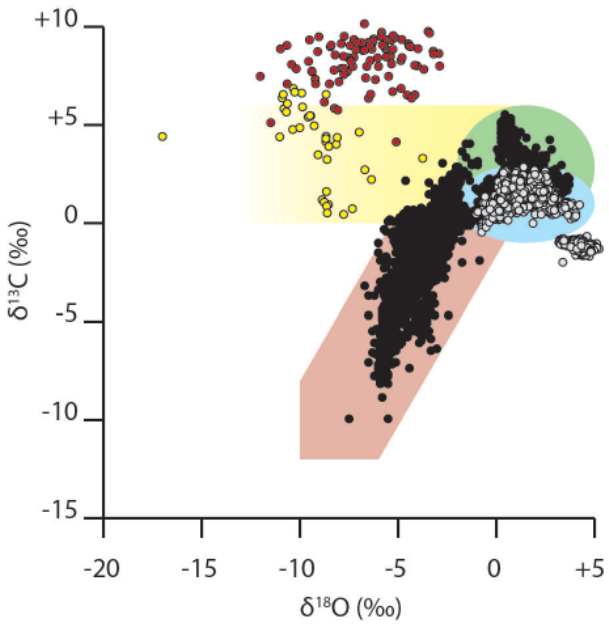

Figure 6. Carbon and oxygen isotopic data from the Etina Formation in South Australia. Red circles are limestones (>80% carbonate) and yellow circles are calcitic cements in deeper-water siltstones.

in shale facies indicate that shale deposition continued under relatively shallow-water conditions. In contrast to the broad and laterally continuous carbonate platforms described above, deposition of the Etina Formation limestone facies is focussed within the peripheral sinks of a system of locally active salt-diapirs on the palaeoshelf margin (McKirdy et al., 2001), occurring as a pair of bulls-eye patterns of depositional thickness with a lateral extent of ~250 km2 across the central Flinders Ranges (Preiss, 1987).

$\delta^{13}C$ values ranging from +7‰ to +10‰ are exclusively recorded by carbonate allochems, cements and microbial precipitates in the limestone-dominated units of the Etina Formation (Figure 2). Across each facies shift from limestones to mixed carbonate and shales, $\delta^{13}C$ values abruptly shift to minimum values of +3‰ to +5‰. These minimum values gradually increase by 3‰ to 5‰ along coarsening trends in underlying shale intervals and towards the base of each limestone unit. Similarly, $\delta^{18}O$ values vary from -3‰ to -12‰ systematically with sediment composition; minimum $\delta^{18}O$ values (-10‰ to -12‰) occur exclusively in shale-dominated intervals while a range of $\delta^{18}O$ values from -8‰ to -3‰ occur in limestone-dominated intervals. These vertical $\delta^{18}O$ trends are offset in comparison to $\delta^{13}C$ and show a second order of variability as smooth ten-metre scale cycles that build toward broader hundred-metre scale trends (Figure 7).

In comparison to Cenozoic marginal environments, shale-dominated units of the Etina Formation plot entirely within the < +6‰ range documented on modern shallow-water bank tops. $\delta^{13}C$ values of > +8‰ and as high as +10‰ are more difficult to explain entirely in the context of Cenozoic platform equivalents as they are up to 4‰ more positive than comparable modern marine carbonate values. The dominant mineralogy in the Etina Formation is calcite and the rare dolomitic beds that are present are similar to adjacent calcitic samples in terms of recorded $\delta^{13}C$ values, indicating that fractionation during dolomitisation post-deposition is unlikely to have played a role in ^{13}C-enrichment. While the loose covariation of $\delta^{13}C$ and $\delta^{18}O$ recorded might support a diagenetic origin, the cyclical pattern of $\delta^{18}O$ variation illustrated in Figure 7 is difficult to explain with a pervasive post-depositional overprint, which is also expected to yield ^{13}C-depleted carbonate that is not present in this section (Knauth and Kennedy, 2009), or as an oceanographic signal where $\delta^{18}O$ values gradually vary by up to 10‰ over tens of metres of stratigraphy and are as low as -12‰. An alternative interpretation is that Etina Formation limestones periodically accumulated under waters that were entirely decoupled from seawater. The Etina Formation is bracketed by deeper-water shales that are occasionally hummocky cross-stratified and blanket the extent of the Adelaide Fold Belt. In contrast, the Etina Formation occurs as a discrete lens of shallow-water carbonate and slightly deeper-water mixed carbonate and siliciclastics that is focussed within a localised sub-basin in the central Flinders Ranges. As sea level fell behind a connecting sill, localised topographic lows peripheral to salt-diapirs may have been periodically isolated entirely from marine connections,

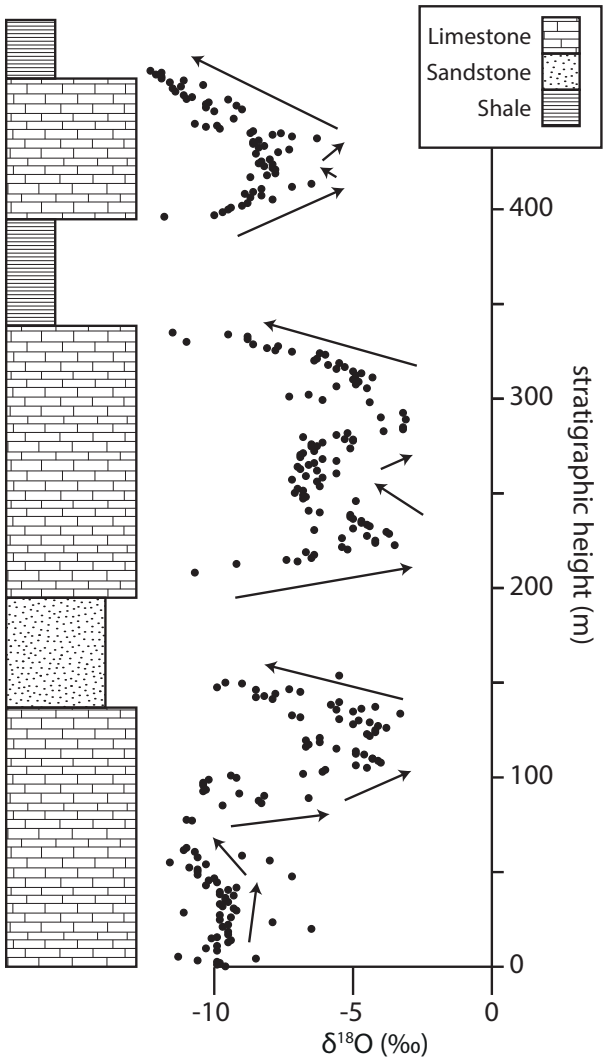

Figure 7. High resolution $\delta^{18}O$ data from the lower Etina Formation showing second-order vertical cyclicity in isotopic variation. Arrows indicate direction of change. Data and stratigraphic measurements from Swanson-Hysell et al. (2010).

accumulating shallow water sediment as the Etina Formation. Under these conditions, the fractionating effects of evaporation and prolific algal photosynthesis may have driven ambient fluid DIC towards $\delta^{13}C$ values of +10‰. As the margin was periodically flooded, represented by sharp facies transitions from limestones to mixed siliciclastics, the dilution of basinal waters with seawater carrying significantly lower $\delta^{13}C$ values is capable of creating a coupling between $\delta^{13}C$ and sediment compositional change, although $\delta^{18}O$ values would also be expected to approach 0‰ rather than declining towards -12‰ as is documented. The cyclical variation observed in $\delta^{18}O$ values could be linked to variations in freshwater influx rather than seawater under extended conditions of hydrologic isolation (Figure 7). In this case, hydrologically-open phases allowed for an increased flux of meteoric waters that were both ^{13}C- and ^{18}O-depleted, while evaporation during hydrologically-closed phases drove $\delta^{18}O$ values to more positive values. Regardless, complex and systematic associations between sediment type, $\delta^{13}C$, and $\delta^{18}O$ values such as those observed in the Etina Formation are difficult to resolve in an open-marine setting where residence times of C and O differ by an order of magnitude, and local lithofacies changes should be insensitive to changes in seawater chemistry, but are common to modern lacustrine environments where $\delta^{13}C$ and $\delta^{18}O$ values range by > 30‰ and are controlled by local carbon cycling processes over atmospheric change (Horton et al.; Talbot, 1990).

4. Discussion

The pervasiveness of ^{13}C-enriched carbonates in the Neoproterozoic geologic record suggests that a common origin for $\delta^{13}C$ values > +3‰ exists. The interpretation proposed in this study relates the sustained positive $\delta^{13}C$ values that are common in carbonate-bearing stratigraphic intervals of Neoproterozoic age to processes documented as significant in modern marginal carbonates, and are capable of being identified in more ancient strata using physical sedimentological data. In general, as local palaeoenvironments become shallow and ambient fluids become increasingly poorly-mixed in response, $\delta^{13}C$ values are expected to gradually increase as local photosynthetic reactions and surface-water evaporation increasingly dominate $\delta^{13}C$ values over seawater and atmospheric exchange. Neoproterozoic carbonate-bearing sections that host sustained ^{13}C-enriched values > +3‰ often preserve a number of

common sedimentological and mineralogical features that are instructive in this regard. Nearly all examples occur as thick packages of carbonate grainstones, packstones, microbial precipitates, and heavily recrystallised sparry carbonate of often ambiguous palaeoenvironmental origin, that are in most cases interpreted to have accumulated on carbonate platforms and ramps at shallow subtidal depths (Day et al., 2004; Halverson et al., 2007; Rose et al., 2013) or in sabkha-type environments in association with evaporite deposits (Southgate, 1991). Evidence for subaerial exposure is present in almost every section examined as mudcracks, karsts and erosive hiatuses (Day et al., 2004; Halverson et al., 2002; Halverson et al., 2007; Southgate, 1991). Finally, dolomite is often the dominant carbonate mineralogy preserved occurring as either a replacement to aragonite and calcite or as a primary authigenic phase (Halverson et al., 2004; Hill et al., 2000; Kenny and Knauth, 2001; Macdonald and Roots, 2009). These observations are consistent with sediment accumulation that took place at or near base-level and is therefore sensitive to subtle variations in water depth that can lead to periodic exposure, hydrologic restriction, and the dominance of local carbon cycling process that drive ^{13}C-enrichment.

While sustained $\delta^{13}C$ values > +3‰ in Neoproterozoic carbonates can be related to similar processes (evaporation and photosynthesis) active on modern carbonate platforms in general, a second order of coupling of $\delta^{13}C$ values and lithofacies is preserved where variations between the most positive and negative $\delta^{13}C$ values change along shallowing and deepening trends (Figure 4). This is true for each of the three shallowing cycles identified in the upper Fifteenmile Group where relatively deeper-water facies record $\delta^{13}C$ values near 0‰ which gradually increase as water depth decreases to subaerial exposure, in the upper Andrée Land Group that records a decrease in $\delta^{13}C$ values from +8‰ to +5‰ as inner-ramp grainstone and microbial carbonates deepen to outer-ramp laminated limestones following a period of karst and exposure, and in the Etina Formation where flooding of the basin coincides with a decline in $\delta^{13}C$ values by > -5‰ (Figure 2). In these examples, the association of water depth and $\delta^{13}C$ values suggests that as sea-level variation drives changes in sediment composition, chemical processes such as evaporation rates and algal photosynthesis also vary in their influence on the $\delta^{13}C$ composition of local fluid DIC. Mixing relationships between isotopically-enriched bank-top carbonate sediment and pelagic carbonates recording more modest $\delta^{13}C$ values (~0‰) are also systematically recorded on modern carbonate platforms that produce similar depth-dependent trends in terms of thickness, range of $\delta^{13}C$ values recorded (~6‰), vertical shape of the $\delta^{13}C$ pattern, and coupled change in sediment composition (Swart and Eberli, 2005). As the modern skeletal pelagic flux is not active in the Neoproterozoic, this type of mixing may analogously occur between the most restricted bank-top carbonate allochems, and relatively deep-water algal mats and inorganic carbonate muds. Significantly, the absence of any skeletal pelagic material on Neoproterozoic bank-tops may extend the theoretical maximum range of $\delta^{13}C$ values recorded on Neoproterozoic carbonate platforms beyond the < +6‰ range recorded on Cenozoic equivalents (Figure 1) and may account in part for Neoproterozoic intervals that record $\delta^{13}C$ values of > +8‰. In the same way that shoaling cycles produce predictable physical trends in local sediment composition and structure, patterns of $\delta^{13}C$ change are expected to be systematic and predictable with changes in local palaeoenvironmental conditions that are commonly linked to sea level as a proxy for hydrologic connectivity.

The recurrence of $\delta^{13}C$ values > +3‰ in the Neoproterozoic stratigraphic record may simply represent the inherent preservational bias toward shallow-water depositional environments in the Neoproterozoic. All carbonate sediment still preserved in the geologic record of Neoproterozoic age accumulated in shallow water marginal basins, inland seaways, and in non-marine basins such as playas and standing alkaline lakes; all deep-marine deposits have since been subducted or metamorphosed. Nearly

all ^{13}C-enriched carbonate in Neoproterozoic-aged sections is recorded by shallow-water sediment that accumulated in water depths of tens of metres where microbial processes are expected to be most prolific. The relatively deep-water deposits that do exist in Neoproterozoic archives are generally slope deposits that do not generally record significant volumes of carbonate directly precipitated from ambient water column fluids. These types of deposits are understood to provide an unreliable record of seawater DIC as the marine flux of pelagic shells was not active in the Neoproterozoic. Instead, carbonate materials that are preserved in these environments are typically swept from landward platforms during storms and re-deposited on the slope by density currents, or are authigenic phases that are isotopically related to pore-fluid processes rather than ambient seawater chemistry. The former process is demonstrated well by the Karibib Formation which records condensed foreslope deposition corresponding to the landward Tsumeb Subgroup of the upper Otavi platform succession in northern Namibia. Following an increase in $\delta^{13}C$ values from -5‰ to +2‰ at the base of the unit, the Karibib Formation preserves scattered $\delta^{13}C$ values ranging from -1‰ to +6‰ in laminated mudstone and interbedded debris flow carbonates. These carbonates, while ^{13}C-enriched, comprise allodapic grains swept from the landward carbonate platform and are conceded by previous workers to record $\delta^{13}C$ values representative of various levels in the Otavi platform (Frimmel, 2010; Halverson et al., 2005), where shallow-water sediments with abundant evidence for exposure record high $\delta^{13}C$ values (up to +10‰). The latter process is demonstrated well by the upper Andrée Land Group that records an abrupt sedimentary transition following subaerial exposure to outer slope deposits characterised by carbonate-poor mudstones, carbonate-rich fine-grained turbidites and channelised carbonate debris flows. Although in some cases samples approach 95% carbonate in their mineralogy, textural and stable-isotopic analysis of these sediments reveals that the vast majority of carbonate preserved here is in the form of an authigenic dolomite phase, with almost no detrital calcite remaining, and record $\delta^{13}C$ values ranging from -4‰ to -10‰ related to sulphate reduction in sediment pore space (Chapter 4). To date, no examples of ^{13}C-enriched carbonate that can be demonstrated to have been precipitated at significant depth directly from the water column and subsequently unaltered during lithification and diagenesis exist.

5. Conclusions

The sustained positive 'background' $\delta^{13}C$ values in the Neoproterozoic stratigraphic record are interpreted to reflect the inherent bias in the Pre-Jurassic stratigraphy record toward shallow-water marginal and intracontinental basins that are influenced and periodically dominated by local carbon-cycling processes. Fractionation of ^{12}C by local photosynthetic effects and evasion of CO_2 during evaporation commonly influence the $\delta^{13}C$ composition of Cenozoic shallow-water carbonates but are accounted for in studies of ocean-atmosphere carbon cycling by comparison with deep-ocean records. As platform carbonate sequences kilometres in thickness are particularly common in the Neoproterozoic stratigraphic record and are inherently shallow, ^{13}C-enriched carbonates are expected to comprise a significant proportion of this record.

References

Amodio, S., Ferreri, V., D'Argenio, B., Weissert, H., and Sprovieri, M., 2008, Carbon-isotope stratigraphy and cyclostratigraphy of shallow-marine carbonates: the case of San Lorenzello, Lower Cretaceous of southern Italy: Cretaceous Research, v. 29, no. 5, p. 803-813.

Banner, J. L., and Hanson, G. N., 1990, Calculation of simultaneous isotopic and trace element variations during water-rock interaction with applications to carbonate diagenesis: Geochimica et Cosmochimica Acta, v. 54, no. 11, p. 3123-3137.

Day, E. S., James, N. P., Narbonne, G. M., and Dalrymple,

R. W., 2004, A sedimentary prelude to Marinoan glaciation, Cryogenian (Middle Neoproterozoic) Keele Formation, Mackenzie Mountains, northwestern Canada: Precambrian Research, v. 133, no. 3–4, p. 223-247.

Fairchild, I. J., and Hambrey, M. J., 1995, Vendian basin evolution in East Greenland and NE Svalbard: Precambrian Research, v. 73, no. 1, p. 217-233.

Flower, B. P., and Kennett, J. P., 1995, Middle Miocene deepwater paleoceanography in the southwest Pacific: relations with East Antarctic Ice Sheet development: Paleoceanography, v. 10, no. 6, p. 1095-1112.

Frederikson, K. S., 2001, A Neoproterozoic carbonate ramp and base-of-slope succession, the Andrée Land Group, Eleonore Bay Supergroup, North East Greenland: Sedimentary facies, stratigraphy and basin evolution [Ph.D. Thesis: University of Copenhagen].

Frimmel, H. E., 2010, On the reliability of stable carbon isotopes for Neoproterozoic chemostratigraphic correlation: Precambrian Research, v. 182, no. 4, p. 239-253.

Gischler, E., Dietrich, S., Harris, D., Webster, J. M., and Ginsburg, R. N., 2013, A comparative study of modern carbonate mud in reefs and carbonate platforms: Mostly biogenic, some precipitated: Sedimentary Geology, v. 292, p. 36-55.

Gischler, E., and Lomando, A. J., 2005, Offshore sedimentary facies of a modern carbonate ramp, Kuwait, northwestern Arabian-Persian Gulf: Facies, v. 50, no. 3-4, p. 443-462.

Gischler, E., Swart, P. K., and Lomando, A. J., 2007, Stable isotopes of carbon and oxygen in modern sediments of carbonate platforms, barrier reefs, atolls, and ramps: patterns and implications: Perspectives in carbonate geology: a tribute to the career of Robert Nathan Ginsburg, p. 61-74.

Halverson, G. P., Hoffman, P. F., Schrag, D. P., and Kaufman, A. J., 2002, A major perturbation of the carbon cycle before the Ghaub glaciation (Neoproterozoic) in Namibia: Prelude to snowball Earth?: Geochemistry Geophysics Geosystems, v. 3, no. 6, p. 1-24.

Halverson, G. P., Hoffman, P. F., Schrag, D. P., Maloof, A. C., and Rice, A. H. N., 2005, Toward a Neoproterozoic composite carbon-isotope record: Geological Society of America Bulletin, v. 117, no. 9-10, p. 1181-1207.

Halverson, G. P., Maloof, A. C., and Hoffman, P. F., 2004, The Marinoan glaciation (Neoproterozoic) in northeast Svalbard: Basin Research, v. 16, no. 3, p. 297-324.

Halverson, G. P., Maloof, A. C., Schrag, D. P., Dudas, F. O., and Hurtgen, M., 2007, Stratigraphy and geochemistry of a ca 800 Ma negative carbon isotope interval in northeastern Svalbard: Chemical Geology, v. 237, no. 1-2, p. 5-27.

Hayes, J. M., Strauss, H., and Kaufman, A. J., 1999, The abundance of C-13 in marine organic matter and isotopic fractionation in the global biogeochemical cycle of carbon during the past 800 Ma: Chemical Geology, v. 161, no. 1-3, p. 103-125.

Higgins, A., Smith, M., Soper, N., Leslie, A., Rasmussen, J. A., and Sønderholm, M., 2001, The Neoproterozoic Hekla Sund Basin, eastern North Greenland: a pre-Iapetan extensional sequence thrust across its rift shoulders during the Caledonian orogeny: Journal of the Geological Society, v. 158, no. 3, p. 487-500.

Hill, A. C., Arouri, K., Gorjan, P., and Walter, M. R., 2000, Geochemistry of marine and nonmarine environments of a Neoproterozoic cratonic carbonate/evaporite: The Bitter Springs Formation, central Australia, in Grotzinger, J. P., and James, N. P., eds., Carbonate sedimentation and diagenesis in the evolving Precambrian world, p. 327-344.

Hoffman, P. F., Halverson, G. P., Domack, E. W., Maloof, A. C., Swanson-Hysell, N. L., and Cox, G. M., 2012, Cryogenian glaciations on the southern tropical paleomargin of Laurentia (NE Svalbard and East Greenland), and a primary origin for the upper Russøya (Islay) carbon isotope excursion: Precambrian Research, v. 206-207, p. 137-158.

Horton, T. W., Defliese, W. F., Tripati, A. K., and Oze, C., Evaporation induced ^{18}O and ^{13}C enrichment in lake systems: A global perspective on hydrologic balance effects: Quaternary Science Reviews (in press).

Jahnert, R. J., and Collins, L. B., 2012, Characteristics, distribution and morphogenesis of subtidal microbial systems in Shark Bay, Australia: Marine Geology, v. 303–306, p. 115-136.

Kenny, R., and Knauth, L. P., 2001, Stable isotope variations in the Neoproterozoic Beck Spring Dolomite and Mesoproterozoic Mescal Limestone paleokarst: Implications for life on land in the Precambrian: Geological Society of America Bulletin, v. 113, no. 5, p. 650-658.

Knauth, L. P., and Kennedy, M. J., 2009, The late Precambrian greening of the Earth: Nature, v. 460, no. 7256, p. 728-732.

Knoll, A., Hayes, J., Kaufman, A., Swett, K., and Lambert, I., 1986, Secular variation in carbon isotope ratios from Upper Proterozoic successions of Svalbard and East Greenland: Nature, v. 321, p 832-838.

Knoll, A., and Swett, K., 1989, Carbonate deposition during the late Proterozoic Era: an example from Spitsbergen: American Journal of Science, v. 290, p. 104-132.

Knoll, A. H., Swett, K., and Burkhardt, E., 1989, Paleoenvironmental distribution of microfossils and stromatolites in the Upper Proterozoic Backlundtoppen Formation, Spitsbergen: Journal of Paleontology, p. 129-145.

Kump, L. R., Junium, C., Arthur, M. A., Brasier, A., Fallick, A., Melezhik, V., Lepland, A., CČrne, A. E., and Luo, G., 2011, Isotopic evidence for massive oxidation of organic matter following the Great Oxidation Event: Science, v. 334, no. 6063, p. 1694-1696.

Lyons, T. W., Reinhard, C. T., and Planavsky, N. J., 2014, The rise of oxygen in Earth's early ocean and atmosphere: Nature, v. 506, no. 7488, p. 307-315.

Macdonald, F., and Roots, C., 2009, Upper Fifteenmile Group in the Ogilvie Mountains and correlations of early Neoproterozoic strata in the northern Cordillera: Yukon Exploration and Geology, p. 237-252.

Macdonald, F. A., Schmitz, M. D., Crowley, J. L., Roots, C. F., Jones, D. S., Maloof, A. C., Strauss, J. V., Cohen, P. A., Johnston, D. T., and Schrag, D. P., 2010, Calibrating the Cryogenian: Science, v. 327, no. 5970, p. 1241-1243.

McKirdy, D. M., Burgess, J. M., Lemon, N. M., Yu, X. K., Cooper, A. M., Gostin, V. A., Jenkins, R. J. F., and Both, R. A., 2001, A chemostratigraphic overview of the late Cryogenian interglacial sequence in the Adelaide Fold-Thrust Belt, South Australia: Precambrian Research, v. 106, no. 1-2, p. 149-186.

Melim, L. A., 2001, Meteoric and marine-burial diagenesis in the subsurface of Great Bahama Bank. In: R.N. Ginsburg (Editor), The Bahamas Drilling Project. SEPM Concepts in Sedimentology

Preiss, W. V. C., 1987, The Adelaide Geosyncline-late Proterozoic stratigraphy, sedimentation, palaeontology and tectonics., Bull. geol. Surv. S. Aust.

Rose, C. V., Maloof, A. C., Schoene, B., Ewing, R. C., Linnemann, U., Hofmann, M., and Cottle, J. M., 2013, The End-Cryogenian Glaciation of South Australia: Geoscience Canada, v. 40, no. 4, p. 256–293.

Schrag, D. P., Higgins, J. A., Macdonald, F. A., and Johnston, D. T., 2013, Authigenic carbonate and the history of the global carbon cycle: Science (New York, N.Y.), v. 339, no. 6119, p. 540-543.

Shackleton, N., 1987, The carbon isotope record of the Cenozoic: History of organic carbon burial and of oxygen in the ocean and atmosphere: Geological Society, London, Special Publications, v. 26, no. 1, p. 423-434.

Shackleton, N. J., and Hall, M. A., 1984, Oxygen and carbon isotope data from Leg 74 foraminifers., in Moore Jr, T. C., and Rabinowitz, P. D., eds., Initial Reports DSDP, Volume 74: Washington: U.S. Government Printing Office, p. 599-612.

Shackleton, N. J., Imbrie, J., and Hall, M. A., 1983, Oxygen

and carbon isotope record of East Pacific core V19-30: implications for the formation of deep water in the late Pleistocene North Atlantic: Earth and Planetary Science Letters, v. 65, no. 2, p. 233-244.

Sheppard, S. M., and Schwarcz, H. P., 1970, Fractionation of carbon and oxygen isotopes and magnesium between coexisting metamorphic calcite and dolomite: Contributions to Mineralogy and Petrology, v. 26, no. 3, p. 161-198.

Shields-Zhou, G., Hill, A., and Macgabhann, B., 2012, The Cryogenian Period, The Geologic Time Scale, Elsevier.

Sønderholm, M., Frederiksen, K. S., Smith, M. P., and Tirsgaard, H., 2008, Neoproterozoic sedimentary basins with glacigenic deposits of the East Greenland Caledonides: Geological Society of America Memoirs, v. 202, p. 99-136.

Southgate, P. N., 1991, A sedimentological model for the Loves Creek Member of the Bitter Springs Formation, northern Amadeus Basin, in Korsch, R. J., and Kennard, J. M., eds., Geological and Geophysical Studies in the Amadeus Basin, Central Australia: Australian Bureu of Mineral Resources, Geology and Geophysics Bulletin 236, p. 113-126.

Stiller, M., Rounick, J. S., and Shasha, S., 1985, Extreme carbon-isotope enrichments in evaporating brines: Nature, v. 316, no. 6027, p. 434-435.

Swanson-Hysell, N. L., Maloof, A. C., Kirschvink, J. L., Evans, D. A. D., Halverson, G. P., and Hurtgen, M. T., 2012, Constraints on Neoproterozoic paleogeography and Paleozoic orogenesis from paleomagnetic records of the Bitter Springs Formation, Amadeus Basin: American Journal of Science, v. 312, no. 8, p. 817-884.

Swanson-Hysell, N. L., Rose, C. V., Calmet, C. C., Halverson, G. P., Hurtgen, M. T., and Maloof, A. C., 2010, Cryogenian Glaciation and the Onset of Carbon-Isotope Decoupling: Science, v. 328, no. 5978, p. 608-611.

Swart, P. K., and Eberli, G., 2005, The nature of the $\delta^{13}C$ of periplatform sediments: Implications for stratigraphy and the global carbon cycle: Sedimentary Geology, v. 175, no. 1-4, p. 115-129.

Talbot, M. R., 1990, A review of the paleohydrological interpretation of carbon and oxygen isotopic-ratios in primary lacustrine carbonates: Chemical Geology, v. 80, no. 4, p. 261-279.

Wright, J. D., Miller, K. G., and Fairbanks, R. G., 1992, Early and middle Miocene stable isotopes: implications for deepwater circulation and climate: Paleoceanography, v. 7, no. 3, p. 357-389.

Zachos, J., Pagani, M., Sloan, L., Thomas, E., and Billups, K., 2001, Trends, rhythms, and aberrations in global climate 65 Ma to present: Science, v. 292, no. 5517, p. 686-693.

Zachos, J. C., Stott, L. D., and Lohmann, K. C., 1994, Evolution of Early Cenozoic marine temperatures: Paleoceanography, v. 9, no. 2, p. 353-387.

Chapter 6

Implications and conclusions

1. Implications for global chemostratigraphic curves

1.1 – The pre-Sturtian $\delta^{13}C$ record

A flurry of new radiometric age dates from reference sections of the pre-Sturtian interval in NW Canada now exist with the potential to better constrain the onset of negative $\delta^{13}C$ values and Cryogenian glaciation in that example and in correlative sections globally. Here, these new dates are considered alongside detailed stratigraphic and isotopic data in order to assess the current state of the pre-Sturtian $\delta^{13}C$ record as well as potential uncertainties in the record that earlier chapters of this study have raised. Composite Neoproterozoic $\delta^{13}C$ records older than Sturtian glacial deposits identify two intervals of low $\delta^{13}C$ values that are superimposed on a ^{13}C-enriched background value of ~+5‰ to +8‰ and interpreted as global seawater $\delta^{13}C$ excursions. The older of these, the Bitter Springs Anomaly, is characterised by a vertical decline in $\delta^{13}C$ values from ^{13}C-enriched values to values of 0‰ to -4‰. The decline toward negative $\delta^{13}C$ values and eventual increase towards positive values provides a pair of stratigraphic isotopic features that are globally correlated, with a seawater excursion established by examples in central Australia, NE Svalbard and NW Canada. Possible correlatives of the Bitter Springs Anomaly also exist in Ethiopia and Scotland, although these examples are poorly stratigraphically constrained and exist as single intervals of negative $\delta^{13}C$ values in largely siliciclastic sections (Alene et al., 2006; Prave et al., 2009). Negative $\delta^{13}C$ values as low as -10‰ are also identified stratigraphically below Sturtian glacial deposits in NE Svalbard, NE Greenland, Scotland, NW Canada and the SW United States, and are globally correlated as the Islay Anomaly. $\delta^{13}C$ values at the base of Sturtian- aged glacial deposits are variable; in some sections terminal carbonates record values as low as -10‰, other sections see an increase in $\delta^{13}C$ values to +8‰ following negative values, while a third class of sections record no negative $\delta^{13}C$ values at any level > 500 m below the base of diamictite-dominated facies. The base of the Sturtian Glaciation is placed at ~717 Ma based on volcanic deposits directly below and into the base of diamictites in the upper Fifteenmile Group. The following discussion considers the three examples that establish the Bitter Springs Anomaly from Australia, NW Canada and NE Svalbard, and examples of the Islay Anomaly in NW Canada, NE Svalbard and NE Greenland where high resolution records exist. The Otavi Group from N Namibia is also considered as it represents an important section from which the post-Bitter Springs Anomaly - pre-Sturtian Glacial interval of the Neoproterozoic $\delta^{13}C$ record is established (eg. Halverson et al., 2005; Shields-Zhou et al., 2012), although this section lacks any negative $\delta^{13}C$ values (Figure 1).

1.2 Bitter Springs Formation, central Australia

In the Amadeus Basin in central Australia, the Bitter Springs Anomaly as it is recorded in the Loves Creek Member of the Bitter Springs Formation follows a sharp increase and decrease in $\delta^{13}C$ values from -2‰ to +7‰ and back to -4‰ that occurs over ~100 m (Figure 1a). Values of -4‰ are maintained for a further 100 m before a step increase in $\delta^{13}C$ values of +6‰ over ~10 m marks the end of the negative $\delta^{13}C$ excursion. The Loves Creek Member sits unconformably above mixed carbonate and evaporites of the lower Bitter Springs Formation Gillen Member and no direct radiometric date constrains the excursion at any stratigraphic level. A 1070 Ma date provides a single age for the Heavitree Quartzite that underlies the Bitter Springs Formation, but is separated from the Loves Creek Member by at least one significant unconformity (at the base of the Loves Creek Member). The Areyonga Formation diamictite that unconformably overlies the Bitter Springs Formation is considered coeval to the Sturtian glaciation, and is further constrained by a Re/Os date of 657.2 ± 5.4 Ma from overlying Aralka Formation siltstones. No negative $\delta^{13}C$ values are recorded by carbonate sediment directly below the Areyonga Formation.

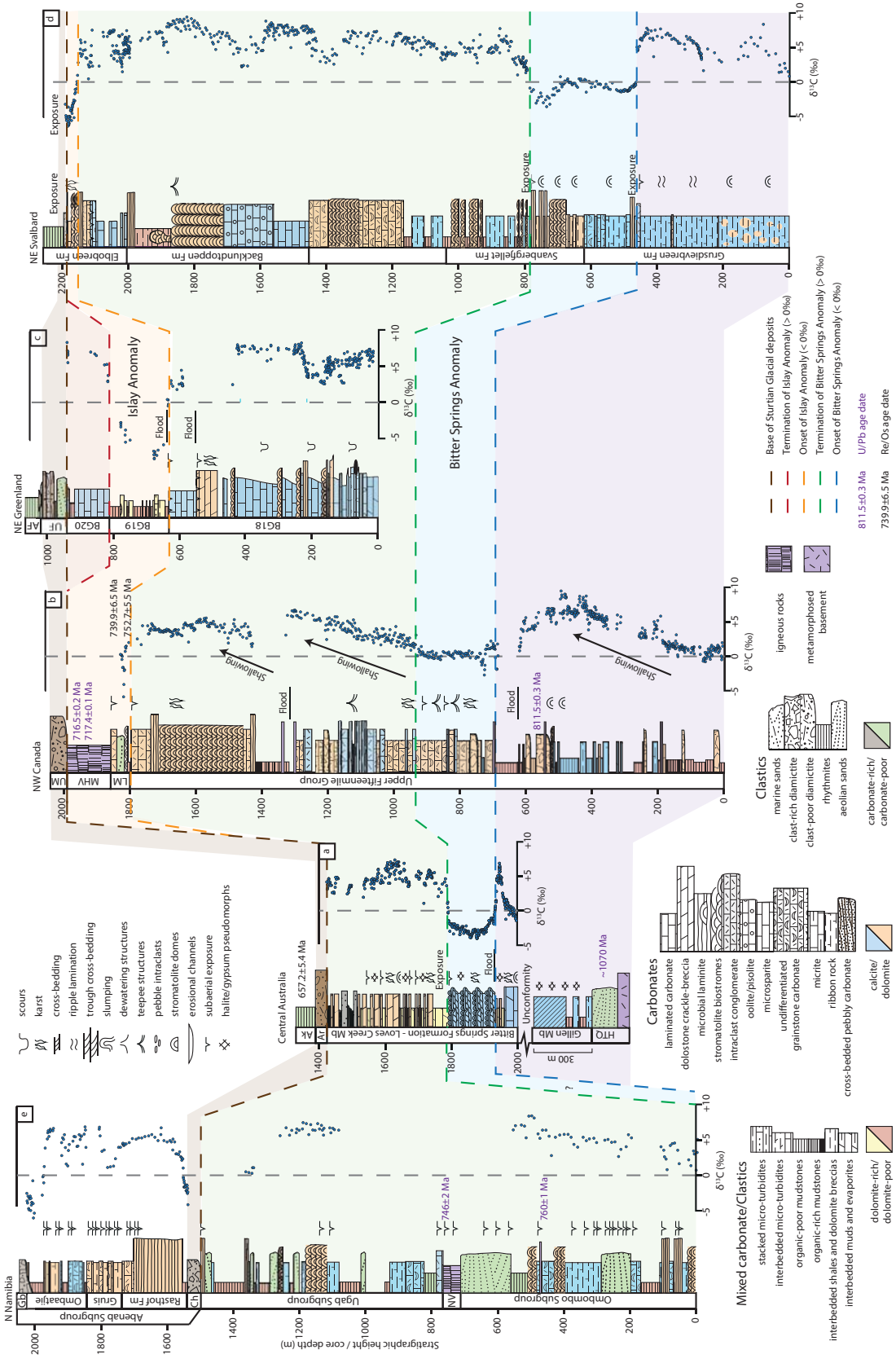

Figure 1. Revised compilation of the pre-Sturtian interval constructed from well-exposed reference sections. a) Bitter Springs Formation. δ13C data from Swanson-Hysell et al. (2010) and this study. HTQ = Heavitree Quartzite, Ar = Areyonga Formation, Ak = Aralka Formation. Gillen Member is the lower member of the Bitter Springs Formation. ~1070 Ma from Schmidt et al. (2006). 657 ± 5.4 Ma from Kendall et al. (2006). b) Upper Fifteenmile Group. Stratigraphic data from Macdonald

and Roots (2009) and Macdonald et al. (2010). δ13C data from (Macdonald et al., 2010). LM = Lower Mount Harper Group, MHV = Mount Harper volcanics, UM = Upper Mount Harper Group. 811.5 ± 0.3 Ma from Macdonald et al. (2010). 752.7 ± 5.5 Ma and 739.9 ± 6.5 Ma from Rooney et al. (2015). c) Upper Andrée Land Group. $\delta^{13}C$ data from this study and Fairchild et al. (2000). BG18-20 are informal 'bed group' formations, UF = Ulvesø Formation, AF = Arena Formation. d) Akademikerbreen and Elbobreen Groups. Stratigraphic and δ13C data from Halverson et al. (2005) and Halverson et al. (2007). E) Ombombo, Ugab and Abenab Subgroups. Stratigraphic and $\delta^{13}C$ data from Halverson et al. (2002) and Halverson et al. (2005). 760 ± 1 Ma from Halverson et al. (2005). 746 ± 2 Ma from Hoffmann and Prave (1996). NV = Naauwpoort Volcanics Ch = Chuos Formation GB = Gaub Formation.

1.3 Upper Fifteenmile Group, NW Canada

The onset of the Bitter Springs Anomaly is constrained by a single direct U/Pb age date of 811.5 Ma from the Ogilvie Mountains of NW Canada (Macdonald et al., 2010, Figure 1b)). This date is recorded in a tuff deposit interbedded with allodapic dolostones at the top of the lower-most shoaling cycle of the upper Fifteenmile Group, approximately 50 m below a decline in $\delta^{13}C$ values from +5‰ to +1‰ and a major flooding surface. ~80 m of subsequent siliciclastic deposits is overlain by dolomitic grainstones and conglomerates that record $\delta^{13}C$ values of 0‰ and mark the onset of the Bitter Springs Anomaly in this locality. While no time constraint exists for the increase in $\delta^{13}C$ values over ~350 m from 0‰ to +6‰ that marks the end of the Bitter Springs Anomaly in the upper Fifteenmile Group, a minimum age is provided by a Re/Os date of 752.7 ± 5.5 Ma from the overlying lower Mount Harper Group, implying that the Bitter Springs Anomaly recorded here is preserved within a window of ~60 Myr. A decline in $\delta^{13}C$ values from +4‰ to values as low as -7‰ in the overlying lower Mount Harper Group is bracketed by a 752.7 ± 5.5 Ma age below and a Re/Os age of 739.9 ± 6.5 Ma age above (Macdonald et al., 2010; Rooney et al., 2015), is correlated to the pre-Sturtian Islay Anomaly, and is the last carbonate-bearing interval stratigraphically below Sturtian glacial deposits. The overlying Mount Harper Volcanics and an interbedded tuff in the lower diamictite unit constrain the onset of glaciogenic deposits here to 716.5 Ma using U/Pb, implying that an unconformity that accounts for ~25 Myr exists between the uppermost carbonate unit and base of the first diamictite here.

1.4 Upper Andrée Land Group, NE Greenland

While no published data exists as-yet reporting the Bitter Springs Anomaly in NE Greenland, the pre-Sturtian record is particularly well preserved (Figure 1c). An abrupt fall in $\delta^{13}C$ values from ~+4‰ to variable but negative $\delta^{13}C$ values as low as -10‰ occurs along a flooding surface. Negative values are sustained for up to 200 m of stratigraphic thickness, before an abrupt increase to $\delta^{13}C$ values of +5‰ to +8‰ occurs across a facies transition to shallow-water platform carbonates in the northern regions of the basin that are further overlain by the Ulvesø Formation, correlated as Sturtian in age based on similarities with the pre-Sturtian interval in NE Svalbard (Hoffman et al., 2012). In sections in the south of the basin, no increase in $\delta^{13}C$ values occurs below the Ulvesø Formation nor is the abrupt facies change to platform carbonates directly below the Ulvesø Formation preserved.

1.5 Akademikerbreen and Polarisbreen Groups, NE Svalbard

In the Akademikerbreen and lower Polarisbreen Groups of NE Svalbard, the onset of the Bitter Springs Anomaly is identified as an abrupt decline from variable $\delta^{13}C$ values of +3‰ to +8‰ to minimum values of -2‰, with a decrease in $\delta^{13}C$ values of -5‰ occurring from sample to sample across an unconformity and exposure surface in the upper Grusdievbreen Formation (Halverson et al., 2007, Figure 1d). $\delta^{13}C$ values gradually increase over ~100 m to δ1‰, before declining to a minimum of -4‰ and increasing again to -1‰ directly below a second exposure surface in the lower Svanbergfjellet Formation. An increase in $\delta^{13}C$ values of +5‰ occurs

across this surface and marks the end of the Bitter Springs Anomaly here. $\delta^{13}C$ values then gradually increase to values of +5‰ to +8‰ that are maintained for > 2 km before declining to -6‰ in the upper Elbobreen Formation and into the base of diamictite deposits correlated as Sturtian in age (Hoffman et al., 2012). This decline to negative $\delta^{13}C$ values is correlated to the Islay Anomaly, and occurs directly below an exposure surface indicated by karstic dissolution and collapse. As yet, no radiometric age-dates are available from any stratigraphic level, with the pre-Sturtian interval previously interpreted as pre-Marinoan and re-interpreted based predominantly on the observation of two discrete glacial intervals.

1.6 Otavi Group, N Namibia

The $\delta^{13}C$ values in the Ombombo Subgroup show a gradual increase from +1‰ to +3‰ to as high as +8‰ over ~575 m of dominantly ribbon limestones (Halverson et al., 2005, Figure 1e). A volcanic ash at ~490 m returns a U/Pb age of 760 ± 1 Ma. The subsequent ~200 m of stratigraphy is dominated by siliciclastic deposition and is capped by a second volcanic deposit (U/Pb 746 ± 2 Ma). A further 300 m of stratigraphy lacks $\delta^{13}C$ data. The mid-Ugab Subgroup records $\delta^{13}C$ values of ~+7‰ that are sustained for ~200 m. Following a further ~75 m of siliciclastic deposition, $\delta^{13}C$ values are 0‰ to +2‰ and are separated from the base of Chuos Formation diamictites interpreted as Sturtian in age.

1.7 The Bitter Springs Anomaly

The dearth of radiometric age dates from NE Svalbard and central Australian sections means that the $\delta^{13}C$ inflection points defining the onset and end of the Bitter Springs Anomaly provide the only stratigraphic tie points available to support correlation between sections. Macdonald et al. (2010) place the onset of the Bitter Springs Anomaly at < 811 Ma based on the upper Fifteenmile Group tuff located ~75 m stratigraphically below an abrupt decline in $\delta^{13}C$ values from +5‰ to 0‰. No direct and independent age dates are available stratigraphically below the $\delta^{13}C$ decline in the Bitter Springs Formation (+7‰ to -4‰) or the upper Grusdievbreen Formation (+5‰ to -2‰). If treated as time-significant, a correlative ~811 Ma date at the base of the Loves Creek Member in the upper Bitter Springs Formation implies that ~260 Myr of time is accounted for as unconformities below this level and above the level of the Heavitree Quartzite which records a U/Pb age of 1070 Ma (Schmidt et al., 2006). The end of the Bitter Springs Anomaly is constrained by Re/Os 752.7 ± 5.5 Ma in the upper Fifteenmile Group. This age occurs ~825 m stratigraphically above the level at which $\delta^{13}C$ values begin to increase from 0‰ and is recorded above at least one major exposure surface. The maximum duration of the Bitter Springs Anomaly is therefore < 58 Myr but likely to be significantly shorter. A U/Pb date from the Ombombo Subgroup in N Namibia of 760 ± 1 Ma might further constrain the duration of the Bitter Springs Anomaly to < 51 Myr, assuming that the gradual increase in $\delta^{13}C$ observed at the base of the reference section records the post-Bitter Springs Anomaly increase in $\delta^{13}C$ values as speculated by Shields-Zhou et al. (2012).

1*.8 The Islay Anomaly*

Re/Os ages of 752.7 ± 5.5 Ma and 739.9 ± 6.5 Ma bracket the interval of negative $\delta^{13}C$ values stratigraphically below Sturtian-aged (Rapitan) glacial deposits in the lower Mount Harper Group of NW Canada (Macdonald et al., 2010; Rooney et al., 2015). A maximum age for the Islay Anomaly is provided by U/Pb at the base of the Ugab Subgroup in N Namibia of 746 ± 2 Ma, assuming that the negative excursion itself is removed by subglacial erosion and succeeded by Chuos glacial deposits at the base of the Abenab Subgroup. As no other radiometric ages are available to directly constrain the timing of negative $\delta^{13}C$ values between basins, correlation of the Islay Anomaly is largely supported by the $\delta^{13}C$ inflection point as values decline to < 0‰ that is assumed to be time significant, and stratigraphic posi-

tion of negative $\delta^{13}C$ values relative to glacial diamictite deposits. The base of the Sturtian glaciation is placed at ~717 Ma from the Upper Mount Harper Group in NW Canada (Rooney et al., 2015).

2. Uncertainties and further considerations

While recent compilations show that the resolution of radiometric age dates in the pre-Sturtian interval is increasing with a growing archive of available Re/Os ages (Macdonald et al., 2010; Rooney et al., 2015), few radiometric dates are available in the key reference sections that also establish composite $\delta^{13}C$ curves for the Neoproterozoic in general. The upper Fifteenmile Group in NW Canada appears to provide the most complete chronostratigraphic framework by which correlations may be tested as the only direct age constraints on the onset of the Bitter Springs Anomaly and Islay Anomaly are derived from this unit. Inter-basinal correlation of Neoproterozoic stratigraphic sections relies heavily on recurring $\delta^{13}C$ patterns and the placement of stratigraphic sections relative to the Sturtian or Marinoan glaciations (eg. Halverson et al., 2005; Shields-Zhou et al., 2012). It is therefore critical that changes in seawater $\delta^{13}C$ values are synchronously recorded within and between all basins that contribute to composite $\delta^{13}C$ curves. The following briefly summarises some uncertainties in this method of correlation that are raised by this study.

The carbonate platform to slope transitions recorded in the upper Andrée Land Group in the NE Greenland Caledonides that records the pre-Sturtian Islay $\delta^{13}C$ Anomaly and is discussed in Chapter 4 are particularly instructive with regard to the basinal reproducibility of $\delta^{13}C$ profiles, where two lateral sections are calibrated along physical stratigraphic boundaries and compared. This calibration relies on a pair of stratigraphic surfaces associated with 1) the fall in sea level across the carbonate ramp, recorded as a karstic collapse-brecciated interval that is sharply overlain by outer-slope mudstone deposition as the platform was drowned and 2) an abrupt transition to aeolian sandstones from outer-ramp laminated carbonates in the shoreward section (Kap Weber) that correlates to the abrupt onset of diamictite deposition in the deeper-water basinal section (Ella Ø). This framework allows for each $\delta^{13}C$ profile to be independently compared along physical time-significant surfaces such that their spatial and temporal synchroneity may be tested across the basin. These data show that across the lower sequence boundary, a step-change in both $\delta^{13}C$ values and depositional environment from +6‰ in ramp carbonates to variable $\delta^{13}C$ values of -4‰ to -10‰ in deeper-water slope mudstone deposits is recorded in both sections. However, the upper sequence boundary that marks the first diamictites of the Sturtian-aged Ulvesø Formation on Ella Ø corresponds to negative $\delta^{13}C$ values (~ -6‰) while the time-correlative aeolian transition on Kap Weber directly overlies platform carbonates that record terminal values of +8‰. The co-occurrence of $\delta^{13}C$ values that vary by > 12‰ across the basin is at odds with a homogeneous basin-wide $\delta^{13}C$ value being recorded. In this case, positive and negative $\delta^{13}C$ values are associated with two different processes that drove carbonate mineralisation in different parts the basin that are physically separated by location and water depth; precipitation and alteration of microbial and grainstone limestones and dolostones on the carbonate ramp-top and precipitation of authigenic dolomite under sulphate reducing conditions in slope-sediment pore fluids. In this example, the vertical transition from positive to negative $\delta^{13}C$ values in the Ella Ø and Kap Weber sections corresponds to the flooding of carbonate platforms and the resulting superposition of slope-facies strata carrying negative $\delta^{13}C$ values above typical platform carbonates that record $\delta^{13}C$ values of +6‰. At Kap Weber, a return to positive $\delta^{13}C$ values occurs because local water depth allowed the re-establishment of the carbonate platform while (isotopically negative) slope mudstone deposition continued on Ella Ø. Critically, the $\delta^{13}C$ inflection points that define the pre-Sturtian Islay Anomaly here are shown to be an asynchronous feature within the context of the basin and is thus not expected to correlate with other examples of the Islay Anomaly in other basins as a time significant feature.

Many individual features of composite $\delta^{13}C$ curves constructed from Neoproterozoic carbonate records are supported by only a handful of individual correlative sections. The Bitter Springs Anomaly demonstrates this paradigm well, where the interpreted global $\delta^{13}C$ excursion is established by sections in central Australia (Hill and Walter, 2000), NW Canada (Macdonald et al., 2010) and Svalbard (Halverson et al., 2007), with other possible correlatives in the Scottish Caledonides (Prave et al., 2009) and Ethiopia (Alene et al., 2006) that record only fragments of stratigraphic and coupled $\delta^{13}C$ data. The terrestrial Bitter Springs Formation is shown to be inherently ambiguous as a tracer for global $\delta^{13}C$ change as it records a series of $\delta^{13}C$ variations that correspond to local palaeoenvironmental shifts in a non-marine basin (Chapter 2), but represents one of three primary examples that ultimately establish the Bitter Springs Anomaly as a global geochemical event. If omitted, the interpretation of a carbon cycle perturbation of global influence beginning after ~811 Ma relies on just two relatively continuous $\delta^{13}C$ records that are not directly linked by independent radiometric ages and vary in magnitude by ~4‰ between some sections (Figure 1).

Sedimentary hiatuses in each contributing $\delta^{13}C$ record are difficult to constrain in the absence of robust biostratigraphic frameworks, but may have a significant influence on the continuity of seawater $\delta^{13}C$ records from Neoproterozoic strata. For example, carbonate sediments that underlie Sturtian-aged glacial deposits often do not record negative $\delta^{13}C$ values. Stratigraphically below the Areyonga Formation in central Australia and the Chuos Formation of northern Namibia minimum $\delta^{13}C$ values are +3‰ and 0‰ respectively. In examples where negative $\delta^{13}C$ values are recorded below Sturtian-aged diamictites, the shape and thickness of the excursion varies from section to section by up to 15‰ (Figure 1). The shift in $\delta^{13}C$ values towards negative values of ~-5‰ (but as low as -10‰) is either sustained into the base of overlying deposits interpreted as Sturtian in equivalence, or increase to positive $\delta^{13}C$ values of up to +8‰ before passing vertically into glaciogenic sediment. A similar situation occurs between sections that establish the pre-Marinoan Trezona Anomaly which, following the reinterpretation of negative $\delta^{13}C$ values that occur below diamictite units in NE Svalbard and NE Greenland as the pre-Sturtian Islay Anomaly (Hoffman et al., 2012), hangs on up to five correlative sections, including four that record $\delta^{13}C$ values < -4‰. In the Trezona Formation in South Australia and the Ardrishaig Formation in the Scottish Caledonides $\delta^{13}C$ values subsequently increase to -2‰ and +1‰ respectively (Prave et al., 2009), while in the upper Ombaatjie Formation in northern Namibia and Keele Formation in NW Canada $\delta^{13}C$ values remain < -4‰ into the base of overlying diamictite (Halverson et al., 2002; Johnston et al., 2012). Again, this disparity is typically explained by varying degrees of subglacial erosion, although the upper Andrée Land group of NE Greenland preserves negative $\delta^{13}C$ values that pass conformably into the base of overlying glacial diamictite (Chapter 4). In the relatively well chronologically-constrained upper Fifteenmile Group in NW Canada, a 752.7 ± 5.5 Ma age occurs stratigraphically below the onset of the Islay Anomaly. In this example, $\delta^{13}C$ values remain < -5‰ in the final carbonate beds preserved, where an age of 739.9 ± 6.5 Ma occurs stratigraphically above this level. A U/Pb date from the Mount Harper Volcanics of ~717 Ma therefore constrains a period of ~22 Myr separating negative $\delta^{13}C$ values from the base of Sturtian glacial deposits, indicating that significant sedimentary thickness has been lost to erosion or that the negative $\delta^{13}C$ excursion here is only casually related to the onset of glaciogenic sedimentation at ~717 Ma. The quantification of sedimentary hiatuses in the Neoproterozoic record is perhaps the most challenging aspect in its interpretation but is fundamental in understanding how variations in $\delta^{13}C$ values in Neoproterozoic strata constrain global changes in the carbon cycle.

As preservation in Neoproterozoic sedimentary records is inherently biased towards shallow-water deposition within intracratonic basins and on margins, this record is predicted to be particularly sensitive to periods of hydrologic restriction and decoupling $\delta^{13}C$ values in ambient waters from seawater. Isotopic decoupling

with seawater in a given basin is expected to be a product of local water depth, hydrologic connectivity and proximity to sources of terrestrial fluids, where more physically isolated conditions are predicted to yield a greater degree of decoupling of basinal fluids from seawater. Chapter 5 investigates this constraint by comparing the ranges of Cenozoic $\delta^{13}C$ values in both pelagic sediments derived from deep-sea cores and on shallow platform carbonates that preserve $\delta^{13}C$ values locally modified by evaporation, photosynthetic fractionation and mineralogical fractionation, as well as 'vital effects' in carbonate-secreting organisms. These types of shallow-marine carbonates comprise some of the closest modern analogues to the shallow subtidal to lagoonal carbonate sediments interpreted by many chemostratigraphic studies of Neoproterozoic strata (eg. Halverson et al., 2002; Halverson et al., 2007; Hoffman et al., 2012; Hoffman and Schrag, 2002; James et al., 2001; Rose et al., 2013). Positive (~+6‰) $\delta^{13}C$ values that are recorded by a significant proportion of the Neoproterozoic sedimentary record (Halverson et al., 2005; Macdonald et al., 2010) and interpreted as sustained but perturbed seawater values are shown to lie largely within the expected range of $\delta^{13}C$ variability that is recorded on Cenozoic carbonate platforms. This implies that similar controls on the isotopic composition recorded by Neoproterozoic examples (eg. hydrological restriction and evaporation) as those influencing the $\delta^{13}C$ composition of non-skeletal carbonates modern carbonate platforms, may have had a pervasive influence on the $\delta^{13}C$ ranges preserved in the Precambrian record. Similarly, negative $\delta^{13}C$ excursions have been documented in Phanerozoic systems following alteration of primary carbonate phases during diagenesis (Swart and Eberli, 2005) that are comparable in shape, magnitude and duration to similar examples that are used to establish Neoproterozoic $\delta^{13}C$ records (Swart and Kennedy, 2011), as well as in epeiric seas (Fanton and Holmden, 2007; Panchuk et al., 2005) and non-marine basins (Talbot and Kelts, 1990). A transient phase of deposition under any of these types of environments is expected to occur as a simple binary pattern in $\delta^{13}C$ records that, as there are only two directions of change possible, is not a unique stratigraphic feature and is unlikely to be time significant between isolated basins.

3. Conclusions

This study casts some doubt on the interpretation of many Neoproterozoic $\delta^{13}C$ excursions as a series of global oceanographic events. However, $\delta^{13}C$ records from Neoproterozoic strata, particularly when considered in parallel to high resolution sedimentological information, remain instructive in palaeoenvironmental interpretation. The Trezona Formation, Bitter Springs Formation and upper Andrée Land Group each show a correlation of lithofacies variations and changes in recorded $\delta^{13}C$ values, suggesting that physical constraints on deposition and the isotopic chemistry of precipitating fluids are related by common processes. In the Bitter Springs Formation and upper Andrée Land Group, a broad correlation with mineralogy is also evident where positive and negative $\delta^{13}C$ values are associated with dolomite-rich and calcite-rich sediment in the Bitter Springs Formation, and calcite-rich and dolomite-rich sediment respectively in the upper Andrée Land Group. The Trezona Formation shows that $\delta^{13}C$ values, local lithofacies associations, Mn/Sr ratios, and Fe concentrations all vary together across the facies change from its lower interbedded mudstone and limestone unit to its upper microbial and grainstone carbonate unit. As associated lithofacies are understood to result from a set of palaeoenvironmental and hydrological conditions, coupled variations in $\delta^{13}C$ values have the potential to inform about changes in local carbon-cycling processes in a given environment. In any basin where atmospheric exchange is not the overwhelmingly dominant process determining the $\delta^{13}C$ composition of ambient fluids, $\delta^{13}C$ values are instead determined by the composition of input fluids, local rates of evaporation and photosynthesis, and the degradation of organic matter. As these processes are influenced by local climatic conditions, changes in basin hydrology, and chemical conditions conducive to algal growth, variations in $\delta^{13}C$ values interpreted alongside physical sedimentological

data are capable of quantifying these effects.

Previous authors have considered the linkage between Precambrian $\delta^{13}C$ records and the biological requirements for the enrichment and depletion of $\delta^{13}C$ values in ancient carbonate sediments. The fundamental process driving the fractionation of ^{12}C from surface carbon reservoirs in the modern Earth is through the synthesis of organic matter during photosynthesis. As such, the contribution or accumulation of degraded organic carbon into a given basin is the primary driver for both water column and pore fluid $\delta^{13}C$ values to become more negative at surface or near-surface conditions. Where negative excursions in Neoproterozoic carbonate successions to values < -5‰ violate the theoretical lower limit on seawater $\delta^{13}C$ values set by mantle inputs, non-steady state changes in ambient fluid chemistry can occur in hydrologically restricted marine basins, or in non-marine environments, that are dominated by meteoric fluid processes over seawater where terrestrial organic matter is the primary source of ^{12}C-enriched carbon. This is true during the precipitation of primary carbonate mineral phases in modern non-marine environments that may be as isotopically negative as -25‰, and in the diagenetic environment through the mixing of meteoric waters and ambient pore-fluids. The expansion of a significant photosynthetic biomass in Neoproterozoic terrestrial environments following what is assumed to have been ~2.5 billion years of marine algae comprising the majority of Earth's inhabitants has been supported based on molecular (Heckman et al., 2001), mineralogical (Kennedy et al., 2006) and isotopic (Knauth and Kennedy, 2009) evidence, and represents an important step-change in the evolution and distribution of biomass across the surface environment. Neoproterozoic-aged deposits of central and South Australia are informative in this context in general, where deposition of carbonate that records negative $\delta^{13}C$ values occurred under shallow water and spatially restricted conditions within broad, flat-lying intracratonic basins. The Trezona Formation records $\delta^{13}C$ values of as low as -10‰ in its lower interval that is interpreted in this study to be a phase of lacustrine deposition (Chapter 3). Negative $\delta^{13}C$ values in restricted basinal waters typically occur in response to degraded organic matter entering the basin as particles or organic acids through groundwater systems, or in-situ degradation under hydrologically closed conditions. A non-marine interpretation of the Trezona Formation depositional environment therefore requires a significant source of organic matter either in ambient lake-waters or in sediment pore fluids to allow $\delta^{13}C$ values of -10‰ to be recorded by mineralising carbonate during lithification and diagenesis. Further, the identification of palaeokarst features associated with a fall in $\delta^{13}C$ values to -9‰ in the upper Trezona Formation (McKirdy et al., 2001) that generally records $\delta^{13}C$ values of ~-3‰ to -5‰ indicates that $\delta^{13}C$ values recorded here respond systematically with evidence for subaerial exposure and the influence of ^{13}C-depleted meteoric fluids. The Bitter Springs Formation in central Australia records a single interval of negative $\delta^{13}C$ values of -4‰ that is bracketed by positive $\delta^{13}C$ values of ~+6‰ recorded by mixed red bed, dolomite and evaporite facies. Negative $\delta^{13}C$ values in the Bitter Springs Formation are recorded exclusively by a regularly-cyclic grainstone and microbial carbonate facies that are interpreted as restricted shallow-marine deposits supported by evidence of subaerial exposure and palaeokarst at the tops of shallowing-upward cycles. $\delta^{13}C$ values of -4‰ are modest in comparison to the -10‰ values recorded by Trezona Formation lacustrine facies, potentially indicating the proportional mixing of seawater (~0‰) and ^{13}C-depleted meteoric waters that would result in less negative $\delta^{13}C$ values as meteoric fluids become increasingly dilute. The recurrence of negative $\delta^{13}C$ values and the geological context of these values within shallow intracratonic basins conducive to the influence of meteoric fluids such as in the Trezona and Bitter Springs Formations is consistent with the expansion of an extensive terrestrial biomass during the Neoproterozoic as proposed by Knauth and Kennedy (2009).

Hydrologically-isolated water bodies are capable of supporting a wide range of water chemistries and other environmental conditions such as fluid temperature

and pH that are not possible in the prohibitively large volume of the open ocean. The $\delta^{13}C$ record of Neoproterozoic carbonates may provide a powerful tool in interpreting these palaeoenvironmental conditions at a basin-scale, with implications for evolutionary events. The first appearance of several complex microfossils occurs broadly within the pre-Sturtian carbonate interval and have been calibrated to the post-Bitter Springs Anomaly interval using composite $\delta^{13}C$ records (Macdonald et al., 2010). Following a lack of examples in older stratigraphy, putative microfossil assemblages from the Tindir Group in NW Canada, Chuar Formation in the Grand Canyon, Beck Spring Formation in Death Valley, the Svanbergfjellet Formation in E Svalbard and famously the Bitter Springs Formation in central Australia (Schopf, 1968; Southgate, 1986) occur within 2 km stratigraphically below interpreted Sturtian Glacial deposits and following the Bitter Springs Anomaly, suggesting that major eukaryotic crown groups including various algal lineages, Rhizaria and Amoebozoa may have diverged during this interval of Earth history (Macdonald et al., 2010). Further, biomarkers analysed from hydrocarbons recovered from the restricted-marine interval of the Bitter Springs Formation are interpreted as lipid remains of predatory eukaryotes (Brocks 2014, pers. comm.). Further, possible examples of early sponge-grade metazoa have been documented on the Otavi Platform in Namibia (~760 Ma, Brain et al., 2012) and in the pre-Marinoan Trezona Formation in South Australia (Maloof et al., 2010). Where recent work has focussed on constraining the relative timing of evolutionary events, little recent work has been completed to characterise the palaeoenvironmental conditions associated with them. The consideration of $\delta^{13}C$ data in the context of specific depositional conditions and individual carbonate textures may be instructive in this regard, where changes in processes such as evaporation in a hydrologically restricted basin can be monitored by vertical changes in $\delta^{13}C$ values. More generally, many examples of preserved microfossil assemblages are preserved in carbonate sediment that also records positive $\delta^{13}C$ values up to +8‰ and as low as -4‰, possibly indicating periods of hydrologic restriction and periodic isolation from seawater (Chapter 5). Isolated basins are capable of hosting large ranges of fluid temperatures, pH, nutrient composition and concentrations, water depths and available oxidants that are unique to a given basin depending on input/output water composition, climate, basin morphology, sediment supply and volume of local biomass. Perhaps the environmental extremes that these types of environments are capable of supporting, relative to seawater, provided the impetus for biologic innovation during the Neoproterozoic. If so, high resolution $\delta^{13}C$ records coupled with robust sedimentological interpretation may provide an important tool in quantifying these conditions.

References

Alene, M., Jenkin, G. R. T., Leng, M. J., and Darbyshire, D. P. F., 2006, The Tambien Group, Ethiopia: An early Cryogenian (ca. 800-735 Ma) Neoproterozoic sequence in the Arabian-Nubian Shield: Precambrian Research, v. 147, no. 1-2, p. 79-99.

Brain, C. K., Prave, A. R., Hoffmann, K. H., Fallick, A. E., Botha, A., Herd, D. A., Sturrock, C., Young, I., Condon, D. J., and Allison, S. G., 2012, The first animals: ca. 760-million-year-old sponge-like fossils from Namibia: South African Journal of Science, v. 108, no. 1-2, p. 83-90.

Fairchild, I. J., Spiro, B., and Herrington, P. M., 2000, Controls on Sr and C isotope compositions of Neoproterozoic Sr-rich limestones of East Greenland and North China, in Grotzinger, J. P., and James, N. P., eds., Carbonate Sedimentation and Diagenesis in the Evolving Precambrian World, Volume 67, p. 297-313.

Fanton, K. C., and Holmden, C., 2007, Sea-level forcing of carbon isotope excursions in epeiric seas: implications for chemostratigraphy: Canadian Journal of Earth Sciences, v. 44, no. 6, p. 807-818.

Halverson, G. P., Hoffman, P. F., Schrag, D. P., and Kaufman, A. J., 2002, A major perturbation of the carbon cycle before the Ghaub glaciation (Neoproterozoic) in Namibia: Prelude to snowball Earth?: Geochemistry Geophysics Geosystems, v. 3, no. 6, p. 1-24.

Halverson, G. P., Hoffman, P. F., Schrag, D. P., Maloof, A. C., and Rice, A. H. N., 2005, Toward a Neoproterozoic composite carbon-isotope record: Geological Society of America Bulletin, v. 117, no. 9-10, p. 1181-1207.

Halverson, G. P., Maloof, A. C., Schrag, D. P., Dudas, F. O., and Hurtgen, M., 2007, Stratigraphy and geochemistry of a ca 800 Ma negative carbon isotope interval in northeastern Svalbard: Chemical Geology, v. 237, no. 1-2, p. 5-27.

Heckman, D. S., Geiser, D. M., Eidell, B. R., Stauffer, R. L., Kardos, N. L., and Hedges, S. B., 2001, Molecular evidence for the early colonization of land by fungi and plants: Science, v. 293, no. 5532, p. 1129-1133.

Hill, A. C., and Walter, M. R., 2000, Mid-Neoproterozoic (similar to 830-750 Ma) isotope stratigraphy of Australia and global correlation: Precambrian Research, v. 100, no. 1-3, p. 181-211.

Hoffman, P. F., Halverson, G. P., Domack, E. W., Maloof, A. C., Swanson-Hysell, N. L., and Cox, G. M., 2012, Cryogenian glaciations on the southern tropical paleomargin of Laurentia (NE Svalbard and East Greenland), and a primary origin for the upper Russøya (Islay) carbon isotope excursion: Precambrian Research, v. 206-207, p. 137-158.

Hoffman, P. F., and Schrag, D. P., 2002, The snowball Earth hypothesis: testing the limits of global change: Terra nova, v. 14, no. 3, p. 129-155.

Hoffmann, K., and Prave, A., 1996, A preliminary note on a revised subdivision and regional correlation of the Otavi Group based on glaciogenic diamictites and associated cap dolostones: Communications of the Geological Survey of Namibia, v. 11, p. 77-82.

James, N. P., Narbonne, G. M., and Kyser, T. K., 2001, Late Neoproterozoic cap carbonates: Mackenzie Mountains, northwestern Canada: precipitation and global glacial meltdown: Canadian Journal of Earth Sciences, v. 38, no. 8, p. 1229-1262.

Johnston, D. T., Macdonald, F. A., Gill, B. C., Hoffman, P. F., and Schrag, D. P., 2012, Uncovering the Neoproterozoic carbon cycle: Nature, v. 483, no. 7389, p. 320-323.

Kendall, B., Creaser, R. A., and Selby, D., 2006, Re-Os geochronology of postglacial black shales in Australia: Constraints on the timing of "Sturtian" glaciation: Geology, v. 34, no. 9, p. 729-732.

Kennedy, M., Droser, M., Mayer, L. M., Pevear, D., and Mrofka, D., 2006, Late Precambrian oxygenation; Inception of the clay mineral factory: Science, v. 311, no. 5766, p. 1446-1449.

Knauth, L. P., and Kennedy, M. J., 2009, The late Precambrian greening of the Earth: Nature, v. 460, no. 7256, p. 728-732.

Macdonald, F., and Roots, C., 2009, Upper Fifteenmile Group in the Ogilvie Mountains and correlations of early Neoproterozoic strata in the northern Cordillera: Yukon Exploration and Geology, p. 237-252.

Macdonald, F. A., Schmitz, M. D., Crowley, J. L., Roots, C. F., Jones, D. S., Maloof, A. C., Strauss, J. V., Cohen, P. A., Johnston, D. T., and Schrag, D. P., 2010, Calibrating the Cryogenian: Science, v. 327, no. 5970, p. 1241-1243.

Maloof, A. C., Rose, C. V., Beach, R., Samuels, B. M., Calmet, C. C., Erwin, D. H., Poirier, G. R., Yao, N., and Simons, F. J., 2010, Possible animal-body fossils in pre-Marinoan limestones from South Australia: Nature Geoscience, v. 3, no. 9, p. 653-659.

McKirdy, D. M., Burgess, J. M., Lemon, N. M., Yu, X. K., Cooper, A. M., Gostin, V. A., Jenkins, R. J. F., and Both, R. A., 2001, A chemostratigraphic overview of the late Cryogenian interglacial sequence in the Adelaide Fold-Thrust Belt, South Australia: Precambrian Research, v. 106, no. 1-2, p. 149-186.

Panchuk, K. M., Holmden, C., and Kump, L. R., 2005, Sensitivity of the epeiric sea carbon isotope record to local-scale carbon cycle processes: Tales from the Mohawkian Sea: Palaeogeography Palaeoclimatology Palaeoecology, v. 228, no. 3-4, p. 320-337.

Prave, A., Fallick, A., Thomas, C., and Graham, C., 2009, A composite C-isotope profile for the Neoproterozoic Dalradian Supergroup of Scotland and Ireland: Journal

of the Geological Society, v. 166, no. 5, p. 845-857.

Rooney, A. D., Strauss, J. V., Brandon, A. D., and Macdonald, F. A., 2015, A Cryogenian chronology: Two long-lasting synchronous Neoproterozoic glaciations: Geology, v. 43, no. 5, p. 459-462.

Rose, C. V., Maloof, A. C., Schoene, B., Ewing, R. C., Linnemann, U., Hofmann, M., and Cottle, J. M., 2013, The End-Cryogenian Glaciation of South Australia: Geoscience Canada, v. 40, no. 4, p. 256–293.

Schmidt, P. W., Williams, G. E., Camacho, A., and Lee, J. K., 2006, Assembly of Proterozoic Australia: implications of a revised pole for the~ 1070 Ma Alcurra Dyke Swarm, central Australia: Geophysical Journal International, v. 167, no. 2, p. 626-634.

Schopf, J. W., 1968, Microflora of the bitter springs formation, late Precambrian, central Australia: Journal of Paleontology, p. 651-688.

Shields-Zhou, G., Hill, A., and Macgabhann, B., 2012, The Cryogenian Period, The Geologic Time Scale, Elsevier.

Southgate, P. N., 1986, Depositional environment and mechanism of preservation of microfossils, upper Proterozoic Bitter Springs Formation, Australia: Geology, v. 14, no. 8, p. 683-686.

Swanson-Hysell, N. L., Rose, C. V., Calmet, C. C., Halverson, G. P., Hurtgen, M. T., and Maloof, A. C., 2010, Cryogenian Glaciation and the Onset of Carbon-Isotope Decoupling: Science, v. 328, no. 5978, p. 608-611.

Swart, P. K., and Eberli, G., 2005, The nature of the $\delta^{13}C$ of periplatform sediments: Implications for stratigraphy and the global carbon cycle: Sedimentary Geology, v. 175, no. 1-4, p. 115-129.

Swart, P. K., and Kennedy, M. J., 2011, Does the Global Stratigraphic Reproducibility of $\delta^{13}C$ in Neoproterozoic Carbonates Require a Marine Origin? A Plio-Pleistocene Comparison: Geology, v. 40, no. 1, p. 87-90..

Talbot, M. R., and Kelts, K., 1990, Paleolimnological signatures from carbon and oxygen isotopic-ratios in carbonates from organic carbon-rich lacustrine sediments, Lacustrine Basin Exploration: Case Studies and Modern Analogs, p. 99-112.

Supplementary Appendices

Appendix 1. Detailed analytical methods

Sample collection

Stratigraphic logs were measured in the field using the standard 'Jacob's Staff' procedure detailed in Compton (1985). 1886 new carbonate and mixed carbonate and siliciclastic samples were collected during stratigraphic logging in the field or examination of drill core material, supplemented by 273 archived samples. In each study, representative samples of all lithofacies were collected in order to quantify any systematic relationships between lithology, mineralogy and geochemistry. Clean limestones were also sampled stratigraphically at variable vertical spacing (1 m – 5 m) to constrain broad stratigraphic trends. Samples to be analysed were cleaned and/or slabbed, with representative samples polished for visual inspection of coarse carbonate phases.

Petrographic analysis

Approximately 130 thin sections were produced to characterise carbonate phases present in representative samples across all sample sets. Select thin sections were treated using standard carbonate staining procedures after the method of Dickson (1966) in order to assess mineralogical variation within individual samples.

1) Two staining solutions were prepared: a) 0.2 g Alizarin Red dissolved in 100 ml of 1.5% HCl, and b) 0.2 g Potassium Ferricyanide dissolved in 100 ml of 1.5% HCl.

2) The above staining solutions were mixed in a 3:2 ration of Alizarin Red and Potassium Ferricyanide respectively

3) Half of each polished thin section was submerged in 1.5% HCl for 15 seconds, then rinsed with deionised water

4) The etched half of each thin section was then submerged in the mixed stain solution for 30 seconds and then rinsed with deionised water

Differentiation of mineralogy was made based on the colour of each carbonate phase following staining:

Carbonate	Treated sample colour
Calcite	Pink
Ferroan Calcite	Purple – blue
Dolomite	None
Ferroan Dolomite	Turquoise
Siderite	None
Magnesite	None

Stable C and O isotope analyses

Powdered sub-samples were collected from clean rock surfaces using a dentist drill. Targeted micro-sampling was conducted on individual carbonate textures, grains and horizons in order to isotopically characterise each discrete carbonate phase and assess the geochemical homogeneity of samples. ~300 mg of powder was collected from each sample where possible. New stable isotope ($\delta^{13}C$ and $\delta^{18}O$) measurements were performed on collected powders at the University of Adelaide and University of Melbourne.

University of Adelaide

~0.8 mg powdered samples were dried in an oven and purged in individual glass reaction vessels. 105% phosphoric acid was manually injected into each sample where CO_2 gas was evolved at 70°C. New stable isotope ($\delta^{13}C$ and $\delta^{18}O$) measurements were performed on evolved CO_2 using continuous-flow isotope-ratio mass spectrometry on a Nu Horizon CF-IRMS (mean analytical precision for $\delta^{13}C$ and $\delta^{18}O$ is ± 0.1‰) following the standard method of Spötl and Vennemann (2003). Re-

sults were normalized to the Vienna Pee Dee Belemnite scale using internal working standards (ANU-P3, UAC-1, CO-8).

University of Melbourne

~0.8 mg powdered samples were dried in an oven and purged in individual glass reaction vessels. 105% phosphoric acid was manually injected into each sample where CO_2 gas was evolved at 70°C. New stable isotope ($\delta^{13}C$ and $\delta^{18}O$) measurements were performed on evolved CO_2 using continuous-flow isotope-ratio mass spectrometry on a AP2003 (mean analytical precision for $\delta^{13}C$ and $\delta^{18}O$ is ± 0.03‰ and ± 0.07‰ respectively) following the standard method of Spötl and Vennemann (2003). Results were normalized to the Vienna Pee Dee Belemnite scale using internal working standards of Carrara Marble (NEW1 – Newcastle), which were cross-checked against the international standards NBS18 and NBS19.

Elemental Mapping

44 rock-chip samples were mounted on SEM stops and polished for SEM analysis on a Fischione SEM Argon Ion Mill at Adelaide Microscopy. Samples were carbon coated and imaged using secondary electron and backscatter electron settings on a Phillips XL30 FEGSEM with EDS attachment and a Jeol JCM-6000 NeoScope Benchtop SEM with EDS attachment. Elemental maps were produced to constrain mineral distribution in fine grained samples.

References

Dickson, J., 1966, Carbonate identification and genesis as revealed by staining: Journal of Sedimentary Research, v. 36, no. 2.

Spötl, C., and Vennemann, T. W., 2003, Continuous-flow isotope ratio mass spectrometric analysis of carbonate minerals: Rapid communications in mass spectrometry, v. 17, no. 9, p. 1004-1006.

Appendix 2. Field locations

Section Name	Subsection	Formation	Sector	Northing	Easting	Type
Trezona Formation						
Trezona Range		Trezona Formation	54J	6538685	278375	Field section
Trezona Range - North		Trezona Formation	54J	6540436	276998	Field section
Trezona Range - South		Trezona Formation	54J	6536007	278394	Field section
Bulls Gap		Trezona Formation	54J	6541366	276474	Field section
Angorichina Station		Trezona Formation	54J	6559767	284716	Field section
Bunkers Range		Trezona Formation	54J	6529910	299532	Field section
Glass Gorge - North		Trezona Formation	54J	6564091	264564	Field section
Glass Gorge - South		Trezona Formation	54J	6562771	265101	Field section
Chambers Gorge		Trezona Formation	54J	6573214	330249	Field section
Warraweena		Trezona Formation	54J	6589282	273074	Field section
Umberatana		Trezona Formation	54J	6652458	319699	Field section
Punch Rest		Trezona Formation	54J	6643867	264934	Field section
Bitter Springs Formation						
Wallara-1		Bitter Springs Formation	53J	7275045	230659	Drill core
BR05DD01		Bitter Springs Formation	52J	7294620	640126	Drill core
Ellery Creek		Bitter Springs Formation	53K	7368440	303446	Field Section
Ross River		Bitter Springs Formation	53K	7392269	446471	Field Section
Andrée Land Group*						
Kap Oswald	RK060812	Bed group 18	26X	8088019	561429	Field Section
Kap Oswald	RK070812	Bed group 18	26X	8087931	561445	Field Section
Kap Oswald	RK080812	Bed group 18	26X	8087585	561286	Field Section
Kap Oswald	RK210812	Bed group 18	26X	8088205	561643	Field Section
Storeelv	RK100812	Bed group 19	-	-	-	Field Section
Storeelv	RK110812	Bed group 19	26X	8086952	561799	Field Section
Kløftelv	RK120812	Bed group 19	26X	8087417	562608	Field Section
Kløftelv	RK160812	Bed group 19	26X	8087542	562549	Field Section
Kløftelv	RK180812	Bed group 19	-	-	-	Field Section
Tømmerbugt	RK140812	Bed group 19	26X	8087188	560647	Field Section

*Collected as a series of sub-sections and used to construct composite in Figure 1, Chapter 4

Appendix 3.1 Bitter Springs Formation stable isotope data from drillcore

Drillhole	Member	Sample No.	Core Depth (m)	$\delta^{13}C_{carb}$	$\delta^{18}O_{carb}$	Lithology
BR05DD01	Johnnys Creek	11J.020	569.70	7.41	-4.13	Laminite
BR05DD01	Johnnys Creek	11J.021	573.06	6.37	-4.82	Laminite
BR05DD01	Johnnys Creek	11J	586.00	5.22	-5.08	Dolomicrosparite
BR05DD01	Johnnys Creek	11J	586.00	5.20	-5.24	Dolomicrosparite
BR05DD01	Johnnys Creek	11J.022	591.89	5.01	-3.29	Laminite
BR05DD01	Johnnys Creek	11J.024	609.95	5.27	-4.76	Laminite
BR05DD01	Johnnys Creek	11J.025	611.40	5.63	-3.88	Laminite
BR05DD01	Johnnys Creek	11J.026	621.19	5.15	-3.46	Red Bed
BR05DD01	Johnnys Creek	11J.027	638.65	7.58	-2.37	Grainstone
BR05DD01	Johnnys Creek	11J.028	641.53	4.74	-2.29	Red Bed
BR05DD01	Johnnys Creek	11J.029	668.70	4.74	-2.85	Laminated Limestone
BR05DD01	Johnnys Creek	11J.030	674.70	4.42	-2.23	Red Bed
BR05DD01	Johnnys Creek	11J.031	684.60	3.27	-5.27	Laminated Limestone
BR05DD01	Johnnys Creek	11J	692.00	4.08	-5.86	Dolomicrosparite
BR05DD01	Johnnys Creek	11J.033	703.80	4.66	-3.53	Microsparite
BR05DD01	Johnnys Creek	11J.034	709.92	4.41	-6.00	Laminated Limestone
BR05DD01	Johnnys Creek	11J.035	719.36	4.46	-3.44	Microsparite
BR05DD01	Johnnys Creek	11J.036	740.49	6.02	-6.16	Laminated Limestone
BR05DD01	Johnnys Creek	11J.037	759.45	5.57	-5.36	Grainstone
BR05DD01	Johnnys Creek	11J.038	762.11	5.51	-5.28	Grainstone
BR05DD01	Johnnys Creek	11J	765.00	5.88	-5.51	Grainstone
BR05DD01	Johnnys Creek	11J.039	765.36	5.56	-5.33	Grainstone
BR05DD01	Johnnys Creek	11J.041	785.44	5.14	-5.40	Laminated Limestone
BR05DD01	Johnnys Creek	11J	802.00	5.91	-6.35	Grainstone
BR05DD01	Johnnys Creek	11J	828.00	3.80	-4.52	Dolomicrosparite
BR05DD01	Johnnys Creek	11J	842.00	5.44	-6.38	Grainstone
BR05DD01	Johnnys Creek	11J.044	857.73	0.70	-13.26	Laminite
BR05DD01	Johnnys Creek	11J.045	864.36	6.17	-7.26	Laminite
BR05DD01	Johnnys Creek	11J	873.00	3.33	-4.57	Grainstone
BR05DD01	Johnnys Creek	11J.046	877.25	5.39	-6.77	Laminite
BR05DD01	Johnnys Creek	11J	884.00	4.92	-9.23	Dolomicrosparite
BR05DD01	Johnnys Creek	11J	892.00	5.94	-8.31	Microsparite
BR05DD01	Johnnys Creek	11J.047	892.21	5.89	-8.41	Laminite
BR05DD01	Johnnys Creek	11J.048	903.04	5.97	-5.17	Microsparite
BR05DD01	Johnnys Creek	11J	912.00	4.15	-6.50	Laminite
BR05DD01	Johnnys Creek	11J	914.00	5.91	-6.53	Dolomicrosparite
BR05DD01	Johnnys Creek	11J.049	923.91	2.90	-6.99	Dolomicrosparite
BR05DD01	Johnnys Creek	11J	924.00	4.69	-6.65	Laminated Limestone
BR05DD01	Johnnys Creek	11J	931.00	4.56	-7.84	Dolomicrosparite
BR05DD01	Johnnys Creek	11J	956.00	4.79	-7.05	Dolomicrosparite
BR05DD01	Johnnys Creek	11J	959.00	4.26	-7.44	Mudflake Conglomerate
BR05DD01	Johnnys Creek	11J.051	959.43	4.27	-7.63	Laminated Limestone
BR05DD01	Johnnys Creek	11J	1041.00	3.72	-7.98	Red Bed
BR05DD01	Johnnys Creek	RK220513.125	1044.95	3.78	-8.22	Red Bed
BR05DD01	Johnnys Creek	RK220513.122	1045.62	4.26	-7.26	Red Bed
BR05DD01	Johnnys Creek	RK220513.120	1046.49	4.44	-10.88	Red Bed
BR05DD01	Johnnys Creek	RK220513.117	1047.40	4.60	-6.96	Red Bed
BR05DD01	Johnnys Creek	RK220513.115	1047.95	3.95	-9.49	Red Bed

Drillhole	Member	Sample No.	Core Depth (m)	$\delta^{13}C_{carb}$	$\delta^{18}O_{carb}$	Lithology
BR05DD01	Johnnys Creek	RK220513.110	1049.39	4.53	-4.61	Red Bed
BR05DD01	Johnnys Creek	RK220513.108	1050.01	4.34	-3.99	Red Bed
BR05DD01	Johnnys Creek	RK220513.106	1050.72	4.42	-3.67	Red Bed
BR05DD01	Johnnys Creek	RK220513.105	1050.98	4.62	-3.67	Red Bed
BR05DD01	Johnnys Creek	RK220513.104	1051.24	4.97	-3.43	Red Bed
BR05DD01	Johnnys Creek	RK220513.101	1052.16	4.07	-4.99	Red Bed
BR05DD01	Johnnys Creek	RK220513.99	1052.90	4.78	-3.52	Red Bed
BR05DD01	Johnnys Creek	RK220513.96	1053.76	5.38	-3.36	Red Bed
BR05DD01	Johnnys Creek	RK220513.92	1054.75	3.94	-3.67	Red Bed
BR05DD01	Johnnys Creek	RK220513.91	1055.18	3.76	-4.24	Red Bed
BR05DD01	Johnnys Creek	RK220513.88	1056.09	4.05	-3.86	Red Bed
BR05DD01	Johnnys Creek	RK220513.86	1056.84	3.39	-4.83	Red Bed
BR05DD01	Johnnys Creek	11J	1057.00	1.47	-6.36	Red Bed
BR05DD01	Johnnys Creek	RK220513.84	1057.35	1.42	-5.69	Red Bed
BR05DD01	Johnnys Creek	RK220513.82	1057.90	1.55	-5.41	Red Bed
BR05DD01	Johnnys Creek	RK220513.80	1058.30	1.55	-6.45	Red Bed
BR05DD01	Johnnys Creek	RK220513.78	1059.02	1.46	-5.10	Red Bed
BR05DD01	Johnnys Creek	RK220513.76	1059.85	0.61	-5.86	Red Bed
BR05DD01	Johnnys Creek	RK220513.74	1060.40	1.03	-5.37	Red Bed
BR05DD01	Johnnys Creek	RK220513.72	1060.91	0.32	-6.27	Red Bed
BR05DD01	Johnnys Creek	RK220513.70	1061.58	0.35	-5.44	Red Bed
BR05DD01	Johnnys Creek	RK220513.66	1062.36	0.74	-5.19	Red Bed
BR05DD01	Johnnys Creek	RK220513.64	1063.02	0.34	-5.33	Red Bed
BR05DD01	Johnnys Creek	RK220513.62	1063.50	1.13	-4.73	Red Bed
BR05DD01	Johnnys Creek	RK220513.61	1064.00	1.07	-4.78	Red Bed
BR05DD01	Johnnys Creek	RK220513.59	1064.30	0.92	-4.96	Red Bed
BR05DD01	Johnnys Creek	RK220513.57	1065.01	1.16	-4.76	Red Bed
BR05DD01	Johnnys Creek	RK220513.56	1065.47	0.23	-5.51	Red Bed
BR05DD01	Johnnys Creek	RK220513.54	1066.00	0.85	-5.36	Red Bed
BR05DD01	Johnnys Creek	RK220513.53	1066.45	1.01	-5.66	Red Bed
BR05DD01	Johnnys Creek	RK220513.52	1066.70	0.54	-5.44	Red Bed
BR05DD01	Johnnys Creek	RK220513.49	1067.65	0.30	-5.26	Red Bed
BR05DD01	Johnnys Creek	RK220513.48	1067.90	0.14	-5.32	Red Bed
BR05DD01	Johnnys Creek	11J	1068.00	0.21	-6.64	Red Bed
BR05DD01	Johnnys Creek	11J	1068.00	0.23	-6.48	Red Bed
BR05DD01	Johnnys Creek	RK220513.47	1068.03	0.45	-5.08	Red Bed
BR05DD01	Johnnys Creek	RK220513.46	1068.30	0.21	-5.33	Red Bed
BR05DD01	Johnnys Creek	RK220513.33	1068.50	0.10	-5.33	Red Bed
BR05DD01	Loves Creek	RK220513.44	1069.10	-0.86	-5.50	Dolomicrosparite
BR05DD01	Loves Creek	RK220513.30	1069.50	-1.18	-5.75	Dolomicrosparite
BR05DD01	Loves Creek	RK220513.43	1069.85	-1.42	-5.88	Laminite
BR05DD01	Loves Creek	11J.056	1069.98	-2.06	-6.08	Dolomicrosparite
BR05DD01	Loves Creek	11J	1070.00	-1.15	-8.18	Dolomicrosparite
BR05DD01	Loves Creek	RK220513.42	1070.04	-2.24	-5.78	Dolomicrosparite
BR05DD01	Loves Creek	RK220513.41	1070.36	-1.99	-5.82	Dolomicrosparite
BR05DD01	Loves Creek	RK220513.40	1070.48	-1.91	-5.98	Dolomicrosparite
BR05DD01	Loves Creek	RK220513.39	1070.68	-1.56	-5.76	Stromatolite
BR05DD01	Loves Creek	RK220513.38	1070.78	-1.29	-6.05	Stromatolite

Drillhole	Member	Sample No.	Core Depth (m)	$\delta^{13}C_{carb}$	$\delta^{18}O_{carb}$	Lithology
BR05DD01	Loves Creek	RK220513.23	1071.60	-0.50	-5.75	Microsparite
BR05DD01	Loves Creek	RK220513.20	1072.55	-1.01	-5.58	Laminite
BR05DD01	Loves Creek	RK220513.19	1073.80	-2.00	-8.11	Stromatolite
BR05DD01	Loves Creek	RK220513.17	1074.45	-1.07	-7.72	Dolomicrosparite
BR05DD01	Loves Creek	RK220513.15	1075.20	-1.57	-6.98	Dolomicrosparite
BR05DD01	Loves Creek	RK220513.12	1076.00	-1.58	-7.22	Dolomicrosparite
BR05DD01	Loves Creek	11J	1077.00	-0.77	-7.95	Grainstone
BR05DD01	Loves Creek	RK220513.29	1077.10	-0.88	-6.90	Grainstone
BR05DD01	Loves Creek	RK220513.26	1079.45	-0.83	-5.77	Laminite
BR05DD01	Loves Creek	RK220513.27	1080.35	-1.06	-5.74	Dolomicrosparite
BR05DD01	Loves Creek	RK220513.10	1081.30	-2.48	-6.98	Grainstone
BR05DD01	Loves Creek	RK220513.8	1082.25	-1.25	-6.11	Grainstone
BR05DD01	Loves Creek	RK220513.6	1083.20	-3.18	-6.96	Microsparite
BR05DD01	Loves Creek	11J.057	1083.54	-3.76	-7.76	Laminated Limestone
BR05DD01	Loves Creek	RK220513.4	1084.35	-2.29	-6.52	Grainstone
BR05DD01	Loves Creek	RK220513.1	1085.70	-2.03	-6.74	Stromatolite
BR05DD01	Loves Creek	11J	1091.00	-3.61	-7.36	Laminated Limestone
BR05DD01	Loves Creek	11J	1096.00	-3.64	-7.71	Mudflake Conglomerate
BR05DD01	Loves Creek	11J.058	1106.69	-2.50	-6.65	Laminated Limestone
BR05DD01	Loves Creek	11J	1108.00	-1.80	-6.07	Dolomicrosparite
BR05DD01	Loves Creek	11J	1108.00	-1.70	-5.75	Dolomicrosparite
BR05DD01	Loves Creek	11J	1119.00	-3.68	-8.54	Grainstone
BR05DD01	Loves Creek	11J	1132.00	-3.27	-6.17	Grainstone
BR05DD01	Loves Creek	11J	1132.00	-3.24	-6.44	Grainstone
BR05DD01	Loves Creek	11J	1140.00	-2.79	-6.49	Dolomicrosparite
BR05DD01	Loves Creek	11J	1154.00	-3.03	-6.80	Dolomicrosparite
BR05DD01	Loves Creek	11J	1160.00	-3.95	-9.05	Dolomicrosparite
BR05DD01	Loves Creek	11J	1165.00	-3.39	-9.00	Dolomicrosparite
BR05DD01	Loves Creek	11J	1170.00	-2.72	-6.74	Dolomicrosparite
BR05DD01	Loves Creek	11J	1184.00	-3.09	-7.33	Dolomicrosparite
BR05DD01	Loves Creek	11J.061	1184.38	-3.03	-7.20	Grainstone
BR05DD01	Loves Creek	11J	1203.00	-3.08	-7.46	Grainstone
BR05DD01	Loves Creek	11J.062	1204.28	-3.12	-7.75	Laminite
BR05DD01	Loves Creek	11J	1218.00	-2.74	-9.15	Laminite
BR05DD01	Loves Creek	11J.063	1224.69	-2.12	-7.48	Microsparite
Wallara-1	Loves Creek	RK280513.1	1967.50	1.54	-6.33	Grainstone
Wallara-1	Loves Creek	RK280513.3	1965.00	0.31	-5.08	Grainstone
Wallara-1	Loves Creek	RK280513.5	1962.90	0.86	-3.46	Grainstone
Wallara-1	Loves Creek	RK280513.7	1961.30	1.44	-4.34	Grainstone
Wallara-1	Loves Creek	RK280513.9	1959.10	1.93	-3.16	Grainstone
Wallara-1	Loves Creek	RK280513.11	1957.80	2.00	-4.72	Grainstone
Wallara-1	Loves Creek	RK280513.14	1956.45	2.59	-3.40	Microsparite
Wallara-1	Loves Creek	RK280513.20	1953.52	3.94	-4.30	Microsparite
Wallara-1	Loves Creek	RK280513.21	1952.90	4.96	-3.94	Microsparite
Wallara-1	Loves Creek	RK280513.22	1952.30	5.01	-3.94	Microsparite
Wallara-1	Loves Creek	RK280513.25	1951.65	4.63	-4.49	Microsparite
Wallara-1	Loves Creek	RK280513.26	1951.30	4.48	-4.78	Grainstone
Wallara-1	Loves Creek	RK280513.27	1950.60	4.43	-5.09	Laminite

Drillhole	Member	Sample No.	Core Depth (m)	$\delta^{13}C_{carb}$	$\delta^{18}O_{carb}$	Lithology
Wallara-1	Loves Creek	RK280513.29	1949.58	4.19	-3.91	Microsparite
Wallara-1	Loves Creek	RK280513.30	1949.10	5.10	-3.62	Grainstone
Wallara-1	Loves Creek	RK280513.31	1948.95	5.18	-3.39	Red Bed
Wallara-1	Loves Creek	RK280513.32	1948.60	5.85	-2.39	Red Bed
Wallara-1	Loves Creek	RK280513.32*	1948.60	5.86	-2.37	Red Bed
Wallara-1	Loves Creek	RK280513.33	1948.26	6.19	-2.71	Dolomicrosparite
Wallara-1	Loves Creek	RK280513.34	1948.03	6.44	-2.73	Red Bed
Wallara-1	Loves Creek	RK280513.35	1947.84	6.63	-2.26	Dolomicrosparite
Wallara-1	Loves Creek	RK280513.37	1947.50	6.72	-2.88	Conglomerate
Wallara-1	Loves Creek	RK280513.39	1946.75	7.10	-2.96	Laminite
Wallara-1	Loves Creek	RK280513.40	1946.10	6.14	-6.93	Stromatolite
Wallara-1	Loves Creek	RK280513.41	1945.70	5.71	-6.03	Laminite
Wallara-1	Loves Creek	RK280513.43	1945.00	5.25	-1.42	Red Bed
Wallara-1	Loves Creek	RK280513.44	1944.40	4.16	-2.60	Red Bed
Wallara-1	Loves Creek	RK280513.45	1943.50	5.07	-1.76	Red Bed
Wallara-1	Loves Creek	RK280513.47	1942.96	4.77	-2.67	Red Bed
Wallara-1	Loves Creek	RK280513.49	1942.00	5.21	-2.06	Red Bed
Wallara-1	Loves Creek	RK280513.51	1941.25	4.40	-3.16	Red Bed
Wallara-1	Loves Creek	RK280513.52	1940.50	4.78	-3.19	Red Bed
Wallara-1	Loves Creek	RK280513.54	1939.30	4.46	-2.98	Red Bed
Wallara-1	Loves Creek	RK280513.56	1938.47	4.61	-3.49	Red Bed
Wallara-1	Loves Creek	RK280513.59	1937.83	2.88	-5.80	Dolomicrosparite
Wallara-1	Loves Creek	RK280513.62	1937.23	1.51	-5.84	Laminite
Wallara-1	Loves Creek	RK280513.64	1936.65	1.34	-6.28	Laminite
Wallara-1	Loves Creek	RK280513.64*	1936.65	1.30	-6.27	Laminite
Wallara-1	Loves Creek	RK280513.66	1935.60	1.31	-5.70	Dolomicrosparite
Wallara-1	Loves Creek	RK280513.68	1934.70	0.72	-5.95	Conglomerate
Wallara-1	Loves Creek	RK280513.70	1933.75	0.34	-5.99	Microsparite
Wallara-1	Loves Creek	RK280513.72	1932.80	-0.15	-6.09	Microsparite
Wallara-1	Loves Creek	RK280513.75	1931.82	-0.52	-6.10	Grainstone
Wallara-1	Loves Creek	RK280513.78	1930.40	-1.21	-6.56	Microsparite
Wallara-1	Loves Creek	RK280513.79	1929.40	-1.97	-7.42	Microsparite

*= repeat analysis

Appendix 3.2 Bitter Springs Formation stable isotope data from field locations

Location	Member	Sample No.	Height (m)	$\delta^{13}C_{carb}$	$\delta^{18}O_{carb}$	Lithology
Ellery Creek	Loves Creek	RK250514.29	0.50	-0.07	-	Stromatolite
Ellery Creek	Johnnys Creek	RK250514.31A	5.00	4.03	-	Dolomicrosparite
Ellery Creek	Johnnys Creek	RK250514.31B	5.00	5.18	-	Dolomicrosparite
Ellery Creek	Johnnys Creek	RK250514.32	13.00	3.41	-	Stromatolite
Ellery Creek	Johnnys Creek	RK250514.33	14.30	4.32	-	Stromatolite
Ellery Creek	Johnnys Creek	RK250514.34	21.30	3.14	-	Red Bed
Ellery Creek	Johnnys Creek	RK250514.35	22.00	2.30	-	Red Bed
Ellery Creek	Johnnys Creek	RK250514.37	42.10	5.17	-	Red Bed
Ellery Creek	Johnnys Creek	RK250514.38	43.20	5.32	-	Red Bed
Ellery Creek	Johnnys Creek	RK250514.40	47.80	5.20	-	Red Bed
Ellery Creek	Johnnys Creek	RK250514.41	54.80	4.92	-	Red Bed
Ellery Creek	Johnnys Creek	RK250514.45	63.50	4.35	-	Red Bed
Ellery Creek	Johnnys Creek	RK250514.46	68.00	4.32	-	Stromatolite
Ellery Creek	Johnnys Creek	RK250514.48	71.10	1.89	-	Stromatolite
Ellery Creek	Johnnys Creek	RK250514.49	74.20	1.25	-	Stromatolite
Ellery Creek	Johnnys Creek	RK250514.51	79.00	3.53	-	Dolomicrosparite
Ellery Creek	Johnnys Creek	RK250514.53	86.20	4.75	-	Red Bed
Ellery Creek	Johnnys Creek	RK250514.54	89.10	5.06	-	Red Bed
Ellery Creek	Johnnys Creek	RK250514.55	94.00	5.05	-	Red Bed
Ellery Creek	Johnnys Creek	RK250514.56	99.00	4.43	-	Red Bed
Ellery Creek	Johnnys Creek	RK250514.57	108.00	3.52	-	Red Bed
Ellery Creek	Johnnys Creek	RK250514.58	110.25	3.93	-	Red Bed
Ellery Creek	Johnnys Creek	RK250514.59	111.75	4.01	-	Red Bed
Ellery Creek	Johnnys Creek	RK250514.60	112.25	3.89	-	Stromatolite
Ellery Creek	Johnnys Creek	RK250514.61A	113.20	3.04	-	Stromatolite
Ellery Creek	Johnnys Creek	RK250514.61B	113.40	3.74	-	Stromatolite
Ellery Creek	Johnnys Creek	RK250514.63	118.10	4.22	-	Dolomicrosparite
Ellery Creek	Johnnys Creek	RK250514.65	135.20	4.46	-	Laminite
Ellery Creek	Johnnys Creek	RK250514.67	139.70	6.67	-	Grainstone
Ellery Creek	Johnnys Creek	RK250514.68	141.80	6.71	-	Dolomicrosparite
Ellery Creek	Johnnys Creek	RK250514.69	144.00	6.85	-	Dolomicrosparite

Letters on the end of the sample number correspond to analysis of different sample components

Appendix 3.3 Bitter Springs Formation drillcore imagery

Core imagery was provided by the Northern Territory Geological Survey (NTGS) from the NTGS dataset for drill-holes Wallara-1, 1990, and BR05-DD01, 2005. Data from this study (white) and Swanson-Hysell et al. (2010; yellow) are superimposed on to NTGS core images in order to illustrate $\delta^{13}C$ variation across the onset and termination of the Bitter Springs Anomaly. Wallara-1 drill core images show depths of 1928.48 – 1943.3 m (Figure 1). BR05DD01 drill core images show depths of 1060.8 – 1076.1 (Figure 2).

Swanson-Hysell, N. L., Rose, C. V., Calmet, C. C., Halverson, G. P., Hurtgen, M. T., and Maloof, A. C., 2010, Cryogenian Glaciation and the Onset of Carbon-Isotope Decoupling: Science, v. 328, no. 5978, p. 608-611.

Figure 1. NTGS core imagery of Wallara-1

Figure 2. NTGS core imagery of BR05DD01

Appendix 4.1 Trezona Formation stable isotope data

Section	Formation	Sample No.	Height (m)	$\delta^{13}C_{carb}$	$\delta^{18}O_{carb}$	Lithology
Angorichina Station	Trezona	RK161112.1	0.00	-	-	Siltstone
Angorichina Station	Trezona	RK161112.2	0.50	-	-	Siltstone
Angorichina Station	Trezona	RK161112.3	1.00	-	-	Siltstone
Angorichina Station	Trezona	RK161112.4	4.00	-	-	Siltstone
Angorichina Station	Trezona	RK161112.5	4.50	-	-	Siltstone
Angorichina Station	Trezona	RK161112.6	5.00	-	-	Laminated Sand
Angorichina Station	Trezona	RK161112.7	6.00	-	-	Siltstone
Angorichina Station	Trezona	RK161112.8	6.10	-	-	Siltstone
Angorichina Station	Trezona	RK161112.9	6.50	-	-	Laminated Sand
Angorichina Station	Trezona	RK161112.10	float	-	-	Siltstone
Angorichina Station	Trezona	RK161112.11	9.50	-	-	Siltstone
Angorichina Station	Trezona	RK161112.12	11.00	-	-	Siltstone
Angorichina Station	Trezona	RK161112.13	12.00	-	-	Siltstone
Angorichina Station	Trezona	RK161112.14	14.00	-	-	Siltstone
Angorichina Station	Trezona	RK161112.15	15.00	-	-	Laminated Sand
Angorichina Station	Trezona	RK161112.16	15.00	-	-	Laminite
Angorichina Station	Trezona	RK161112.17	17.00	-	-	Mudflake Conglomerate
Angorichina Station	Trezona	RK161112.18	17.25	-	-	Ooid Grainstone
Angorichina Station	Trezona	RK161112.19	18.00	-	-	Mudflake Conglomerate
Angorichina Station	Trezona	RK161112.20	21.00	-4.50	-8.13	Siltstone Concretion
Angorichina Station	Trezona	RK161112.21	24.00	-4.38	-8.04	Siltstone Concretion
Angorichina Station	Trezona	RK161112.22	24.50	-	-	Laminated Sand
Angorichina Station	Trezona	RK161112.23	26.00	-5.41	-7.74	Laminated Sand
Angorichina Station	Trezona	RK161112.24	26.25	-4.08	-13.46	Siltstone
Angorichina Station	Trezona	RK161112.25	27.50	-4.31	-8.68	Siltstone Concretion
Angorichina Station	Trezona	RK161112.26	27.75	-2.46	-12.01	Laminated Sand
Angorichina Station	Trezona	RK161112.27^	28.00	-7.75	-13.05	Laminite
Angorichina Station	Trezona	RK161112.28	30.00	-1.84	-9.24	Siltstone
Angorichina Station	Trezona	RK161112.29	32.25	-	-	Siltstone
Angorichina Station	Trezona	RK161112.30	32.00	-8.27	-13.33	Mudflake Conglomerate
Angorichina Station	Trezona	RK161112.31^	34.50	-4.97	-9.22	Siltstone
Angorichina Station	Trezona	RK161112.32^	36.50	-8.20	-12.47	Mudflake Conglomerate
Angorichina Station	Trezona	RK161112.33	39.00	-	-	Siltstone
Angorichina Station	Trezona	RK161112.34	42.25	-3.39	-13.30	Red Sand
Angorichina Station	Trezona	RK161112.35	45.00	-	-	Mudflake Conglomerate
Angorichina Station	Trezona	RK161112.36	48.50	-8.18	-12.42	Intraclast Grainstone
Angorichina Station	Trezona	RK161112.37	51.00	-	-	Mudflake Conglomerate
Angorichina Station	Trezona	RK161112.38	53.00	-8.56	-13.19	Mudflake Conglomerate
Angorichina Station	Trezona	RK161112.39	54.50	-3.48	-13.93	Siltstone
Angorichina Station	Trezona	RK161112.40	57.00	-9.22	-14.49	Laminated Sand
Angorichina Station	Trezona	RK161112.41	59.00	-6.52	-9.78	Siltstone
Angorichina Station	Trezona	RK161112.42^	60.25	-7.48	-11.52	Siltstone
Angorichina Station	Trezona	RK161112.43	62.00	-	-	Laminated Sand
Angorichina Station	Trezona	RK161112.44	64.00	-6.00	-14.99	Siltstone Concretion
Angorichina Station	Trezona	RK161112.45	65.50	-8.90	-13.72	Laminated Sand
Angorichina Station	Trezona	RK161112.46	66.00	-	-	Siltstone Concretion
Angorichina Station	Trezona	RK161112.47	67.00	-8.20	-13.26	Laminite
Angorichina Station	Trezona	RK161112.48	68.50	-8.54	-13.35	Mudflake Conglomerate

Section	Formation	Sample No.	Height (m)	$\delta^{13}C_{carb}$	$\delta^{18}O_{carb}$	Lithology
Angorichina Station	Trezona	RK161112.49	71.00	-8.41	-13.64	Laminated Sand
Angorichina Station	Trezona	RK161112.50	72.50	-8.44	-13.00	Intraclast Grainstone
Angorichina Station	Trezona	RK161112.50	72.50	-8.45	-13.11	Intraclast Grainstone
Angorichina Station	Trezona	RK161112.51	74.00	-3.44	-13.93	Siltstone Concretion
Angorichina Station	Trezona	RK161112.52	77.00	-8.56	-13.21	Intraclast Grainstone
Angorichina Station	Trezona	RK161112.53	79.50	-8.88	-14.55	Laminated Sand
Angorichina Station	Trezona	RK161112.54^	83.00	-8.13	-12.42	Ooid Grainstone
Angorichina Station	Trezona	RK161112.56	84.50	-	-	Siltstone
Angorichina Station	Trezona	RK161112.57	85.00	-3.59	-1.57	Siltstone Concretion
Angorichina Station	Trezona	RK161112.58	86.50	-	-	Intraclast Grainstone
Angorichina Station	Trezona	RK161112.59	91.00	-	-	Siltstone
Angorichina Station	Trezona	RK161112.60^	95.50	-7.99	-12.55	Laminite
Angorichina Station	Trezona	RK161112.61	97.00	-8.51	-12.98	Laminite
Angorichina Station	Trezona	RK161112.62	101.00	-	-	Laminated Sand
Angorichina Station	Trezona	RK161112.63	104.00	-2.67	-11.49	Siltstone
Angorichina Station	Trezona	RK161112.64	105.00	-	-	Red Sand
Angorichina Station	Trezona	RK161112.65	106.00	-8.49	-13.59	Red Sand
Angorichina Station	Trezona	RK161112.66	106.50	-8.37	-12.58	Intraclast Grainstone
Angorichina Station	Trezona	RK161112.67	107.25	-7.99	-12.55	Laminite
Angorichina Station	Trezona	RK161112.68^	108.00	-7.43	-7.49	Laminite
Angorichina Station	Trezona	RK161112.69	113.50	-7.02	-10.83	Laminite
Angorichina Station	Trezona	RK161112.70	115.50	-6.78	-10.63	Laminite
Angorichina Station	Trezona	RK161112.71^	117.00	-7.60	-11.53	Laminite
Angorichina Station	Trezona	RK161112.72	118.50	-7.68	-10.57	Laminite
Angorichina Station	Trezona	RK161112.73	120.00	-7.45	-9.80	Ooid Grainstone
Angorichina Station	Trezona	RK161112.74^	121.00	-7.58	-9.11	Ooid Grainstone
Angorichina Station	Trezona	RK171112.1	124.00	4.45	0.80	Laminite
Angorichina Station	Trezona	RK171112.2	124.50	-6.86	-9.62	Microsparite
Angorichina Station	Trezona	RK171112.3^	126.50	-6.82	-9.76	Microsparite
Angorichina Station	Trezona	RK171112.4	129.00	-6.91	-10.59	Microsparite
Angorichina Station	Trezona	RK171112.5^	132.50	-7.26	-10.22	Ooid Grainstone
Angorichina Station	Trezona	RK171112.6	133.00	-7.38	-10.68	Ooid Grainstone
Angorichina Station	Trezona	RK171112.7	134.00	-4.16	-4.84	Stromatolite
Angorichina Station	Trezona	RK171112.8^	135.00	-6.63	-9.83	Stromatolite
Angorichina Station	Trezona	RK171112.9	136.50	-6.85	-10.43	Laminite
Angorichina Station	Trezona	RK171112.10	138.50	-7.17	-10.45	Laminite
Angorichina Station	Trezona	RK171112.11	140.00	-	-	Laminite
Angorichina Station	Trezona	RK171112.12^	144.50	-7.11	-9.65	Laminite
Angorichina Station	Trezona	RK171112.13	146.00	-7.10	-10.35	Ooid Grainstone
Angorichina Station	Trezona	RK171112.14	146.50	-6.17	-9.20	Laminite
Angorichina Station	Trezona	RK171112.15	147.50	-6.58	-10.31	Intraclast Microsparite
Angorichina Station	Trezona	RK171112.15	147.50	-6.83	-10.15	Intraclast Microsparite
Angorichina Station	Trezona	RK171112.16	148.50	-6.74	-10.85	Microsparite
Angorichina Station	Trezona	RK171112.17	149.50	-6.62	-10.75	Microsparite
Angorichina Station	Trezona	RK171112.18	151.50	-6.66	-10.74	Laminite
Angorichina Station	Trezona	RK171112.19	153.50	-6.62	-10.43	Laminite
Angorichina Station	Trezona	RK171112.20	156.50	-	-	Microsparite
Angorichina Station	Trezona	RK171112.21	156.50	-6.26	-11.52	Microsparite
Angorichina Station	Trezona	RK171112.22^	158.00	-6.35	-10.93	Intraclast Microsparite
Angorichina Station	Trezona	RK171112.23	164.00	-5.96	-11.24	Mudflake Conglomerate

Section	Formation	Sample No.	Height (m)	$\delta^{13}C_{carb}$	$\delta^{18}O_{carb}$	Lithology
Angorichina Station	Trezona	RK171112.24	165.75	-5.82	-11.10	Mudflake Conglomerate
Angorichina Station	Trezona	RK171112.25	166.75	-5.90	-11.05	Laminite
Angorichina Station	Trezona	RK171112.26	169.00	-4.62	-9.92	Stromatolite
Angorichina Station	Trezona	RK171112.27	170.50	-5.62	-9.89	Microsparite
Angorichina Station	Trezona	RK171112.28	171.50	-5.08	-10.60	Laminite
Angorichina Station	Trezona	RK171112.29	173.00	-4.97	-11.03	Laminite
Angorichina Station	Trezona	RK171112.30	174.50	-4.97	-11.07	Laminite
Angorichina Station	Trezona	RK171112.31^	175.75	-3.61	-8.08	Siltstone
Angorichina Station	Trezona	RK171112.32	177.25	-5.17	-10.97	Siltstone
Angorichina Station	Trezona	RK171112.33	179.00	-4.88	-9.42	Siltstone
Angorichina Station	Trezona	RK171112.34	180.25	-	-	Intraclast Microsparite
Angorichina Station	Trezona	RK171112.35	181.50	-5.11	-11.18	Stromatolite
Angorichina Station	Trezona	RK171112.36^	182.00	-5.12	-10.99	Intraclast Microsparite
Angorichina Station	Trezona	RK171112.37	183.50	-5.44	-8.98	Stromatolite
Angorichina Station	Trezona	RK171112.38	184.50	-4.60	-11.29	Stromatolite
Angorichina Station	Trezona	RK171112.39	187.00	-4.39	-10.75	Stromatolite
Angorichina Station	Trezona	RK171112.40	188.00	-4.59	-10.82	Mudflake Conglomerate
Angorichina Station	Trezona	RK171112.41	191.25	-4.50	-10.77	Stromatolite
Angorichina Station	Trezona	RK171112.42	194.00	-	-	Laminite
Angorichina Station	Trezona	RK171112.43	195.50	-3.78	-10.27	Laminite
Angorichina Station	Trezona	RK171112.44	197.00	-3.93	-10.67	Laminite
Angorichina Station	Trezona	RK171112.45	200.00	-3.73	-10.33	Laminite
Angorichina Station	Trezona	RK171112.46	203.00	-3.68	-10.41	Laminite
Angorichina Station	Trezona	RK171112.47^	206.00	-3.47	-9.67	Laminite
Angorichina Station	Trezona	RK171112.48	209.25	-2.95	-9.27	Ooid Grainstone
Angorichina Station	Trezona	RK171112.49	212.75	-2.95	-10.34	Ooid Grainstone
Angorichina Station	Trezona	RK171112.50	213.00	-2.54	-10.96	Ooid Grainstone
Angorichina Station	Trezona	RK171112.51	216.00	-2.72	-11.69	Laminite
Angorichina Station	Trezona	RK171112.52	219.00	-2.67	-11.57	Stromatolite
Angorichina Station	Trezona	RK171112.53	222.00	-2.64	-11.64	Stromatolite
Angorichina Station	Trezona	RK171112.54	223.50	-	-	Ooid Grainstone
Angorichina Station	Trezona	RK171112.55	225.50	-2.33	-12.77	Ooid Grainstone
Angorichina Station	Trezona	RK171112.56	220.00	-1.58	-12.58	Flaggy Siltstone
Angorichina Station	Trezona	RK171112.57	230.00	-1.43	-14.08	Ooid Grainstone
Angorichina Station	Trezona	RK171112.58^	231.00	-1.76	-12.84	Ooid Grainstone
Angorichina Station	Trezona	RK171112.59	234.00	-	-	Massive feldspathic sand
Angorichina Station	Trezona	RK171112.60	-14.00	-	-	Red Sand
Angorichina Station	Trezona	RK171112.61	-12.50	-	-	Red Sand
Angorichina Station	Trezona	RK171112.62	-11.75	-	-	Red Sand
Angorichina Station	Trezona	RK171112.63	-10.00	-	-	Red Sand
Trezona Range	Trezona	RK260411.1	0.25	-	-	Siltstone
Trezona Range	Trezona	RK260411.2^	2.25	-9.00	-11.10	Siltstone Concretion
Trezona Range	Trezona	RK260411.3^	3.00	-9.17	-11.41	Mudflake Conglomerate
Trezona Range	Trezona	RK260411.4	7.75	-9.57	-10.37	Mudflake Conglomerate
Trezona Range	Trezona	RK260411.4	7.75	-9.20	-11.18	Mudflake Conglomerate
Trezona Range	Trezona	RK260411.5	8.50	-7.26	-8.56	Intraclastic Microsparite
Trezona Range	Trezona	RK260411.5	8.50	-7.33	-8.76	Intraclastic Microsparite
Trezona Range	Trezona	RK260411.6	10.00	-	-	Mudflake Conglomerate
Trezona Range	Trezona	RK260411.7^	11.25	-10.27	-11.42	Mudflake Conglomerate
Trezona Range	Trezona	RK260411.8	12.25	-	-	Siltstone

Section	Formation	Sample No.	Height (m)	$\delta^{13}C_{carb}$	$\delta^{18}O_{carb}$	Lithology
Trezona Range	Trezona	RK260411.9	13.00	-	-	Siltstone
Trezona Range	Trezona	RK260411.10	15.25	-	-	Mudflake Conglomerate
Trezona Range	Trezona	RK260411.11	19.50	-8.09	-8.14	Fine Sand
Trezona Range	Trezona	RK260411.12	16.50	-	-	Siltstone
Trezona Range	Trezona	RK260411.13	float	-	-	Red Sand
Trezona Range	Trezona	RK260411.14	float	-	-	Intraclastic Microsparite
Trezona Range	Trezona	RK260411.15^	float	-10.01	-11.25	Stromatolite
Trezona Range	Trezona	RK260411.16	28.50	-	-	Mudflake Conglomerate
Trezona Range	Trezona	RK260411.17	float	-	-	Red Sand
Trezona Range	Trezona	RK260411.18	float	-	-	Stromatolite
Trezona Range	Trezona	RK260411.19^	53.50	-9.00	-11.30	Red Sand
Trezona Range	Trezona	RK260411.20^	54.25	-9.32	-11.76	Red Sand
Trezona Range	Trezona	RK260411.21^	55.00	-8.67	-11.51	Stromatolite
Trezona Range	Trezona	RK260411.22	55.25	-8.85	-11.74	Mud Drape
Trezona Range	Trezona	RK260411.23	57.00	-8.38	-11.38	Intraclast Conglomerate
Trezona Range	Trezona	RK260411.24	57.25	-8.39	-10.28	Intraclast Conglomerate
Trezona Range	Trezona	RK260411.25^	57.50	-8.72	-11.88	Red Sand
Trezona Range	Trezona	RK260411.26^	60.75	-8.72	-11.76	Stromatolite
Trezona Range	Trezona	RK260411.27	60.50	-7.89	-10.94	Intraclast Conglomerate
Trezona Range	Trezona	RK260411.28	68.50	-	-	Red Sand
Trezona Range	Trezona	RK260411.29	69.75	-	-	Siltstone
Trezona Range	Trezona	RK260411.30^	73.50	-8.20	-9.60	Intraclast Conglomerate
Trezona Range	Trezona	RK260411.31	74.00	-8.03	-10.46	Intraclast Conglomerate
Trezona Range	Trezona	RK260411.31	74.00	-8.03	-10.94	Intraclast Conglomerate
Trezona Range	Trezona	RK260411.32	89.25	-7.94	-8.81	Intraclast Conglomerate
Trezona Range	Trezona	RK260411.32	89.25	-7.92	-10.01	Intraclast Conglomerate
Trezona Range	Trezona	RK260411.33	89.75	-7.36	-10.09	Siltstone
Trezona Range	Trezona	RK260411.34	91.00	-7.91	-9.82	Intraclast Conglomerate
Trezona Range	Trezona	RK260411.35	92.00	-7.65	-7.88	Intraclast Conglomerate
Trezona Range	Trezona	RK260411.35	92.00	-7.73	-8.23	Intraclast Conglomerate
Trezona Range	Trezona	RK260411.36	101.00	-	-	Siltstone
Trezona Range	Trezona	RK260411.37^	110.00	-8.68	-11.19	Intraclast Conglomerate
Trezona Range	Trezona	RK260411.38	111.00	-8.02	-11.01	Stromatolite
Trezona Range	Trezona	RK260411.39^	110.50	-8.40	-10.60	Stromatolite
Trezona Range	Trezona	RK260411.40	124.25	-8.29	-8.44	Siltstone Concretion
Trezona Range	Trezona	RK260411.41	131.00	-8.05	-11.31	Microbialite
Trezona Range	Trezona	RK260411.42^	135.50	-8.18	-10.81	Stromatolite
Trezona Range	Trezona	RK260411.43	139.50	-7.71	-10.65	Marl
Trezona Range	Trezona	RK260411.44^	142.00	-8.20	-11.06	Intraclast Conglomerate
Trezona Range	Trezona	RK260411.45	152.75	-	-	Intraclastic Microsparite
Trezona Range	Trezona	RK260411.46	156.00	-	-	Mudflake Conglomerate
Trezona Range	Trezona	RK260411.47	159.25	-	-	Intraclastic Microsparite
Trezona Range	Trezona	RK260411.48	163.00	-	-	Laminite
Trezona Range	Trezona	RK260411.49^	172.50	-10.12	-10.24	Intraclastic Microsparite
Trezona Range	Trezona	RK260411.50	179.25	-	-	Intraclastic Microsparite
Trezona Range	Trezona	RK260411.51	182.25	-	-	Intraclast Conglomerate
Trezona Range	Trezona	RK260411.52^	185.75	-7.89	-10.61	Intraclast Conglomerate
Trezona Range	Trezona	RK260411.53	188.00	-	-	Styolitic Microsparite
Trezona Range	Trezona	RK260411.54	196.25	-	-	Microsparite
Trezona Range	Trezona	RK260411.55	198.00	-	-	Stromatolite

Section	Formation	Sample No.	Height (m)	$\delta^{13}C_{carb}$	$\delta^{18}O_{carb}$	Lithology
Trezona Range	Trezona	RK260411.56	201.00	-	-	Microsparite
Trezona Range	Trezona	RK260411.57	203.75	-	-	Red Sand
Trezona Range	Trezona	RK270411.58	209.50	-	-	Laminite
Trezona Range	Trezona	RK270411.59	210.75	-	-	Laminite
Trezona Range	Trezona	RK270411.60^	212.75	-8.00	-10.50	Stromatolite
Trezona Range	Trezona	RK270411.61	213.25	-	-	Laminite
Trezona Range	Trezona	RK270411.62	220.25	-7.48	-10.44	Microsparite
Trezona Range	Trezona	RK270411.63^	222.00	-7.74	-10.15	Laminite
Trezona Range	Trezona	RK270411.64	233.50	-	-	Laminite
Trezona Range	Trezona	RK270411.65^	235.25	-8.13	-9.37	Intraclast Conglomerate
Trezona Range	Trezona	RK270411.66	236.00	-6.64	-10.07	Stromatolite
Trezona Range	Trezona	RK270411.67	236.75	-6.88	-9.60	Siltstone Concretion
Trezona Range	Trezona	RK270411.68	237.50	-7.20	-9.99	Laminite
Trezona Range	Trezona	RK270411.68	237.50	-7.27	-9.99	Laminite
Trezona Range	Trezona	RK270411.69	248.00	-6.83	-10.16	Laminite
Trezona Range	Trezona	RK270411.70	248.50	-6.88	-10.04	Intraclast Conglomerate
Trezona Range	Trezona	RK270411.71^	249.00	-6.81	-9.67	Laminite
Trezona Range	Trezona	RK270411.72	249.50	-7.22	-10.08	Intraclast Conglomerate
Trezona Range	Trezona	RK270411.73	255.00	-6.77	-9.91	Laminite
Trezona Range	Trezona	RK270411.74^	257.50	-7.22	-10.14	Laminite
Trezona Range	Trezona	RK270411.75	258.00	-6.65	-9.91	Intraclast Conglomerate
Trezona Range	Trezona	RK270411.76^	260.50	-6.34	-7.82	Laminite
Trezona Range	Trezona	RK270411.77	281.25	-6.80	-9.22	Intraclast Conglomerate
Trezona Range	Trezona	RK270411.78^	281.75	-6.37	-9.01	Stromatolite
Trezona Range	Trezona	RK270411.79	283.00	-6.17	-8.90	Intraclast Conglomerate
Trezona Range	Trezona	RK270411.80	286.25	-6.27	-7.75	Oolitic Microsparite
Trezona Range	Trezona	RK270411.81^	288.75	-6.20	-7.86	Oolitic Microsparite
Trezona Range	Trezona	RK270411.82	291.50	-4.91	-10.71	Oolitic Microsparite
Trezona Range	Trezona	RK270411.83	293.50	-6.09	-9.00	Intraclast Conglomerate
Trezona Range	Trezona	RK270411.84	294.75	-5.46	-8.93	Stromatolite
Trezona Range	Trezona	RK270411.85	300.50	-8.53	-6.60	Oolitic Microsparite
Trezona Range	Trezona	RK270411.86^	303.25	-5.56	-8.86	Oolitic Microsparite
Trezona Range	Trezona	RK270411.87	304.00	-4.71	-8.40	Stromatolite
Trezona Range	Trezona	RK270411.88	308.75	-	-	Laminite
Trezona Range	Trezona	RK270411.89	310.50	-	-	Intraclast Conglomerate
Trezona Range	Trezona	RK270411.90	320.50	-	-	Intraclast Conglomerate
Trezona Range	Trezona	RK270411.91^	324.00	-5.15	-8.62	Stromatolite
Trezona Range	Trezona	RK270411.92	327.00	-8.48	-11.44	Stromatolite
Trezona Range	Trezona	RK270411.93	331.00	-7.98	-11.67	Intraclast Conglomerate
Trezona Range	Trezona	RK270411.94	333.50	-	-	Stromatolite
Trezona Range	Trezona	RK270411.95	336.00	-8.63	-10.58	Oolitic Microsparite
Trezona Range	Trezona	RK270411.96	338.25	-7.76	-11.51	Stromatolite
Trezona Range	Trezona	RK270411.97	342.00	-7.46	-10.35	Intraclast Conglomerate
Trezona Range	Trezona	RK270411.98	343.75	-	-	Stromatolite
Trezona Range	Trezona	RK270411.99	347.00	-	-	Stromatolite
Trezona Range	Trezona	RK270411.100	347.50	-	-	Intraclast Conglomerate
Trezona Range	Trezona	RK270411.101^	349.00	-4.40	-8.89	Stromatolite
Trezona Range	Enorama	RK280411.1	3.25	-	-	Shale
Trezona Range	Enorama	RK280411.2	10.25	-	-	Shale
Trezona Range	Enorama	RK280411.3	11.00	-	-	Sandstone

Section	Formation	Sample No.	Height (m)	$\delta^{13}C_{carb}$	$\delta^{18}O_{carb}$	Lithology
Trezona Range	Enorama	RK280411.4	12.50	-	-	Sandstone
Trezona Range	Enorama	RK280411.5	14.00	-	-	Sandstone
Trezona Range	Enorama	RK280411.6	21.00	-	-	Shale
Trezona Range	Trezona	RK280411.7	43.50	-	-	Mudflake Conglomerate
Trezona Range	Trezona	RK280411.8	60.00	-	-	Siltstone
Trezona Range	Trezona	RK280411.9	61.50	-	-	Mudflake Conglomerate
Trezona Range	Trezona	RK280411.10	64.50	-	-	Mudflake Conglomerate
Trezona Range	Trezona	RK280411.11	66.00	-	-	Mudflake Conglomerate
Trezona Range	Trezona	RK280411.13	73.50	-	-	Siltstone
Bull's Gap	Enorama	RK191112.1	0.25	-	-	Siltstone
Bull's Gap	Enorama	RK191112.2	0.28	-	-	Shale
Bull's Gap	Enorama	RK191112.3	0.98	-	-	Siltstone
Bull's Gap	Enorama	RK191112.4	0.87	-	-	Siltstone Cement
Bull's Gap	Trezona	RK191112.5	1.23	-	-	Lower Paleosol
Bull's Gap	Trezona	RK191112.6	0.33	-	-	Siltstone Cement
Bull's Gap	Trezona	RK191112.7	0.83	-	-	Siltstone
Bull's Gap	Trezona	RK191112.8	1.50	-	-	Siltstone
Bull's Gap	Trezona	RK191112.9	1.31	-	-	Siltstone Cement
Bull's Gap	Trezona	RK191112.10	1.34	-	-	Siltstone
Bull's Gap	Trezona	RK191112.11	1.17	-	-	Siltstone Cement
Bull's Gap	Trezona	RK191112.12	1.68	-	-	Siltstone Cement
Bull's Gap	Trezona	RK191112.13	0.85	-	-	Siltstone Cement
Bull's Gap	Trezona	RK191112.14	1.56	-	-	Siltstone Concretion
Bull's Gap	Trezona	RK191112.15	0.87	-	-	Siltstone Cement
Bull's Gap	Trezona	RK191112.16	0.78	-	-	Siltstone
Bull's Gap	Trezona	RK191112.18	1.24	-	-	Lower Paleosol
Bull's Gap	Trezona	RK191112.19	1.30	-	-	Upper Paleosol
Glass Gorge-North	Trezona	MK011110.1~	115.50	-8.47	-13.02	Mudflake Conglomerate
Glass Gorge-North	Trezona	MK011110.2~	116.25	-8.34	-12.43	Mudflake Conglomerate
Glass Gorge-North	Trezona	MK011110.3~	117.00	-8.74	-13.04	Mudflake Conglomerate
Glass Gorge-North	Trezona	MK011110.4~	117.75	-8.61	-12.84	Mudflake Conglomerate
Glass Gorge-North	Trezona	MK011110.5~	117.75	-8.48	-13.20	Mudflake Conglomerate
Glass Gorge-North	Trezona	MK011110.6~	118.50	-8.32	-12.33	Cemented Sandstone
Glass Gorge-North	Trezona	MK011110.7~	118.50	-9.18	-12.70	Cemented Sandstone
Glass Gorge-North	Trezona	MK011110.8~	119.25	-8.77	-12.74	Cemented Sandstone
Glass Gorge-North	Trezona	MK011110.9~	120.00	-5.03	-7.42	Siltstone
Glass Gorge-North	Trezona	MK011110.10~	120.00	-7.98	-11.62	Siltstone Cement
Glass Gorge-North	Trezona	MK011110.11~	120.00	-4.10	-4.77	Siltstone Cement
Glass Gorge-North	Trezona	MK011110.12~	121.50	-4.79	-3.42	Siltstone Cement
Glass Gorge-North	Trezona	MK011110.13~	121.50	-6.72	-4.49	Calcite Vein
Glass Gorge-North	Trezona	MK011110.14~	122.25	-3.08	-4.30	Siltstone
Glass Gorge-North	Trezona	MK011110.15~	123.00	-5.80	-9.92	Calcite Spar
Glass Gorge-North	Trezona	MK011110.16~	123.75	-3.83	-4.82	Marl
Glass Gorge-North	Trezona	MK011110.17~	126.00	-7.80	-12.09	Mudflake Conglomerate
Glass Gorge-North	Trezona	MK011110.18~	126.00	-8.48	-13.27	Mudflake Conglomerate
Glass Gorge-North	Trezona	MK011110.19~	126.75	-8.40	-11.66	Mudflake Conglomerate
Glass Gorge-North	Trezona	MK011110.20~	126.75	-8.37	-12.78	Mudflake Conglomerate
Glass Gorge-North	Trezona	MK011110.21~	127.50	-8.60	-13.11	Mudflake Conglomerate
Glass Gorge-North	Trezona	MK011110.22~	129.00	-8.40	-13.05	Cemented Sandstone
Glass Gorge-North	Trezona	MK011110.23~	133.50	-5.93	-8.31	Siltstone Cement

Section	Formation	Sample No.	Height (m)	$\delta^{13}C_{carb}$	$\delta^{18}O_{carb}$	Lithology
Glass Gorge-North	Trezona	MK011110.24~	133.50	-5.47	-7.89	Siltstone Cement
Glass Gorge-North	Trezona	MK011110.25~	133.50	-8.36	-12.93	Mudflake Conglomerate
Glass Gorge-North	Trezona	MK011110.26~	134.25	-8.80	-16.43	Mudflake Conglomerate
Glass Gorge-North	Trezona	MK011110.27~	135.00	-9.59	-13.23	Cemented Sandstone
Glass Gorge-North	Trezona	MK011110.28~	136.50	-9.23	-12.78	Cemented Sandstone
Glass Gorge-North	Trezona	MK011110.29~	136.50	-8.50	-12.32	Siltstone
Glass Gorge-North	Trezona	MK011110.30~	138.00	-8.46	-13.20	Mudflake Conglomerate
Glass Gorge-North	Trezona	MK011110.31~	139.50	-8.62	-13.49	Mudflake Conglomerate
Glass Gorge-North	Trezona	MK011110.32~	139.50	-8.32	-12.40	Red Rand
Glass Gorge-North	Trezona	MK011110.33~	139.50	-8.37	-13.33	Mudflake Conglomerate
Glass Gorge-North	Trezona	MK011110.34~	141.00	-8.13	-11.66	Siltstone Cement
Glass Gorge-North	Trezona	MK011110.37~	145.50	-8.56	-12.53	Red Sand
Glass Gorge-North	Trezona	MK011110.38~	147.00	-8.82	-12.97	Cemented Sandstone
Glass Gorge-North	Trezona	MK011110.39~	147.00	-8.76	-12.69	Oolitic Microsparite
Glass Gorge-North	Trezona	MK011110.40~	147.75	-8.58	-10.33	Mudflake Conglomerate
Glass Gorge-North	Trezona	MK011110.41~	149.25	-9.57	-13.09	Mudflake Conglomerate
Glass Gorge-North	Trezona	MK011110.42~	150.00	-9.98	-13.09	Siltstone
Glass Gorge-North	Trezona	MK011110.43~	151.50	-10.78	-12.86	Siltstone
Glass Gorge-North	Trezona	MK011110.44~	153.00	-6.20	-9.10	Siltstone Concretion
Glass Gorge-North	Trezona	MK011110.45~	153.00	-10.25	-13.39	Siltstone Concretion
Glass Gorge-North	Trezona	MK011110.46~	154.50	-8.55	-11.96	Siltstone Concretion
Glass Gorge-North	Trezona	MK011110.49~	161.25	-9.12	-11.32	Intraclastic Dolostone
Glass Gorge-North	Trezona	MK011110.50~	162.75	-8.73	-12.77	Red Bed
Glass Gorge-North	Trezona	MK011110.51~	163.50	-9.07	-14.54	Mudflake Conglomerate
Glass Gorge-North	Trezona	MK011110.52~	163.50	-9.03	-12.86	Mudflake Conglomerate
Glass Gorge-North	Trezona	MK011110.53~	165.00	-8.86	-13.56	Mudflake Conglomerate
Glass Gorge-North	Trezona	MK011110.54~	165.75	-8.83	-13.50	Mudflake Conglomerate
Glass Gorge-North	Trezona	MK011110.56~	166.50	-8.66	-12.84	Mudflake Conglomerate
Glass Gorge-North	Trezona	MK011110.57~	168.00	-8.89	-13.37	Mudflake Conglomerate
Glass Gorge-North	Trezona	MK011110.59~	184.50	-8.77	-14.15	Mudflake Conglomerate
Glass Gorge-North	Trezona	MK011110.60~	195.00	-8.36	-12.76	Mudflake Conglomerate
Glass Gorge-North	Trezona	MK011110.62~	202.50	-8.63	-13.63	Muddy Carbonte
Glass Gorge-North	Trezona	MK011110.63~	203.25	-8.10	-13.41	Muddy Carbonte
Glass Gorge-North	Trezona	MK011110.64~	204.00	-8.35	-14.82	Cross-bedded Microsparite
Glass Gorge-North	Trezona	MK011110.65~	205.50	-1.16	-25.98	Vein Calcite
Glass Gorge-North	Trezona	MK011110.66~	210.00	-7.45	-18.55	Mudflake Conglomerate
Glass Gorge-North	Trezona	MK011110.69~	213.00	-8.35	-13.53	Stromatolite
Glass Gorge-North	Trezona	MK011110.72~	214.50	-8.28	-13.75	Stromatolite
Glass Gorge-North	Trezona	MK011110.74~	214.50	-8.28	-13.17	Cemented Sandstone
Glass Gorge-North	Trezona	MK011110.75~	214.50	-7.68	-12.08	Laminite
Glass Gorge-North	Trezona	MK011110.77~	216.00	-7.82	-14.44	Stromatolite
Glass Gorge-North	Trezona	MK011110.80~	216.00	-8.13	-13.40	Stromatolite
Glass Gorge-North	Trezona	MK011110.81~	216.75	-7.63	-11.93	Stromatolite
Glass Gorge-North	Trezona	MK011110.83~	217.50	-7.73	-13.68	Stromatolite
Glass Gorge-North	Trezona	MK011110.85~	219.00	-7.23	-12.48	Stromatolite
Glass Gorge-North	Trezona	MK011110.87~	222.00	-7.60	-13.61	Stromatolite
Glass Gorge-North	Trezona	MK011110.88~	222.75	-6.68	-11.68	Stromatolite
Glass Gorge-North	Trezona	MK011110.90~	223.50	-6.92	-12.99	Stromatolite
Glass Gorge-North	Trezona	MK011110.91~	224.25	-7.15	-12.66	Stromatolite

Section	Formation	Sample No.	Height (m)	$\delta^{13}C_{carb}$	$\delta^{18}O_{carb}$	Lithology
Glass Gorge-North	Trezona	MK011110.92~	226.50	-6.32	-12.90	Stromatolite
Glass Gorge-North	Trezona	MK011110.93~	228.00	-4.66	-13.10	Stromatolite
Glass Gorge-North	Trezona	MK011110.94~	228.75	-3.85	-13.16	Stromatolite
Glass Gorge-North	Trezona	MK011110.95~	229.50	-3.12	-12.64	Stromatolite
Glass Gorge-North	Trezona	MK011110.96~	231.00	-4.87	-13.52	Stromatolite
Glass Gorge-North	Trezona	MK011110.97~	232.50	-1.36	-9.02	Stromatolite
Glass Gorge-South	Enorama	RK240312.1	0.00	-	-	Siltstone
Glass Gorge-South	Enorama	RK240312.2	0.00	-	-	Siltstone
Glass Gorge-South	Enorama	RK240312.3	0.00	-	-	Siltstone
Glass Gorge-South	Enorama	RK240312.4	5.25	-	-	Siltstone
Glass Gorge-South	Enorama	RK240312.5	5.75	-	-	Siltstone Cement
Glass Gorge-South	Enorama	RK240312.6	12.00	-	-	Siltstone
Glass Gorge-South	Enorama	RK240312.7	21.00	-	-	Siltstone Cement
Glass Gorge-South	Enorama	RK240312.8	26.00	-	-	Siltstone Concretion
Glass Gorge-South	Enorama	RK240312.9	33.00	-	-	Siltstone Cement
Glass Gorge-South	Enorama	RK240312.10	41.25	-	-	Siltstone Cement
Glass Gorge-South	Enorama	RK240312.11	46.50	-	-	Siltstone Cement
Glass Gorge-South	Enorama	RK240312.12	66.00	-	-	Siltstone Cement
Glass Gorge-South	Enorama	RK240312.13	66.00	-	-	Siltstone Cement
Glass Gorge-South	Trezona	RK240312.14	112.50	-	-	Cemented Sandstone
Glass Gorge-South	Trezona	RK240312.15	113.00	-	-	Mudflake Conglomerate
Glass Gorge-South	Trezona	RK240312.16	113.40	-	-	Marl
Glass Gorge-South	Trezona	RK240312.17	113.65	-	-	Laminite
Glass Gorge-South	Trezona	RK240312.18	114.00	-	-	Marl
Glass Gorge-South	Trezona	RK240312.19	114.25	-	-	Mudflake Conglomerate
Glass Gorge-South	Trezona	RK240312.20	117.00	-	-	Siltstone
Glass Gorge-South	Trezona	RK240312.21	120.00	-	-	Mudflake Conglomerate
Glass Gorge-South	Trezona	RK240312.22	121.00	-	-	Mudflake Conglomerate
Glass Gorge-South	Trezona	RK240312.23	121.50	-	-	Laminite
Glass Gorge-South	Trezona	RK240312.24	123.25	-	-	Laminite
Glass Gorge-South	Trezona	RK240312.25	126.00	-	-	Siltstone Cement
Glass Gorge-South	Trezona	RK240312.26	127.00	-	-	Mudflake Conglomerate
Glass Gorge-South	Trezona	RK240312.27	129.50	-	-	Mudflake Conglomerate
Glass Gorge-South	Trezona	RK240312.28	130.00	-	-	Siltstone Cement
Glass Gorge-South	Trezona	RK240312.29	131.00	-	-	Siltstone Cement
Glass Gorge-South	Trezona	RK240312.30	131.50	-	-	Mudflake Conglomerate
Glass Gorge-South	Trezona	RK240312.31	133.25	-	-	Mudflake Conglomerate
Glass Gorge-South	Trezona	RK240312.32	134.50	-	-	Siltstone Cement
Glass Gorge-South	Trezona	RK240312.33	135.25	-	-	Mudflake Conglomerate
Glass Gorge-South	Trezona	RK240312.34	138.50	-	-	Siltstone Cement
Glass Gorge-South	Trezona	RK240312.35	139.00	-	-	Siltstone Cement
Glass Gorge-South	Trezona	RK240312.36	139.50	-	-	Mudflake Conglomerate
Glass Gorge-South	Trezona	RK240312.37	140.50	-	-	Mudflake Conglomerate
Glass Gorge-South	Trezona	RK240312.38	141.00	-	-	Siltstone Cement
Glass Gorge-South	Trezona	RK240312.39	143.00	-	-	Siltstone Cement
Glass Gorge-South	Trezona	RK240312.40	146.50	-	-	Siltstone Cement
Glass Gorge-South	Trezona	RK240312.41	150.25	-	-	Siltstone Cement
Glass Gorge-South	Trezona	RK240312.42	151.00	-	-	Siltstone Cement
Glass Gorge-South	Trezona	RK240312.43	154.00	-	-	Siltstone Cement
Glass Gorge-South	Trezona	RK240312.44	155.00	-	-	Siltstone Cement

Section	Formation	Sample No.	Height (m)	$\delta^{13}C_{carb}$	$\delta^{18}O_{carb}$	Lithology
Glass Gorge-South	Trezona	RK240312.45	157.00	-	-	Siltstone Cement
Glass Gorge-South	Trezona	RK240312.46	159.50	-	-	Siltstone Cement
Glass Gorge-South	Trezona	RK240312.47	160.50	-	-	Siltstone Cement
Glass Gorge-South	Trezona	RK240312.48	169.00	-	-	Siltstone Cement
Glass Gorge-South	Trezona	RK240312.50	171.00	-	-	Siltstone Cement
Glass Gorge-South	Trezona	RK240312.51	174.50	-	-	Siltstone Cement
Glass Gorge-South	Trezona	RK240312.52	175.50	-	-	Stromatolite
Glass Gorge-South	Trezona	RK250312.1	180.00	-	-	Siltstone Cement
Glass Gorge-South	Trezona	RK250312.2	181.25	-6.63	-9.52	Siltstone Cement
Glass Gorge-South	Trezona	RK250312.3	184.00	-	-	Mudflake Conglomerate
Glass Gorge-South	Trezona	RK250312.4	185.50	-	-	Mudflake Conglomerate
Glass Gorge-South	Trezona	RK250312.5	187.00	-	-	Siltstone Cement
Glass Gorge-South	Trezona	RK250312.6	187.25	-	-	Mudflake Conglomerate
Glass Gorge-South	Trezona	RK250312.7	188.00	-	-	Calcite Vein
Glass Gorge-South	Trezona	RK250312.8	188.50	-	-	Siltstone Cement
Glass Gorge-South	Trezona	RK250312.9	189.00	-	-	Siltstone Cement
Glass Gorge-South	Trezona	RK250312.10	190.00	-	-	Siltstone Cement
Glass Gorge-South	Trezona	RK250312.11	191.50	-	-	Laminated Sand
Glass Gorge-South	Trezona	RK250312.12	192.50	-	-	Cemented Sandstone
Glass Gorge-South	Trezona	RK250312.13	194.25	-11.83	-13.00	Cemented Sandstone
Glass Gorge-South	Trezona	RK250312.14	198.00	-	-	Mudflake Conglomerate
Glass Gorge-South	Trezona	RK250312.15	199.00	-	-	Stromatolite
Glass Gorge-South	Trezona	RK250312.16	199.50	-	-	Mudflake Conglomerate
Glass Gorge-South	Trezona	RK250312.17	201.50	-	-	Stromatolite
Glass Gorge-South	Trezona	RK250312.18	202.00	-	-	Mudflake Conglomerate
Glass Gorge-South	Trezona	RK250312.19	202.25	-	-	Marl
Glass Gorge-South	Trezona	RK250312.20	204.25	-	-	Mudflake Conglomerate
Glass Gorge-South	Trezona	RK250312.21	205.00	-	-	Siltstone Cement
Glass Gorge-South	Trezona	RK250312.22	205.50	-	-	Mudflake Conglomerate
Glass Gorge-South	Trezona	RK250312.23	207.25	-	-	Siltstone Cement
Glass Gorge-South	Trezona	RK250312.24	212.25	-	-	Siltstone Cement
Glass Gorge-South	Trezona	RK250312.25	216.00	-	-	Mudflake Conglomerate
Glass Gorge-South	Trezona	RK250312.26	217.00	-	-	Siltstone Cement
Glass Gorge-South	Trezona	RK250312.27	219.50	-7.87	-12.67	Red Sand (Cement)
Glass Gorge-South	Trezona	RK250312.28	220.00	-	-	Mudflake Conglomerate
Glass Gorge-South	Trezona	RK250312.29	222.00	-	-	Siltstone Cement
Glass Gorge-South	Trezona	RK250312.30	224.00	-	-	Mudflake Conglomerate
Glass Gorge-South	Trezona	RK250312.31	225.50	-	-	Cemented Sandstone
Glass Gorge-South	Trezona	RK250312.32	227.50	-	-	Siltstone Cement
Glass Gorge-South	Trezona	RK250312.33	228.50	-	-	Siltstone Cement
Glass Gorge-South	Trezona	RK250312.34	230.00	-	-	Red Sand
Glass Gorge-South	Trezona	RK250312.35	230.50	-	-	Fine Sand
Glass Gorge-South	Trezona	RK250312.36	231.00	-	-	Marl
Glass Gorge-South	Trezona	RK250312.37	230.50	-8.56	-12.81	Sandy Marl
Glass Gorge-South	Trezona	RK250312.38	232.00	-8.28	-12.87	Oolitic Microsparite
Glass Gorge-South	Trezona	RK250312.39	232.50	-	-	Marl
Glass Gorge-South	Trezona	RK250312.40	232.75	-	-	Marl
Glass Gorge-South	Trezona	RK250312.41	235.00	-	-	Fine Sand
Glass Gorge-South	Trezona	RK250312.42	239.50	-	-	Intraclast Conglomerate
Glass Gorge-South	Trezona	RK250312.43	240.00	-	-	Red Sand

Section	Formation	Sample No.	Height (m)	$\delta^{13}C_{carb}$	$\delta^{18}O_{carb}$	Lithology
Glass Gorge-South	Trezona	RK250312.44	240.75	-8.18	-12.74	Intraclast Conglomerate
Glass Gorge-South	Trezona	RK250312.45	241.25	-	-	Intraclast Conglomerate
Glass Gorge-South	Trezona	RK250312.46	243.50	-	-	Red Sand
Glass Gorge-South	Trezona	RK250312.48	246.50	-	-	Red Sand
Glass Gorge-South	Trezona	RK250312.49	247.00	-	-	Intraclast Conglomerate
Glass Gorge-South	Trezona	RK250312.50	250.00	-	-	Intraclast Conglomerate
Glass Gorge-South	Trezona	RK250312.51	251.00	-	-	Red Sand
Glass Gorge-South	Trezona	RK250312.52	251.50	-8.32	-12.73	Intraclast Conglomerate
Glass Gorge-South	Trezona	RK250312.53	252.50	-	-	Stromatolite
Glass Gorge-South	Trezona	RK250312.54	252.75	-	-	Intraclast Conglomerate
Glass Gorge-South	Trezona	RK250312.55	253.00	-	-	Oolitic Microsparite
Glass Gorge-South	Trezona	RK250312.56	253.50	-	-	Red Sand
Glass Gorge-South	Trezona	RK250312.57	255.50	-	-	Red Sand
Glass Gorge-South	Trezona	RK250312.58	260.50	-	-	Stromatolite
Glass Gorge-South	Trezona	RK250312.59	262.00	-7.02	-11.91	Stromatolite
Glass Gorge-South	Trezona	RK250312.60	264.50	-	-	Laminite
Glass Gorge-South	Trezona	RK250312.61	268.00	-	-	Laminite
Glass Gorge-South	Trezona	RK250312.62	269.50	-6.75	-11.32	Laminite
Glass Gorge-South	Trezona	RK250312.63	271.00	-	-	Intraclast Conglomerate
Glass Gorge-South	Trezona	RK250312.64	272.50	-	-	Laminite
Glass Gorge-South	Trezona	RK250312.65	273.50	-	-	Laminite
Glass Gorge-South	Trezona	RK250312.66	274.50	-	-	Laminite
Glass Gorge-South	Trezona	RK250312.67	275.50	-5.94	-12.47	Laminite
Glass Gorge-South	Trezona	RK250312.68	276.00	-	-	Laminite
Glass Gorge-South	Trezona	RK250312.69	277.00	-	-	Laminite
Glass Gorge-South	Trezona	RK250312.70	277.50	-	-	Laminite
Glass Gorge-South	Trezona	RK250312.71	278.50	-6.33	-12.79	Laminite
Glass Gorge-South	Trezona	RK250312.72	279.50	-	-	Laminite
Glass Gorge-South	Trezona	RK250312.73	281.50	-	-	Laminite
Glass Gorge-South	Trezona	RK250312.74	282.00	-	-	Laminite
Glass Gorge-South	Trezona	RK250312.75	283.00	-	-	Laminite
Glass Gorge-South	Trezona	RK250312.76	284.25	-	-	Laminite
Glass Gorge-South	Trezona	RK250312.77	285.50	-5.78	-13.10	Laminite
Glass Gorge-South	Trezona	RK250312.78	286.00	-	-	Laminite
Glass Gorge-South	Trezona	RK250312.79	287.00	-	-	Stromatolite
Glass Gorge-South	Trezona	RK250312.80	288.50	-5.14	-14.78	Laminite
Glass Gorge-South	Trezona	RK250312.81	289.75	-	-	Sand Drape
Glass Gorge-South	Trezona	RK250312.82	290.50	-	-	Laminite
Glass Gorge-South	Trezona	RK250312.83	291.00	-3.84	-13.36	Laminite
Warraweena	Trezona	RK240413.3^	14.00	-5.80	-13.23	Laminite
Warraweena	Trezona	RK240413.3*	14.00	-5.70	-	Laminite
Warraweena	Trezona	RK240413.4	15.00	-6.74	-	Laminite
Warraweena	Trezona	RK240413.5	15.25	-7.87	-	Stromatolite
Warraweena	Trezona	RK240413.7	20.25	-5.91	-11.86	Siltstone
Warraweena	Trezona	RK240413.7	20.25	-5.87	-11.64	Siltstone
Warraweena	Trezona	RK240413.8	21.00	-7.51	-	Mudflake Conglomerate
Warraweena	Trezona	RK240413.9	22.25	-7.98	-	Mudflake Conglomerate
Warraweena	Trezona	RK240413.11^	27.25	-7.58	-13.95	Laminite
Warraweena	Trezona	RK240413.12	30.00	-5.45	-7.85	Siltstone
Warraweena	Trezona	RK240413.13	33.50	-7.72	-12.77	Siltstone

Section	Formation	Sample No.	Height (m)	$\delta^{13}C_{carb}$	$\delta^{18}O_{carb}$	Lithology
Warraweena	Trezona	RK240413.14	35.50	-7.68	-	Mudflake Conglomerate
Warraweena	Trezona	RK240413.15	36.75	-6.20	-9.81	Siltstone
Warraweena	Trezona	RK240413.15	36.75	-5.99	-9.56	Siltstone
Warraweena	Trezona	RK240413.16^	37.75	-7.77	-16.11	Mudflake Conglomerate
Warraweena	Trezona	RK240413.17	43.25	-6.80	-10.04	Siltstone
Warraweena	Trezona	RK240413.18	45.00	-6.13	-11.99	Cemented Sand
Warraweena	Trezona	RK240413.19A	46.75	-9.05	-	Laminite
Warraweena	Trezona	RK240413.19B	46.75	-7.95	-	Laminite
Warraweena	Trezona	RK240413.20^	47.75	-8.37	-14.19	Mudflake Conglomerate
Warraweena	Trezona	RK240413.20*	47.75	-8.96	-	Mudflake Conglomerate
Warraweena	Trezona	RK240413.21	48.50	-7.73	-	Mudflake Conglomerate
Warraweena	Trezona	RK240413.25	53.75	-6.77	-5.25	Siltstone
Warraweena	Trezona	RK240413.27A	58.50	-7.77	-	Mudflake Conglomerate
Warraweena	Trezona	RK240413.27B	58.50	-7.70	-	Mudflake Conglomerate
Warraweena	Trezona	RK240413.28A^	59.50	-7.58	-14.24	Mudflake Conglomerate
Warraweena	Trezona	RK240413.28A*	59.50	-7.86	-	Mudflake Conglomerate
Warraweena	Trezona	RK240413.28B	59.50	-2.44	-	Mudflake Conglomerate
Warraweena	Trezona	RK240413.30	65.00	-5.25	-	Siltstone
Warraweena	Trezona	RK240413.29^	67.25	-6.74	-12.73	Mudflake Conglomerate
Warraweena	Trezona	RK240413.29*	67.25	-7.43	-	Mudflake Conglomerate
Warraweena	Trezona	RK240413.31	73.50	-6.07	-	Cemented Sand
Warraweena	Trezona	RK240413.33	79.75	-7.62	-	Mudflake Conglomerate
Warraweena	Trezona	RK240413.34^	80.75	-4.60	-4.74	Siltstone
Warraweena	Trezona	RK240413.34*	80.75	-4.65	-	Siltstone
Warraweena	Trezona	RK240413.35	82.75	-7.69	-	Mudflake Conglomerate
Warraweena	Trezona	RK240413.36	84.50	-8.31	-	Mudflake Conglomerate
Warraweena	Trezona	RK240413.37^	86.25	-5.63	-8.85	Siltstone
Warraweena	Trezona	RK240413.37*	86.25	-5.73	-	Siltstone
Warraweena	Trezona	RK240413.38	88.25	-1.44	-	Siltstone
Warraweena	Trezona	RK240413.39	90.00	-7.95	-	Mudflake Conglomerate
Warraweena	Trezona	RK240413.40	93.00	-7.39	-	Mudflake Conglomerate
Warraweena	Trezona	RK240413.41	94.25	-7.95	-	Mudflake Conglomerate
Warraweena	Trezona	RK240413.42^	95.75	-6.66	-11.89	Laminite
Warraweena	Trezona	RK240413.42*	95.75	-6.02	-	Laminite
Warraweena	Trezona	RK240413.43	96.50	-7.43	-	Intraclast Conglomerate
Warraweena	Trezona	RK240413.44^	98.00	-7.24	-14.06	Intraclast Conglomerate
Warraweena	Trezona	RK240413.45	100.00	-7.06	-	Intraclast Conglomerate
Warraweena	Trezona	RK240413.46	101.00	-5.70	-	Intraclast Conglomerate
Warraweena	Trezona	RK240413.47^	102.00	-5.15	-7.95	Laminite
Warraweena	Trezona	RK240413.47*	102.00	-5.28	-	Laminite
Warraweena	Trezona	RK240413.48	103.00	-5.34	-	Laminite
Warraweena	Trezona	RK240413.49	104.00	-1.50	-	Laminite
Warraweena	Trezona	RK240413.50^	105.00	-6.98	-14.67	Laminite
Warraweena	Trezona	RK240413.50*	105.00	-7.00	-	Laminite
Warraweena	Trezona	RK240413.51	106.75	-6.25	-	Laminite
Warraweena	Trezona	RK240413.52	108.75	-7.06	-	Laminite
Warraweena	Trezona	RK240413.53^	110.00	-6.12	-14.54	Laminite
Warraweena	Trezona	RK240413.53*	110.00	-6.11	-	Laminite
Warraweena	Trezona	RK240413.54	111.25	-6.51	-14.89	Laminite
Warraweena	Trezona	RK240413.54*	111.25	-6.51	-14.89	Laminite

Section	Formation	Sample No.	Height (m)	$\delta^{13}C_{carb}$	$\delta^{18}O_{carb}$	Lithology
Warraweena	Trezona	RK240413.55	113.25	-4.19	-10.74	Dolomitized Laminite
Warraweena	Trezona	RK240413.56	114.50	-4.64	-9.62	Dolomitized Laminite
Warraweena	Trezona	RK240413.56	114.50	-4.64	-9.62	Dolomitized Laminite
Warraweena	Trezona	RK240413.57	115.25	-4.30	-19.76	Dolomitized Laminite
Warraweena	Trezona	RK240413.58	115.25	-2.75	-1.92	Dolomitized Laminite
Warraweena	Trezona	RK240413.59	115.25	-3.57	-1.73	Dolomitized Laminite
Warraweena	Trezona	RK240413.59^	115.25	-3.89	-1.55	Dolomitized Laminite
Chambers Gorge	Trezona	RK180413.1	0.00	-1.57	-9.07	Mudflake Conglomerate
Chambers Gorge	Trezona	RK180413.2	3.25	-8.35	-16.08	Mudflake Conglomerate
Chambers Gorge	Trezona	RK180413.3	5.00	-8.29	-15.71	Stromatolite
Chambers Gorge	Trezona	RK180413.4	13.00	-	-	Siltstone Cement
Chambers Gorge	Trezona	RK180413.5	16.00	-	-	Mudflake Conglomerate
Chambers Gorge	Trezona	RK180413.6	16.50	-	-	Siltstone Concretion
Chambers Gorge	Trezona	RK180413.7	17.75	-	-	Laminated Siltstone
Chambers Gorge	Trezona	RK180413.8	25.00	-6.96	-14.08	Mudflake Conglomerate
Chambers Gorge	Trezona	RK180413.9	29.00	-	-	Siltstone Cement
Chambers Gorge	Trezona	RK180413.10	37.40	-	-	Siltstone
Chambers Gorge	Trezona	RK180413.11	47.75	-	-	Siltstone
Chambers Gorge	Trezona	RK180413.12	48.00	-	-	Siltstone
Chambers Gorge	Trezona	RK180413.13	56.00	-	-	Mudflake Conglomerate
Chambers Gorge	Trezona	RK180413.14	58.00	-	-	Mudflake Conglomerate
Chambers Gorge	Trezona	RK180413.15	62.00	-	-	Mudflake Conglomerate
Bunkers Range	Trezona	RK290411.1	0.39	-5.36	-7.31	Siltstone
Bunkers Range	Trezona	RK290411.2	1.18	-	-	Siltstone
Bunkers Range	Trezona	RK290411.3^	7.46	-8.39	-12.60	Mudflake Conglomerate
Bunkers Range	Trezona	RK290411.4^	25.51	-8.12	-11.74	Mudflake Conglomerate
Bunkers Range	Trezona	RK290411.5^	36.50	-7.85	-10.31	Mudflake Conglomerate
Bunkers Range	Trezona	RK290411.6	38.86	-5.58	-7.71	Siltstone
Bunkers Range	Trezona	RK290411.7	41.61	-	-	Mudflake Conglomerate
Bunkers Range	Trezona	RK290411.8	41.61	-4.92	-7.73	Siltstone
Bunkers Range	Trezona	RK290411.9^	42.39	-8.60	-11.13	Mudflake Conglomerate
Bunkers Range	Trezona	RK290411.10	42.78	-	-	Mudflake Conglomerate
Bunkers Range	Trezona	RK290411.11	Float	-	-	Mudcracked Marl
Bunkers Range	Trezona	RK290411.12	43.18	-5.42	-8.20	Sandstone
Bunkers Range	Trezona	RK290411.13	43.57	-4.95	-8.01	Sandstone
Bunkers Range	Trezona	RK290411.14	43.96	-4.53	-8.05	Sandstone
Bunkers Range	Trezona	RK290411.15^	45.14	-7.66	-10.27	Mudflake Conglomerate
Bunkers Range	Trezona	RK290411.16	46.32	-	-	Mudflake Conglomerate
Bunkers Range	Trezona	RK290411.17	47.10	-	-	Mudflake Conglomerate
Bunkers Range	Trezona	RK290411.18	47.10	-5.04	-7.21	Sandstone
Bunkers Range	Trezona	RK290411.19	47.89	-	-	Mudflake Conglomerate
Bunkers Range	Trezona	RK290411.20	48.28	-	-	Mudflake Conglomerate
Bunkers Range	Trezona	RK290411.21	48.67	-	-	Mudflake Conglomerate
Bunkers Range	Trezona	RK290411.22	49.06	-	-	Mudflake Conglomerate
Bunkers Range	Trezona	RK290411.23^	49.46	-8.20	-11.07	Mudflake Conglomerate
Bunkers Range	Trezona	RK290411.24	Float	-	-	Mudcracked Marl
Bunkers Range	Trezona	RK290411.25	Float	-	-	Mudcracked Marl
Bunkers Range	Trezona	RK290411.26^	55.34	-7.51	-8.80	Sandstone
Bunkers Range	Trezona	RK290411.27	56.91	-	-	Mudflake Conglomerate
Bunkers Range	Trezona	RK290411.28	58.88	-4.58	-7.91	Sandstone

Section	Formation	Sample No.	Height (m)	$\delta^{13}C_{carb}$	$\delta^{18}O_{carb}$	Lithology
Bunkers Range	Trezona	RK290411.29^	60.05	-7.75	-11.11	Mudflake Conglomerate
Bunkers Range	Trezona	RK290411.30	60.84	-	-	Mudflake Conglomerate
Bunkers Range	Trezona	RK290411.31	61.62	-	-	Strom
Bunkers Range	Trezona	RK290411.32	62.80	-	-	Mudflake Conglomerate
Bunkers Range	Trezona	RK290411.33^	64.37	-6.67	-8.39	Mudflake Conglomerate
Bunkers Range	Trezona	RK290411.34	65.55	-	-	Laminated sand
Bunkers Range	Trezona	RK290411.35	67.51	-	-	Mudflake Conglomerate
Bunkers Range	Trezona	RK290411.36	67.90	-	-	Mudflake Conglomerate
Bunkers Range	Trezona	RK290411.37	69.87	-	-	Intraclast Conglomerate
Bunkers Range	Trezona	RK290411.38^	70.65	-8.32	-9.97	Sandstone
Bunkers Range	Trezona	RK290411.39	71.83	-	-	Mudflake Conglomerate
Bunkers Range	Trezona	RK290411.40	72.22	-	-	Sandstone
Bunkers Range	Trezona	RK290411.41	108.72	-4.88	-7.73	Siltstone
Bunkers Range	Trezona	RK290411.42^	109.51	-8.47	-11.77	Mudflake Conglomerate
Bunkers Range	Trezona	RK290411.43	110.69	-	-	Mudflake Conglomerate
Bunkers Range	Trezona	RK290411.44	113.04	-	-	Mudflake Conglomerate
Bunkers Range	Trezona	RK290411.45	114.61	-	-	Marl
Bunkers Range	Trezona	RK290411.46	114.61	-	-	Mudflake Conglomerate
Bunkers Range	Trezona	RK290411.47^	114.61	-9.00	-9.87	Mudflake Conglomerate
Bunkers Range	Trezona	RK290411.48	116.57	-	-	Mudflake Conglomerate
Bunkers Range	Trezona	RK290411.49	Float	-	-	Mudflake Conglomerate
Bunkers Range	Trezona	RK290411.50	Float	-	-	Red Sands (Laminated)
Bunkers Range	Trezona	RK290411.51^	123.25	-8.61	-11.23	Mudflake Conglomerate
Bunkers Range	Trezona	RK290411.52	125.60	-	-	Mudflake Conglomerate
Bunkers Range	Trezona	RK290411.53	127.96	-	-	Mudflake Conglomerate
Bunkers Range	Trezona	RK290411.54^	129.53	-8.54	-10.31	Mudflake Conglomerate
Bunkers Range	Trezona	RK290411.55^	136.98	-7.54	-9.93	Laminated Sand
Bunkers Range	Trezona	RK290411.56^	140.12	-8.62	-10.50	Mudflake Conglomerate
Bunkers Range	Trezona	RK290411.57	140.91	-	-	Laminated Sand
Bunkers Range	Trezona	RK290411.58	142.09	-	-	Marl
Bunkers Range	Trezona	RK290411.59	142.87	-	-	Marl
Bunkers Range	Trezona	RK300411.1	143-147.5	-	-	Intraclast Conglomerate
Bunkers Range	Trezona	RK300411.2	143-147.5	-	-	Marl
Bunkers Range	Trezona	RK300411.3	143-147.5	-	-	Oolitic Conglomerate
Bunkers Range	Trezona	RK300411.4	143-147.5	-	-	Marl
Bunkers Range	Trezona	RK300411.5	143-147.5	-	-	Oolitic Conglomerate
Bunkers Range	Trezona	RK300411.6	143-147.5	-	-	Marl
Bunkers Range	Trezona	RK300411.7	143-147.5	-	-	Mudflake Conglomerate
Bunkers Range	Trezona	RK300411.8	143-147.5	-	-	Marl
Bunkers Range	Trezona	RK300411.9	143-147.5	-	-	Mudflake Conglomerate
Bunkers Range	Trezona	RK300411.10	143-147.5	-	-	Mudflake Conglomerate
Bunkers Range	Trezona	RK300411.11	143-147.5	-	-	Marl
Bunkers Range	Trezona	RK300411.12	143-147.5	-	-	Mudflake Conglomerate
Bunkers Range	Trezona	RK300411.13	143-147.5	-	-	Marl
Bunkers Range	Trezona	RK300411.14	143-147.5	-	-	Mudflake Conglomerate
Bunkers Range	Trezona	RK300411.15	143-147.5	-	-	Marl
Bunkers Range	Trezona	RK300411.16	143-147.5	-	-	Mudflake Conglomerate
Bunkers Range	Trezona	RK300411.17	143-147.5	-	-	Marl
Bunkers Range	Trezona	RK300411.18	143-147.5	-	-	Marl
Bunkers Range	Trezona	RK300411.19	143-147.5	-	-	Marl

Section	Formation	Sample No.	Height (m)	$\delta^{13}C_{carb}$	$\delta^{18}O_{carb}$	Lithology
Bunkers Range	Trezona	RK300411.20	143-147.5	-	-	Mudflake Conglomerate
Bunkers Range	Trezona	RK300411.21	143-147.5	-	-	Marl
Bunkers Range	Trezona	RK300411.22^	147.50	-8.27	-10.56	Mudflake Conglomerate
Bunkers Range	Trezona	RK300411.23	147.5-154	-	-	Marl
Bunkers Range	Trezona	RK300411.24	147.5-154	-	-	Mudflake Conglomerate
Bunkers Range	Trezona	RK300411.25	147.5-154	-	-	Marl
Bunkers Range	Trezona	RK300411.26	147.5-154	-	-	Mudflake Conglomerate
Bunkers Range	Trezona	RK300411.27	147.5-154	-	-	Marl
Bunkers Range	Trezona	RK300411.28	147.5-154	-	-	Mudflake Conglomerate
Bunkers Range	Trezona	RK300411.29	147.5-154	-	-	Marl
Bunkers Range	Trezona	RK300411.30	147.5-154	-	-	Mudflake Conglomerate
Bunkers Range	Trezona	RK300411.31	147.5-154	-	-	Marl
Bunkers Range	Trezona	RK300411.32	147.5-154	-	-	Mudflake Conglomerate
Bunkers Range	Trezona	RK300411.33	147.5-154	-	-	Marl
Bunkers Range	Trezona	RK300411.34	147.5-154	-	-	Marl
Bunkers Range	Trezona	RK300411.35	147.5-154	-	-	Mudflake Conglomerate
Bunkers Range	Trezona	RK300411.36	147.5-154	-	-	Marl
Bunkers Range	Trezona	RK300411.37	147.5-154	-	-	Mudflake Conglomerate
Bunkers Range	Trezona	RK300411.38	147.5-154	-	-	Marl
Bunkers Range	Trezona	RK300411.39	147.5-154	-	-	Mudflake Conglomerate
Bunkers Range	Trezona	RK300411.40	154.25	-	-	Mudflake Conglomerate
Bunkers Range	Trezona	RK300411.41^	155.43	-9.33	-10.84	Mudflake Conglomerate
Bunkers Range	Trezona	RK300411.42	157.79	-	-	Red Sands (Laminated)
Bunkers Range	Trezona	RK300411.43	159.75	-	-	Red Sands (Laminated)
Bunkers Range	Trezona	RK300411.44	160.53	-	-	Mudflake Conglomerate
Bunkers Range	Trezona	RK300411.45^	161.71	-8.68	-9.34	Red Sands (Laminated)
Bunkers Range	Trezona	RK300411.46	163.28	-	-	Mudflake Conglomerate
Bunkers Range	Trezona	RK300411.47	163.67	-	-	Stromatolite
Bunkers Range	Trezona	RK300411.48^	165.24	-8.61	-8.32	Mudflake Conglomerate
Bunkers Range	Trezona	RK300411.49	166.81	-	-	Red Sands (Laminated)
Bunkers Range	Trezona	RK300411.50^	167.99	-7.76	-10.99	Strom
Bunkers Range	Trezona	RK300411.51	170.35	-	-	Mudflake Conglomerate
Bunkers Range	Trezona	RK300411.52	171.13	-	-	Mud w/ sand drapes
Bunkers Range	Trezona	RK300411.53	173.49	-	-	Laminated Fine Sand
Bunkers Range	Trezona	RK300411.54	174.27	-	-	Stromatolite
Bunkers Range	Trezona	RK300411.55^	175.84	-7.12	-10.13	Oolitic Grainstone
Bunkers Range	Trezona	RK300411.56	175.84	-	-	Oolitic Grainstone
Bunkers Range	Trezona	RK300411.57	177.41	-	-	Marl with Sandy Drapes
Bunkers Range	Trezona	RK300411.58^	182.12	-8.85	-7.93	Microsparite
Bunkers Range	Trezona	RK300411.59^	186.05	-6.84	-9.14	Microsparite
Bunkers Range	Trezona	RK300411.60	187.22	-	-	Oolitic Grainstone
Bunkers Range	Trezona	RK300411.61	187.62	-	-	Vein Calcite
Bunkers Range	Trezona	RK300411.62^	189.58	-7.49	-9.54	Oolitic Grainstone
Bunkers Range	Trezona	RK300411.63	191.15	-	-	Oolitic Grainstone
Bunkers Range	Trezona	RK300411.64^	192.72	-7.13	-8.92	Oolitic Grainstone
Bunkers Range	Trezona	RK300411.65	195.47	-	-	Oolitic Grainstone
Bunkers Range	Trezona	RK300411.66^	198.21	-7.17	-8.61	Microbialite
Bunkers Range	Trezona	RK300411.67^	200.96	-6.86	-9.39	Intraclastic Breccia
Bunkers Range	Trezona	RK300411.68	203.71	-	-	Intraclastic Breccia
Bunkers Range	Trezona	RK300411.69^	208.03	-7.28	-8.12	Microsparite

Section	Formation	Sample No.	Height (m)	$\delta^{13}C_{carb}$	$\delta^{18}O_{carb}$	Lithology
Bunkers Range	Trezona	RK300411.70^	213.52	-6.53	-9.13	Intraclastic Breccia
Bunkers Range	Trezona	RK300411.71	217.84	-	-	Microbialite
Bunkers Range	Trezona	RK300411.72^	218.62	-6.78	-9.85	Stromatolite
Bunkers Range	Trezona	RK300411.73	223.33	-	-	Microsparite
Bunkers Range	Trezona	RK300411.74	220.59	-	-	Microsparite
Bunkers Range	Trezona	RK300411.75^	224.90	-6.77	-8.45	Intraclastic Breccia
Bunkers Range	Trezona	RK300411.76	229.61	-	-	Stromatolite
Bunkers Range	Trezona	RK300411.77^	233.54	-6.48	-9.22	Intraclastic Breccia
Bunkers Range	Trezona	RK300411.78	235.50	-	-	Stromatolite
Bunkers Range	Trezona	RK300411.79	237.46	-	-	Stromatolite
Bunkers Range	Trezona	RK300411.80^	241.39	-6.22	-9.44	Stromatolite
Bunkers Range	Trezona	RK300411.81	243.74	-	-	Stromatolite
Bunkers Range	Trezona	RK300411.82^	246.10	-5.80	-9.41	Stromatolite
Bunkers Range	Trezona	RK300411.83	249.24	-	-	Stromatolite
Bunkers Range	Trezona	RK300411.84^	251.20	-5.55	-9.59	Stromatolite
Bunkers Range	Trezona	RK300411.85	254.73	-	-	Stromatolite
Bunkers Range	Trezona	RK300411.86^	259.44	-7.49	-5.84	Stromatolite
Bunkers Range	Trezona	RK300411.87	262.19	-	-	Microsparite
Bunkers Range	Trezona	RK300411.88^	262.98	-5.66	-8.76	Oolitic Grainstone
Bunkers Range	Trezona	RK300411.89	264.15	-	-	Stromatolite
Bunkers Range	Trezona	RK300411.90^	265.72	-5.76	-8.99	Stromatolite
Bunkers Range	Trezona	RK300411.91	268.08	-	-	Stromatolite
Bunkers Range	Trezona	RK300411.92^	268.86	-5.46	-8.90	Oolitic Grainstone
Bunkers Range	Trezona	RK010511.1^	276.32	-5.64	-9.52	Laminite
Bunkers Range	Trezona	RK010511.2	276.71	-	-	Microsparite
Bunkers Range	Trezona	RK010511.3	279.07	-	-	Microsparite
Bunkers Range	Trezona	RK010511.4	279.46	-	-	Intraclast Conglomerate
Bunkers Range	Trezona	RK010511.5	281.82	-	-	Intraclast Conglomerate
Bunkers Range	Trezona	RK010511.6	282.60	-	-	Intraclast Conglomerate
Bunkers Range	Trezona	RK010511.7	Float	-	-	-
Bunkers Range	Trezona	RK010511.8	279.85	-	-	Intraclast Conglomerate
Bunkers Range	Trezona	RK010511.9	280.01	-	-	Intraclast Conglomerate
Bunkers Range	Trezona	RK010511.10	280.25	-	-	Intraclast Conglomerate
Bunkers Range	Trezona	RK010511.11	280.48	-	-	Marl
Bunkers Range	Trezona	RK010511.12	280.72	-	-	Intraclast Conglomerate
Bunkers Range	Trezona	RK010511.13	281.03	-	-	Marl
Bunkers Range	Trezona	RK010511.14	281.27	-	-	Intraclast Conglomerate
Bunkers Range	Trezona	RK010511.15	281.42	-	-	Marl
Bunkers Range	Trezona	RK010511.16	281.66	-	-	Intraclast Conglomerate
Bunkers Range	Trezona	RK010511.17	281.97	-	-	Marl
Bunkers Range	Trezona	RK010511.18	282.21	-	-	Intraclast Conglomerate
Bunkers Range	Trezona	RK010511.19	282.60	-	-	Marl
Bunkers Range	Trezona	RK010511.20	282.99	-	-	Intraclast Conglomerate
Bunkers Range	Trezona	RK010511.21	283.39	-	-	Marl
Bunkers Range	Trezona	RK010511.22	283.78	-	-	Intraclast Conglomerate
Bunkers Range	Trezona	RK010511.23	286.92	-	-	Intraclast Conglomerate
Bunkers Range	Trezona	RK010511.24	287.31	-	-	Stromatolite
Bunkers Range	Trezona	RK010511.25	287.70	-	-	Intraclast Conglomerate
Bunkers Range	Trezona	RK010511.26	287.78	-	-	Marl
Bunkers Range	Trezona	RK010511.27^	287.94	-5.76	-7.40	Oolitic Grainstone

Section	Formation	Sample No.	Height (m)	$\delta^{13}C_{carb}$	$\delta^{18}O_{carb}$	Lithology
Bunkers Range	Trezona	RK010511.28	288.10	-	-	Intraclast Conglomerate
Bunkers Range	Trezona	RK010511.29	291.24	-	-	Laminite
Bunkers Range	Trezona	RK010511.30	293.20	-	-	Laminite
Bunkers Range	Trezona	RK010511.31	294.77	-	-	Stromatolite
Bunkers Range	Trezona	RK010511.32	296.73	-	-	Stromatolite
Bunkers Range	Trezona	RK010511.33	299.09	-	-	Stromatolite
Bunkers Range	Trezona	RK010511.34	305.76	-	-	Stromatolite
Bunkers Range	Trezona	RK010511.35^	309.29	-4.03	-9.14	Stromatolite
Bunkers Range	Trezona	RK010511.36^	313.61	-3.75	-7.87	Stromatolite
Bunkers Range	Trezona	RK010511.37	320.67	-	-	Stromatolite
Bunkers Range	Trezona	RK010511.38^	329.70	-3.71	-9.06	Stromatolite
Bunkers Range	Trezona	RK010511.39^	340.30	-2.78	-8.72	Stromatolite
Bunkers Range	Trezona	RK010511.40	345.01	-	-	Intraclast Conglomerate
Bunkers Range	Trezona	RK010511.41^	346.58	-2.80	-10.24	Stromatolite
Bunkers Range	Trezona	RK010511.42^	353.64	-2.83	-10.74	Stromatolite
Bunkers Range	Trezona	RK010511.43^	357.18	-3.36	-10.49	Stromatolite
Bunkers Range	Trezona	RK010511.44^	362.28	-3.26	-11.77	Stromatolite
Bunkers Range	Trezona	RK010511.45^	362.28	-3.19	-11.38	Stromatolite
Bunkers Range	Trezona	RK010511.46^	364.24	-3.33	-10.88	Red Siltstone
Bunkers Range	Trezona	RK010511.47^	365.81	-3.00	-8.93	Red Siltstone
Bunkers Range	Trezona	RK010511.48^	408.20	-3.34	-7.55	Red Siltstone
Bunkers Range	Enorama	RK050111B.1	9.42	-	-	Siltstone
Bunkers Range	Enorama	RK050111B.2	16.49	-	-	Caliche
Bunkers Range	Enorama	RK050111B.3	27.08	-	-	Caliche
Bunkers Range	Enorama	RK050111B.4	35.72	-	-	Siltstone
Bunkers Range	Enorama	RK050111B.5	37.29	-	-	Siltstone Concretion
Bunkers Range	Enorama	RK050111B.6	38.86	-	-	Siltstone
Bunkers Range	Enorama	RK050111B.7	43.18	-	-	Siltstone
Bunkers Range	Enorama	RK050111B.8	45.92	-	-	Siltstone
Bunkers Range	Enorama	RK050111B.9	49.46	-	-	Siltstone
Bunkers Range	Enorama	RK050111B.10	54.56	-	-	Siltstone
Bunkers Range	Trezona	RK050111B.11	111.25	-	-	Laminated Fine Sand
Bunkers Range	Trezona	RK050111B.12	112.75	-	-	Laminated Fine Sand
Bunkers Range	Trezona	RK050111B.13	113.00	-	-	Siltstone
Bunkers Range	Trezona	RK050111B.14	113.75	-	-	Laminated Fine Sand
Bunkers Range	Trezona	RK050111B.15	114.25	-	-	Laminated Fine Sand
Bunkers Range	Trezona	RK050111B.16	115.00	-	-	Laminated Fine Sand
Bunkers Range	Trezona	RK050111B.17	115.75	-	-	Laminated Fine Sand
Bunkers Range	Trezona	RK050111B.18	116.25	-	-	Laminated Fine Sand
Bunkers Range	Trezona	RK050111B.19	117.25	-	-	Laminated Fine Sand
Bunkers Range	Trezona	RK050111B.20	121.25	-	-	Mudflake Conglomerate
Bunkers Range	Trezona	RK050111B.21	122.75	-	-	Mudflake Conglomerate
Bunkers Range-2	Trezona	MK061596.1	0.79	-9.17	-11.78	Mudflake Conglomerate
Bunkers Range-2	Trezona	MK061596.2	1.18	-8.58	-12.02	Mudflake Conglomerate
Bunkers Range-2	Trezona	MK061596.2	1.18	-8.67	-11.85	Mudflake Conglomerate
Bunkers Range-2	Trezona	MK061596.3	3.14	-9.18	-10.96	Mudflake Conglomerate
Bunkers Range-2	Trezona	MK061596.3	3.14	-8.37	-12.33	Mudflake Conglomerate
Bunkers Range-2	Trezona	MK061596.4^	7.85	-9.99	-11.27	Fine Sand
Bunkers Range-2	Trezona	MK061596.4*	7.85	-8.00	-10.49	Fine Sand
Bunkers Range-2	Trezona	MK061596.4**	7.85	-7.84	-10.29	Fine Sand

Section	Formation	Sample No.	Height (m)	$\delta^{13}C_{carb}$	$\delta^{18}O_{carb}$	Lithology
Bunkers Range-2	Trezona	MK061596.5	10.99	-10.25	-11.23	Fine Sand
Bunkers Range-2	Trezona	MK061596.6	34.54	-8.97	-11.63	Mudflake Conglomerate
Bunkers Range-2	Trezona	MK061596.7	35.33	-8.67	-10.78	Mudflake Conglomerate
Bunkers Range-2	Trezona	MK061596.8	36.11	-9.12	-8.85	Mudflake Conglomerate
Bunkers Range-2	Trezona	MK061596.8	36.11	-8.79	-10.60	Mudflake Conglomerate
Bunkers Range-2	Trezona	MK061596.9^	36.90	-8.49	-11.38	Mudflake Conglomerate
Bunkers Range-2	Trezona	MK061596.9*	36.90	-8.75	-10.44	Mudflake Conglomerate
Bunkers Range-2	Trezona	MK061596.10	37.29	-9.36	-7.38	Intraclastic Grainstone
Bunkers Range-2	Trezona	MK061596.10	37.29	-8.82	-9.97	Intraclastic Grainstone
Bunkers Range-2	Trezona	MK061596.11	37.68	-8.62	-11.38	Intraclastic Grainstone
Bunkers Range-2	Trezona	MK061596.11*	37.68	-8.74	-11.25	Intraclastic Grainstone
Bunkers Range-2	Trezona	MK061596.12	39.25	-8.35	-11.50	Intraclastic Grainstone
Bunkers Range-2	Trezona	MK061596.13	47.10	-8.93	-11.33	Mudflake Conglomerate
Bunkers Range-2	Trezona	MK061596.14	54.95	-8.89	-10.48	Intraclastic Grainstone
Bunkers Range-2	Trezona	MK061596.14	54.95	-9.28	-10.67	Intraclastic Grainstone
Bunkers Range-2	Trezona	MK061596.15^	40.00	-8.66	-12.22	Limestone
Bunkers Range-2	Trezona	MK061596.16	43.50	-8.53	-11.37	Stromatolite
Bunkers Range-2	Trezona	MK061596.17	46.50	-8.82	-10.40	Limestone
Bunkers Range-2	Trezona	MK061596.17*	46.50	-8.93	-10.30	Limestone
Bunkers Range-2	Trezona	MK061596.18	54.00	-8.60	-9.89	Intraclastic Grainstone
Bunkers Range-2	Trezona	MK061596.18	54.00	-8.92	-9.89	Limestone
Bunkers Range-2	Trezona	MK061596.19	60.00	-8.31	-11.42	Limestone
Bunkers Range-2	Trezona	MK061596.20	61.00	-9.06	-11.09	Intraclastic Grainstone
Bunkers Range-2	Trezona	MK061596.21	62.00	-8.86	-10.18	Intraclastic Grainstone
Bunkers Range-2	Trezona	MK061596.22	63.20	-8.58	-10.93	Microbial Mat
Bunkers Range-2	Trezona	MK061596.22	63.20	-8.55	-10.98	Limestone
Bunkers Range-2	Trezona	MK061596.23	66.00	-8.83	-11.07	Intraclastic Grainstone
Bunkers Range-2	Trezona	MK061596.24	float	-8.25	-10.58	Mudflake Conglomerate
Bunkers Range-2	Trezona	MK061596.25	float	-8.41	-11.20	Oolitic Grainstone
Bunkers Range-2	Trezona	MK061596.25*	float	-8.29	-10.79	Oolitic Grainstone
Bunkers Range-2	Trezona	MK061596.26	76.00	-8.45	-10.51	Oolitic Grainstone
Bunkers Range-2	Trezona	MK061596.27	80.00	-9.85	-10.40	Intraclastic
Bunkers Range-2	Trezona	MK061596.27	80.00	-8.57	-10.29	Limestone
Bunkers Range-2	Trezona	MK061596.28^	85.00	-8.74	-10.61	Limestone
Bunkers Range-2	Trezona	MK061596.29	86.00	-8.34	-10.01	Intraclastic Grainstone
Bunkers Range-2	Trezona	MK061596.30	90.00	-	-	Limestone
Bunkers Range-2	Trezona	MK061596.31	91.00	-	-	Intraclastic Grainstone
Bunkers Range-2	Trezona	MK061596.31	91.00	-8.94	-10.43	Limestone
Bunkers Range-2	Trezona	MK061596.32^	92.00	-8.44	-10.84	Limestone
Bunkers Range-2	Trezona	MK061596.33^	93.00	-7.80	-11.14	Intraclastic Grainstone
Bunkers Range-2	Trezona	MK061596.33*	93.00	-8.14	-10.53	Intraclastic Grainstone
Bunkers Range-2	Trezona	MK061596.34	94.00	-8.08	-10.36	Laminite
Bunkers Range-2	Trezona	MK061596.34*	94.00	-7.94	-10.34	Laminite
Bunkers Range-2	Trezona	MK061596.35	98.00	-7.65	-10.58	Limestone
Bunkers Range-2	Trezona	MK061696.10	float	-	-	Limestone
Bunkers Range-2	Trezona	MK061696.11	197.82	-	-	Limestone
Bunkers Range-2	Trezona	MK061696.12^	200.96	-6.74	-9.31	Limestone
Bunkers Range-2	Trezona	MK061696.13	204.10	-6.41	-8.73	Stromatolite
Bunkers Range-2	Trezona	MK061696.14	205.67	-6.44	-8.03	Limestone
Bunkers Range-2	Trezona	MK061696.14*	205.67	-6.37	-7.95	Limestone

Section	Formation	Sample No.	Height (m)	$\delta^{13}C_{carb}$	$\delta^{18}O_{carb}$	Lithology
Bunkers Range-2	Trezona	MK061696.15	210.38	-6.35	-8.19	Laminite
Bunkers Range-2	Trezona	MK061696.16^	215.09	-8.48	-11.88	Limestone
Bunkers Range-2	Trezona	MK061696.17	219.80	-6.00	-8.24	Laminite
Bunkers Range-2	Trezona	MK061696.18	233.93	-5.82	-8.58	Stromatolite
Bunkers Range-2	Trezona	MK061696.19	235.50	-5.95	-8.36	Microsparite
Bunkers Range-2	Trezona	MK061696.20	237.07	-5.93	-8.42	Oolitic Grainstone
Bunkers Range-2	Trezona	MK061696.21^	238.64	-5.71	-8.52	Limestone
Bunkers Range-2	Trezona	MK061696.22	241.78	-5.68	-7.65	Limestone
Bunkers Range-2	Trezona	MK061696.23	248.06	-5.52	-8.23	Limestone
Bunkers Range-2	Trezona	MK061696.24	252.77	-5.38	-8.37	Oolitic Grainstone
Bunkers Range-2	Trezona	MK061696.24*	252.77	-5.54	-7.77	Oolitic Grainstone
Bunkers Range-2	Trezona	MK061696.25	254.34	-5.65	-7.48	Oolitic Grainstone
Bunkers Range-2	Trezona	MK061696.26	255.91	-5.29	-8.46	Limestone
Bunkers Range-2	Trezona	MK061696.27	257.48	-5.03	-8.18	Intraclastic Grainstone
Bunkers Range-2	Trezona	MK061696.28	259.05	-4.52	-7.88	Marl
Bunkers Range-2	Trezona	MK061696.29	263.76	-4.48	-8.38	Laminite
Bunkers Range-2	Trezona	MK061696.29*	263.76	-3.95	-7.87	Laminite
Bunkers Range-2	Trezona	MK061696.30	268.47	-4.48	-8.74	Laminite
Bunkers Range-2	Trezona	MK061696.31^	271.61	-4.56	-9.27	Laminite
Bunkers Range-2	Trezona	MK061696.31*	271.61	-4.70	-9.14	Laminite
Bunkers Range-2	Trezona	MK061696.32	277.89	-4.60	-8.85	Limestone
Bunkers Range-2	Trezona	MK061696.33^	281.03	-4.02	-8.80	Limestone
Bunkers Range-2	Trezona	MK061696.34^	284.17	-3.37	-7.39	Limestone
Bunkers Range-2	Trezona	MK061696.35^	287.31	-3.87	-8.88	Limestone
Bunkers Range-2	Trezona	MK061696.36^	290.45	-3.62	-8.60	Limestone
Bunkers Range-2	Trezona	MK061696.37	293.59	-3.76	-8.84	Intraclastic Grainstone
Bunkers Range-2	Trezona	MK061696.38^	296.73	-3.60	-9.04	Limestone
Bunkers Range-2	Trezona	MK061696.39^	299.87	-3.38	-8.94	Limestone
Bunkers Range-2	Trezona	MK061696.40	304.58	-3.64	-9.58	Microsparite
Bunkers Range-2	Trezona	MK061696.40*	304.58	-3.61	-9.18	Microsparite
Bunkers Range-2	Trezona	MK061696.41	308.51	-2.84	-8.93	Limestone
Bunkers Range-2	Trezona	MK061696.42^	312.43	-2.84	-9.63	Limestone
Bunkers Range-2	Trezona	MK061696.43	314.79	-2.78	-10.20	Limestone
Bunkers Range-2	Trezona	MK061696.44	315.57	-2.88	-9.74	Microsparite
Bunkers Range-2	Trezona	MK061696.45	320.28	-3.21	-10.88	Microsparite
Umberatana Station	Amberoona	MK300312.7	1.00	-	-	Sandstone
Umberatana Station	Amberoona	MK300312.8	2.00	-7.40	-11.77	Laminated Sand
Umberatana Station	Amberoona	MK300312.9	5.00	-	-	Laminated Sand
Umberatana Station	Amberoona	MK300312.10	6.00	-	-	Laminated Sand
Umberatana Station	Amberoona	MK300312.11	7.00	-	-	Fe-Stained Breccia
Umberatana Station	Amberoona	MK300312.12	7.50	-	-	Fe-Stained Breccia
Umberatana Station	Amberoona	MK300312.13	9.00	-	-	Laminated Sand
Umberatana Station	Amberoona	MK300312.14	10.00	-	-	Laminated Sand
Umberatana Station	Amberoona	MK300312.15	10.50	-	-	Dolomicrite
Umberatana Station	Amberoona	MK300312.16	11.00	-	-	Laminated Sand
Umberatana Station	Amberoona	MK300312.17	12.00	-	-	Interbedded Sand/Marl
Umberatana Station	Amberoona	MK300312.18	14.00	-	-	Interbedded Sand/Marl
Umberatana Station	Amberoona	MK300312.19	15.00	-	-	Interbedded Sand/Marl
Umberatana Station	Amberoona	MK300312.20	15.50	-	-	Interbedded Sand/Marl
Umberatana Station	Amberoona	MK300312.21	19.00	-	-	Interbedded Sand/Marl

Section	Formation	Sample No.	Height (m)	$\delta^{13}C_{carb}$	$\delta^{18}O_{carb}$	Lithology
Umberatana Station	Amberoona	MK300312.22	20.00	-	-	Interbedded Sand/Marl
Umberatana Station	Amberoona	MK300312.23	23.00	-	-	Interbedded Sand/Marl
Umberatana Station	Amberoona	MK300312.24	29.00	-	-	Interbedded Sand/Marl
Umberatana Station	Amberoona	MK300312.25	33.00	-6.65	-13.25	Interbedded Sand/Marl
Umberatana Station	Amberoona	MK300312.26	35.00	-8.04	-13.21	Interbedded Sand/Marl
Umberatana Station	Amberoona	MK300312.27	37.00	-	-	Interbedded Sand/Marl
Umberatana Station	Amberoona	MK300312.28	39.00	-7.35	-13.55	Interbedded Sand/Marl
Umberatana Station	Amberoona	MK300312.29	40.00	-7.63	-13.50	Interbedded Sand/Marl
Umberatana Station	Amberoona	MK300312.30	41.00	-	-	Laminated Sand
Umberatana Station	Amberoona	MK300312.31	50.00	-	-	Laminated Sand
Umberatana Station	Amberoona	MK300312.32	60.00	-	-	Laminated Sand
Umberatana Station	Amberoona	MK300312.33	55.00	-	-	Laminated Sand
Umberatana Station	Amberoona	MK300312.34	60.00	-	-	Laminated Sand
Umberatana Station	Amberoona	MK300312.35	65.00	-	-	Laminated Sand
Umberatana Station	Amberoona	MK300312.36A	75.00	-4.82	-13.16	Interbedded Sand/Marl
Umberatana Station	Amberoona	MK300312.36B	75.00	-4.96	-13.04	Interbedded Sand/Marl
Umberatana Station	Amberoona	MK300312.37	77.00	-3.95	-13.45	Interbedded Sand/Marl
Umberatana Station	Amberoona	MK300312.38	78.00	-5.47	-13.19	Interbedded Sand/Marl
Umberatana Station	Amberoona	MK300312.39	79.00	-4.40	-13.12	Interbedded Sand/Marl
Umberatana Station	Amberoona	MK300312.40	89.00	-	-	Laminated Sand
Umberatana Station	Amberoona	MK300312.41A	96.00	-3.58	-13.34	Interbedded Sand/Marl
Umberatana Station	Amberoona	MK300312.41B	96.00	-3.47	-13.23	Interbedded Sand/Marl
Umberatana Station	Amberoona	MK300312.42	0.00	-3.47	-13.23	Interbedded Sand/Marl
Umberatana Station	Amberoona	MK300312.43	97.00	-	-	Interbedded Sand/Marl
Umberatana Station	Amberoona	MK300312.44	99.00	-3.49	-13.08	Interbedded Sand/Marl
Umberatana Station	Amberoona	MK300312.45	100.00	-3.41	-13.70	Interbedded Sand/Marl
Umberatana Station	Amberoona	MK300312.46	101.00	-	-	Interbedded Sand/Marl
Umberatana Station	Amberoona	MK300312.47	102.00	-3.86	-13.61	Interbedded Sand/Marl
Umberatana Station	Amberoona	MK300312.48	104.00	-3.54	-13.23	Interbedded Sand/Marl
Umberatana Station	Amberoona	MK300312.49	105.00	-3.42	-13.32	Interbedded Sand/Marl
Umberatana Station	Amberoona	MK300312.50	106.00	-3.20	-13.54	Interbedded Sand/Marl
Umberatana Station	Amberoona	MK300312.51	107.00	-3.35	-13.13	Interbedded Sand/Marl
Umberatana Station	Amberoona	MK300312.52A	108.00	-3.30	-13.35	Interbedded Sand/Marl
Umberatana Station	Amberoona	MK300312.52B	108.00	-3.21	-13.20	Interbedded Sand/Marl
Umberatana Station	Amberoona	MK300312.53	110.00	-2.57	-11.29	Interbedded Sand/Marl
Umberatana Station	Amberoona	MK300312.54	114.00	-3.00	-12.76	Interbedded Sand/Marl
Umberatana Station	Amberoona	MK300312.55	117.00	-	-	Interbedded Sand/Marl
Umberatana Station	Amberoona	MK300312.56	119.00	-3.50	-13.01	Interbedded Sand/Marl
Umberatana Station	Amberoona	MK300312.57	120.00	-	-	Interbedded Sand/Marl
Umberatana Station	Amberoona	MK300312.58	120.00	-3.32	-12.35	Interbedded Sand/Marl
Umberatana Station	Amberoona	MK300312.59	121.00	-	-	Interbedded Sand/Marl
Umberatana Station	Amberoona	MK300312.60	123.00	-	-	Interbedded Sand/Marl
Umberatana Station	Amberoona	MK300312.61	125.00	-	-	Laminated Sand
Umberatana Station	Amberoona	MK300312.62	126.00	-3.82	-13.24	Interbedded Sand/Marl
Umberatana Station	Amberoona	MK300312.63	127.00	-3.70	-13.28	Interbedded Sand/Marl
Umberatana Station	Amberoona	MK300312.64	128.00	-3.66	-12.91	Interbedded Sand/Marl
Umberatana Station	Amberoona	MK300312.65	129.00	-	-	Interbedded Sand/Marl
Umberatana Station	Amberoona	MK300312.66	130.00	-3.23	-11.94	Interbedded Sand/Marl
Umberatana Station	Amberoona	MK300312.67	131.00	-3.77	-13.70	Interbedded Sand/Marl
Umberatana Station	Amberoona	MK300312.68	132.00	-3.91	-13.44	Interbedded Sand/Marl

Section	Formation	Sample No.	Height (m)	$\delta^{13}C_{carb}$	$\delta^{18}O_{carb}$	Lithology
Umberatana Station	Amberoona	MK300312.69	134.00	-4.32	-13.52	Interbedded Sand/Marl
Umberatana Station	Amberoona	MK300312.70	135.00	-4.11	-13.09	Interbedded Sand/Marl
Umberatana Station	Amberoona	MK300312.71	138.00	-5.06	-12.71	Interbedded Sand/Marl
Umberatana Station	Amberoona	MK300312.72	140.00	-	-	Laminated Sand
Umberatana Station	Amberoona	MK300312.73	161.00	-2.32	-11.29	Interbedded Sand/Marl
Umberatana Station	Amberoona	MK300312.74	162.00	-	-	Interbedded Sand/Marl
Umberatana Station	Amberoona	MK300312.75	163.00	-3.29	-13.59	Interbedded Sand/Marl
Umberatana Station	Amberoona	MK300312.76	165.00	-	-	Interbedded Sand/Marl
Umberatana Station	Amberoona	MK300312.77	173.00	-	-	Laminated Sand
Umberatana Station	Amberoona	MK300312.78	182.00	-	-	Interbedded Sand/Marl
Umberatana Station	Amberoona	MK300312.79	184.00	-	-	Interbedded Sand/Marl
Umberatana Station	Amberoona	MK300312.80A	185.00	-	-	Interbedded Sand/Marl
Umberatana Station	Amberoona	MK300312.80B	185.00	-3.38	-12.36	Interbedded Sand/Marl
Umberatana Station	Amberoona	MK300312.81	186.00	-2.76	-13.30	Interbedded Sand/Marl
Umberatana Station	Amberoona	MK300312.87	187.00	-	-	Interbedded Sand/Marl
Umberatana Station	Amberoona	MK300312.88	188.00	-3.18	-12.86	Interbedded Sand/Marl
Umberatana Station	Amberoona	MK300312.89	189.00	-2.85	-12.62	Interbedded Sand/Marl
Umberatana Station	Amberoona	MK300312.90	190.00	-2.80	-13.77	Interbedded Sand/Marl
Umberatana Station	Amberoona	MK300312.91	190.00	-2.95	-13.14	Interbedded Sand/Marl
Umberatana Station	Amberoona	MK300312.92	201.00	-2.66	-13.10	Interbedded Sand/Marl
Umberatana Station	Amberoona	MK300312.93	203.00	-2.99	-13.06	Interbedded Sand/Marl
Umberatana Station	Amberoona	MK300312.94	204.00	-3.03	-13.14	Interbedded Sand/Marl
Umberatana Station	Amberoona	MK300312.95	205.00	-2.81	-12.95	Interbedded Sand/Marl
Umberatana Station	Amberoona	MK300312.96A	206.00	-3.04	-12.89	Interbedded Sand/Marl
Umberatana Station	Amberoona	MK300312.96B	206.00	-2.88	-12.44	Interbedded Sand/Marl
Umberatana Station	Amberoona	MK300312.97	207.00	-2.68	-12.77	Interbedded Sand/Marl
Umberatana Station	Amberoona	MK300312.98	210.00	-2.50	-11.31	Interbedded Sand/Marl
Umberatana Station	Amberoona	MK300312.99	211.00	-3.15	-12.91	Interbedded Sand/Marl
Umberatana Station	Amberoona	MK300312.100	212.00	-2.98	-11.78	Interbedded Sand/Marl
Umberatana Station	Amberoona	MK300312.101	214.00	-2.71	-13.52	Interbedded Sand/Marl
Umberatana Station	Amberoona	MK300312.102	215.00	-3.01	-13.28	Interbedded Sand/Marl
Umberatana Station	Amberoona	MK300312.103	216.00	-2.90	-13.21	Interbedded Sand/Marl
Umberatana Station	Amberoona	MK300312.104	217.00	-3.36	-13.09	Interbedded Sand/Marl
Umberatana Station	Amberoona	MK300312.105	217.50	-2.85	-12.86	Interbedded Sand/Marl
Umberatana Station	Amberoona	MK300312.106	218.00	-	-	Interbedded Sand/Marl
Umberatana Station	Amberoona	MK300312.107	219.00	-3.10	-13.60	Interbedded Sand/Marl
Umberatana Station	Amberoona	MK300312.107	219.00	-2.86	-13.58	Interbedded Sand/Marl
Umberatana Station	Amberoona	MK300312.108	220.00	-3.31	-13.76	Interbedded Sand/Marl
Umberatana Station	Amberoona	MK300312.109	121.00	-	-	Interbedded Sand/Marl
Umberatana Station	Amberoona	MK300312.110	123.00	-3.22	-13.63	Interbedded Sand/Marl
Umberatana Station	Amberoona	MK300312.111	123.00	-2.93	-13.31	Interbedded Sand/Marl
Umberatana Station	Amberoona	MK300312.112	124.00	-2.57	-13.75	Interbedded Sand/Marl
Umberatana Station	Amberoona	MK300312.113	127.00	-	-	Interbedded Sand/Marl
Umberatana Station	Amberoona	MK300312.114	230.00	-3.09	-13.32	Interbedded Sand/Marl
Umberatana Station	Amberoona	MK300312.115	232.00	-	-	Interbedded Sand/Marl
Umberatana Station	Amberoona	MK300312.116	235.00	-2.58	-13.11	Interbedded Sand/Marl
Umberatana Station	Amberoona	MK300312.117	237.00	-	-	Interbedded Sand/Marl
Umberatana Station	Amberoona	MK300312.118	240.00	-2.97	-12.99	Interbedded Sand/Marl
Umberatana Station	Amberoona	MK300312.119	241.00	-3.21	-12.98	Interbedded Sand/Marl
Umberatana Station	Amberoona	MK300312.120	245.00	-	-	Laminated Sand

Section	Formation	Sample No.	Height (m)	$\delta^{13}C_{carb}$	$\delta^{18}O_{carb}$	Lithology
Umberatana Station	Amberoona	MK300312.121	251.00	-3.56	-13.51	Laminated Sand
Umberatana Station	Amberoona	MK300312.122	253.00	-	-	Interbedded Sand/Marl
Umberatana Station	Amberoona	MK300312.123	254.00	-3.34	-12.10	Interbedded Sand/Marl
Umberatana Station	Amberoona	MK300312.124	254.50	-	-	Interbedded Sand/Marl
Umberatana Station	Amberoona	MK300312.125	254.50	-2.50	-13.33	Interbedded Sand/Marl
Umberatana Station	Amberoona	MK300312.126	255.50	-2.63	-13.66	Interbedded Sand/Marl
Umberatana Station	Amberoona	MK300312.127	256.00	-2.64	-14.47	Interbedded Sand/Marl
Umberatana Station	Amberoona	MK300312.128	257.00	-2.14	-13.65	Interbedded Sand/Marl
Umberatana Station	Amberoona	MK300312.129	257.50	-2.19	-13.77	Interbedded Sand/Marl
Umberatana Station	Amberoona	MK300312.130	258.00	-3.06	-13.76	Interbedded Sand/Marl
Umberatana Station	Amberoona	MK300312.131	258.50	-2.33	-13.79	Interbedded Sand/Marl
Umberatana Station	Amberoona	MK300312.132	259.00	-1.45	-14.03	Interbedded Sand/Marl
Umberatana Station	Amberoona	MK300312.133	266.00	-	-	Laminated Sand
Umberatana Station	Amberoona	MK300312.134	271.00	-	-	Stromatolite
Punch Rest-Top	Amberoona	RK181112.1	0.00	-	-	Siltstone
Punch Rest-Top	Amberoona	RK181112.2	1.00	-	-	Siltstone
Punch Rest-Top	Amberoona	RK181112.3	1.50	-2.64	-11.60	Siltstone
Punch Rest-Top	Amberoona	RK181112.3	1.50	-3.66	-12.89	Siltstone
Punch Rest-Top	Amberoona	RK181112.4	2.00	-	-	Siltstone
Punch Rest-Top	Amberoona	RK181112.5	2.25	-1.88	-9.43	Siltstone
Punch Rest-Top	Amberoona	RK181112.6	3.00	-	-	Siltstone
Punch Rest-Top	Amberoona	RK181112.7	3.25	-	-	Siltstone
Punch Rest-Top	Amberoona	RK181112.8	4.00	-	-	Siltstone
Punch Rest-Top	Amberoona	RK181112.9	5.50	-	-	Siltstone
Punch Rest-Top	Amberoona	RK181112.10	6.25	-	-	Siltstone
Punch Rest-Top	Amberoona	RK181112.11	7.50	-	-	Siltstone
Punch Rest-Top	Amberoona	RK181112.12	8.00	-1.83	-9.73	Siltstone
Punch Rest-Top	Amberoona	RK181112.13	9.00	-2.53	-10.99	Siltstone
Punch Rest-Top	Amberoona	RK181112.14	11.50	-	-	Siltstone
Punch Rest-Top	Amberoona	RK181112.15	17.00	-2.88	-10.48	Siltstone
Punch Rest-Top	Amberoona	RK181112.16	20.00	-5.71	-8.98	Siltstone
Punch Rest-Top	Amberoona	RK181112.17	20.00	-	-	Marl
Punch Rest-Top	Amberoona	RK181112.18	21.50	-	-	Siltstone
Punch Rest-Top	Amberoona	RK181112.19	22.00	-	-	Siltstone
Punch Rest-Top	Amberoona	RK181112.20	22.75	-	-	Siltstone
Punch Rest-Top	Amberoona	RK181112.21	23.50	-	-	Siltstone
Punch Rest-Top	Amberoona	RK181112.22	25.00	-	-	Siltstone
Punch Rest-Top	Amberoona	RK181112.23	25.25	-	-	Siltstone
Punch Rest-Top	Amberoona	RK181112.24	28.25	-	-	Laminite
Punch Rest-Top	Amberoona	RK181112.25	29.00	-	-	Laminite
Punch Rest-Top	Amberoona	RK181112.26	29.78	-	-	Laminite
Punch Rest-Top	Amberoona	RK181112.27	30.00	-	-	Laminite
Punch Rest-Top	Amberoona	RK181112.28	30.00	-	-	Marl Rip-Up
Punch Rest-Top	Amberoona	RK181112.29	30.00	-	-	Sandy Drapes
Punch Rest-Base	Amberoona	RK181112.30	0.50	-	-	Siltstone Cement
Punch Rest-Base	Amberoona	RK181112.31	4.75	-	-	Nodular Dolomicrite
Punch Rest-Base	Amberoona	RK181112.32	5.00	-	-	Siltstone
Punch Rest-Base	Amberoona	RK181112.33	6.00	-	-	Siltstone
Punch Rest-Base	Amberoona	RK181112.34	7.50	-	-	Siltstone
Punch Rest-Base	Amberoona	RK181112.35	10.50	-	-	Siltstone

Section	Formation	Sample No.	Height (m)	$\delta^{13}C_{carb}$	$\delta^{18}O_{carb}$	Lithology
Punch Rest-Base	Amberoona	RK181112.36	13.00	-	-	Siltstone
Punch Rest-Base	Amberoona	RK181112.37	14.00	-	-	Dolomicrite Lense
Punch Rest-Base	Amberoona	RK181112.38	15.50	-	-	Dolomicrite Lense
Punch Rest-Base	Amberoona	RK181112.39	16.75	-	-	Nodular Dolomicrite
Punch Rest-Base	Amberoona	RK181112.40	17.25	-	-	Nodular Dolomicrite
Punch Rest-Base	Amberoona	RK181112.41	21.00	-	-	Nodular Dolomicrite
Punch Rest-Base	Amberoona	RK181112.42	23.00	-	-	Siltstone
Punch Rest-Base	Amberoona	RK181112.43	25.00	-	-	Siltstone
Punch Rest-Base	Amberoona	RK181112.44	30.25	-	-	Siltstone
Punch Rest-Base	Amberoona	RK181112.45	35.00	-	-	Microsparite
Punch Rest-Base	Amberoona	RK181112.46	37.00	-	-	Microsparite
Punch Rest-Base	Amberoona	RK181112.47	38.00	-	-	Siltstone
Punch Rest-Base	Amberoona	RK181112.48	39.75	-	-	Microsparite
Punch Rest-Base	Amberoona	RK181112.49	42.00	-	-	Microsparite
Punch Rest-Base	Amberoona	RK181112.50	45.00	-	-	Nodular Dolomicrite
Punch Rest-Base	Amberoona	RK181112.51	47.50	-	-	Nodular Dolomicrite
Punch Rest-Base	Amberoona	RK181112.52	50.75	-	-	Dolomicrite Lense
Punch Rest-Base	Amberoona	RK181112.53	54.00	-	-	Microsparite
Punch Rest-Base	Amberoona	RK181112.54	57.50	-	-	Dolomicrite Lense
Punch Rest-Base	Amberoona	RK181112.55	67.50	-	-	Siltstone
Punch Rest-Base	Amberoona	RK181112.56	67.25	-	-	Coarse Silt
Punch Rest-Base	Amberoona	RK181112.57	72.00	-	-	Dolomicrite Lense
Punch Rest-Base	Amberoona	RK181112.58	71.50	-	-	Coarse Silt
Punch Rest-Base	Amberoona	RK181112.59	69.00	-	-	Coarse Silt
Punch Rest-Base	Amberoona	RK181112.60	74.50	-	-	Coarse Silt
Punch Rest-Base	Amberoona	RK181112.61	76.00	-	-	Coarse Silt

*= repeat analysis ^= isotopic data analysed at Melbourne University ~= isotopic data analysed at the California Institute of Technology

Letters on the end of the sample number correspond to analysis of different sample components

Appendix 4.2 Trezona Formation trace element data

Section	Formation	Sample No.	$\delta^{13}C_{carb}$	$\delta^{18}O_{carb}$	Fe (ppm)	Mn (ppm)	Sr (ppm)	Mn/Sr
Bunkers Range-2	Trezona	MK061596.1	-9.17	-11.78	2813.61	928.61	248.00	3.74
Bunkers Range-2	Trezona	MK061596.2	-8.58	-12.02	3311.42	1074.60	423.96	2.53
Bunkers Range-2	Trezona	MK061596.3	-9.18	-10.96	4845.59	1260.51	625.34	2.02
Bunkers Range-2	Trezona	MK061596.4	-8.00	-10.49	3195.82	1442.40	297.52	4.85
Bunkers Range-2	Trezona	MK061596.5	-10.25	-11.23	2857.09	1514.96	235.94	6.42
Bunkers Range-2	Trezona	MK061596.6	-8.97	-11.63	2193.16	1538.36	310.99	4.95
Bunkers Range-2	Trezona	MK061596.7	-8.67	-10.78	3149.93	1025.87	500.57	2.05
Bunkers Range-2	Trezona	MK061596.8	-9.12	-8.85	3034.78	773.86	767.56	1.01
Bunkers Range-2	Trezona	MK061596.9	-8.75	-10.44	3972.71	559.93	585.50	0.96
Bunkers Range-2	Trezona	MK061596.10A	-9.36	-7.38	2215.82	780.82	740.96	1.05
Bunkers Range-2	Trezona	MK061596.10B	-	-	2333.47	1974.47	620.53	3.18
Bunkers Range-2	Trezona	MK061596.11	-8.62	-11.38	2441.10	479.31	833.55	0.58
Bunkers Range-2	Trezona	MK061596.12	-8.35	-11.50	2905.81	428.74	812.91	-
Bunkers Range-2	Trezona	MK061596.13	-8.93	-11.33	2492.89	671.24	1010.52	0.66
Bunkers Range-2	Trezona	MK061596.14	-8.89	-10.48	2888.52	641.38	338.72	1.89
Bunkers Range-2	Trezona	MK061596.15	-8.66	-12.22	1651.05	702.05	701.65	1.00
Bunkers Range-2	Trezona	MK061596.16	-8.53	-11.37	2504.38	1063.56	625.61	1.70
Bunkers Range-2	Trezona	MK061596.17	-8.82	-10.40	5208.07	958.59	803.02	1.19
Bunkers Range-2	Trezona	MK061596.18	-8.60	-9.89	4007.36	1503.44	879.94	1.71
Bunkers Range-2	Trezona	MK061596.19	-8.31	-11.42	3579.29	644.83	620.69	1.04
Bunkers Range-2	Trezona	MK061596.20	-9.06	-11.09	4400.76	1167.23	535.67	2.18
Bunkers Range-2	Trezona	MK061596.21	-8.86	-10.18	5816.99	2422.87	759.69	3.19
Bunkers Range-2	Trezona	MK061596.22	-8.58	-10.93	5393.36	691.62	580.76	1.19
Bunkers Range-2	Trezona	MK061596.23	-8.83	-11.07	4025.50	1189.11	560.06	2.12
Bunkers Range-2	Trezona	MK061596.24	-8.25	-10.58	3797.47	609.12	940.13	0.65
Bunkers Range-2	Trezona	MK061596.25	-8.41	-11.20	3685.72	737.60	984.97	0.75
Bunkers Range-2	Trezona	MK061596.26	-8.45	-10.51	3480.93	1085.55	851.14	1.28
Bunkers Range-2	Trezona	MK061596.27	-9.85	-10.40	5460.14	864.77	813.21	1.06
Bunkers Range-2	Trezona	MK061596.28	-8.74	-10.61	3561.13	796.13	456.80	1.74
Bunkers Range-2	Trezona	MK061596.29	-8.34	-10.01	2755.38	1045.39	396.77	2.63
Bunkers Range-2	Trezona	MK061596.30	-	-	4709.89	934.87	715.63	1.31
Bunkers Range-2	Trezona	MK061596.31	-	-	5421.46	936.15	766.21	1.22
Bunkers Range-2	Trezona	MK061596.32A	-8.44	-10.84	3858.17	1068.87	381.26	2.80
Bunkers Range-2	Trezona	MK061596.32B	-	-	3873.34	717.64	368.42	1.95
Bunkers Range-2	Trezona	MK061596.33	-8.14	-10.53	3135.26	473.39	964.32	0.49
Bunkers Range-2	Trezona	MK061596.34	-8.08	-10.36	3149.78	627.34	542.73	1.16
Bunkers Range-2	Trezona	MK061596.35A	-7.65	-10.58	2230.36	484.04	777.65	0.62
Bunkers Range-2	Trezona	MK061596.35B	-	-	20.14	12.93	2852.84	0.00
Bunkers Range-2	Trezona	MK061696.10	-	-	1604.68	1888.91	49.63	38.06
Bunkers Range-2	Trezona	MK061696.11	-8.74	-11.25	1493.36	1899.65	54.24	35.02
Bunkers Range-2	Trezona	MK061696.12	-6.74	-9.31	2398.27	211.27	185.49	1.14
Bunkers Range-2	Trezona	MK061696.12A	-	-	1656.99	146.42	564.96	0.26
Bunkers Range-2	Trezona	MK061696.12B	-	-	1481.16	135.32	522.12	0.26
Bunkers Range-2	Trezona	MK061696.13	-6.41	-8.73	1640.65	117.93	1207.63	0.10
Bunkers Range-2	Trezona	MK061696.14	-6.44	-8.03	1529.80	162.58	626.58	0.26
Bunkers Range-2	Trezona	MK061696.15	-6.35	-8.19	2128.68	297.47	456.38	0.65

Section	Formation	Sample No.	$\delta^{13}C_{carb}$	$\delta^{18}O_{carb}$	Fe (ppm)	Mn (ppm)	Sr (ppm)	Mn/Sr
Bunkers Range-2	Trezona	MK061696.16	-8.48	-11.88	1732.17	216.12	624.63	0.35
Bunkers Range-2	Trezona	MK061696.17	-6.00	-8.24	2603.43	240.16	567.72	0.42
Bunkers Range-2	Trezona	MK061696.18	-5.82	-8.58	1951.33	178.64	564.16	0.32
Bunkers Range-2	Trezona	MK061696.19	-5.95	-8.36	1169.45	100.05	609.02	0.16
Bunkers Range-2	Trezona	MK061696.20	-5.93	-8.42	1378.39	112.19	1249.88	0.09
Bunkers Range-2	Trezona	MK061696.21	-5.71	-8.52	1715.78	171.60	2997.46	0.06
Bunkers Range-2	Trezona	MK061696.22	-5.68	-7.65	2019.58	206.56	798.54	0.26
Bunkers Range-2	Trezona	MK061696.23	-5.52	-8.23	2090.57	105.94	1326.81	0.08
Bunkers Range-2	Trezona	MK061696.24	-5.38	-8.37	1818.90	106.91	1563.27	0.07
Bunkers Range-2	Trezona	MK061696.25A	-5.65	-7.48	1257.88	43.90	2046.61	0.02
Bunkers Range-2	Trezona	MK061696.25B	-	-	1261.98	86.99	1170.73	0.07
Bunkers Range-2	Trezona	MK061696.26	-5.29	-8.46	3392.48	415.56	604.74	0.69
Bunkers Range-2	Trezona	MK061696.27	-5.03	-8.18	4440.21	610.53	858.78	0.71
Bunkers Range-2	Trezona	MK061696.28	-4.52	-7.88	2334.20	233.71	113.13	2.07
Bunkers Range-2	Trezona	MK061696.29	-4.48	-8.38	2022.54	309.35	864.20	0.36
Bunkers Range-2	Trezona	MK061696.30	-4.48	-8.74	1651.55	211.06	495.14	0.43
Bunkers Range-2	Trezona	MK061696.31	-4.70	-9.14	2306.26	155.31	591.26	0.26
Bunkers Range-2	Trezona	MK061696.32	-4.60	-8.85	3635.28	203.83	416.18	0.49
Bunkers Range-2	Trezona	MK061696.33	-4.02	-8.80	1354.90	115.47	615.34	0.19
Bunkers Range-2	Trezona	MK061696.34	-3.37	-7.39	4978.95	311.65	436.72	0.71
Bunkers Range-2	Trezona	MK061696.35	-3.87	-8.88	2565.85	234.23	380.82	0.62
Bunkers Range-2	Trezona	MK061696.36	-3.62	-8.60	2244.10	147.53	365.63	0.40
Bunkers Range-2	Trezona	MK061696.37	-3.76	-8.84	2137.50	160.85	1857.16	0.09
Bunkers Range-2	Trezona	MK061696.38	-3.60	-9.04	1661.90	193.64	356.46	0.54
Bunkers Range-2	Trezona	MK061696.39	-3.38	-8.94	2227.15	203.79	360.28	0.57
Bunkers Range-2	Trezona	MK061696.40	-3.64	-9.58	2006.31	192.34	360.98	0.53
Bunkers Range-2	Trezona	MK061696.41	-2.84	-8.93	2093.00	257.86	354.71	0.73
Bunkers Range-2	Trezona	MK061696.42	-2.84	-9.63	3384.97	336.16	370.24	0.91
Bunkers Range-2	Trezona	MK061696.43	-2.78	-10.20	1814.13	243.91	330.63	0.74
Bunkers Range-2	Trezona	MK061696.44	-2.88	-9.74	2483.87	308.38	403.27	0.76
Bunkers Range-2	Trezona	MK061696.45	-3.21	-10.88	2026.13	268.72	283.66	0.95

*A and B signify separate analyses (do not correspond to Appendix 4.1)

Appendix 5.1 Andrée Land Group stable isotope data from bed group 18

Section	Formation	Sample No.	Height (m)	$\delta^{13}C_{carb}$	$\delta^{18}O_{carb}$	Lithology
Kap Oswald	Bed group 18	RK210812.1	0.35	7.03	-5.19	Dolomicrosparite
Kap Oswald	Bed group 18	RK210812.2	1.30	6.75	-6.05	Dolomicrosparite
Kap Oswald	Bed group 18	RK210812.3	1.70	6.35	-6.13	Mudflake Conglomerate
Kap Oswald	Bed group 18	RK210812.4A	2.05	5.65	-4.34	Silty Microsparite
Kap Oswald	Bed group 18	RK210812.4B	2.05	5.60	-5.70	Silty Microsparite
Kap Oswald	Bed group 18	RK210812.5	3.95	6.33	-5.89	Dolomicrosparite
Kap Oswald	Bed group 18	RK210812.6	7.00	6.95	-5.66	Dolomicrosparite
Kap Oswald	Bed group 18	RK210812.7	8.10	6.09	-5.21	Dolomicrosparite
Kap Oswald	Bed group 18	RK210812.8	9.40	6.15	-4.74	Dolomicrosparite
Kap Oswald	Bed group 18	RK210812.9	10.65	5.86	-5.70	Mudstone
Kap Oswald	Bed group 18	RK210812.10	10.80	6.49	-4.29	Dolomicrosparite
Kap Oswald	Bed group 18	RK210812.11	10.80	7.32	-6.04	Microsparite
Kap Oswald	Bed group 18	RK210812.12	11.45	-	-	Organic Shale
Kap Oswald	Bed group 18	RK210812.13	11.45	-	-	Organic Shale
Kap Oswald	Bed group 18	RK210812.14	11.45	-	-	Organic Shale
Kap Oswald	Bed group 18	RK210812.15	11.45	-	-	Organic Shale
Kap Oswald	Bed group 18	RK210812.16	11.45	-	-	Organic Shale
Kap Oswald	Bed group 18	RK210812.17	11.45	-	-	Organic Shale
Kap Oswald	Bed group 18	RK210812.18	11.45	-	-	Organic Shale
Kap Oswald	Bed group 18	RK210812.19	11.45	-	-	Organic Shale
Kap Oswald	Bed group 18	RK210812.20A	12.70	5.80	-3.59	Microsparite
Kap Oswald	Bed group 18	RK210812.20B	12.70	7.31	-5.32	Microsparite
Kap Oswald	Bed group 18	RK210812.21	13.45	7.12	-5.44	Laminated Clayey Limestone
Kap Oswald	Bed group 18	RK210812.22	16.30	6.75	-4.57	Dolomicrosparite
Kap Oswald	Bed group 18	RK210812.23A	18.15	6.50	-5.08	Shrinkage cracks
Kap Oswald	Bed group 18	RK210812.23B	18.15	6.46	-4.95	Shrinkage cracks
Kap Oswald	Bed group 18	RK210812.24	18.45	-	-	Dolomicrosparite
Kap Oswald	Bed group 18	RK210812.25	19.90	-	-	Pisolitic Packstone
Kap Oswald	Bed group 18	RK210812.26	20.90	-	-	Laminite
Kap Oswald	Bed group 18	RK210812.27	19.90	7.06	-5.79	Shrinkage Cracks
Kap Oswald	Bed group 18	RK210812.28	23.60	6.94	-5.56	Pisolitic Packstone
Kap Oswald	Bed group 18	RK210812.29	33.70	7.00	-5.80	Pisolitic Packstone
Kap Oswald	Bed group 18	RK210812.30	35.20	6.10	-6.16	Pisolitic Packstone
Kap Oswald	Bed group 18	RK210812.31A	40.50	5.94	-6.35	Pisolitic Packstone
Kap Oswald	Bed group 18	RK210812.31B	40.50	6.66	-5.95	Pisolitic Packstone
Kap Oswald	Bed group 18	RK210812.32	41.50	6.72	-3.57	Laminated Dolostones
Kap Oswald	Bed group 18	RK210812.33	45.50	6.01	-6.54	Pisolitic Packstone
Kap Oswald	Bed group 18	RK210812.34	46.30	6.04	-5.79	Microsparite
Kap Oswald	Bed group 18	RK210812.35	46.30	5.83	-4.92	Mudflake Conglomerate
Kap Oswald	Bed group 18	RK210812.36A	57.00	5.69	-6.32	Microsparite
Kap Oswald	Bed group 18	RK210812.36B	57.00	5.65	-6.21	Microsparite
Kap Oswald	Bed group 18	RK050812.1	40.10	5.22	-6.95	Oolitic Packstone
Kap Oswald	Bed group 18	RK050812.2	41.60	5.72	-6.40	Microsparite
Kap Oswald	Bed group 18	RK050812.3	43.60	6.46	-5.38	Microsparite
Kap Oswald	Bed group 18	RK050812.4	43.85	4.76	-6.25	Oolitic Packstone
Kap Oswald	Bed group 18	RK050812.5^	46.60	5.19	-6.69	Pisolitic Packstone
Kap Oswald	Bed group 18	RK050812.6	48.85	-	-	Pisolitic Packstone
Kap Oswald	Bed group 18	RK050812.7	49.60	5.96	-5.69	Oolitic Packstone

Section	Formation	Sample No.	Height (m)	$\delta^{13}C_{carb}$	$\delta^{18}O_{carb}$	Lithology
Kap Oswald	Bed group 18	RK050812.8A	50.60	4.82	-5.24	Microsparite
Kap Oswald	Bed group 18	RK050812.8B	50.60	5.26	-5.43	Microsparite
Kap Oswald	Bed group 18	RK050812.9	51.10	5.58	-5.54	Oolitic Packstone
Kap Oswald	Bed group 18	RK050812.10	53.60	5.73	-5.72	Oolitic Packstone
Kap Oswald	Bed group 18	RK050812.11	54.60	6.17	-7.24	Oolitic Packstone
Kap Oswald	Bed group 18	RK050812.12	56.60	6.66	-1.04	Oolitic Packstone
Kap Oswald	Bed group 18	RK050812.13	58.10	6.03	-5.01	Oolitic Packstone
Kap Oswald	Bed group 18	RK050812.14	58.60	-	-	Pisolitic Packstone (Chert)
Kap Oswald	Bed group 18	RK050812.15	61.60	5.38	-4.65	Oolitic Packstone
Kap Oswald	Bed group 18	RK050812.16	62.60	5.11	-5.93	Pisolitic Packstone
Kap Oswald	Bed group 18	RK050812.17	64.10	5.90	-6.21	Pisolitic Packstone
Kap Oswald	Bed group 18	RK050812.18	69.10	5.15	-6.00	Microsparite
Kap Oswald	Bed group 18	RK050812.19	70.60	6.18	-3.94	Microsparite
Kap Oswald	Bed group 18	RK050812.20	72.10	5.10	-3.15	Shaley Dolomicrosparite
Kap Oswald	Bed group 18	RK050812.21	72.60	5.71	-5.50	Mudflake Conglomerate
Kap Oswald	Bed group 18	RK050812.22	74.10	5.97	-3.99	Microsparite
Kap Oswald	Bed group 18	RK050812.23^	75.10	5.27	-6.17	Shaley Dolomicrosparite
Kap Oswald	Bed group 18	RK050812.23*	75.10	5.42	-7.51	Shaley Dolomicrosparite
Kap Oswald	Bed group 18	RK050812.24	78.10	6.96	-2.93	Oolitic Packstone
Kap Oswald	Bed group 18	RK050812.25	80.10	4.97	-5.55	Shaley Dolomicrosparite
Kap Oswald	Bed group 18	RK050812.26	81.60	5.80	-4.66	Microsparite
Kap Oswald	Bed group 18	RK050812.27	82.10	5.87	-6.04	Pisolitic Packstone
Kap Oswald	Bed group 18	RK050812.28	83.60	5.27	-6.80	Pisolitic Packstone
Kap Oswald	Bed group 18	RK050812.29	85.10	-	-	Microsparite
Kap Oswald	Bed group 18	RK050812.30	87.60	6.73	-6.84	Microsparite
Kap Oswald	Bed group 18	RK050812.31A^	88.35	2.68	-7.84	Shaley Dolomicrosparite
Kap Oswald	Bed group 18	RK050812.31B	88.35	5.74	-5.92	Shaley Dolomicrosparite
Kap Oswald	Bed group 18	RK050812.32	89.35	-	-	Shaley Dolomicrosparite
Kap Oswald	Bed group 18	RK050812.33	90.60	-	-	Shaley Dolomicrosparite
Kap Oswald	Bed group 18	RK050812.34^	93.35	2.70	-6.62	Oolitic Packstone
Kap Oswald	Bed group 18	RK050812.35	94.10	5.30	-7.43	Mudflake Conglomerate
Kap Oswald	Bed group 18	RK050812.36	95.10	5.75	-6.60	Oolitic Packstone
Kap Oswald	Bed group 18	RK050812.37^	96.10	2.95	-7.27	Oolitic Packstone
Kap Oswald	Bed group 18	RK050812.38A^	98.35	3.72	-8.88	Dolomicrosparite
Kap Oswald	Bed group 18	RK050812.38B	98.35	5.14	-7.96	Dolomicrosparite
Kap Oswald	Bed group 18	RK050812.39A^	101.10	3.73	-8.91	Microsparite
Kap Oswald	Bed group 18	RK050812.39B	101.10	5.21	-8.61	Microsparite
Kap Oswald	Bed group 18	RK050812.40A^	103.35	3.55	-8.52	Shaley Dolomicrosparite
Kap Oswald	Bed group 18	RK050812.40B	103.35	5.73	-7.31	Shaley Dolomicrosparite
Kap Oswald	Bed group 18	RK050812.41	104.10	5.01	-8.10	Microsparite
Kap Oswald	Bed group 18	RK050812.42	105.60	5.81	-7.45	Microsparite
Kap Oswald	Bed group 18	RK050812.43	107.60	5.55	-10.12	Microsparite
Kap Oswald	Bed group 18	RK050812.44	109.60	5.49	-9.40	Microsparite
Kap Oswald	Bed group 18	RK050812.45	114.10	5.91	-7.86	Pisolitic Packstone (Chert)
Kap Oswald	Bed group 18	RK050812.46	117.60	4.64	-10.37	Pisolitic Packstone
Kap Oswald	Bed group 18	RK050812.47	118.60	5.01	-9.65	Pisolitic Packstone
Kap Oswald	Bed group 18	RK050812.48	119.60	5.54	-15.85	Pisolitic Packstone
Kap Oswald	Bed group 18	RK050812.49A	120.10	-	-	Intraclastic Dolostone
Kap Oswald	Bed group 18	RK050812.49B	120.10	5.43	-11.14	Intraclastic Dolostone
Kap Oswald	Bed group 18	RK050812.50	121.60	5.43	-7.68	Intraclastic Dolostone

Section	Formation	Sample No.	Height (m)	$\delta^{13}C_{carb}$	$\delta^{18}O_{carb}$	Lithology
Kap Oswald	Bed group 18	RK050812.51	122.10	5.27	-6.03	Laminated Dolomicrites
Kap Oswald	Bed group 18	RK050812.52	122.60	5.14	-6.48	Intraclastic Dolostone
Kap Oswald	Bed group 18	RK050812.53	123.35	5.11	-7.42	Intraclastic Dolostone
Kap Oswald	Bed group 18	RK050812.54	123.85	-	-	Intraclastic Dolostone
Kap Oswald	Bed group 18	RK050812.55	124.60	4.43	-7.32	Stromatolite
Kap Oswald	Bed group 18	RK050812.56	124.85	-	-	Intraclastic Dolostone
Kap Oswald	Bed group 18	RK050812.57	127.10	5.21	-7.23	Intraclastic Dolostone
Kap Oswald	Bed group 18	RK050812.58A	127.60	4.18	-6.08	Stromatolite
Kap Oswald	Bed group 18	RK050812.58B	127.60	4.16	-5.43	Stromatolite
Kap Oswald	Bed group 18	RK050812.58C	127.60	4.28	-4.36	Stromatolite
Kap Oswald	Bed group 18	RK050812.59	129.10	3.74	-2.98	Intraclastic Dolostone
Kap Oswald	Bed group 18	RK050812.60	129.60	3.99	-4.70	Intraclastic Dolostone
Kap Oswald	Bed group 18	RK050812.61	131.35	4.06	-2.79	Intraclastic Dolostone
Kap Oswald	Bed group 18	RK050812.62	132.35	-	-	Intraclastic Dolostone
Kap Oswald	Bed group 18	RK050812.63	133.60	4.76	-7.91	Fissile Dolostone
Kap Oswald	Bed group 18	RK050812.64	134.85	4.68	-8.09	Oolitic Packstone
Kap Oswald	Bed group 18	RK050812.65	135.85	5.06	-6.90	Oolitic Packstone
Kap Oswald	Bed group 18	RK050812.66	136.10	5.01	-7.17	Laminite
Kap Oswald	Bed group 18	RK050812.67	136.35	5.52	-4.40	Stromatolite
Kap Oswald	Bed group 18	RK050812.68	137.60	4.43	-7.77	Dolarenite
Kap Oswald	Bed group 18	RK050812.69	139.10	4.43	-6.83	Oolitic Packstone
Kap Oswald	Bed group 18	RK050812.70	140.10	4.30	-6.97	Oolitic Packstone
Kap Oswald	Bed group 18	RK050812.71	140.60	4.19	-8.31	Oolitic Packstone
Kap Oswald	Bed group 18	RK050812.72	141.10	4.53	-8.83	Microsparite
Kap Oswald	Bed group 18	RK050812.73	142.10	4.25	-8.28	Microsparite
Kap Oswald	Bed group 18	RK050812.74	142.85	4.38	-6.59	Pisolitic Packstone
Kap Oswald	Bed group 18	RK060812.1^	130.60	6.26	-8.23	Microsparite
Kap Oswald	Bed group 18	RK060812.2	130.60	5.39	-6.66	Microsparite
Kap Oswald	Bed group 18	RK060812.3	130.60	5.54	-6.38	Microsparite
Kap Oswald	Bed group 18	RK060812.4	129.60	5.72	-7.07	Oolitic Packstone
Kap Oswald	Bed group 18	RK060812.5	131.35	5.47	-6.62	Microbialite
Kap Oswald	Bed group 18	RK060812.6	131.60	4.65	-6.76	Oolitic Packstone
Kap Oswald	Bed group 18	RK060812.7^	131.85	5.95	-6.35	Laminite
Kap Oswald	Bed group 18	RK060812.8	132.10	4.33	-6.87	Intraclastic Dolostone
Kap Oswald	Bed group 18	RK060812.9	132.30	4.86	-6.44	Laminite
Kap Oswald	Bed group 18	RK060812.10	132.35	4.33	-8.00	Oolitic Packstone
Kap Oswald	Bed group 18	RK060812.11A	132.40	4.41	-7.32	Laminite
Kap Oswald	Bed group 18	RK060812.11B	132.40	4.37	-6.77	Laminite
Kap Oswald	Bed group 18	RK060812.11C	132.40	4.56	-7.03	Laminite
Kap Oswald	Bed group 18	RK060812.12	133.35	4.49	-7.36	Laminite
Kap Oswald	Bed group 18	RK060812.13	134.10	5.27	-4.05	Intraclastic Dolostone
Kap Oswald	Bed group 18	RK060812.14	135.60	4.82	-4.71	Intraclastic Dolostone
Kap Oswald	Bed group 18	RK060812.15	136.85	4.43	-4.51	Intraclastic Dolostone
Kap Oswald	Bed group 18	RK060812.15*^	136.85	6.11	-5.67	Intraclastic Dolostone
Kap Oswald	Bed group 18	RK060812.16	137.10	4.12	-6.28	Stromatolite
Kap Oswald	Bed group 18	RK060812.17	137.60	5.88	-7.48	Flaggy Microsparite
Kap Oswald	Bed group 18	RK060812.18	138.10	4.23	-7.22	Flaggy Microsparite
Kap Oswald	Bed group 18	RK060812.18*^	138.10	5.05	-6.67	Flaggy Microsparite
Kap Oswald	Bed group 18	RK060812.19	139.10	3.36	-7.45	Stromatolite
Kap Oswald	Bed group 18	RK060812.20	139.60	4.51	-7.13	Shrinkage Crack

Section	Formation	Sample No.	Height (m)	$\delta^{13}C_{carb}$	$\delta^{18}O_{carb}$	Lithology
Kap Oswald	Bed group 18	RK060812.21	140.60	4.77	-7.07	Laminite
Kap Oswald	Bed group 18	RK060812.22A	140.85	5.04	-5.86	Laminite
Kap Oswald	Bed group 18	RK060812.22B	140.85	6.26	-2.88	Laminite
Kap Oswald	Bed group 18	RK060812.23A	141.60	5.01	-6.66	Oolitic Packstone
Kap Oswald	Bed group 18	RK060812.23B	141.60	5.09	-6.20	Oolitic Packstone
Kap Oswald	Bed group 18	RK060812.24	141.60	5.10	-6.64	Oolitic Packstone
Kap Oswald	Bed group 18	RK060812.25	144.10	4.88	-6.71	Oolitic Packstone
Kap Oswald	Bed group 18	RK060812.26A^	129.60	5.55	-6.28	Oolitic Packstone
Kap Oswald	Bed group 18	RK060812.26B	129.60	5.14	-6.92	Oolitic Packstone
Kap Oswald	Bed group 18	RK060812.27	129.60	4.30	-8.65	Oolitic Packstone
Kap Oswald	Bed group 18	RK060812.28	145.60	4.18	-6.18	Oolitic Packstone
Kap Oswald	Bed group 18	RK060812.29	146.60	2.54	-7.72	Stromatolite
Kap Oswald	Bed group 18	RK060812.30	147.60	2.91	-6.64	Laminite
Kap Oswald	Bed group 18	RK060812.31	149.75	-	-	Dolostone
Kap Oswald	Bed group 18	RK060812.32	149.90	2.66	-8.71	Oolitic Dolopackstone
Kap Oswald	Bed group 18	RK060812.32*^	149.90	5.66	-7.21	Oolitic Dolopackstone
Kap Oswald	Bed group 18	RK060812.33	150.35	2.59	-6.04	Oolitic Dolopackstone
Kap Oswald	Bed group 18	RK060812.34	155.50	2.73	-5.17	Oolitic Dolopackstone
Kap Oswald	Bed group 18	RK060812.35	156.50	2.98	-5.13	Oolitic Dolopackstone
Kap Oswald	Bed group 18	RK060812.36	159.40	2.84	-4.97	DoloMicrosparite
Kap Oswald	Bed group 18	RK060812.37	160.65	-	-	Oolitic Dolopackstone
Kap Oswald	Bed group 18	RK060812.38	166.15	-	-	Oolitic Dolopackstone
Kap Oswald	Bed group 18	RK060812.39	166.55	3.80	-4.31	Mudflake Conglomerate
Kap Oswald	Bed group 18	RK060812.40	167.35	3.66	-6.23	Oolitic Dolopackstone
Kap Oswald	Bed group 18	RK060812.41	170.35	3.99	-7.15	Oolitic Dolopackstone
Kap Oswald	Bed group 18	RK060812.42	175.75	3.78	-4.93	Oolitic Dolopackstone
Kap Oswald	Bed group 18	RK060812.43	182.35	-	-	Oolitic Dolopackstone
Kap Oswald	Bed group 18	RK060812.44	181.75	4.05	-5.18	Oolitic Dolopackstone
Kap Oswald	Bed group 18	RK060812.44*^	181.75	5.20	-9.24	Oolitic Dolopackstone
Kap Oswald	Bed group 18	RK060812.45	182.05	3.78	-4.57	Pisolitic Dolopackstone
Kap Oswald	Bed group 18	RK060812.46	182.65	3.82	-5.34	Pisolitic Dolopackstone
Kap Oswald	Bed group 18	RK060812.47	182.90	3.41	-4.48	Oolitic Dolopackstone
Kap Oswald	Bed group 18	RK060812.48C^	195.60	5.42	-15.68	Dolarenite
Kap Oswald	Bed group 18	RK060812.48A	195.60	3.81	-5.52	Dolarenite
Kap Oswald	Bed group 18	RK060812.48B	195.60	3.64	-7.38	Dolarenite
Kap Oswald	Bed group 18	RK060812.49^	195.60	5.41	-10.65	Dolarenite
Kap Oswald	Bed group 18	RK060812.50	195.60	3.74	-4.45	Dolarenite
Kap Oswald	Bed group 18	RK060812.51A	-	3.30	-2.66	Microsparite
Kap Oswald	Bed group 18	RK060812.51B	-	3.44	-7.08	Microsparite
Kap Oswald	Bed group 18	RK060812.51C	-	4.15	-5.18	Microsparite
Kap Oswald	Bed group 18	RK060812.54A	-	4.75	-4.47	Microsparite
Kap Oswald	Bed group 18	RK060812.54B	-	4.76	-5.71	Microsparite
Kap Oswald	Bed group 18	RK070812.1^	195.80	3.43	-3.14	Laminite
Kap Oswald	Bed group 18	RK070812.2^	196.35	3.50	-4.63	Stromatolite
Kap Oswald	Bed group 18	RK070812.3^	196.40	3.82	-4.99	Mudflake Conglomerate
Kap Oswald	Bed group 18	RK070812.4^	196.45	4.00	-3.93	Karst
Kap Oswald	Bed group 18	RK070812.5^	197.00	3.57	-2.89	Stromatolite
Kap Oswald	Bed group 18	RK070812.6^	197.40	3.65	-2.84	Laminite
Kap Oswald	Bed group 18	RK070812.7	197.70	-	-	Intraclast Packstone
Kap Oswald	Bed group 18	RK070812.8^	197.90	3.87	-2.42	Laminite

Section	Formation	Sample No.	Height (m)	$\delta^{13}C_{carb}$	$\delta^{18}O_{carb}$	Lithology
Kap Oswald	Bed group 18	RK070812.9^	198.55	4.52	-5.49	Microsparite
Kap Oswald	Bed group 18	RK070812.10^	199.20	3.51	-3.11	Dolostone
Kap Oswald	Bed group 18	RK070812.11^	200.50	3.63	-2.08	Dolomicrosparite
Kap Oswald	Bed group 18	RK070812.12^	201.10	4.55	-4.46	Stromatolite
Kap Oswald	Bed group 18	RK070812.13^	201.85	4.20	-3.43	Laminite
Kap Oswald	Bed group 18	RK070812.14^	202.80	4.43	-2.96	Laminite
Kap Oswald	Bed group 18	RK070812.15^	204.25	4.79	-4.59	Stromatolite
Kap Oswald	Bed group 18	RK070812.16^	205.10	5.51	-2.71	Mudflake Conglomerate
Kap Oswald	Bed group 18	RK070812.17^	205.80	5.46	-5.16	Laminite
Kap Oswald	Bed group 18	RK070812.18^	206.95	5.83	-4.81	Stromatolite
Kap Oswald	Bed group 18	RK070812.19^	207.95	6.42	-2.86	Stromatolite
Kap Oswald	Bed group 18	RK070812.20^	208.70	5.58	-5.79	Stromatolite
Kap Oswald	Bed group 18	RK070812.21^	209.35	5.25	-6.55	Stromatolite
Kap Oswald	Bed group 18	RK070812.22^	209.40	6.18	-5.27	Stromatolite
Kap Oswald	Bed group 18	RK070812.23^	210.60	5.98	-8.75	Oolitic Packstone
Kap Oswald	Bed group 18	RK070812.24^	211.85	6.90	-7.45	Oolitic Packstone
Kap Oswald	Bed group 18	RK070812.25^	212.60	6.79	-7.80	Oolitic Packstone
Kap Oswald	Bed group 18	RK070812.26^	213.85	6.13	-7.62	Oolitic Packstone
Kap Oswald	Bed group 18	RK070812.27^	215.10	7.15	-6.15	Oolitic Packstone
Kap Oswald	Bed group 18	RK070812.28^	216.10	8.19	-4.27	Oolitic Packstone
Kap Oswald	Bed group 18	RK070812.29^	217.35	7.74	-5.40	Oolitic Packstone
Kap Oswald	Bed group 18	RK070812.30	225.60	-	-	Oolitic Packstone
Kap Oswald	Bed group 18	RK070812.31	219.10	-	-	Stromatolite
Kap Oswald	Bed group 18	RK070812.32^	220.10	6.68	-7.48	Stromatolite
Kap Oswald	Bed group 18	RK070812.33^	220.60	7.54	-7.23	Oolitic Packstone
Kap Oswald	Bed group 18	RK070812.34	221.60	-	-	Oolitic Packstone
Kap Oswald	Bed group 18	RK070812.35^	222.10	7.86	-6.32	Stromatolite
Kap Oswald	Bed group 18	RK070812.36	223.10	-	-	Stromatolite
Kap Oswald	Bed group 18	RK070812.37	224.60	-	-	Stromatolite
Kap Oswald	Bed group 18	RK070812.38A^	225.10	7.60	-6.58	Pisolitic Packstone
Kap Oswald	Bed group 18	RK070812.38B^	225.10	8.00	-5.65	Pisolitic Packstone
Kap Oswald	Bed group 18	RK070812.39^	226.10	7.30	-6.00	Stromatolite
Kap Oswald	Bed group 18	RK070812.40^	227.85	7.10	-7.94	Oolitic Packstone
Kap Oswald	Bed group 18	RK070812.41^	226.85	7.29	-5.75	Stromatolite
Kap Oswald	Bed group 18	RK070812.42^	228.85	7.18	-7.31	Oolitic Packstone
Kap Oswald	Bed group 18	RK070812.43^	229.10	7.11	-7.89	Laminated Dolostone
Kap Oswald	Bed group 18	RK070812.44^	229.60	6.92	-7.46	Pisolitic Packstone
Kap Oswald	Bed group 18	RK070812.45^	230.60	7.17	-7.66	Stromatolite
Kap Oswald	Bed group 18	RK070812.46^	231.10	6.88	-6.97	Stromatolite
Kap Oswald	Bed group 18	RK070812.47^	232.60	6.96	-6.92	Stromatolite
Kap Oswald	Bed group 18	RK070812.48^	234.85	7.93	-3.08	Stromatolite
Kap Oswald	Bed group 18	RK070812.49^	235.85	7.68	-4.90	Stromatolite
Kap Oswald	Bed group 18	RK070812.50^	236.60	7.34	-6.13	Stromatolite
Kap Oswald	Bed group 18	RK070812.51^	237.10	6.71	-7.13	Stromatolite
Kap Oswald	Bed group 18	RK070812.52	-	-	-	Microsparite
Kap Oswald	Bed group 18	RK070812.53	-	-	-	Microsparite
Kap Oswald	Bed group 18	RK070812.54^	-	0.92	-8.18	Oolitic Packstone
Kap Oswald	Bed group 18	RK070812.55^	-	4.26	-7.63	Oolitic Packstone
Kap Oswald	Bed group 18	RK070812.56^	-	7.66	-7.31	Stromatolite
Kap Oswald	Bed group 18	RK070812.57^	-	6.34	-6.11	Neomorphosed Microspar

Section	Formation	Sample No.	Height (m)	$\delta^{13}C_{carb}$	$\delta^{18}O_{carb}$	Lithology
Kap Oswald	Bed group 18	RK070812.58^	-	7.65	-10.77	Oolitic Packstone
Kap Oswald	Bed group 18	RK070812.59^	-	7.33	-6.57	Microsparite
Kap Oswald	Bed group 18	RK070812.60^	-	7.91	-5.62	Flaggy Microsparite
Kap Oswald	Bed group 18	RK070812.61^	-	7.58	-9.16	Flaggy Microsparite
Kap Oswald	Bed group 18	RK080812.1^	471.20	5.34	-7.51	Current Laminated Dolostone
Kap Oswald	Bed group 18	RK080812.2	472.20	5.21	-0.49	Current Laminated Dolostone
Kap Oswald	Bed group 18	RK080812.3^	473.20	5.18	-2.99	Current Laminated Dolostone
Kap Oswald	Bed group 18	RK080812.3*	473.20	5.30	-1.83	Current Laminated Dolostone
Kap Oswald	Bed group 18	RK080812.4A	474.20	4.52	-4.87	Current Laminated Dolostone
Kap Oswald	Bed group 18	RK080812.4B	474.20	-	-	Current Laminated Dolostone
Kap Oswald	Bed group 18	RK080812.5A	float	-	-	Collapse Breccia
Kap Oswald	Bed group 18	RK080812.5B	float	5.50	-3.34	Collapse Breccia
Kap Oswald	Bed group 18	RK080812.5C	float	5.36	-1.35	Collapse Breccia
Kap Oswald	Bed group 18	RK080812.6A	float	4.64	-7.32	Collapse Breccia
Kap Oswald	Bed group 18	RK080812.6B	float	-	-	Collapse Breccia
Kap Oswald	Bed group 18	RK080812.7^	481.70	3.91	-3.15	Collapse Breccia
Kap Oswald	Bed group 18	RK080812.8	482.70	3.83	-3.11	Collapse Breccia
Kap Oswald	Bed group 18	RK080812.9^	483.70	4.97	-8.55	Collapse Breccia
Kap Oswald	Bed group 18	RK080812.10^	512.20	5.07	-8.89	Bituminous Microsparry Limestone
Kap Oswald	Bed group 18	RK080812.11	513.20	4.50	-8.47	Bituminous Microsparry Limestone
Kap Oswald	Bed group 18	RK080812.12	514.20	5.18	-6.99	Bituminous Microsparry Limestone
Kap Oswald	Bed group 18	RK080812.13^	515.20	3.78	-12.09	Bituminous Microsparry Limestone
Kap Oswald	Bed group 18	RK080812.14	516.20	5.22	-8.39	Bituminous Microsparry Limestone
Kap Oswald	Bed group 18	RK080812.15	517.20	5.55	-6.63	Bituminous Microsparry Limestone
Kap Oswald	Bed group 18	RK080812.16	518.20	5.70	-8.75	Bituminous Microsparry Limestone
Kap Oswald	Bed group 18	RK080812.17^	526.20	6.43	-6.81	Bituminous Microsparry Limestone
Kap Oswald	Bed group 18	RK080812.18	527.20	6.10	-6.10	Bituminous Microsparry Limestone
Kap Oswald	Bed group 18	RK080812.19	528.20	6.20	-5.63	Bituminous Microsparry Limestone
Kap Oswald	Bed group 18	RK080812.20^	533.20	6.10	-6.95	Bituminous Microsparry Limestone
Kap Oswald	Bed group 18	RK080812.21	533.45	6.14	-8.04	Bituminous Microsparry Limestone
Kap Oswald	Bed group 18	RK080812.22	533.70	6.59	-5.73	Bituminous Microsparry Limestone
Kap Oswald	Bed group 18	RK080812.23	468.70	-	-	Current Laminated Dolostone
Kap Oswald	Bed group 18	RK080812.24	469.70	-	-	Current Laminated Dolostone
Kap Oswald	Bed group 18	RK080812.25	470.70	-	-	Current Laminated Dolostone
Kap Oswald	Bed group 18	RK080812.26	471.20	-	-	Current Laminated Dolostone
Kap Oswald	Bed group 18	RK080812.27	474.70	-	-	Current Laminated Dolostone
Kap Oswald	Bed group 18	RK080812.28	481.70	-	-	Collapse Breccia
Kap Oswald	Bed group 18	RK080812.29	482.95	-	-	Collapse Breccia
Kap Oswald	Bed group 18	RK080812.30	485.20	-	-	Oolitic Packstone
Kap Oswald	Bed group 18	RK080812.31	485.70	-	-	Oolitic Packstone
Kap Oswald	Bed group 18	RK080812.32	486.20	-	-	Oolitic Packstone
Kap Oswald	Bed group 18	RK080812.33	487.20	-	-	Microsparite
Kap Oswald	Bed group 18	RK080812.34	487.70	-	-	Microsparite
Kap Oswald	Bed group 18	RK080812.35	497.20	-	-	Bituminous Microsparry Limestone
Kap Oswald	Bed group 18	RK080812.36	498.20	-	-	Bituminous Microsparry Limestone
Kap Oswald	Bed group 18	RK080812.37	498.70	-	-	Bituminous Microsparry Limestone
Kap Oswald	Bed group 18	RK080812.38	499.20	-	-	Bituminous Microsparry Limestone
Kap Oswald	Bed group 18	RK080812.39	500.70	-	-	Bituminous Microsparry Limestone
Kap Oswald	Bed group 18	RK080812.40	504.20	-	-	Bituminous Microsparry Limestone
Kap Oswald	Bed group 18	RK080812.41	-	-	-	Bituminous Microsparry Limestone

Section	Formation	Sample No.	Height (m)	$\delta^{13}C_{carb}$	$\delta^{18}O_{carb}$	Lithology
Kap Oswald	Bed group 18	RK080812.42	-	-	-	Bituminous Microsparry Limestone
Kap Oswald	Bed group 18	RK080812.43	-	-	-	Bituminous Microsparry Limestone
Kap Oswald	Bed group 18	RK080812.44	-	-	-	Bituminous Microsparry Limestone
Kap Oswald	Bed group 18	RK080812.45	-	-	-	Bituminous Microsparry Limestone

*= repeat analysis ^= isotopic data analysed at Melbourne University

Letters on the end of the sample number correspond to analysis of different sample components

Appendix 5.2 Andrée Land Group stable isotope data from bed group 19

Section	Formation	Sample No.	Height (m)	$\delta^{13}C_{carb}$	$\delta^{18}O_{carb}$	Lithology
Storeelv	Bed group 19	RK100812.1	0.00	-	-	Dolomicrite - Silty
Storeelv	Bed group 19	RK100812.2^	1.50	-5.24	-4.40	Dolomicrite - Silty
Storeelv	Bed group 19	RK100812.3	2.25	-	-	Dolomicrite - Silty
Storeelv	Bed group 19	RK100812.4	2.50	-	-	Nodular Dolomite
Storeelv	Bed group 19	RK100812.5	2.75	-	-	Mudstone
Storeelv	Bed group 19	RK100812.6	3.00	-	-	Dolomicrite - Silty
Storeelv	Bed group 19	RK100812.7	4.00	-7.22	-2.95	Dolomicrite - Silty
Storeelv	Bed group 19	RK100812.8	4.75	-	-	Mudstone
Storeelv	Bed group 19	RK100812.9^	6.50	-8.25	-4.40	Nodular Dolomite
Storeelv	Bed group 19	RK100812.10	6.75	-	-	Mudstone
Storeelv	Bed group 19	RK100812.11	9.00	-8.82	-3.99	Mudstone
Storeelv	Bed group 19	RK100812.12	10.50	-	-	Mudstone
Storeelv	Bed group 19	RK100812.13	12.50	-	-	Mudstone
Storeelv	Bed group 19	RK100812.14	15.75	-12.95	-4.24	Mudstone
Storeelv	Bed group 19	RK100812.15	16.00	-	-	Mudstone
Storeelv	Bed group 19	RK100812.16	19.00	-	-	Mudstone
Storeelv	Bed group 19	RK100812.17	21.50	-	-	Mudstone
Storeelv	Bed group 19	RK100812.18	22.50	-	-	Mudstone
Storeelv	Bed group 19	RK100812.19	24.75	-	-	Mudstone
Storeelv	Bed group 19	RK100812.20	29.25	-	-	Mudstone
Storeelv	Bed group 19	RK100812.21	32.00	-7.92	-3.35	Mudstone
Storeelv	Bed group 19	RK100812.22	35.00	-	-	Dolomicrite - Silty
Storeelv	Bed group 19	RK100812.23	37.00	-	-	Mudstone
Storeelv	Bed group 19	RK100812.24	38.00	-8.09	-3.69	Dolomicrite - Silty
Storeelv	Bed group 19	RK100812.25^	39.00	-7.89	-4.19	Mudstone
Storeelv	Bed group 19	RK100812.26	40.75	-	-	Mudstone
Storeelv	Bed group 19	RK100812.27	45.00	-9.35	-10.11	Dolomicrite - Silty
Storeelv	Bed group 19	RK100812.28	45.00	-	-	Mudstone
Storeelv	Bed group 19	RK100812.29	46.25	-	-	Dolomicrite - Silty
Storeelv	Bed group 19	RK100812.30	47.75	-	-	Dolomicrite - Silty
Storeelv	Bed group 19	RK100812.31	49.00	-	-	Dolomicrite - Silty
Storeelv	Bed group 19	RK100812.32	49.50	-	-	Mudstone
Storeelv	Bed group 19	RK100812.33A^	51.25	-6.40	-5.04	Dolomicrite - Silty
Storeelv	Bed group 19	RK100812.33B^	51.25	-5.94	-3.45	Dolomicrite - Silty
Storeelv	Bed group 19	RK100812.34	52.25	-	-	Dolomicrite - Silty
Storeelv	Bed group 19	RK100812.35	54.50	-5.49	-4.28	Dolomicrite - Silty
Storeelv	Bed group 19	RK100812.36	59.00	-	-	Dolomicrite - Silty
Storeelv	Bed group 19	RK100812.37^	61.00	-2.75	-7.16	Mudstone
Storeelv	Bed group 19	RK100812.38	63.00	-	-	Mudstone
Storeelv	Bed group 19	RK100812.39	64.50	-	-	Mudstone
Storeelv	Bed group 19	RK100812.40	67.00	-5.35	-2.94	Mudstone
Storeelv	Bed group 19	RK110812.1	70.00	-7.07	-4.36	Mudstone
Storeelv	Bed group 19	RK110812.2^	71.00	-7.28	-4.65	Mudstone
Storeelv	Bed group 19	RK110812.3	72.00	-6.53	-3.62	Mudstone
Storeelv	Bed group 19	RK110812.4	74.50	-	-	Mudstone
Storeelv	Bed group 19	RK110812.5	-	-	-	Not Collected
Storeelv	Bed group 19	RK110812.6	77.00	-6.76	-4.13	Dolomicrite - Silty
Storeelv	Bed group 19	RK110812.7^	80.00	-7.49	-9.71	Dolomicrite - Silty

Section	Formation	Sample No.	Height (m)	$\delta^{13}C_{carb}$	$\delta^{18}O_{carb}$	Lithology
Storeelv	Bed group 19	RK110812.8	81.00	-6.95	-5.25	Dolomicrite - Silty
Storeelv	Bed group 19	RK110812.9	82.00	-6.03	-5.73	Mudstone
Storeelv	Bed group 19	RK110812.10	84.00	-	-	Mudstone
Storeelv	Bed group 19	RK110812.11	85.25	-7.61	-8.58	Mudstone
Storeelv	Bed group 19	RK110812.12	86.50	-	-	Mudstone
Storeelv	Bed group 19	RK110812.13	87.00	-	-	Mudstone
Storeelv	Bed group 19	RK110812.14	88.00	-	-	Mudstone
Storeelv	Bed group 19	RK110812.15^	89.00	-5.94	-4.60	Dolomicrite - Silty
Storeelv	Bed group 19	RK110812.16	91.00	-	-	Mudstone
Storeelv	Bed group 19	RK110812.17	92.50	-6.83	-4.55	Mudstone
Storeelv	Bed group 19	RK110812.18	93.75	-	-	Mudstone
Storeelv	Bed group 19	RK110812.19	95.25	-	-	Dolomicrite - Silty
Storeelv	Bed group 19	RK110812.20	96.50	-	-	Dolomicrite - Silty
Storeelv	Bed group 19	RK110812.21^	97.00	-8.45	-5.23	Dolomicrite - Silty
Storeelv	Bed group 19	RK110812.22	98.00	-	-	Dolomicrite - Silty
Storeelv	Bed group 19	RK110812.23	104.00	-5.93	-4.34	Dolomicrite - Silty
Storeelv	Bed group 19	RK110812.24	105.00	-	-	Dolomicrite - Silty
Storeelv	Bed group 19	RK110812.25	111.50	-5.05	-8.01	Dolomicrite - Silty
Storeelv	Bed group 19	RK110812.26	113.00	-	-	Dolomicrite - Silty
Storeelv	Bed group 19	RK110812.27^	114.50	-4.15	-8.33	Dolomicrite - Silty
Storeelv	Bed group 19	RK110812.28	121.50	-	-	Mudstone
Storeelv	Bed group 19	RK110812.29A^	122.50	-5.10	-6.48	Debris Flow
Storeelv	Bed group 19	RK110812.29B^	122.50	-4.66	-6.15	Debris Flow
Storeelv	Bed group 19	RK110812.30	122.75	-	-	Mudstone
Storeelv	Bed group 19	RK110812.31	123.75	-	-	Mudstone
Storeelv	Bed group 19	RK110812.32	129.00	-	-	Mudstone
Storeelv	Bed group 19	RK110812.33	131.75	-	-	Mudstone
Storeelv	Bed group 19	RK110812.34^	134.50	-6.49	-7.11	Debris Flow
Storeelv	Bed group 19	RK110812.35^	151.25	-3.14	-8.15	Ribbon Limestone
Storeelv	Bed group 19	RK110812.36	152.50	-	-	Ribbon Limestone
Storeelv	Bed group 19	RK110812.37	153.25	-	-	Ribbon Limestone
Storeelv	Bed group 19	RK110812.38^	154.00	-3.00	-8.19	Mudflake Conglomerate
Storeelv	Bed group 19	RK110812.39	155.50	-	-	Mudflake Conglomerate
Kløftelv	Bed group 19	RK120812.1^	1.75	-3.91	-7.38	Ribbon Limestone
Kløftelv	Bed group 19	RK120812.2^	2.50	-3.22	-6.48	Mudflake Conglomerate
Kløftelv	Bed group 19	RK120812.2^	2.50	-3.90	-8.08	Mudflake Conglomerate
Kløftelv	Bed group 19	RK120812.3^	3.00	-4.83	-7.44	Mudstone
Kløftelv	Bed group 19	RK120812.4	3.50	-	-	Mudflake Conglomerate
Kløftelv	Bed group 19	RK120812.5	4.00	-	-	Mudflake Conglomerate
Kløftelv	Bed group 19	RK120812.6	4.75	-	-	Mudstone
Kløftelv	Bed group 19	RK120812.7	5.25	-	-	Dolomicrite - Silty
Kløftelv	Bed group 19	RK120812.8	6.00	-	-	Dolomicrite - Silty
Kløftelv	Bed group 19	RK120812.9	7.00	-	-	Mudstone
Kløftelv	Bed group 19	RK120812.10^	8.00	-3.48	-8.74	Debris Flow
Kløftelv	Bed group 19	RK120812.11^	10.00	-5.43	-5.04	Mudstone
Kløftelv	Bed group 19	RK120812.12	11.00	-	-	Debris Flow
Kløftelv	Bed group 19	RK120812.13	12.50	-6.24	-4.20	Mudstone
Kløftelv	Bed group 19	RK120812.14	13.50	-	-	Mudstone
Kløftelv	Bed group 19	RK120812.15	16.50	-	-	Mudstone
Kløftelv	Bed group 19	RK120812.16	21.00	-	-	Mudstone

Section	Formation	Sample No.	Height (m)	$\delta^{13}C_{carb}$	$\delta^{18}O_{carb}$	Lithology
Kløftelv	Bed group 19	RK120812.17	21.50	-	-	Mudstone
Kløftelv	Bed group 19	RK120812.18A	25.90	-	-	Organic Mudstone
Kløftelv	Bed group 19	RK120812.18B	25.90	-	-	Organic Mudstone
Kløftelv	Bed group 19	RK120812.18C	25.90	-	-	Organic Mudstone
Kløftelv	Bed group 19	RK120812.18D	25.90	-	-	Organic Mudstone
Kløftelv	Bed group 19	RK120812.18E	25.90	-	-	Organic Mudstone
Kløftelv	Bed group 19	RK120812.18F	25.90	-	-	Organic Mudstone
Kløftelv	Bed group 19	RK120812.18G	25.90	-	-	Organic Mudstone
Kløftelv	Bed group 19	RK120812.18H	25.90	-	-	Organic Mudstone
Kløftelv	Bed group 19	RK120812.19	26.00	-	-	Mudstone
Kløftelv	Bed group 19	RK120812.20^	29.75	-11.17	-8.70	Microsparite
Kløftelv	Bed group 19	RK120812.21	32.25	-	-	Mudstone
Kløftelv	Bed group 19	RK120812.22	34.50	-	-	Mudstone
Kløftelv	Bed group 19	RK120812.23	37.25	-	-	Mudstone
Kløftelv	Bed group 19	RK120812.24	41.25	-	-	Mudstone
Kløftelv	Bed group 19	RK120812.25	48.00	-	-	Mudstone
Kløftelv	Bed group 19	RK120812.26	52.50	-	-	Sand
Kløftelv	Bed group 19	RK120812.27	53.50	-	-	Pyritic Nodules
Kløftelv	Bed group 19	RK120812.28	55.00	-	-	Sand
Kløftelv	Bed group 19	RK120812.29	59.50	-5.33	-9.23	Mudstone
Kløftelv	Bed group 19	RK120812.30	66.00	-	-	Pyritic Nodules
Kløftelv	Bed group 19	RK120812.31	69.50	-	-	Mudstone
Kløftelv	Bed group 19	RK120812.32	74.50	-	-	Mudstone
Kløftelv	Bed group 19	RK120812.33	79.00	-	-	Mudstone
Kløftelv	Bed group 19	RK160812.1	0.25	-	-	Mudstone
Kløftelv	Bed group 19	RK160812.2	1.50	-	-	Mudstone
Kløftelv	Bed group 19	RK160812.3	4.75	-	-	Mudstone
Kløftelv	Bed group 19	RK160812.4	9.85	-	-	Mudstone
Kløftelv	Bed group 19	RK160812.5^	11.75	-8.18	-3.30	Dolomicrite - Silty
Kløftelv	Bed group 19	RK160812.6	15.00	-	-	Mudstone
Kløftelv	Bed group 19	RK160812.7	15.75	-	-	Mudstone
Kløftelv	Bed group 19	RK160812.8	16.75	-	-	Mudstone
Kløftelv	Bed group 19	RK160812.9	18.00	-	-	Mudstone
Kløftelv	Bed group 19	RK160812.10	18.25	-	-	Dolomicrite - Silty
Kløftelv	Bed group 19	RK160812.11	19.50	-	-	Dolomicrite - Silty
Kløftelv	Bed group 19	RK160812.12	20.00	-	-	Mudstone
Kløftelv	Bed group 19	RK160812.13^	25.00	-7.19	-5.12	Mudstone
Kløftelv	Bed group 19	RK160812.14	30.00	-	-	Dolomicrite - Silty
Kløftelv	Bed group 19	RK160812.15	-	-	-	Dolomicrite - Silty
Kløftelv	Bed group 19	RK160812.16	31.00	-	-	Sand
Kløftelv	Bed group 19	RK160812.17	31.25	-	-	Mudflake Conglomerate
Kløftelv	Bed group 19	RK160812.18	31.75	-	-	Sand
Kløftelv	Bed group 19	RK160812.19	31.85	-	-	Sand
Kløftelv	Bed group 19	RK160812.20^	35.50	-5.91	-5.34	Mudstone
Kløftelv	Bed group 19	RK160812.21	-	-	-	Upper Contact - Limey Channel
Kløftelv	Bed group 19	RK180812.1	-	-	-	Dolomicrite - Silty
Kløftelv	Bed group 19	RK180812.2^	45.50	-6.92	-5.31	Mudstone
Kløftelv	Bed group 19	RK180812.3	50.00	-	-	Dolomicrite - Silty
Kløftelv	Bed group 19	RK180812.4	53.00	-	-	Mudstone
Kløftelv	Bed group 19	RK180812.5A^	53.50	-6.61	-6.48	Concretion

Section	Formation	Sample No.	Height (m)	$\delta^{13}C_{carb}$	$\delta^{18}O_{carb}$	Lithology
Kløftelv	Bed group 19	RK180812.5B^	53.50	-6.43	-5.20	Concretion
Kløftelv	Bed group 19	RK180812.6^	55.00	-6.52	-5.30	Dolomicrite - Silty
Kløftelv	Bed group 19	RK180812.7	56.00	-	-	Mudstone
Kløftelv	Bed group 19	RK180812.8	58.25	-	-	Mudstone
Kløftelv	Bed group 19	RK180812.9^	60.00	-6.96	-6.41	Mudstone
Kløftelv	Bed group 19	RK180812.10	64.00	-	-	Mudstone
Kløftelv	Bed group 19	RK180812.11	68.50	-	-	Mudstone
Kløftelv	Bed group 19	RK180812.12^	70.50	-7.34	-8.08	Dolomicrite - Silty
Kløftelv	Bed group 19	RK180812.13	72.00	-	-	Mudstone
Kløftelv	Bed group 19	RK180812.14	74.00	-	-	Dolomicrite - Silty
Kløftelv	Bed group 19	RK180812.16	-	-	-	Dolomicrite - Silty
Tømmerbugt	Bed group 19	RK140812.1	0.00	-	-	Mudstone
Tømmerbugt	Bed group 19	RK140812.2	1.00	-	-	Mudstone
Tømmerbugt	Bed group 19	RK140812.3	2.50	-	-	Mudstone
Tømmerbugt	Bed group 19	RK140812.4	3.00	-	-	Mudstone
Tømmerbugt	Bed group 19	RK140812.5	4.25	-	-	Mudstone
Tømmerbugt	Bed group 19	RK140812.6	5.25	-	-	Mudstone
Tømmerbugt	Bed group 19	RK140812.7	7.50	-	-	Mudstone
Tømmerbugt	Bed group 19	RK140812.8	9.00	-	-	Mudstone
Tømmerbugt	Bed group 19	RK140812.9	10.75	-	-	Mudstone
Tømmerbugt	Bed group 19	RK140812.10	12.50	-	-	Mudstone
Tømmerbugt	Bed group 19	RK140812.12	14.50	-	-	Mudstone
Tømmerbugt	Bed group 19	RK140812.13	16.50	-	-	Mudstone
Tømmerbugt	Bed group 19	RK140812.14	20.00	-	-	Mudstone
Tømmerbugt	Bed group 19	RK140812.15	21.00	-	-	Concretion
Tømmerbugt	Bed group 19	RK140812.16	21.00	-	-	Concretion
Tømmerbugt	Bed group 19	RK140812.17	23.00	-	-	Mudstone
Tømmerbugt	Bed group 19	RK140812.18	28.50	-	-	Mudstone
Tømmerbugt	Bed group 19	RK140812.19	28.00	-	-	Concretion
Tømmerbugt	Bed group 19	RK140812.20	32.25	-	-	Mudstone
Tømmerbugt	Bed group 19	RK140812.21	33.25	-	-	Mudstone
Tømmerbugt	Bed group 19	RK140812.22	34.00	-	-	Mudstone
Tømmerbugt	Bed group 19	RK140812.23	35.00	-	-	Mudstone

^= isotopic data analysed at Melbourne University

Letters on the end of the sample number correspond to analysis of different sample components

Appendix 5.3 Andrée Land Group stable isotope data from other locations

Section	Member	Sample No.	Height (m)	$\delta^{13}C_{carb}$	$\delta^{18}O_{carb}$	Lithology
Kap Weber	Bed group 18.13	PG046	86.80	7.29	-5.42	Microsparry Limestone
Kap Weber	Bed group 18.13	PG050	77.20	7.73	-4.99	Microsparry Limestone
Kap Weber	Bed group 18.16	PG074	19.60	2.32	-6.74	Dolomitic Microsparry Limestone
Kap Weber	Bed group 18.16	PG074*	19.60	2.28	-6.68	Dolomitic Microsparry Limestone
Kap Weber	Bed group 18.16	PG075	19.00	3.38	-5.01	Dolomitic Microsparry Limestone
Kap Weber	Bed group 18.16	PG076	18.50	2.32	-7.35	Dolomitic Microsparry Limestone
Kap Weber	Bed group 18.16	PG077	18.50	2.59	-5.21	Dolomitic Microsparry Limestone
Kap Weber	Bed group 18.16	PG078	17.90	3.59	-5.96	Dolomitic Microsparry Limestone
Kap Weber	Bed group 18.16	PG079	17.50	2.36	-6.77	Dolomitic Microsparry Limestone
Kap Weber	Bed group 18.16	PG080	14.80	2.69	-5.11	Dolomitic Microsparry Limestone
Kap Weber	Bed group 18.16	PG081	14.80	4.48	-1.60	Dolomicrospar
Kap Weber	Bed group 18.16	PG003	14.30	2.61	-6.44	Dolomitic Microsparry Limestone
Kap Weber	Bed group 18.16	PG001	7.40	2.55	-6.48	Dolomitic Microsparry Limestone
Kap Weber	Bed group 18.16	PG001*	7.40	2.61	-6.34	Dolomitic Microsparry Limestone
Kap Weber	Bed group 18.16	PG002	0.90	1.80	-5.45	Dolomitic Microsparry Limestone
Kap Weber	Bed group 19.1	PG004	19.50	2.26	-5.40	Intraclastic Calcarenite
Kap Weber	Bed group 19.1	PG005	14.20	2.62	-5.74	Intraclastic Calcarenite
Kap Weber	Bed group 19.1	PG006	14.20	3.04	-5.88	Intraclastic Calcarenite
Kap Weber	Bed group 19.1	PG008	5.50	-0.23	-6.79	Intraclastic Calcarenite
Kap Weber	Bed group 19.1	PG007	5.00	0.36	-7.01	Intraclastic Calcarenite
Kap Weber	Bed group 19.1	PG009	4.80	-0.48	-4.70	Intraclastic Calcarenite
Kap Weber	Bed group 19.1	PG009*	4.80	-0.58	-4.86	Intraclastic Calcarenite
Kap Weber	Bed group 19.1	PG010	2.00	0.42	-7.50	Intraclastic Calcarenite
Kap Weber	Bed group 19.2	PG013	24.00	-5.87	-3.52	Dolomicrite
Kap Weber	Bed group 19.2	PG014	6.80	-6.61	-4.51	Dolomicrite
Kap Weber	Bed group 19.2	PG015	2.80	-7.34	-3.99	Dolomicrite
Kap Weber	Bed group 19.3	PG016	4.70	-6.83	-3.01	Dolomicrite
Kap Weber	Bed group 19.3	PG017	4.70	-7.18	-3.85	Dolomicrite
Kap Weber	Bed group 19.3	PG018	2.70	-8.32	-7.25	Calcareous Dolomicrite
Kap Weber	Bed group 19.3	PG019	2.70	-7.82	-8.05	Calcareous Dolomicrite
Kap Weber	Bed group 19.3	PG020	1.40	-7.25	-4.40	Dolomicrite
Kap Weber	Bed group 19.3	PG020*	1.40	-7.27	-4.49	Dolomicrite
Kap Weber	Bed group 19.3	PG021	0.60	-6.75	-4.95	Dolomicrite
Kap Weber	Bed group 19.5	PG023	17.80	-5.22	-7.15	Microsparry Limestone
Kap Weber	Bed group 19.5	PG024	3.40	-5.50	-6.72	Microsparry Limestone
Kap Weber	Bed group 19.5	PG025	2.40	-3.81	-5.09	Microsparry Limestone
Kap Weber	Bed group 19.5	PG026	2.00	-4.51	-6.47	Microsparry Limestone
Kap Weber	Bed group 19.6	PG027	0.50	-2.80	-5.03	Calcareous Dolorudite
Kap Weber	Bed group 19.6	PG028	0.50	-2.78	-4.63	Microsparry Limestone
Kap Weber	Bed group 19.6	PG029	0.50	-3.09	-6.99	Microsparry Limestone
Kap Weber	Bed group 19.6	PG029	0.50	-2.93	-6.78	Microsparry Limestone
Kap Weber	Bed group 19.6	PG030	0.50	-3.39	-5.64	Calcareous Dolorudite
Kap Weber	Bed group 20.1	PG037	43.20	7.03	-3.49	Microsparry Limestone
Kap Weber	Bed group 20.1	PG036	55.60	6.77	-4.35	Microsparry Limestone
Kap Weber	Bed group 20.1	PG035	60.50	6.54	-6.35	Microsparry Limestone
Kap Weber	Bed group 20.1	PG034	85.50	5.24	-5.76	Microsparry Limestone
Kap Weber	Bed group 20.1	PG033	92.70	5.3	-3.27	Microsparry Limestone
Kap Weber	Bed group 20.1	PG032	95.60	2.98	-3.59	Microsparry Limestone

Section	Member	Sample No.	Height (m)	$\delta^{13}C_{carb}$	$\delta^{18}O_{carb}$	Lithology
Kap Weber	Bed group 20.1	PG031	96.60	3.76	-3.56	Microsparry Limestone
Kap Weber	Bed group 20.3	PG043	2.60	7.22	-7.09	Intraclastic Calcarenite
Kap Weber	Bed group 20.3	PG045	4.60	8.93	-8.28	Microsparry Limestone
Kap Weber	Bed group 20.3	PG040	4.60	7.1	-6.73	Microsparry Limestone
Kap Weber	Bed group 20.3	PG039	4.60	6.79	-5.89	Microsparry Limestone
Ella Ø	Bed group 18.9	PG426	24.10	7.41	-4.56	Cherty Oolitic Limestone
Ella Ø	Bed group 18.9	PG427	17.00	7.31	-5.55	Microsparry/Oolitic Limestone
Ella Ø	Bed group 18.9	PG429	2.50	7.08	-4.54	Intraclastic Dolomitic Limestone
Ella Ø	Bed group 18.9	PG430	2.50	6.65	-5.47	Intraclastic Dolomitic Limestone
Ella Ø	Bed group 18.11	PG432A	114.20	7.49	-5.34	Microsparry Limestone
Ella Ø	Bed group 18.11	PG432B	114.20	7.19	-5.39	Microsparry Limestone
Ella Ø	Bed group 18.11	PG433A	92.10	7.77	-5.23	Microsparry Limestone
Ella Ø	Bed group 18.11	PG433A*	92.10	7.88	-5.07	Microsparry Limestone
Ella Ø	Bed group 18.11	PG433B	92.10	5.95	-5.48	Microsparry Limestone
Ella Ø	Bed group 18.11	PG434A	80.80	5.72	-3.72	Microsparry/Oolitic Limestone
Ella Ø	Bed group 18.11	PG434B	80.80	7.27	-5.35	Microsparry/Oolitic Limestone
Ella Ø	Bed group 18.11	PG436A	62.50	7.35	-5.44	Microsparry Limestone/Oolitic Calcarenite
Ella Ø	Bed group 18.11	PG436B	62.50	7.35	-5.19	Microsparry Limestone/Oolitic Calcarenite
Ella Ø	Bed group 18.11	PG437	52.80	6.97	-4.95	Microsparry Limestone
Ella Ø	Bed group 18.11	PG438	51.20	6.96	-4.73	Microsparry Limestone
Ella Ø	Bed group 18.11	PG439	41.80	7.36	-5.51	Peloidal Calcarenite
Ella Ø	Bed group 18.11	PG439*	41.80	7.56	-4.93	Peloidal Calcarenite
Ella Ø	Bed group 18.11	PG440	37.40	7.78	-6.08	Oolitic Limestone
Ella Ø	Bed group 18.11	PG442	29.80	7.36	-5.85	Microsparry Limestone
Ella Ø	Bed group 18.11	PG443	13.60	7.72	-5.77	Oolitic Limestone
Ella Ø	Bed group 18.11	PG444	12.60	7.78	-4.79	Microsparry Limestone
Ella Ø	Bed group 18.11	PG446A	5.30	6.91	-7.41	Microsparry Limestone
Ella Ø	Bed group 18.11	PG446B	5.30	7.70	-5.26	Microsparry Limestone/Shrinkage Crack Cement
Ella Ø	Bed group 18.12	PG448A	19.20	6.66	-10.49	Cherty Oolitic Dolostone
Ella Ø	Bed group 18.12	PG448A*	19.20	7.14	-10.69	Cherty Oolitic Dolostone
Ella Ø	Bed group 18.12	PG448B	19.20	7.26	-12.42	Cherty Oolitic Dolostone
Ella Ø	Bed group 18.12	PG448C	19.20	7.31	-10.96	Cherty Oolitic Dolostone
Ella Ø	Bed group 18.12	PG449	18.00	7.54	-11.46	Peloidal Dolarenite
Ella Ø	Bed group 18.12	PG449	18.00	7.65	-11.35	Peloidal Dolarenite
Ella Ø	Bed group 18.12	PG451A	15.60	7.69	-10.27	Peloidal Dolarenite
Ella Ø	Bed group 18.12	PG451B	15.60	7.93	-10.33	Peloidal Dolarenite
Ella Ø	Bed group 18.12	PG452	13.70	7.43	-11.97	Peloidal Dolarenite
Ella Ø	Bed group 18.12	PG454	0.90	2.44	-14.20	Microsparry Limestone
Ella Ø	Ulvesø - Diamictite	EFE77A	-	-5.22	-0.45	Mud Stringer
Ella Ø	Ulvesø - Diamictite	EFE77B	-	-6.25	-13.11	Aggregate Clast
Ella Ø	Ulvesø - Diamictite	EFE77E	-	-0.33	0.23	White Clast
Ella Ø	Ulvesø - Diamictite	EFE77I	-	3.33	-0.31	Limestone Clast
Ella Ø	Ulvesø - Diamictite	EFE77K	-	-5.08	-3.87	Mud Stringer
Ella Ø	Ulvesø - Diamictite	EFE80A	-	4.30	-7.04	Dolomite Clast
Ella Ø	Ulvesø - Diamictite	EFE80B	-	-3.97	-7.15	Limestone Clast
Ella Ø	Ulvesø - Diamictite	EFE80C	-	-4.86	-9.51	Limestone Clast
Ella Ø	Ulvesø - Diamictite	EFE155A	-	-5.32	-6.33	Matrix Carbonate
Ella Ø	Ulvesø - Diamictite	EFE155B	-	-3.66	-5.84	Limestone Clast
Ella Ø	Ulvesø - Diamictite	EFE155C	-	-5.24	-5.12	Limestone Clast

Section	Member	Sample No.	Height (m)	$\delta^{13}C_{carb}$	$\delta^{18}O_{carb}$	Lithology
Ella Ø	Ulvesø - Diamictite	EFE155D	-	0.30	-0.41	Limestone Clast
Ella Ø	Ulvesø - Diamictite	EFE155E	-	4.09	-0.94	Dolomite Clast
Ella Ø	Ulvesø - Diamictite	EFE155F	-	-1.68	-5.50	Limestone Clast
Ella Ø	Ulvesø - Diamictite	EFE155G	-	4.62	-6.31	Dolomite clast
Ella Ø	Ulvesø - Limestone Lens	EFE150A	-	3.63	-0.63	Matrix
Ella Ø	Ulvesø - Limestone Lens	EFE150L	-	-4.41	-5.54	Microspar
Ella Ø	Ulvesø - Limestone Lens	EFE150B	-	0.15	-7.74	Limestone Clast
Ella Ø	Ulvesø - Limestone Lens	EFE150C	-	1.08	-7.03	Limestone Clast
Ella Ø	Ulvesø - Limestone Lens	EFE150D	-	-0.40	-6.11	Matrix
Ella Ø	Ulvesø - Limestone Lens	EFE150E	-	1.31	-5.98	Microspar
Ella Ø	Ulvesø - Limestone Lens	EFE150E	-	4.31	-0.06	Microspar
Ella Ø	Ulvesø - Limestone Lens	EFE150F	-	-0.61	-4.81	Microspar
Ella Ø	Ulvesø - Limestone Lens	EFE150G	-	-1.47	-6.10	Microspar
Ella Ø	Ulvesø - Limestone Lens	EFE150H	-	1.21	-5.66	Microspar
Ella Ø	Ulvesø - Limestone Lens	EFE150I	-	0.29	-6.32	Microspar
Ella Ø	Ulvesø - Limestone Lens	EFE150J	-	1.28	-4.68	Microspar
Ella Ø	Ulvesø - Limestone Lens	EFE150K	-	-1.38	-6.40	Microspar
Ella Ø	Ulvesø - Limestone Lens	EFE151A	-	1.34	-8.23	Matrix
Ella Ø	Ulvesø - Limestone Lens	EFE151B	-	0.69	-6.87	Limestone Clast
Ella Ø	Ulvesø - Limestone Lens	EFE151C	-	1.73	-5.43	Microspar
Ella Ø	Ulvesø - Limestone Lens	EFE151D	-	-0.09	-4.90	Microspar
Ella Ø	Ulvesø - Limestone Lens	EFE151E	-	0.78	-5.60	Microspar

*= repeat analysis

Letters on the end of the sample number correspond to analysis of different sample components

Appendix 6. Etina Formation stable isotope data

Section	Formation	Sample No.	Height (m)	$\delta^{13}C_{carb}$	$\delta^{18}O_{carb}$	Lithology
Bunkers Range	Etina	RK190413.1	1.50	5.90	-10.84	Sandstone
Bunkers Range	Etina	RK190413.2	7.25	5.53	-9.47	Limestone Concretion
Bunkers Range	Etina	RK190413.3	11.50	4.83	-10.39	Cemented Siltstone
Bunkers Range	Etina	RK190413.4	27.00	4.92	-10.03	Cemented Siltstone
Bunkers Range	Etina	RK190413.5	41.00	5.47	-9.60	Cemented Siltstone
Bunkers Range	Etina	RK190413.6	43.00	6.93	-10.36	Mudflake Conglomerate
Bunkers Range	Etina	RK200413.1	50.00	-	-	Siltstone
Bunkers Range	Etina	RK200413.2	58.25	-	-	Sandy Limestone
Bunkers Range	Etina	RK200413.3	56.00	7.95	-10.21	Sandy Limestone
Bunkers Range	Etina	RK200413.4	59.50	9.24	-6.33	Sandy Limestone
Bunkers Range	Etina	RK200413.5	70.50	7.42	-9.24	Sandy Limestone
Bunkers Range	Etina	RK200413.6	79.70	7.17	-8.51	Sandy Limestone
Bunkers Range	Etina	RK200413.7	83.10	8.52	-7.55	Cross-Bedded Sandy Limestone
Bunkers Range	Etina	RK200413.8	85.40	-	-	Cross-Bedded Sandy Limestone
Bunkers Range	Etina	RK200413.9	86.10	8.54	-7.25	Cross-Bedded Sandy Limestone
Bunkers Range	Etina	RK200413.10	86.50	-	-	Cross-Bedded Sandy Limestone
Bunkers Range	Etina	RK200413.11	88.00	7.96	-7.90	Cross-Bedded Sandy Limestone
Bunkers Range	Etina	RK200413.12	89.00	-	-	Intraclast Conglomerate
Bunkers Range	Etina	RK200413.13A	93.50	7.28	-8.02	Oolitic Grainstone
Bunkers Range	Etina	RK200413.13B	93.50	8.06	-7.31	Oolitic Grainstone
Bunkers Range	Etina	RK200413.14	102.00	-	-	Oolitic Grainstone
Bunkers Range	Etina	RK200413.15	105.10	7.88	-7.76	Dolomicrite
Bunkers Range	Etina	RK200413.16A	120.80	7.80	-7.59	Intraclast Conglomerate
Bunkers Range	Etina	RK200413.16B	120.80	8.59	-7.79	Intraclast Conglomerate
Bunkers Range	Etina	RK200413.17	123.10	8.96	-6.33	Oolitic Grainstone
Bunkers Range	Etina	RK200413.18	135.60	9.23	-4.45	Oolitic Grainstone
Bunkers Range	Etina	RK200413.19	155.00	-	-	Cemented Sand
Bunkers Range	Etina	RK200413.20	160.00	-	-	Cemented Sand
Bunkers Range	Etina	RK200413.21	156.00	-	-	Siltstone
Bunkers Range	Etina	RK200413.22	156.90	-	-	Siltstone
Bunkers Range	Etina	RK200413.23	157.90	-	-	Siltstone
Bunkers Range	Etina	RK200413.24	159.20	-	-	Siltstone
Bunkers Range	Etina	RK200413.25	160.80	5.71	-9.82	Siltstone
Bunkers Range	Etina	RK200413.26	161.30	-	-	Siltstone
Bunkers Range	Etina	RK200413.27	162.70	-	-	Siltstone
Bunkers Range	Etina	RK200413.28	165.50	4.90	-7.72	Siltstone
Bunkers Range	Etina	RK200413.29	168.20	-	-	Siltstone
Bunkers Range	Etina	RK200413.30	169.50	7.94	-10.03	Siltstone
Bunkers Range	Etina	RK200413.31	171.40	-	-	Siltstone
Bunkers Range	Etina	RK200413.32A	172.90	7.61	-9.76	Siltstone
Bunkers Range	Etina	RK200413.33	179.20	-	-	Sandy Limestone
Bunkers Range	Etina	RK200413.34	181.20	-	-	Sandy Limestone
Bunkers Range	Etina	RK200413.35	182.80	-	-	Sandy Limestone
Bunkers Range	Etina	RK200413.36A	184.30	8.83	-9.11	Sandy Limestone
Bunkers Range	Etina	RK200413.37	186.00	-	-	Sandy Limestone
Bunkers Range	Etina	RK200413.38	187.80	-	-	Sandy Limestone
Bunkers Range	Etina	RK200413.39	189.20	8.17	-10.45	Sandy Limestone
Bunkers Range	Etina	RK200413.40	194.20	-	-	Massive Sandstone

Section	Formation	Sample No.	Height (m)	$\delta^{13}C_{carb}$	$\delta^{18}O_{carb}$	Lithology
Bunkers Range	Etina	RK200413.41	196.60	9.15	-10.69	Cross-Bedded Sandy Limestone
Bunkers Range	Etina	RK200413.42	197.70	-	-	Cross-Bedded Sandy Limestone
Bunkers Range	Etina	RK200413.43	198.70	-	-	Cross-Bedded Sandy Limestone
Bunkers Range	Etina	RK200413.44	202.20	-	-	Cross-Bedded Sandy Limestone
Bunkers Range	Etina	RK200413.45A	204.40	9.11	-4.42	Cross-Bedded Sandy Limestone
Bunkers Range	Etina	RK200413.46	208.60	-	-	Cross-Bedded Sandy Limestone
Bunkers Range	Etina	RK200413.47A	211.80	8.98	-3.96	Cross-Bedded Sandy Limestone
Bunkers Range	Etina	RK200413.48	213.70	-	-	Cross-Bedded Sandy Limestone
Bunkers Range	Etina	RK200413.49	216.50	9.87	-3.44	Cross-Bedded Sandy Limestone
Bunkers Range	Etina	RK200413.50	220.30	8.85	-3.18	Cross-Bedded Sandy Limestone
Bunkers Range	Etina	RK200413.51A	224.00	7.09	-7.11	Siltstone
Bunkers Range	Etina	RK200413.52	226.80	6.61	-4.12	Oolitic Grainstone
Bunkers Range	Etina	RK200413.53	228.00	-	-	Micrite
Bunkers Range	Etina	RK200413.55A	230.80	9.78	-3.37	Oolitic Grainstone
Bunkers Range	Etina	RK200413.56	234.00	-	-	Oolitic Grainstone
Bunkers Range	Etina	RK200413.57	241.40	9.44	-5.54	Cross-Bedded Sandy Limestone
Bunkers Range	Etina	RK200413.58	244.60	9.45	-4.79	Sandy Limestone
Bunkers Range	Etina	RK200413.59	247.00	8.94	-6.68	Microbial Laminite
Bunkers Range	Etina	RK200413.60	247.50	5.92	-8.25	Laminite
Bunkers Range	Etina	RK200413.61	248.00	8.97	-5.62	Oolitic Grainstone
Bunkers Range	Etina	RK200413.62	249.50	-	-	Microbial Laminite
Bunkers Range	Etina	RK200413.63	251.00	8.07	-6.59	Microbial Laminite
Bunkers Range	Etina	RK200413.64	253.00	9.11	-5.70	Oolitic Grainstone
Bunkers Range	Etina	RK220413.1A	258.50	7.97	-7.77	Sandy Limestone
Bunkers Range	Etina	RK220413.1B	258.50	-	-	Sandy Limestone
Bunkers Range	Etina	RK220413.2	259.80	7.93	-7.38	Sandy Limestone
Bunkers Range	Etina	RK220413.3A	264.50	8.20	-5.32	Oolitic Grainstone
Bunkers Range	Etina	RK220413.3A*	264.50	8.04	-7.47	Oolitic Grainstone
Bunkers Range	Etina	RK220413.3B	264.50	-	-	Oolitic Grainstone
Bunkers Range	Etina	RK220413.4	269.00	-	-	Siltstone
Bunkers Range	Etina	RK220413.5	272.50	6.43	-6.50	Sandy Limestone
Bunkers Range	Etina	RK220413.6	275.90	8.60	-6.48	Sandy Limestone
Bunkers Range	Etina	RK220413.7	278.00	7.65	-7.77	Sandy Limestone
Bunkers Range	Etina	RK220413.8	282.80	7.91	-7.36	Sandy Limestone
Bunkers Range	Etina	RK220413.9	284.00	5.02	-9.29	Laminated Dolomicrite
Bunkers Range	Etina	RK220413.10	287.50	-	-	Laminated Dolomicrite
Bunkers Range	Etina	RK220413.11	292.00	4.69	-6.98	Conglomerate
Bunkers Range	Etina	RK220413.12	295.40	4.59	-9.75	Siltstone
Bunkers Range	Etina	RK220413.13A	297.50	5.05	-9.80	Resistant Shale
Bunkers Range	Etina	RK220413.13A*	297.50	4.41	-9.77	Resistant Shale
Bunkers Range	Etina	RK220413.13B	297.50	5.13	-10.26	Resistant Shale
Bunkers Range	Etina	RK220413.14	300.00	3.91	-9.67	Shale
Bunkers Range	Etina	RK220413.15	304.50	5.81	-9.97	Resistant Shale
Bunkers Range	Etina	RK220413.16	303.50	-	-	Siltstone
Bunkers Range	Etina	RK220413.17	307.30	5.83	-10.04	Cemented Siltstone
Bunkers Range	Etina	RK220413.18A	316.00	8.66	-8.22	Sandy Limestone
Bunkers Range	Etina	RK220413.18A*	316.00	5.76	-9.59	Sandy Limestone
Bunkers Range	Etina	RK220413.18B	316.00	9.08	-8.46	Sandy Limestone
Bunkers Range	Etina	RK220413.19	320.00	-	-	Dolospar Rip-Up Clast
Bunkers Range	Etina	RK220413.20A	322.00	7.48	-6.65	Microbial Laminite

Section	Formation	Sample No.	Height (m)	$\delta^{13}C_{carb}$	$\delta^{18}O_{carb}$	Lithology
Bunkers Range	Etina	RK220413.20B	322.00	8.39	-7.41	Microbial Laminite
Bunkers Range	Etina	RK220413.21	322.50	9.14	-7.44	Oolitic Grainstone
Bunkers Range	Etina	RK220413.22A	323.00	8.10	-5.48	Oolitic Grainstone
Bunkers Range	Etina	RK220413.22B	323.00	8.69	-5.88	Oolitic Grainstone
Bunkers Range	Etina	RK220413.23	327.50	9.30	-6.52	Pebbly Microspar
Bunkers Range	Etina	RK220413.24	332.50	8.78	-6.09	Pebbly Microspar
Bunkers Range	Etina	RK220413.25A	335.00	8.10	-4.01	Dolomicrite
Bunkers Range	Etina	RK220413.25B	335.00	8.59	-5.37	Dolomicrite
Bunkers Range	Etina	RK220413.26	35.25	8.65	-5.27	Intraclast Conglomerate
Bunkers Range	Etina	RK220413.26*	35.25	8.36	-5.31	Intraclast Conglomerate
Bunkers Range	Etina	RK220413.27A	335.00	8.94	-7.15	Microbial Laminite
Bunkers Range	Etina	RK220413.27B	335.00	9.62	-7.75	Microbial Laminite
Bunkers Range	Etina	RK220413.28A	342.00	8.95	-5.25	Oolitic Grainstone
Bunkers Range	Etina	RK220413.28B	342.00	9.08	-4.33	Oolitic Grainstone
Bunkers Range	Etina	RK220413.29	346.80	4.89	-6.28	Oolitic Grainstone
Bunkers Range	Etina	RK220413.30	347.50	8.37	-4.84	Dolomicrite
Bunkers Range	Etina	RK220413.31	350.00	8.52	-4.78	Dolomicrite
Bunkers Range	Etina	RK220413.32	352.00	-	-	Laminated Microspar
Bunkers Range	Etina	RK220413.33	354.50	6.94	-4.83	Laminated Microspar
Bunkers Range	Etina	RK220413.34	357.50	-	-	Oolitic Grainstone
Bunkers Range	Etina	RK220413.35	360.50	8.09	-2.85	Oolitic Grainstone
Bunkers Range	Etina	RK220413.36	365.00	8.73	-2.89	Oolitic Grainstone
Bunkers Range	Etina	RK220413.37	366.10	-	-	Oolitic Grainstone
Bunkers Range	Etina	RK220413.38	370.00	6.60	-4.52	Stromatolite
Bunkers Range	Etina	RK220413.39	373.30	-	-	Microsparite
Bunkers Range	Etina	RK220413.40	375.00	7.56	-5.47	Microbial Laminite
Bunkers Range	Etina	RK220413.41	379.00	8.13	-4.13	Oolitic Grainstone
Bunkers Range	Etina	RK220413.42	382.10	4.00	-5.06	Oolitic Grainstone
Bunkers Range	Etina	RK220413.43	384.00	8.51	-6.04	Microbial Laminite
Bunkers Range	Etina	RK220413.44	386.50	6.71	-5.14	Microbial Laminite
Bunkers Range	Etina	RK220413.45	394.50	8.37	-6.42	Microbial Laminite
Bunkers Range	Etina	RK220413.46	396.50	9.28	-6.84	Microbial Laminite
Bunkers Range	Etina	RK220413.47	399.50	10.26	-6.71	Microbial Laminite
Bunkers Range	Etina	RK220413.48	404.25	8.56	-5.59	Microbial Laminite
Bunkers Range	Etina	RK220413.49A	409.50	9.42	-5.33	Gritty Sand
Bunkers Range	Etina	RK220413.49B	409.50	8.38	-6.03	Gritty Sand
Bunkers Range	Etina	RK220413.50	414.00	9.23	-2.77	Oolitic Grainstone
Bunkers Range	Etina	RK220413.51	420.00	8.07	-5.99	Microbial Laminite
Bunkers Range	Etina	RK220413.52	424.70	5.65	-5.12	Flake Conglomerate
Bunkers Range	Etina	RK220413.52*	424.70	5.46	-5.17	Flake Conglomerate
Bunkers Range	Etina	RK220413.53A	431.25	9.17	-5.79	Microbial Laminite
Bunkers Range	Etina	RK220413.53B	431.25	9.48	-6.24	Microbial Laminite
Bunkers Range	Etina	RK220413.54	437.20	8.63	-6.02	Microbial Laminite
Bunkers Range	Etina	RK220413.54*	437.20	8.33	-5.73	Microbial Laminite
Bunkers Range	Etina	RK220413.55	442.50	8.71	-3.16	Oolitic Grainstone
Bunkers Range	Etina	RK220413.56	448.50	7.92	-3.66	Oolitic Grainstone
Bunkers Range	Etina	RK220413.57	453.50	-	-	Oolitic Grainstone
Bunkers Range	Etina	RK220413.58	458.00	8.49	-4.06	Oolitic Grainstone
Bunkers Range	Etina	RK220413.58*	458.00	8.19	-4.06	Oolitic Grainstone
Bunkers Range	Etina	RK220413.59	463.50	9.54	-5.14	Sandy Limestone

Section	Formation	Sample No.	Height (m)	$\delta^{13}C_{carb}$	$\delta^{18}O_{carb}$	Lithology
Bunkers Range	Etina	RK220413.60	464.25	6.63	-4.37	Sandy Limestone
Bunkers Range	Etina	RK220413.61	467.50	9.38	-6.27	Sandy Limestone
Bunkers Range	Etina	RK280413.1	478.50	6.78	-5.26	Oolitic Grainstone
Bunkers Range	Etina	RK280413.2	481.00	-	-	Sandy Limestone
Bunkers Range	Etina	RK280413.3	482.00	9.65	-5.24	Stromatolites
Bunkers Range	Etina	RK280413.4	482.50	-	-	Microbial Laminite
Bunkers Range	Etina	RK280413.5	485.00	7.39	-6.15	Sandy Limestone
Bunkers Range	Etina	RK280413.6	488.50	-	-	Intraclast Conglomerate
Bunkers Range	Etina	RK280413.7	491.50	9.61	-5.85	Microbial Laminite
Bunkers Range	Etina	RK280413.8	494.50	-	-	Sandy Limestone
Bunkers Range	Etina	RK280413.9	495.50	8.18	-6.23	Sandy Limestone
Bunkers Range	Etina	RK280413.10	497.50	-	-	Microbial Laminite
Bunkers Range	Etina	RK280413.11	500.25	7.88	-8.27	Siltstone
Bunkers Range	Etina	RK280413.12	503.25	7.80	-9.40	Siltstone
Bunkers Range	Etina	RK280413.13	509.00	-	-	Siltstone
Bunkers Range	Etina	RK280413.14	513.00	1.71	-7.67	Siltstone
Bunkers Range	Etina	RK280413.15	520.50	-	-	Siltstone
Bunkers Range	Etina	RK280413.16	528.25	3.74	-5.91	Siltstone
Bunkers Range	Etina	RK280413.17	532.50	6.25	-9.03	Cemented Sand
Bunkers Range	Etina	RK280413.18	533.25	7.18	-9.22	Microbial Laminite
Bunkers Range	Etina	RK280413.19	541.50	6.64	-6.39	Stromatolites
Bunkers Range	Etina	RK280413.20	544.50	9.43	-9.53	Sandy Limestone
Bunkers Range	Etina	RK280413.21	547.50	5.83	-8.08	Sandy Limestone
Bunkers Range	Etina	RK280413.22	547.50	-	-	Sandy Limestone
Bunkers Range	Etina	RK280413.23	553.00	4.19	-5.08	Sandy Limestone
Bunkers Range	Etina	RK280413.24	555.60	-	-	Siltstone
Bunkers Range	Etina	RK280413.25	559.25	8.33	-9.58	Sandy Limestone
Bunkers Range	Etina	RK280413.26	565.00	-	-	Laminated Micrite
Bunkers Range	Etina	RK280413.27	570.50	9.13	-6.44	Sandy Limestone
Bunkers Range	Etina	RK280413.28	571.50	-	-	Sandy Limestone
Bunkers Range	Etina	RK280413.29	572.50	9.45	-7.25	Sandy Limestone
Bunkers Range	Etina	RK280413.30	574.50	-	-	Microbial Laminite
Bunkers Range	Etina	RK280413.31	578.50	8.93	-6.75	Microbial Laminite
Bunkers Range	Etina	RK280413.32	583.00	-	-	Microbial Laminite
Bunkers Range	Etina	RK280413.33	585.00	8.89	-6.79	Microbial Laminite
Bunkers Range	Etina	RK280413.34	592.00	-	-	Sandy Limestone
Bunkers Range	Etina	RK280413.35	600.00	9.31	-7.09	Microbial Laminite
Bunkers Range	Etina	RK280413.36	607.00	-	-	Stromatolite
Bunkers Range	Etina	RK280413.37	610.50	8.32	-7.40	Stromatolite
Bunkers Range	Etina	RK280413.38	617.00	-	-	Stromatolite
Bunkers Range	Etina	RK280413.39	624.00	8.91	-6.70	Stromatolite
Bunkers Range	Etina	RK280413.40	633.50	-	-	Microbial Laminite
Bunkers Range	Etina	RK280413.41	635.50	9.16	-8.42	Sandy Limestone
Bunkers Range	Etina	RK280413.42	638.00	-	-	Stromatolite
Bunkers Range	Etina	RK280413.43	643.00	9.24	-7.90	Sandy Limestone
Bunkers Range	Etina	RK280413.44	648.50	-	-	Sandy Limestone
Bunkers Range	Etina	RK280413.45	655.00	7.83	-9.41	Microsparite
Bunkers Range	Etina	RK280413.46	657.50	-	-	Microbial Laminite
Bunkers Range	Etina	RK280413.47	667.00	7.17	-10.68	Microbial Laminite
Bunkers Range	Etina	RK280413.48	672.00	5.18	-11.52	Microbial Laminite

Section	Formation	Sample No.	Height (m)	$\delta^{13}C_{carb}$	$\delta^{18}O_{carb}$	Lithology
Bunkers Range	Etina	RK290413.1	673.00	2.26	-6.35	Siltstone
Bunkers Range	Etina	RK290413.2	683.00	0.97	-8.56	Siltstone
Bunkers Range	Etina	RK290413.3	694.00	1.22	-8.88	Siltstone
Bunkers Range	Etina	RK290413.4	704.00	3.29	-8.63	Siltstone
Bunkers Range	Etina	RK290413.5	715.00	5.99	-9.89	Cemented Siltstone
Bunkers Range	Etina	RK290413.6	719.50	5.73	-10.72	Cemented Siltstone
Bunkers Range	Etina	RK290413.7	732.00	4.21	-8.69	Cemented Siltstone
Bunkers Range	Etina	RK290413.8	741.00	3.96	-8.54	Siltstone
Bunkers Range	Etina	RK290413.9	753.00	-	-	Siltstone
Bunkers Range	Etina	RK290413.10	763.00	0.47	-7.78	Siltstone
Bunkers Range	Etina	RK290413.11	774.00	-	-	Siltstone
Bunkers Range	Etina	RK290413.12	784.00	0.76	-7.33	Siltstone
Bunkers Range	Etina	RK290413.13	795.00	1.10	-8.78	Siltstone
Bunkers Range	Etina	RK290413.14	805.00	4.48	-8.68	Cemented Siltstone
Bunkers Range	Etina	RK290413.15	815.00	5.54	-9.51	Siltstone
Bunkers Range	Etina	RK290413.16	828.00	6.16	-10.67	Siltstone
Bunkers Range	Etina	RK290413.17A	841.00	6.45	-10.93	Sandstone
Bunkers Range	Etina	RK290413.17B	841.00	6.70	-9.93	Sandstone
Bunkers Range	Etina	RK290413.18	843.50	7.56	-12.06	Microbial Laminite
Bunkers Range	Etina	RK290413.19	845.00	6.24	-8.77	Sandy Limestone
Bunkers Range	Etina	RK290413.20	852.00	-	-	Cemented Sands
Bunkers Range	Etina	RK290413.21	857.00	-	-	Cemented Siltstone
Bunkers Range	Etina	RK290413.22	860.50	-	-	Pebbly Limestone
Bunkers Range	Etina	RK290413.23	870.50	-	-	Cross-Bedded Sandy Limestone
Bunkers Range	Etina	RK290413.24	878.50	-	-	Cross-Bedded Sandy Limestone
Bunkers Range	Etina	RK290413.25	882.50	-	-	Stromatolites
Bunkers Range	Etina	RK290413.26	889.50	-	-	Stromatolites
Bunkers Range	Etina	RK290413.27	894.00	-	-	Stromatolites
Bunkers Range	Etina	RK290413.28	894.50	-	-	Cemented Siltstone
Bunkers Range	Etina	RK290413.29	905.00	0.89	-8.65	Siltstone
Bunkers Range	Etina	RK290413.30	916.00	-1.14	-9.27	Siltstone
Bunkers Range	Etina	RK290413.31	933.00	4.07	-8.16	Siltstone
Bunkers Range	Etina	RK290413.32	950.00	3.53	-9.09	Siltstone
Bunkers Range	Etina	RK290413.33	959.50	4.36	-8.69	cemented Shale
Bunkers Range	Etina	RK290413.34	970.00	3.35	-3.72	Siltstone
Bunkers Range	Etina	RK290413.35	973.00	6.63	-8.68	Sandstone
Bunkers Range	Etina	RK290413.36	974.50	6.75	-10.29	Stromatolites
Bunkers Range	Etina	RK290413.37	986.00	9.59	-9.05	Sandy Limestone
Bunkers Range	Etina	RK290413.38	1005.25	0.54	-8.62	Siltstone
Bunkers Range	Etina	RK290413.39	1015.00	2.76	-6.69	Siltstone
Bunkers Range	Etina	RK290413.40	1025.90	4.42	-8.11	Cemented Shale
Bunkers Range	Etina	RK290413.41	1030.00	6.63	-10.88	Stromatolites
Bunkers Range	Etina	RK290413.42A	1032.00	4.47	-17.08	Pebbly Microsparite
Bunkers Range	Etina	RK290413.42B	1032.00	1.64	-8.66	Pebbly Microsparite
Bunkers Range	Etina	RK290413.42C	1032.00	4.45	-11.06	Pebbly Microsparite
Bunkers Range	Etina	RK290413.43	1035.00	8.97	-11.02	Pebbly Microsparite
Bunkers Range	Etina	RK290413.44	1035.50	-	-	Pebbly Microsparite
Bunkers Range	Etina	RK290413.45	1036.00	-	-	Pebbly Microsparite
Bunkers Range	Etina	RK290413.46	1037.00	-	-	Pebbly Microsparite
Bunkers Range	Etina	RK290413.47	1038.50	-	-	Pebbly Microsparite

*= repeat analysis
Letters on the end of the sample number correspond to analysis of different sample components